



Provided by the author(s) and University of Galway in accordance with publisher policies. Please cite the published version when available.

|                  |   |
|------------------|---|
| Title            | Development of a tidal flow model for optimisation of tidal turbine arrays      |
| Author(s)        | Phoenix, Anna   |
| Publication Date | 2018-02-19  |
| Item record      | <a href="http://hdl.handle.net/10379/7145">http://hdl.handle.net/10379/7145</a> |

Downloaded 2024-04-26T23:25:43Z

Some rights reserved. For more information, please see the item record link above.



# DEVELOPMENT OF A TIDAL FLOW MODEL FOR OPTIMISATION OF TIDAL TURBINE ARRAYS

BY  
ANNA PHOENIX

Dissertation submitted to NUI, Galway in partial fulfilment  
of the requirements for the degree of PhD

Discipline of Civil Engineering  
College of Engineering and Informatics  
National University of Ireland, Galway  
September 2017

Head of Discipline  
Dr Bryan McCabe

Supervisor  
Dr Stephen Nash

## Declaration

I declare that this dissertation, in whole or in part, has not been submitted to any University as an exercise for a degree. I further declare that, except where reference is given, the work is entirely my own.

Signed:

---

Anna Phoenix

September 2017

## **Dedication**

I dedicate this thesis to my Mum and Dad. Without them I would never have gotten this far. And to Donnacha, for always being there for me.

## **Abstract**

Tidal current turbines have the potential to provide a proportion of global energy requirements. Installations to date have been singular test devices but commercial application will involve multiple devices deployed in farms. The viability of large-scale tidal turbine arrays will depend on the expected energy yield of the farm and the associated hydro-environmental impacts. The effects are, as yet, still relatively unknown although numerical models have been used to show that they can be significant.

In this study a 2D hydrodynamic tidal flow model has been developed to facilitate the modelling of tidal turbine arrays so that one can determine an optimum array layout with regard to both power capture and hydrodynamic impacts. This involved a number of model development stages to facilitate (1) calculation of the available resource, (2) simulation of energy extraction, (3) power quantification and (4) implementation of the array optimisation algorithm.

The first model development stage was to establish and implement a methodology which accurately quantifies available resource. This research is based on horizontal axis turbines, whose fixed orientation results in maximum energy extraction occurring when flow is travelling perpendicular to the turbine swept area. The methodology therefore utilises harmonic and ellipse analyses to determine the primary direction of current flow at a site, which is then used to quantify available power. This results in a higher degree of sophistication compared to traditional approaches which are based on the total velocity vector.

The tidal flow model was next developed to enable simulation of tidal energy extraction via the momentum sink approach. This requires parameterisation of the turbine thrust coefficient which is theoretically defined based on the undisturbed velocity upstream of a turbine but

is usually calculated using the local velocity at the turbine. A sensitivity analysis concluded that if calculation of the thrust is based on localised current velocities it is necessary to specify a localised thrust coefficient. Based on this finding, a thrust coefficient chart has been developed from which suitable localised thrust coefficients can be determined based on the turbine grid cell blockage ratio for a particular model grid cell. The third stage of development involved incorporating a power quantification calculation into the energy extraction model. The power extracted by an individual turbine is based on the model-calculated turbine thrust.

The final stage of model development involved developing an optimisation algorithm which determines an optimal array configuration for maximum energy capture whilst employing spatial and environmental impact constraints. This algorithm was incorporated into the numerical model and application of the fully developed model to test cases demonstrated that optimal arrays should be staggered, thereby producing higher efficiencies than symmetrical inline arrays.

This is the first optimisation model to relate hydro-environmental impacts to the level of energy extraction. The fully developed model could be extremely useful for determining the economic viability of proposed arrays, enabling determination of environmentally-safe levels of tidal energy extraction, and completion of a realistic and accurate cost-benefit analysis for early stage tidal energy projects. It is therefore, potentially, a very valuable tool for tidal energy researchers and turbine developers.

## **Acknowledgements**

The author wishes to thank Prof Padraic O'Donoghue for facilities granted and for supporting this research.

The author would also like to thank the Irish Research Council for funding this research.

Thank you to my supervisor, Dr Stephen Nash, for his technical advice, encouragement and guidance throughout the last four years. I would also like to thank my research group director, Prof Michael Hartnett, for his support during the course of this research. Many thanks to all the engineering staff for helping me through my studies.

Big thanks to all my friends for the much needed chats and support. Especially Raydo, for all the brain-storming and gossip sessions, Moroney, for being a great housemate and of course Kima and Cosmo. Special thanks to Donnacha for all his love and support, even through the meltdowns. And to mum, thanks for everything.

# Table of Contents

|   |             |
|---|-------------|
| <b>Declaration .....</b>  | <b>ii</b>   |
| <b>Dedication.....</b>  | <b>iii</b>  |
| <b>Abstract .....</b>   | <b>iv</b>   |
| <b>Acknowledgements .....</b>                                   | <b>vi</b>   |
| <b>Table of Contents.....</b>                                   | <b>vii</b>  |
| <b>List of Figures .....</b>                                    | <b>xiv</b>  |
| <b>Mathematical Notations.....</b>                              | <b>xxvi</b> |
| <b>1 Introduction .....</b>                                     | <b>1</b>    |
| 1.1 Tidal Energy .....  | 1           |
| 1.2 Numerical Modelling.....                                    | 3           |
| 1.3 Aims and Objectives .....                                   | 5           |
| 1.4 Thesis Layout and Content .....                             | 6           |
| 1.5 Publications.....   | 9           |
| <b>2 Literature Review .....</b>                                | <b>10</b>   |
| 2.1 Introduction .....  | 10          |
| 2.2 Tides and Tidal Currents .....                              | 11          |
| 2.3 Tidal Stream Energy Devices.....                            | 14          |
| 2.4 Tidal Stream Resource Assessment .....                      | 16          |
| 2.4.1 Introduction.....   | 16          |
| 2.4.2 Kinetic Energy Flux.....                                  | 17          |
| 2.4.3 Resource Assessment Methodologies.....                    | 18          |
| 2.4.4 Factors Affecting Accuracy of Resource Assessments.....   | 20          |
| 2.4.4.1 Current Velocity Data used in Resource Assessments..... | 20          |
| 2.4.4.2 Formulation of available power equation.....            | 22          |
| 2.4.4.3 Turbine Impacts.....                                    | 24          |

|          |   |           |
|----------|---|-----------|
| 2.5      | Approaches to Numerical Modelling of Tidal Turbines ..... | 24        |
| 2.5.1    | Turbine Representation.....                               | 25        |
| 2.5.2    | Momentum Sink Approach.....                               | 27        |
| 2.5.3    | Array Optimisation.....                                   | 29        |
| 2.6      | Hydro-environmental Impacts of Tidal Turbines.....        | 30        |
| 2.6.1    | Summary of Environment Impact Studies.....                | 31        |
| 2.6.2    | Pilot Studies.....  | 32        |
| 2.6.3    | Laboratory and Numerical Model Studies.....               | 34        |
| 2.7      | Hydrodynamic Impacts of Tidal Turbines .....              | 40        |
| 2.7.1    | Hydrodynamic Effects: Single Turbine.....                 | 40        |
| 2.7.1.1  | Reduced Wake Velocities.....                              | 40        |
| 2.7.1.2  | Accelerated Bypass Velocities.....                        | 43        |
| 2.7.1.3  | Turbulence.....   | 43        |
| 2.7.1.4  | Water Levels.....   | 44        |
| 2.7.2    | Hydrodynamic Effects: Arrays.....                         | 44        |
| 2.8      | Environmental Impacts of Tidal Turbines .....             | 46        |
| 2.9      | Summary and Conclusions .....                             | 48        |
| <b>3</b> | <b>Numerical Modelling Theory .....</b>                   | <b>52</b> |
| 3.1      | Introduction .....  | 52        |
| 3.1.1    | Model Description .....                                   | 53        |
| 3.1.2    | Justification of Model Choice.....                        | 55        |
| 3.2      | Governing Equations.....                                  | 55        |
| 3.2.1    | Finite Difference Formulations .....                      | 58        |
| 3.3      | Model Accuracy, Stability and Resolution .....            | 58        |
| 3.4      | Model Architecture .....                                  | 60        |
| 3.5      | The Nested Model.....                                     | 62        |

|          |   |           |
|----------|---|-----------|
| 3.5.1    | Nested Model Grids .....  | 62        |
| 3.6      | MSN One-way Nested Model.....                                       | 64        |
| 3.7      | The Open Boundary Problem.....                                      | 66        |
| 3.7.1    | Specification of the Open Boundary.....                             | 68        |
| 3.7.2    | Model Architecture .....  | 69        |
| 3.8      | Tidal Flushing.....   | 71        |
| 3.9      | Tidal Harmonics and Tidal Ellipse Analysis.....                     | 71        |
| 3.9.1    | Tidal Harmonic Analysis.....  | 72        |
| 3.9.2    | Tidal Harmonic Analysis Software.....                               | 78        |
| 3.9.3    | Tidal Ellipse Theory.....   | 83        |
| <b>4</b> | <b>Resource Assessment .....</b>                                    | <b>86</b> |
| 4.1      | Introduction .....  | 86        |
| 4.2      | Tidal Resource Assessment.....                                      | 87        |
| 4.2.1    | Traditional Methodologies for Available Resource<br>Assessment..... | 87        |
| 4.2.2    | New Methodology for Available Resource Assessment .....             | 87        |
| 4.3      | The Shannon Estuary Model.....                                      | 88        |
| 4.3.1    | General Description of the Shannon Estuary .....                    | 88        |
| 4.3.2    | Model Description .....   | 90        |
| 4.3.3    | Model validation .....  | 92        |
| 4.4      | Development of Model to Implement New resource<br>Assessment.....   | 95        |
| 4.4.1    | Importance of Considering Flow Direction.....                       | 95        |
| 4.4.2    | Development of Resource Assessment Model.....                       | 96        |
| 4.5      | Shannon Estuary Case Study Results .....                            | 98        |
| 4.5.1    | Testing of the Ellipse Code .....                                   | 99        |
| 4.5.2    | Available Resource Assessments .....                                | 102       |

|          |  |            |
|----------|--|------------|
| 4.5.3    | Site Identification and Device Orientation.....          | 109        |
| 4.5.4    | Preferred Berths.....                                    | 112        |
| 4.5.5    | Tidal Current Analysis.....                              | 112        |
| 4.5.6    | Frequency of Resource Availability.....                  | 114        |
| 4.5.7    | Recommended Deployment Sites.....                        | 123        |
| 4.6      | Effect of River Flow on Resource Assessment.....         | 128        |
| 4.7      | Summary and Conclusions.....                             | 129        |
| <b>5</b> | <b>Energy Extraction Model.....</b>                      | <b>132</b> |
| 5.1      | Introduction.....  | 132        |
| 5.2      | Development of the Energy Extraction Model.....          | 133        |
| 5.2.1    | Turbine Representation within the Model.....             | 133        |
| 5.2.2    | Development of Model Architecture.....                   | 136        |
| 5.2.3    | Incorporation of Energy Extraction into Source Code..... | 140        |
| 5.3      | Thrust and Power Calculation.....                        | 146        |
| 5.3.1    | Turbine Thrust Coefficient.....                          | 146        |
| 5.3.2    | Power Output.....  | 147        |
| 5.4      | Model Application: Idealised Domain.....                 | 149        |
| 5.4.1    | Model Set-up.....  | 149        |
| 5.4.2    | Model Sensitivity to the Thrust Coefficient.....         | 150        |
| 5.4.3    | Operating Conditions.....                                | 154        |
| 5.4.4    | Model Validation.....                                    | 158        |
| 5.5      | Case Study of the Shannon Estuary.....                   | 159        |
| 5.5.1    | Hydrodynamic Numerical Model.....                        | 159        |
| 5.5.2    | Model Details.....                                       | 159        |
| 5.5.3    | Model Validation.....                                    | 160        |
| 5.5.4    | Impact of $C'_T$ Specification on Energy Capture.....    | 161        |

|          |  |            |
|----------|--|------------|
| 5.6      | Modelling Array Impacts on Residence Times .....                   | 168        |
| 5.6.1    | Model Set-up.....  | 169        |
| 5.6.2    | Array Configurations .....   | 171        |
| 5.6.3    | Impact on Current Velocities .....                                 | 173        |
| 5.6.3.1  | Headland Domain .....  | 173        |
| 5.6.3.2  | Headland and Island Domain.....                                    | 178        |
| 5.6.4    | Impact on Flushing.....  | 181        |
| 5.6.4.1  | Headland Domain .....  | 181        |
| 5.6.4.2  | Headland and Island Domain.....                                    | 183        |
| 5.7      | Summary and Conclusions .....                                      | 185        |
| <b>6</b> | <b>Optimisation of Tidal Turbine Arrays .....</b>                  | <b>187</b> |
| 6.1      | Introduction .....   | 187        |
| 6.2      | Turbine Spacing.....   | 187        |
| 6.2.1    | Model Set-up.....  | 188        |
| 6.2.2    | Numerical Simulations.....   | 188        |
| 6.3      | Development of Optimisation Model .....                            | 199        |
| 6.3.1    | Power Maximisation .....   | 201        |
| 6.3.2    | Power Maximisation and Impact Minimisation:.....                   | 203        |
| 6.4      | Development of Model Architecture .....                            | 206        |
| 6.5      | Testing Power Calculations for Multiple Turbines .....             | 210        |
| 6.5.1    | Model Set-up.....  | 210        |
| 6.5.2    | Power Quantification .....   | 210        |
| 6.6      | Testing the Optimisation Model.....                                | 213        |
| 6.6.1    | Testing of Turbine Placement based on Available Power ...          | 214        |
| 6.6.2    | Testing of Turbine Placement based on Velocity Constraint<br>..... | 215        |

|         |   |            |
|---------|---|------------|
| 6.7     | Comparison with a Published Study.....  | 217        |
| 6.8     | Model Application: Idealised Domain .....   | 221        |
| 6.8.1   | Model Set-up.....   | 221        |
| 6.8.2   | Array Configurations .....  | 222        |
| 6.8.3   | Opt_P Results .....   | 224        |
| 6.8.4   | Opt_P&V Results .....   | 231        |
| 6.9     | Case Study of the Shannon Estuary .....   | 235        |
| 6.9.1   | Hydrodynamic Numerical Model .....  | 235        |
| 6.9.2   | Model Scenarios .....   | 236        |
| 6.9.3   | Array Configurations .....  | 238        |
| 6.9.4   | Energy Capture .....  | 243        |
| 6.9.5   | Impact on Current Velocities .....  | 246        |
| 6.9.6   | Application of the Impact Constraint.....   | 249        |
| 6.10    | Summary and Conclusions .....   | 251        |
|         | <b>7 Summary and Conclusions.....</b>   | <b>253</b> |
| 7.1     | Summary.....  | 253        |
| 7.2     | Conclusions.....  | 258        |
| 7.3     | Recommendations for Further Research .....  | 261        |
|         | <b>References.....</b>  | <b>263</b> |
|         | <b>Appendix A: Review of Hydro-environmental Impacts of Tidal<br/>Energy Extraction .....</b> | <b>282</b> |
| A.1     | Hydrodynamic Impacts of Tidal Turbines .....  | 283        |
| A.1.1   | Hydrodynamic Effects: Single Turbine .....  | 283        |
| A.1.1.1 | Reduced Wake Velocities.....  | 284        |
| A.1.1.2 | Accelerated Bypass Velocities.....  | 290        |
| A.1.1.3 | Turbulence.....   | 290        |

|         |   |            |
|---------|---|------------|
| A.1.1.4 | Water Levels.....   | 291        |
| A.1.2   | Hydrodynamic Effects: Arrays.....   | 292        |
| A.1.2.1 | Wake Merging.....   | 292        |
| A.1.2.2 | Array Effects on Velocities.....  | 293        |
| A.1.2.3 | Array Effects on Water Levels.....  | 296        |
| A.2     | Environmental Impacts of Tidal Turbines.....  | 299        |
| A.2.1   | Suspended Sediments.....  | 299        |
| A.2.2   | Tidal Flushing.....   | 304        |
| A.2.3   | Other Water Quality Measures.....   | 306        |
|         | <b>Appendix B: Recursion Formulae.....</b>  | <b>308</b> |
|         | <b>Appendix C: Method of Least Squares Fit for Tidal Harmonic<br/>Analysis.....</b> | <b>317</b> |

## List of Figures

|  |    |
|--|----|
| Figure 1.1: SeaGen tidal turbine (Source: Siemens UK, 2010).....   | 2  |
| Figure 1.2: Tidal turbine array (Source: SRM Projects LTD, 2012)....   | 3  |
| Figure 2.1: Illustration of generation of tides (Source: Fallon, 2012).<br>.....   | 12 |
| Figure 2.2: Illustration of high and low tides (Source: Boon, 2017)..  | 13 |
| Figure 2.3: Illustration of generation of Spring and Neap tides<br>(Source: Fallon, 2012). .....   | 13 |
| Figure 2.4: (a) Horizontal axis turbine, (b) vertical axis turbine, (c)<br>oscillating hydrofoil, (d) enclosed tips (venturi), (e) Archimedes screw<br>(f) tidal kite. ....  | 14 |
| Figure 2.5: Numerical approaches to representation of tidal turbines<br>in CFD models. ....  | 27 |
| Figure 2.6: In-situ turbines for which some environmental impact data<br>are available: (a) MCT's SeaGen turbine, (b) Verdant Power's Dyno<br>turbine (c) the SCHOTTEL tidal generator.....  | 33 |
| Figure 2.7: (a) 0.8m diameter scaled rotor (Myers & Bahaj, 2009) and<br>(b) mesh disc rotor simulator (Myers & Bahaj, 2010) used in<br>laboratory studies of turbine impacts. ....   | 35 |
| Figure 2.8: Longitudinal variation in $U_g$ for (a) single scaled rotors<br>(reproduced from: Bahaj et al. (2007); Myers & Bahaj (2009); Myers<br>& Bahaj (2010); Stallard et al. (2013)) and (b) 3 porous discs of<br>different $C_T$ values (reproduced from: Bahaj et al. (2007); Myers &<br>Bahaj (2009); Myers & Bahaj (2010); Stallard et al. (2013)). ..... | 41 |
| Figure 3.2: A shallow, well-mixed water body. ....   | 56 |
| Figure 3.3: Principle of the two-dimensional model (Nash, 2010). ....  | 56 |
| Figure 3.4: Flowchart of model subroutines. ....   | 61 |
| Figure 3.5: Nested model grid structure (Nash, 2010). ....   | 63 |
| Figure 3.6: Schematic of a one-way nested model grids with a 3:1<br>spatial nesting ratio: (a) the parent and child grids, (b) a detail of the<br>child grid interface (shaded cells represent child grid boundary)<br>(Nash, 2010). ....  | 64 |

|  |    |
|--|----|
| Figure 3.7: The nesting procedure. Subscripts $p$ and $c$ denote parent and child grids (Nash, 2010). .....  | 65 |
| Figure 3.8: Schematic of the internal boundary configuration for a 3:1 nesting ratio (Nash & Hartnett, 2014). .....  | 69 |
| Figure 3.9: Flowchart of model subroutines including amendments for one-way nesting. ....  | 70 |
| Figure 3.10: Example of tidal gauge data plot (Marine Institute, 2017). .....  | 72 |
| Figure 3.11: A tidal curve resulting from its individual constituents (Naval Postgraduate School (Department of Oceanography), 2015). .....  | 75 |
| Figure 3.12: Flowchart of the HTAS model implemented in DIVAST. ....   | 80 |
| Figure 3.13 Flowchart of modified DIVAST model to include HTAS. ....   | 83 |
| Figure 3.14: Basic parameters of a current ellipse. ....   | 84 |
| Figure 3.15: Examples of tidal current ellipses indicating (a) rectilinear, (b) rotary flow. ....  | 85 |
| Figure 4.1: (a) Potential current energy sites in Ireland (estimated practical energy resource is shown in GWh/y) (SEI, 2006) (b) Map of the Shannon estuary (Source: Google Maps). .... | 89 |
| Figure 4.3: Composite map of SIFP study area (Source: SIFP, 2013). .....   | 89 |
| Figure 4.4 Bathymetry plot of Shannon estuary (legend shows mean water depth in m). ....   | 91 |
| Figure 4.5: River flow data for (a) Shannon, (b) Fergus rivers (Source: OPW). .....  | 91 |
| Figure 4.6: Extent of model domain and locations of measured data for tidal elevations (T1-T6) and tidal current velocities (C1 & C2) used to validate the model. ....                   | 93 |
| Figure 4.8: Comparison of measured water elevation data against the predicted model elevation data at T2 and T5 (Data courtesy: Shannon Foynes Port Company). ....                       | 94 |

|   |     |
|---|-----|
| Figure 4.9: Comparison of measured current velocity data against the predicted model current data at C1 (Data courtesy: Fallon et al. 2014).....  | 94  |
| Figure 4.10: Comparison of measured current velocity data against the predicted model current data at C2 for 4th January 2003 (Data courtesy:SEI, 2004). .....  | 94  |
| Figure 4.11: Flow chart outlining main steps in resource assessment methodology. ....   | 96  |
| Figure 4.12: Water elevation boundary data resulting from tidal constituent data.....   | 99  |
| Figure 4.13: Cahercon ellipse validation location.....  | 100 |
| Figure 4.14: Model outputs at Cahercon: (a) Direction of flow over 3 tidal cycles (b) total velocity vectors at 0.5 hour intervals over 1 tidal cycle (c) tidal current ellipses for relevant harmonic constituents determined for a period of 3 tidal cycles. .... | 100 |
| Figure 4.16: Mean available power for the Shannon estuary determined using the (a) FFA (b) TVA and (c) PDA (Units of legend: $W/m^2$ ). ....  | 103 |
| Figure 4.17: Spring tide currents at (a) peak flood and (b) peak ebb (legend shows current speed in m/s). ....  | 104 |
| Figure 4.18: Percentage difference between available powers calculated using (a) FFA and TVA, (b) TVA and PDA (legend shows percentage differences in %). ....  | 106 |
| Figure 4.19: Spring and neap current velocities over one tidal cycle at Cahercon location. ....   | 107 |
| Figure 4.20: Ratios of peak ebb velocities to peak flood velocities. Value > 1 indicates larger peak ebb velocities. ....   | 107 |
| Figure 4.21: (a) Flow direction, (b) Available power ( $W/m^2$ ) over 2 tidal cycles as determined using TVA and PDA at locations (a) 1, (b) 2, (c) 3.....  | 108 |
| Figure 4.22: Ratio of $M_2$ major axis to the sum of all constituent's major axis. ....   | 110 |

|  |     |
|--|-----|
| Figure 4.23: Ratio of minor to major axis (ER) of $M_2$ ellipses across the Shannon estuary.....   | 111 |
| Figure 4.24: Angle of inclination of $M_2$ ellipse across the Shannon estuary, measured counter-clockwise from North.....  | 111 |
| Figure 4.25: Suitable deployment locations based on power availability and flow direction.....   | 111 |
| Figure 4.26: Locations of interest (A-F).....  | 112 |
| Figure 4.27: (a) Tidal current ellipses and (b-d) comparison of VTA and PDA assessments at location A for (b) current velocity data, (c) frequency of power availability and (d) available power in each velocity range..... | 115 |
| Figure 4.28: (a) Tidal current ellipses and (b-c) comparison of VTA and PDA assessments at location B for (b) current velocity data and (c) frequency of power availability.....   | 116 |
| Figure 4.29: (a) Tidal current ellipses and (b-c) comparison of VTA and PDA assessments at location C for (b) current velocity data and (c) frequency of power availability.....   | 117 |
| Figure 4.30: (a) Tidal current ellipses and (b-c) comparison of VTA and PDA assessments at location D for (b) current velocity data and (c) frequency of power availability.....   | 118 |
| Figure 4.31: (a) Tidal current ellipses and (b-c) comparison of VTA and PDA assessments at location E for (b) current velocity data and (c) frequency of power availability.....   | 119 |
| Figure 4.32: (a) Tidal current ellipses and (b-c) comparison of VTA and PDA assessments at location F for (b) current velocity data and (c) frequency of power availability.....   | 120 |
| Figure 4.33: Locations of interest (G-K) and available power as determined using PDA (Units of legend: $W/m^2$ ). .....  | 124 |
| Figure 4.35: Comparison of time-varying total and primary direction velocities at locations of interest (G-K).....   | 125 |
| Figure 4.36: Comparison of (a) frequency of power availability and (b) available power in each velocity range at locations (1) I, (2) J and (3) K determined using both methods.....   | 126 |

|   |     |
|---|-----|
| Figure 4.37: Change in available powers calculated with and without river flow based on FFA. ....   | 129 |
| Figure 5.1: One dimensional linear momentum actuator disc theory in open channel flow (Houlsby et al. 2008).....  | 134 |
| Figure 5.2: Flowchart of coarse model subroutines, including the energy extraction code (subroutines which have been modified/ added to include energy extraction are shaded blue).....               | 138 |
| Figure 5.3: Flowchart of nested MSN model subroutines, including the energy extraction code (subroutines which have been modified/ added to include energy extraction are shaded blue).....           | 139 |
| Figure 5.4: (a) Comparison of $P_{E(th)}$ to $P_{E(mod)}$ for each model scenario, (b) comparison of total current velocities at turbine grid cell (I, J).....  | 151 |
| Figure 5.5: Percentage differences in peak velocities for a single turbine scenario relative to a no turbine scenario using $C_T$ values of (a) 0.8, (b) 0.9, (c) 1.0, (d) 1.3, (e) 2.0, (f) 3.0..... | 152 |
| Figure 5.6: Changes in current speed (%) along the longitudinal wake centreline for a range of $C_T$ values.....  | 153 |
| Figure 5.7: Thrust sensitivity chart.....   | 155 |
| Figure 5.8: Relationship of thrust sensitivity to grid cell blockage ratio.....   | 155 |
| Figure 5.9: (a) Comparison of $P_{E(th)}$ and $P_{E(mod)}$ , (b) impact of turbine deployment on $V_m$ for a single turbine model scenario of grid spacing 16m and depth 50m.....                     | 157 |
| Figure 5.10: (a) Comparison of $P_{E(th)}$ and $P_{E(mod)}$ , (b) impact of turbine deployment on $V_m$ for a single turbine model scenario of grid spacing 40m and depth 40m.....                    | 157 |
| Figure 5.11: Velocity deficits due to a single turbine.....   | 159 |
| Figure 5.12: Extent of domains, mean water depths and turbine locations (denoted TB) for Shannon model.....   | 161 |
| Figure 5.13: Comparison of (a) spring (b) neap measured and modelled current velocities at C1 (Source: Fallon et al. (2014))....  | 161 |

|  |     |
|--|-----|
| Figure 5.14: Turbine 1: Comparison of (1) power capture and (2) velocity time-series over a spring tidal cycle for (a) CG189 model, (b) NG63 model and (c) NG21 model.....                             | 163 |
| Figure 5.15: Turbine 2: Comparison of (1) power capture and (2) velocity time-series over a spring tidal cycle for (a) CG189 model, (b) NG63 model and (c) NG21 model.....                             | 164 |
| Figure 5.16: Turbine 3: Comparison of (1) power capture and (2) velocity time-series over a spring tidal cycle for (a) CG189 model, (b) NG63 model and (c) NG21 model.....                             | 165 |
| Figure 5.17: Turbine 4: Comparison of (1) power capture and (2) velocity time-series over a spring tidal cycle for (a) CG189 model, (b) NG63 model and (c) NG21 model.....                             | 166 |
| Figure 5.18: Idealised tidal environments: (a) headland, (b) headland and island.....  | 170 |
| Figure 5.19: Turbine arrays deployed in headland domain: (a) 50T_1RD, (b) 50T_3RD, (c) 50T_5RD, (d) 84T_3RD, (e) 364T_1RD.....   | 172 |
| Figure 5.20: Turbine arrays deployed in headland and island domain: (a) 25T_1RD, (b) 25T_3RD, (c) 81T_1RD.....   | 173 |
| Figure 5.21: Peak ebb current velocities for each model scenario: (a) No Turbine, (b) 50T_1RD, (c) 50T_3RD, (d) 50T_5RD, (e) 84T_3RD, (f) 364T_1RD (legend shows total current velocities in m/s)..... | 174 |
| Figure 5.22: Percentage change in peak ebb current velocities for each model scenario: (a) 50T_1RD, (b) 50T_3RD, (c) 50T_5RD, (d) 84T_3RD, (e) 364T_1RD (legend % difference (%)).....                 | 175 |
| Figure 5.23: Peak ebb current velocities for 364T_1RD model scenario based on (a) $C'_T = 1.3$ and (b) $C'_T = 1.0$ .....  | 177 |
| Figure 5.24: Percentage change in peak ebb current velocities for 364T_1RD model scenario based on $C'_T = 1.3$ and $C'_T = 1.0$ .....   | 178 |
| Figure 5.25: Peak ebb current velocities for each model scenario: (a) No Turbine, (b) 25T_1RD, (c) 25T_3RD, (d) 81T_1RD (legend shows total current velocities in m/s).....                            | 179 |

|   |     |
|---|-----|
| Figure 5.26: Percentage change in peak ebb current velocities for each model scenario: (a) 25T_1RD, (b) 25T_3RD, (c) 81T_1RD (legend % difference (%)).....   | 180 |
| Figure 5.27: (a) Peak ebb current velocities for 364T_1RD model scenario based on $C'_T = 1.0$ , (b) percentage change in peak ebb current velocities for 364T_1RD model scenario based on $C'_T = 1.3$ and $C'_T = 1.0$ .....  | 180 |
| Figure 5.28: Regions of dye injection in headland domain (legend shows dye concentration (CN) in $\text{mg}/\text{m}^3$ ).....  | 182 |
| Figure 5.29: Average residence times, $\tau_r$ for each model scenario: (a) No Turbine, (b) 50T_1RD, (c) 50T_3RD, (d) 50T_5RD, (e) 84T_3RD, (f) 364T_1RD (legend shows residence time in days).....   | 183 |
| Figure 5.30: Regions of dye injection in headland and island domain (legend shows dye concentration (CN) in $\text{mg}/\text{m}^3$ ).....   | 184 |
| Figure 5.31: Average residence times, $\tau_r$ for each model scenario: (a) No Turbine, (b) 25T_1RD, (c) 25T_3RD, (d) 81T_1RD (legend shows residence time in days).....  | 184 |
| Figure 6.1: Percentage difference in velocities at peak ebb for a single turbine for (a) the full model domain (units: %) (b) along the longitudinal wake centreline, and (c) along a number of lateral transects at various distances downstream of the turbine..... | 190 |
| Figure 6.2: (a) Current velocities over one tidal cycle before (NT) and after (T) turbine deployment, (b) power extracted by a single turbine over one tidal cycle, (c) energy capture per cycle of a single turbine. ....  | 191 |
| Figure 6.3: Percentage difference in velocities at peak ebb for deployment of (a) 2 turbines with no downstream spacing (b) 2 turbines with 3rd downstream spacing (c) 2 turbines with 5rd downstream spacing (d) a single turbine (units of legend: %).....          | 193 |
| Figure 6.4: Percentage difference in peak ebb velocities along longitudinal wake centreline for 1 turbine and 2 turbines deployed at 0RD, 3RD and 5RD downstream spacing.....   | 193 |
| Figure 6.5: Power extracted by each turbine (MW) at downstream spacings of (a) 0RD (b) 3RD and (c) 5RD. ....  | 194 |

|   |     |
|---|-----|
| Figure 6.6: Percentage difference in velocities at peak ebb for deployment of two turbines with lateral spacings of (a) 1RD (b) 3RD (c) 5RD (d) 10RD (units of legend: %). .....  | 197 |
| Figure 6.7: Percentage difference (%) downstream of two turbines deployed at (a) 1RD (b) 3RD (c) 5RD (d) 10RD.....  | 198 |
| Figure 6.8: Energy capture per cycle by each turbine at lateral spacings of (a) 1RD (b) 3RD and (c) 5RD (d) 10RD. ....  | 198 |
| Figure 6.10: Optimisation algorithm based on power.....   | 203 |
| Figure 6.10: Optimisation algorithm based on power and velocity impacts. ....   | 205 |
| Figure 6.11: Flowchart of DIVAST model subroutines. Including optimisation code based on both power and impact on velocities (subroutines which have been modified/ added to include optimisation are shaded).....                      | 208 |
| Figure 6.12: Flowchart of nested MSN model subroutines. Including optimisation code based on both power and impact on velocities (subroutines which have been modified/ added to include optimisation are shaded).....                  | 209 |
| Figure 6.14: Flowchart of nested MSN model subroutines. Including optimisation code based on both power and impact on velocities (subroutines which have been modified/ added to include optimisation are shaded).....                  | 209 |
| Figure 6.14: Comparison of $P_{E(th)}$ and $P_{E(mod)}$ for (a) T1, (b) T2, (c) T3, (d) T4. ....  | 212 |
| Figure 6.15 (a): $\varepsilon_{ava}$ (b) $\varepsilon_{Undis}$ calculated for T1 – T4.....  | 213 |
| Figure 6.16: Mean $P_{ava NT}$ for (a) $N_T=0$ , (b) $N_T=1$ , (c) $N_T=2$ , (d) $N_T=3$ (legend shows power in MW). Filled circles indicate turbines already added. Hollow circles indicate location of next turbine to be added. .... | 215 |
| Figure 6.17: Peak current velocity after 3 turbines deployed (legend shows peak current velocity in m/s). ....  | 216 |
| Figure 6.18: Mean $P_{ava TN}$ for $N_T=2$ (legend shows power in MW). ....   | 216 |

|   |     |
|---|-----|
| Figure 6.19: Peak current velocity after T3 is re-positioned (legend shows peak current velocity in m/s). .....   | 217 |
| Figure 6.20: (a) Model scenario selected for comparison (dashed lines show the specified turbine area) (b) initial turbine positions (Source: Funke et al. (2014)). .....                                       | 218 |
| Figure 6.21: Model domain showing peak velocity vectors and turbine deployment site (deployment site represented by black rectangle and total velocity vectors shown at every 4 <sup>th</sup> grid cell). ..... | 219 |
| Figure 6.22: Optimised turbine positions; (a) author's model (b) Funke's model.....   | 220 |
| Figure 6.23: Peak flood current velocities after array deployment; (a) author's model (b) Funke's model.....  | 220 |
| Figure 6.24: Inline array layout.....   | 223 |
| Figure 6.25: Opt_P array configurations resulting from scenario (a) O1, (b) O2, (c) O3, (d) O4. ....  | 223 |
| Figure 6.26: Opt_P&V array configurations resulting from scenario (a) O1, (b) O2, (c) O3, (d) O4.....   | 223 |
| Figure 6.27: (a) % difference in peak flood current velocities (b) energy capture (kWh/cycle) (c) turbine efficiency ( $\epsilon_{Undis}$ ), for scenarios 1-5 (INL-O4) .....                                   | 227 |
| Figure 6.28: Undisturbed current velocities across the channel.....   | 229 |
| Figure 6.29: (a) % difference in peak flood current velocities (b) energy capture (kWh/cycle) (c) turbine efficiency ( $\epsilon_{Undis}$ ), for scenarios (1) O1, (2) O2, (3) O3. ....                         | 233 |
| Figure 6.30: Extent of domains and mean water depths for Shannon model (legend shows mean water depth in m).....  | 236 |
| Figure 6.31: Suitable deployment locations based on power availability and flow direction.....  | 237 |
| Figure 6.32: NG21 optimised array configuration (locations where $H < H_{min}$ are shaded grey, legend shows $P_{ava N_T=18}$ in MW). ....  | 238 |
| Figure 6.33: Opt_P array configurations for CG189 Inline array. ....  | 239 |

|  |     |
|--|-----|
| Figure 6.34: Opt_P array configurations for (a) NG63, (b) NG21, resulting from scenario (1) INL, (2) O1, (3) O2 (contour shows mean water depth in m). .....   | 240 |
| Figure 6.35: Opt_P&V array configurations for (a) NG63, (b) NG21, resulting from scenario (2) O1 (contour shows mean water depth in m).....                    | 241 |
| Figure 6.36: (a) Undisturbed peak flood current velocities across (1) CG189, (2) NG63, (3) NG21 model domains, (b) time trace velocities for each domain. .... | 242 |
| Figure 6.37: Energy capture (kWh/cycle) for (a) NG63 and (b) NG21 resulting from scenario (1) INL, (2) O1, (3) O2.....   | 244 |
| Figure 6.38: % change in peak flood velocities after array deployment for (a) CG189, (b) NG63, (c) NG21, resulting from scenario (1) IN, (2) O1, (3) O2.....   | 247 |
| Figure 6.39: % change in peak flood velocities after array deployment for (a) NG63, (b) NG21, resulting from scenario O1. ....                                 | 250 |

## List of Tables

|  |     |
|--|-----|
| Table 2.1: Details of laboratory studies of energy removal impacts (w = tank width, d = water depth, $v_0$ = velocity, I = turbulence, h = water surface elevation) (*d not given, taken as max operating depth) ..... | 37  |
| Table 2.2: Details of CFD model impact studies (WL = water level, V = velocity, ST = suspended sediment, Oth = other). .....   | 38  |
| Table 3.1: Tidal harmonic constituents (NOAA, 2017). .....   | 76  |
| Table 4.1: Principal Model Parameters. ....  | 92  |
| Table 4.2: Tidal constituents included in analysis. ....   | 97  |
| Table 4.3: Tidal Constituent Data. ....  | 99  |
| Table 4.4: Average annual available power at preferred berths using different assessment approaches. ....  | 128 |
| Table 5.1: Sections of code modified or added to incorporate tidal energy extraction. ....   | 140 |
| Table 5.2: Model representation of energy extraction variables. ....   | 141 |
| Table 5.3: Peak power output (MW) and velocity deficit at turbine (%) determined for varying $C_T$ specifications. ....  | 153 |
| Table 5.4: Model details and optimum $C'_T$ values. ....   | 155 |
| Table 5.5: Resulting relative percentage differences (%) in $P_{E(th)}$ and $P_{E(mod)}$ estimates determined over 1 tidal cycle for each model scenario. ....   | 157 |
| Table 5.6: Principal Model Parameters. ....  | 160 |
| Table 5.7: Individual Model Parameters. ....   | 162 |
| Table 5.8: Summary of Shannon Estuary Assessment showing optimum $C'_T$ and modelled $C_P$ values and the relative velocity deficit, due to turbine deployment, expressed as a percentage (%). ....                    | 167 |
| Table 5.9: Basic model parameters. ....  | 170 |
| Table 5.10: Array configurations and acronyms. ....  | 172 |
| Table 6.1: Basic model parameters. ....  | 188 |
| Table 6.2: Energy Capture (kWh) based on the Farm method and author's approach. ....   | 196 |
| Table 6.3: Optimisation model parameters and symbols. ....   | 201 |

|   |     |
|---|-----|
| Table 6.4: Sections of code modified or added to incorporate array optimisation.....                            | 207 |
| Table 6.5: Model parameters (Source: Funke et al. (2014)). .....  | 218 |
| Table 6.6: Principal model details .....  | 221 |
| Table 6.7: Legend for turbine colours. ....   | 224 |
| Table 6.8: Total mean energy capture (kWh/cycle) and undisturbed efficiency of each array. ....                 | 228 |
| Table 6.9: Total energy captured (kWh/cycle) and power coefficient, $C_{P\_Undis}$ , for array O1, O2, O3 ..... | 234 |
| Table 6.10 Principal Model Parameters of the MSN Shannon Estuary Model. ....                                    | 236 |
| Table 6.11 Legend for turbine colours. ....   | 243 |
| Table 6.: $\epsilon_{Undis}$ for each array modelled within each domain. ....                                   | 245 |
| Table 6.13: $\epsilon_{Undis}$ for each O1 array modelled within NG63 and NG21. ....                            | 250 |

## Mathematical Notations

|                  |  |
|------------------|--|
| $A$              | cross-sectional area   |
| $A_T$            | turbine swept area   |
| $B$              | open boundary operator   |
| $C$              | Chezy bed roughness coefficient                                  |
| $C^*$            | air-water interfacial resistance coefficient                     |
| $CG$             | child grid   |
| $C_n$            | courant number   |
| $C_P$            | power coefficient  |
| $C_T$            | turbine thrust coefficient                                       |
| $D_{xx}, D_{xy}$ | depth mean dispersion coefficients in x-direction                |
| $D_{yx}, D_{yy}$ | depth mean dispersion coefficients in y-direction                |
| $E_K$            | kinetic energy   |
| $f$              | Coriolis parameter   |
| $F_{C/P}$        | child/parent model forcing                                       |
| $g$              | gravitational acceleration                                       |
| $H$              | total water depth  |
| $h$              | depth below MWL  |
| $I, J$           | x- ,y- coordinate directions of computational grid used by model |
| $i, j$           | x- , y- coordinate of grid cell on computational grid            |
| $L$              | partial differential operator                                    |
| $m$              | mass   |
| $N$              | number of turbines in an array                                   |
| $n$              | time-step level  |
| $PG$             | parent grid  |
| $q_x$            | depth integrated volumetric flux component in x-direction        |
| $q_y$            | depth integrated volumetric flux component in y-direction        |
| $S$              | depth integrated solute concentration                            |
| $t$              | time   |
| $T_r$            | average residence time   |
| $U$              | depth integrated velocity component in x-direction               |
| $u$              | localised velocity component x-direction                         |

|               |  |
|---------------|--|
| $V$           | depth integrated velocity component in y -direction                  |
| $v$           | localised velocity component y-direction                             |
| $w$           | localised velocity component z-direction                             |
| $W_x$         | wind velocity component x-direction                                  |
| $W_y$         | wind velocity component y-direction                                  |
| $x, y, z$     | coordinate directions in three-dimensional Cartesian plane           |
| $Z$           | water surface elevation (above or below mean water level)            |
| $\Theta$      | angle of ellipse inclination   |
| $\beta$       | momentum correction factor for non-uniform vertical velocity profile |
| $\Gamma$      | boundary   |
| $\Delta t$    | time-step  |
| $\Delta x$    | x-direction grid spacing   |
| $\Delta y$    | y-direction grid spacing   |
| $\varepsilon$ | depth mean eddy viscosity  |
| $\zeta$       | water surface elevation (above or below MWL)                         |
| $\rho_a$      | air density  |
| $\rho$        | fluid density  |
| $\phi$        | state variable   |
| $\Omega_p$    | model domain   |

# 1 Introduction

## 1.1 Tidal Energy

Tidal stream energy has the potential to contribute significantly to global energy requirements with worldwide tidal resource estimated at over 120TW/h per annum (Tidal Energy Today, 2016). Tidal turbines can be used to harness the kinetic energy found in fast moving tidal currents. Suitable tidal stream sites for horizontal axis turbines are those with peak current speeds in the range of 2m/s but devices generally begin to generate power at around 0.8m/s (Polagye et al. 2011). Tidal current speeds in the open ocean are only of the order of 0.1m/s, but the interaction of tidal waves with coastal topography, such as headlands, islands and narrow straits between adjacent landmasses, can result in generation of current speeds in excess of 2m/s. The complex topography found in estuaries can also induce strong current flow. Suitable sites are therefore in coastal waters and will be highly localised in area. The Pentland Firth in Scotland, for example, is well known for its exceptionally fast currents which can exceed 5m/s (Adcock et al. 2013). In Ireland, the Shannon estuary on the west coast possesses strong currents in the region of 2-3m/s and has been identified as a potential deployment site (SEI, 2004).

Tidal turbine technology is still in the early stages of development, with only a small number of devices developed to full-scale. The world's first commercial-scale turbine deployment was the 1.2MW SeaGen turbine (Figure 1.1), developed by Marine Current Turbines (MCT) and deployed in Strangford Lough, Northern Ireland. Other successful deployments of full-scale, or close to full-scale, devices include the 1MW OpenHydro turbine deployed in the Bay of Fundy, Canada, and Alstom's 1MW turbine deployed in Orkney, Scotland. In 2007, Verdant Power's Roosevelt Island Tidal Energy (RITE) project saw the deployment of the world's first grid-connected tidal turbine

array comprising six 5m diameter turbines. The on-going MeyGen project is currently the largest tidal stream energy project worldwide. With plans to generate up to 398MW through deployment in the Pentland Firth, it is the only commercial turbine array to have begun construction (Atlantis Project, 2017). All of these projects involve horizontal axis turbines which are the most common turbine design to date; this research is therefore based on simulation of horizontal axis turbines (HAT).

To date, the commercial viability of tidal turbines has been tested using single devices, but commercial application will likely involve hundreds of devices deployed in farms, analogous to wind (turbine) farms and investigation into the operation and impacts of large-scale tidal turbine arrays has yet to be significantly explored. Tidal energy is a highly attractive renewable energy source due to its predictable nature; however; the commercial viability of tidal turbine technology will largely depend on the expected energy capture and associated environmental impacts.



**Figure 1.1: SeaGen tidal turbine (Source: Siemens UK, 2010).**

The hydro-environmental impacts of tidal turbines can include both near-field effects in the waters immediately adjacent to the turbines, and far-field effects such as alteration of the estuary-wide tidal

regime. The hydrodynamic impacts from deployment of a single turbine include an area of reduced velocities downstream of the turbine, called the turbine wake, and accelerated bypass flows to either side of the turbine. These impacts are limited to the near-field and are relatively well understood, it is generally accepted that the far-field effects of singular device deployments will be negligible (Nash & Phoenix (2017); Polagye et al. (2011)). However, large-scale arrays have the potential to affect much greater changes in their far-field environments with research showing potential for large reductions in current velocities inside, and upstream and downstream, of the array, and consequential impacts on mixing, mass transport and primary production (Nash & Phoenix, 2017). The significance of these effects is, as yet, relatively unknown. The aim of this research is to develop a coastal ocean model that can determine optimised layouts of tidal turbine arrays with respect to power capture and environmental impacts. Such a model could be extremely useful when determining the economic viability of proposed arrays.



**Figure 1.2: Tidal turbine array (Source: SRM Projects LTD, 2012).**

## **1.2 Numerical Modelling**

Since their introduction in the 1960s/70s, numerical models of coastal waters have been constantly evolving in accuracy and complexity. Whilst models vary in their processes and parameters of

interest, they serve the same purpose: to simulate complex dynamic systems and enable predictions of potential changes to the system, for example predicting the impacts of tidal turbine deployments. Due to the limited number of commercial-scale turbine deployments to date, there is very little available measured data on the hydro-environmental impacts of these devices. In this absence of field data numerical models, validated against laboratory data, have been used to investigate the potential impacts of tidal turbine deployments. As numerical models can accurately simulate hydrodynamics in space and time they can be an invaluable tool for (1) investigating the resulting impacts of tidal energy extraction and (2) quantifying potential energy yields from a turbine or array.

The present research first involved the modification of a 2D hydrodynamic tidal flow model to simulate the effects of tidal energy extraction. This developed model was used to quantify power output from a turbine, or array, and to investigate both the impacts of individual turbines and the interactions between turbines. The model was further developed with the incorporation of an optimisation algorithm which determined optimal array configurations based on maximising power output and minimising impacts on current flow. In order to maximise energy capture, one must first know how much energy is available for capture. The energy extraction model was therefore developed to implement a resource assessment methodology where harmonic and ellipse analyses are used to determine the primary direction of current flow at a site.

Computational cost is an important and often limiting consideration in numerical modelling. For a hydrodynamic model to be economically viable, optimisation of cost must be achieved. Computational cost can generally be defined by the model's simulation time; thus, minimising the simulation time will keep costs down. However, as the complexity of a model increases so does its computational cost, primarily due to the inclusion of more parameters. To reduce high

computational costs many coastal hydrodynamic models are resolved at relatively low spatial resolutions, with grid spacings much larger than a tidal turbine rotor diameter. As a result these low resolution models have reduced accuracy when used to simulate turbine impacts and energy capture. A solution to this problem is the use of nested models, which allow localised high spatial resolution in a selected area of interest, e.g. around a turbine array, thus reducing processing times and computational expenses. This research therefore also involves the use of a one-way nested model, to allow resolution of a turbine array at the turbine scale. This enables the simulation of interactions between individual turbines and should therefore allow a more accurate assessment of the resulting impacts of turbine deployment and power output from a turbine or array.

### **1.3 Aims and Objectives**

The primary aim of this research was the development of a numerical model for optimising tidal turbine arrays relative to both power output and potential hydro-environmental impacts. This involved a number of objectives:

- Development of a methodology for quantifying the resource available for extraction by a tidal turbine and implementation of same in a tidal flow model
- Modification of the tidal flow model to enable simulation of energy extraction by tidal turbines
- Development of a methodology for quantifying power capture of a turbine or array and implementation of same in the energy extraction model
- Development of an optimisation algorithm to determine optimal array configurations and implementation of this in the developed energy extraction model
- Application of the final optimisation model to idealised domains and a case study site, the Shannon estuary

The models used in this research are the 2D finite difference Depth Integrated Velocity and Solute Transport model (DIVAST) and the Multi-Scale Nested model (MSN). The DIVAST model was developed by Prof Roger Falconer of Cardiff University and has been successfully applied to many coastal and estuarine modelling studies to simulate tidal energy extraction (e.g. Ahmadian & Falconer (2012); Fallon et al. (2014); Nash et al. (2015); Willis et al. (2010)). The nested model used for this research was developed by Dr S Nash and Prof M Hartnett at National University of Ireland Galway and has also been extensively tested and validated (e.g. Nash & Hartnett (2010); Nash & Hartnett (2014); Olbert et al. (2017)).

The novelty of this work is the development of the automated optimisation model, which has the ability to optimise array layouts based on both energy capture and the hydrodynamic impacts. At present only one other automated approach has been found in the literature - the gradient-based optimisation approach developed by Funke et al. (2014). However, their study, although applied to an idealised representation of the Pentland Firth, is not developed at estuary scale level. Their optimisation is also solely based on power and does not consider the resulting impacts of tidal energy extraction.

#### **1.4 Thesis Layout and Content**

The layout and content of this thesis are as follows:

Chapter 2 presents a literature review of relevant research including resource quantification and tidal turbine modelling. Different approaches to quantifying the undisturbed tidal resource are outlined. This involves discussion of traditional approaches to resource assessment, including the factors affecting their accuracy such as the formulation of the available power equation. The different approaches to numerical simulation of tidal energy extraction are

discussed with a focus on turbine representation. This is used to inform the development of the energy extraction model. A review of the hydro-environmental impacts of tidal turbines is undertaken with a view to incorporating an 'impact constraint' in the optimisation model. The hydrodynamic impacts of both single devices and arrays are discussed; this includes impacts on current velocities and water levels. In relation to environmental impacts, an overview of relevant impacts is presented, including suspended sediments, tidal flushing and other water quality measures and a summary of published literature relating to these impacts is included. The novel aspects of the present research are then outlined relative to the findings of the literature review.

Chapter 3 presents the theory behind the two-dimensional numerical model, DIVAST, and the MSN one-way nested model. The governing differential equations and their formulations are outlined and discussed and the model solution scheme is described. The one-way nesting procedure is outlined and the model grid structure, boundary specifications and interpolation scheme are discussed. The theory behind tidal flushing is presented as the use of flushing as a proxy for environmental impact of turbines was investigated during the research. The fundamentals of tidal harmonics and tidal ellipse analyses are also presented, including details on the tidal harmonic analysis software which was incorporated into the developed models.

Chapter 4 presents the development of a sophisticated resource assessment approach which utilises harmonic analysis and tidal ellipses to incorporate flow direction into the available power equation. Two established methods for quantifying the power that is available from tidal currents, and the author's new methodology, are tested and compared. The development of the DIVAST model to implement the new resource assessment approach is discussed and testing / validation of the new model is presented. A resource assessment study is then carried out on a case study site - the

Shannon estuary - using the different approaches. This involved validation of the Shannon model, an initial resource assessment across the estuary and, based on this, selection of potential tidal energy berths and a more detailed resource assessment at the selected sites.

Chapter 5 presents the development of the DIVAST and MSN models to simulate the effects of turbine deployment and quantify energy capture, i.e. the development of the energy extraction models. This involved modification of the governing momentum equations (discussed in Chapter 3). The chapter also presents the development and testing of new source code to facilitate calculation of power capture. The model developments were tested using idealised domains and the Shannon estuary case study. A study into the impact of array configuration on the resulting hydro-environmental impacts is presented which includes assessment of the impact on current velocities and flushing times, and the results of this study are discussed.

Chapter 6 presents the development of the optimisation model. The importance of turbine placement regarding maximising energy capture is explored. Subsequently, the development of the optimisation algorithm and its incorporation into the energy extraction model are presented and described in detail. The fully developed model is applied to an idealised domain for initial testing and then applied to the Shannon estuary. Results from different array configurations, including the model's optimised layouts, are presented.

Chapter 7 presents a summary of the research, along with the author's final conclusions and recommendations for future progressions of this research.

## 1.5 Publications

The following journal paper has been published in the journal of *Renewable and Sustainable Energy Reviews*:

Nash S, Phoenix A (2017). "A review of the current understanding of the hydro-environmental impacts of energy removal by tidal turbines." *Renewable and Sustainable Energy Reviews* 80: 648-662, doi: [10.1016/j.rser.2017.05.289](https://doi.org/10.1016/j.rser.2017.05.289)

The following journal paper has been submitted for peer review to the *Journal of Renewable and Sustainable Energy*:

Phoenix A, Nash S. "Modelling the hydrodynamic impacts of tidal turbines using a momentum sink approach: Sensitivity to the thrust coefficient."

The follow peer-reviewed International Conference Paper has been published from this research:

Phoenix A, Nash S (2016). "Tidal stream resource assessment of the Shannon estuary", *Proceedings of the Civil engineering research in Ireland Conference (CERI)*, NUI Galway, 29<sup>th</sup>-30<sup>th</sup> August, 2016.

## 2 Literature Review

### 2.1 Introduction

An over-reliance on fossil fuels and heightened climate change concerns has led to an increase in the need for sustainable green energy resources. This has been further driven by the EU's renewable energy directive, which sets a target for Europe of 20% final energy consumption from renewable energy resources by 2020 (European Commission, 2017b) and at least 27% by 2030 (European Commission, 2017a). Each EU country have set their own national 2020 renewable energy targets, ranging from 10% in Malta to 49% in Sweden, with Ireland's target at 16% (European Commission, 2017b). Extraction of tidal stream energy, i.e. the kinetic energy in marine currents, has the potential to contribute to achieving these ambitious targets. It is a highly predictable green energy source and so makes for an attractive alternative to fossil fuels.

Horizontal axis tidal stream energy turbines require operating conditions of strong peak current flows in the range of 2.0-2.5m/s in mean water depths of 20-50m (Lewis et al. 2015). Current speeds of this magnitude are rarely found in the open ocean; however, interactions of tidal waves with coastal topography and bathymetry can lead to accelerated flows, examples being flows through narrow straits, such as the Pentland Firth in Scotland (Adcock et al. 2013), long, narrow estuaries, such as the Shannon estuary in Ireland (Fallon, 2012), and around islands or headlands (Neill et al. 2012).

Whilst tidal stream energy is a favourable form of renewable energy the technology is still in its infancy with deployments to date limited to single devices, e.g. 'SeaGen' a 1.2MW device installed in Strangford Lough, Northern Ireland. Progression to full-scale commercial deployments will likely involve large numbers of turbines in arrays analogous to wind farms; for example, the Meygen consortium

propose to deploy 386 1MW turbines in the Pentland Firth (Meygen, 2013). At present, the resulting hydro-environmental impacts of large-scale turbine arrays are still relatively unknown; however, numerical modelling studies have shown they have the potential to be substantial. The commercial viability of tidal turbine technology will depend on both the expected energy yield and the severity of the resulting impacts on the marine environment in which they are deployed.

This review focuses on tidal energy extraction, to begin; a background into tides, tidal currents and tidal energy devices is given. This is followed by a review of approaches to tidal stream resource assessment which includes methodologies for quantifying the available resource, accuracy within resource assessment approaches and the importance of incorporating the hydrodynamic impacts of tidal turbine deployment into a resource assessment. This leads on to a summary review of published numerical and experimental studies assessing the hydrodynamic and environmental impact of turbine deployments, with a focus on turbine representation and the associated impacts of both single turbines and arrays. The full review is included in Appendix A.

## **2.2 Tides and Tidal Currents**

Tides are the periodic rise and fall of sea level due to the gravitational attraction between the earth, sun and moon. The resulting horizontal movement of water is referred to as the tidal current. Consider Figure 2.1. Water on the earth's surface is drawn towards the moon by its gravitational pull but since the attractive force is stronger closer to the source of the gravitational field the pull on the side of the earth closest to the moon will be greater than that on the opposite side, creating a bulge in the water surface on the closest side of the earth. The earth and moon rotate around the centre of mass of the earth-moon system, creating a centripetal force which creates a second bulge in surface water on the far side of the

earth (Thompson, 2007). The gravitational force of the sun is also a tide generating force, whilst much larger than the moon in mass, it is much further away and so has a lesser effect on tidal variations in the earth's waters.

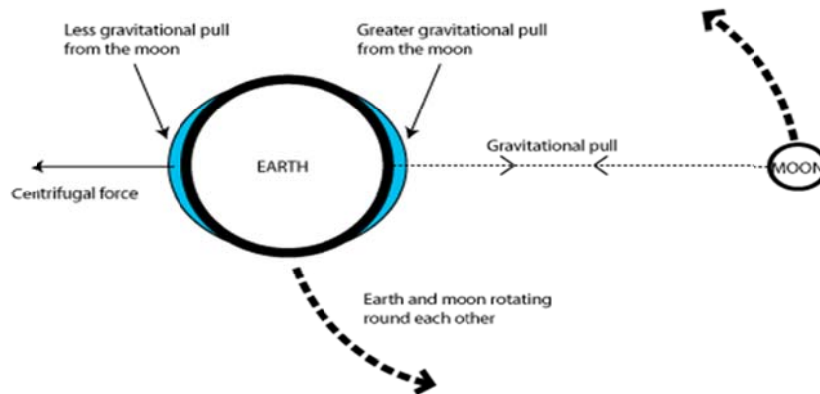


**Figure 2.1: Illustration of generation of tides (Source: Fallon, 2012).**

The rotation of the Earth results in tidal oscillations, generally experienced twice daily. The tide will rise until it reaches a peak value, known as high tide (high water), and then begins to fall to a minimum value, known as low tide (low water) (Figure 2.2). The vertical difference in tidal height between consecutive high and low tides is referred to as the tidal range. It varies over time and for different locations (Hicks, 2006).

The nature of the tide in any location is determined by the tide generating forces, with the specific sinusoidal oscillations being dependent on the distribution of forces. A lunar day is defined as the period between times when the moon is above the same point on the earth, equal to 24 hours and 50 minutes (Thompson, 2007). The primary lunar force, therefore, produces a sinusoidal tide, with two high tides and two low tides occurring in a single lunar day, termed a semi-diurnal tide. Tides can also be characterised as diurnal, in which only one tidal cycle occurs over the course of one lunar day.

Tidal variations are also seen over longer time periods, such as the spring-neap cycle, which repeats approximately every 14 days as the moon orbits the earth. Spring and neap tides result from the combined lunar-solar forces. During a new, or full, moon the gravitation pull of the moon and sun are in the same direction, generating spring tides whose tidal ranges are greater than the average monthly range (Hicks, 2006). In the first and last quarter of the lunar phase the lunar and solar forces are misaligned, resulting in neap tides whose tidal ranges are less than average (see Figure 2.3).

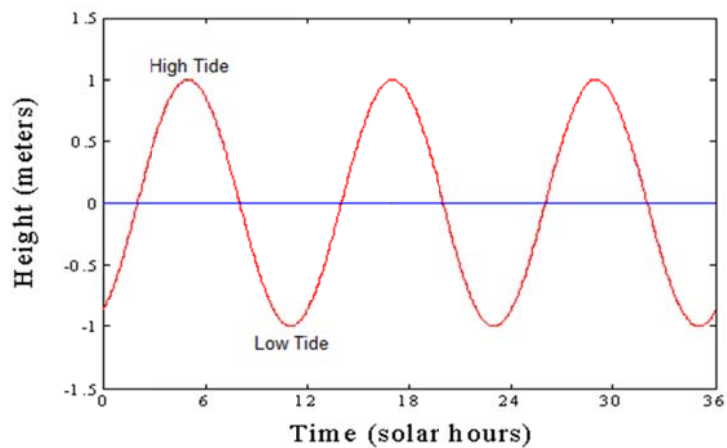


Figure 2.2: Illustration of high and low tides (Source: Boon, 2017).

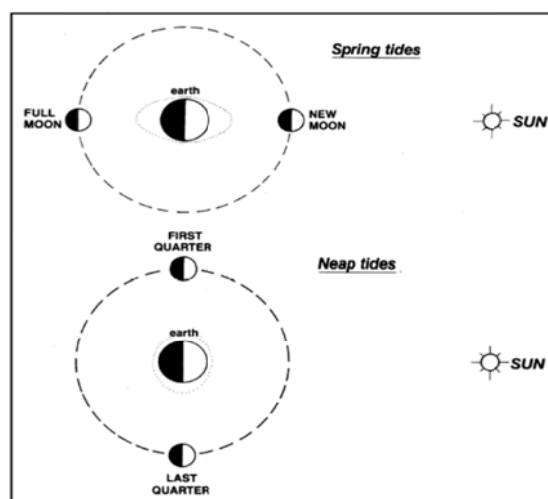
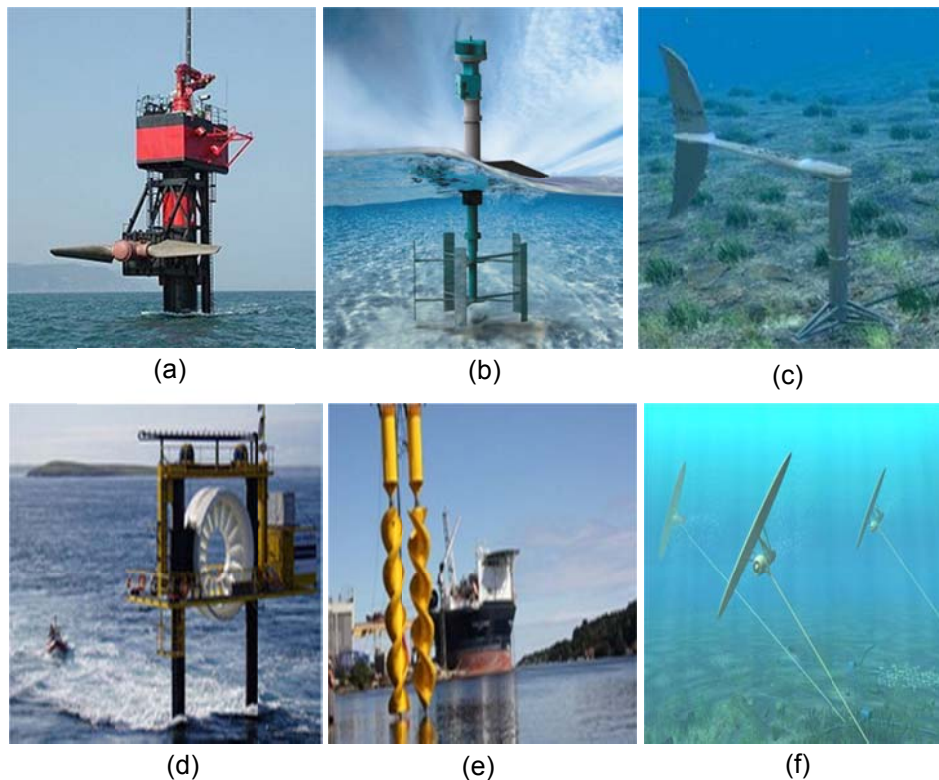


Figure 2.3: Illustration of generation of Spring and Neap tides (Source: Fallon, 2012).

Currents are the horizontal movement of water and are defined as either 'tidal' or 'non-tidal'. Tidal currents are the periodic horizontal flow of water associated with the rising and falling of the tide whilst non-tidal currents arise from any non-tidal factors, including bathymetry, Coriolis force, meteorological effects, freshwater inflows, density, temperature and salinity (Fallon, 2012).

### 2.3 Tidal Stream Energy Devices

Tidal energy is available in two forms: (1) the potential energy arising from the rise and fall of the water level or (2) the kinetic energy of tidal currents, also known as tidal streams. The development of tidal stream energy devices is on-going, with many devices in the early stages of research and development, a small number developed to scale model testing and an even smaller number at the full-scale prototype stage. The European Marine Energy Centre (2015) (EMEC) have identified six main types of tidal energy convertors (Figure 2.4).



**Figure 2.4: (a) Horizontal axis turbine, (b) vertical axis turbine, (c) oscillating hydrofoil, (d) enclosed tips (venturi), (e) Archimedes screw (f) tidal kite.**

*Horizontal axis turbine:* Horizontal axis turbines operate in a manner similar to wind turbines. The device is placed in water and the axis of rotation is horizontal and parallel to current flow. The force of the moving tidal current flowing across the turbine blades causes them to rotate, generating power. Generally the turbine has 2-3 blades, but more are possible and multiple turbines may be attached to the same structure (SEAI, 2017).

*Vertical axis turbines:* Vertical axis turbine operation is similar to horizontal axis turbines, but the turbine blades are vertical and so the axis of rotation is perpendicular to direction of current flow.

*Oscillating hydrofoil:* Hydrodynamic lift and drag forces are induced from the pressure difference as current flows over the wings, these forces drive the fluid in a hydraulic system which operates an electrical generator.

*Enclosed tips (venturi):* In a venturi device, the turbine is placed in a duct which concentrates the flowing current. The concentrated current flow can drive the turbine directly or the resulting pressure difference can be used to drive an air-turbine.

*Archimedes screw:* The device is helical corkscrew-shaped so that current flows up and through the spiral, causing rotation of the turbines and generating energy.

*Tidal kite:* In a tidal kite device, the turbine is located under the wing of the kite and the kite is tethered to the sea bed. The current flow is accelerated through the looping motion of the kite as it 'flies' in a figure-of-eight shape above its anchor point.

The most common tidal stream energy device design to date is the horizontal axis turbine. In 2003, Marine Current Turbine's (MCT) horizontal axis design was the world's first open-sea deployment of a

tidal turbine. In 2007, Verdant Power's Roosevelt Island Tidal Energy (RITE) project saw the deployment of the world's first grid-connected tidal turbine array comprising six 5m diameter horizontal axis turbines. This was followed in 2008, by the world's first commercial-scale turbine deployment - MCT's 1.2MW 'SeaGen' device, comprising two 16m horizontal axis rotors. Since then, other tidal turbine developers (e.g. Alstrom, Andritz Hydro Hammerfest, Atlantis Resources, OpenHydro, Scotrenewables) have followed suit with successful deployments of full-scale, or close to full-scale, horizontal axis turbines. Due to their place at the forefront of the tidal stream energy device sector, this research is based on simulation of the impacts of horizontal axis turbines and any further reference to tidal turbines throughout this thesis implies horizontal axis turbines.

## **2.4 Tidal Stream Resource Assessment**

### **2.4.1 Introduction**

Assessment of the available tidal stream energy is a fundamental step towards the progression of commercial tidal power generation. The aim of a resource assessment study is to quantify the power available for extraction at a particular site. Whilst other factors, such as the associated hydro-environmental impacts, survival of equipment or access for maintenance and integration with the power distribution network (Blunden & Bahaj, 2007), may limit the selection of a site for turbine deployment, the available tidal power will be the primary influencing factor. Assessments of the available tidal resource have been produced since the 1970's (e.g. Evans (1987); Fraenkel & Musgrove (1979); Wyman & Peachey (1979)); however, the approaches used to estimate the available tidal resource are continually developing. Accuracy is an important factor in resource assessments as underestimation of a resource could result in a project being deemed unviable due to insufficient resource, whilst overestimation could result in a significant underperformance between expected and actual power generation.

Tidal stream resource assessment has been described as an iterative process consisting of four fundamental stages (Blunden & Bahaj, 2007):

- 1 Selection of sites suitable for placing arrays of tidal stream generators – this is dependent on the current flow speed and the range of depths suitable for a particular generator type
- 2 Sizing and rating of the generating device to maximise extracted energy over the device's lifespan, accounting for long-term variations in flow speed, deviation of flow from rectilinear movement and the vertical flow profile
- 3 Investigation of different arrangements of generators with the aim of maximising energy extracted
- 4 Investigation of the effect of the tidal stream generator array on tidal parameters

#### **2.4.2 Kinetic Energy Flux**

The primary stage of a tidal stream resource assessment as identified by Blunden & Bahaj (2007) is arguably the most important step. Suitable sites for turbine deployment are determined based on the power that is available for extraction from tidal flows. Quantification of the available power can be determined as follows.

The energy available from tidal current flow is the kinetic energy of the moving water which can be expressed as:

$$E_k = 0.5mV^2 \quad (2.1)$$

where  $m$  is the mass of the moving fluid (kg) and  $V$  is the fluid velocity (m/s).

The mass of fluid flowing through a given cross-sectional area,  $A$ , per second can be defined as:

$$\dot{m} = m/t = \rho AV \quad (2.2)$$

where  $\rho$  is the fluid density ( $\text{kg/m}^3$ ). The power,  $P$ , can then be calculated by dividing equation (2.1) by time and substituting for  $\dot{m}$ , to give:

$$P = 0.5\rho Au^3 \quad (2.3)$$

where  $u$  is defined as the free-stream current speed and  $P$  is commonly known as the available resource.

### 2.4.3 Resource Assessment Methodologies

Estimations of tidal stream energy resources can be defined under various classifications (Boyle (2004); SEI (2004)):

- *Theoretical resource*: the total energy available for harvesting from tidal currents in a region of interest without incorporating technical, economic or environmental limitations, i.e. the undisturbed resource.
- *Technical resource*: the maximum power that can be extracted from accessible tidal streams using the latest turbine technology.
- *Practical resource*: the technical resource reduced when taking into account constraints such as transportation issues, access to the electricity grid or problems of intermittent supply. Further limitations on sea or technology use due to public opinion may also reduce the technical resource further and are difficult to quantify since they may only become clear when planning permission is sought and environmental submissions are lodged.
- *Accessible resource*: The practical resource limited by site specific regulatory constraints such as environmental, energy policies and planning constraints.
- *Viable resource*: The accessible resource limited by commercial constraints such as development costs, market rewards, timing and risks.

The most commonly used classifications are the theoretical and technical resource.

A resource method commonly used in previous literature is the farm method (e.g. Black and Veatch (2004); Blunden & Bahaj (2006); SEI (2004); Whittaker et al. (2003)). This method is based on the undisturbed resource; it considers a farm of tidal turbine devices deployed in an array and determines the technical resource by assuming each device extracts a given percentage of the theoretical resource based on the device efficiency. The 'extractable energy' therefore depends solely on the size, number, density and efficiency of the turbines deployed in the array. A weakness of this approach is that changes in the available resource due to energy extraction are not accounted for. More recent studies have shown energy extraction by tidal turbines will alter the flow regime, hence altering the available resource (e.g. Bahaj et al. (2007); Draper et al. (2010); Maganga et al. (2010); Myers & Bahaj (2010); Plew & Stevens (2013); Sun et al. (2008); Stallard et al. (2013)).

A modification to the farm method was developed by Black and Veatch (B&V) and Robert Gordon University (RGU) and applied to assess the UK tidal resource (Black & Veatch, 2005). This method considers the impact of tidal energy extraction on tidal flows by incorporating a 'significant impact factor' (SIF) to constrain the theoretical resource, re-defining the technical resource as the maximum power that can be extracted without significant environmental impacts. The technical resource is thereby estimated as the theoretical resource multiplied by the SIF which it was assumed would be site dependent and should, ideally, be determined for sites individually (Black & Veatch, 2005). Representative SIF values were identified by modelling a number of case study sites. Using the Pentland Firth for illustration, it was proposed that since the low and high range velocities were substantially less affected by tidal energy extraction the SIF would be primarily dependent on

'acceptable' changes to mid-range velocity. Based on earlier modelling results and existing knowledge of each site's environmental sensitivity, mid-range velocity changes and acceptable SIFs were determined for ten chosen key sites. The acceptable changes in velocities lay in the range of 10-15% while the associated SIF values ranged from 8-20%. Black & Veatch (2005) thus adopted a SIF value of 20% to preliminarily assess the UK tidal resource. The approach was further refined for a 2011 assessment where sites were assessed on a site-by-site basis (Black & Veatch, 2011). Sites were classified as one of three types of tidal flows (hydraulic current, resonant basin and tidal streaming) for which different 'significant change' limits had been identified (a 10% change in mid-range velocity or a 0.2m change in tidal range) and the associated SIFs were determined.

#### **2.4.4 Factors Affecting Accuracy of Resource Assessments**

There are a number of factors which can affect the accuracy of a resource assessment. The two main differences between published resource assessment methodologies are (1) the type of current velocity data used and (2) the formulation of the available power equation (2.3).

##### **2.4.4.1 Current Velocity Data used in Resource Assessments**

The power available for extraction (equation (2.3)) is the fundamental aspect of a tidal resource assessment. Given that power is proportional to current velocity cubed, the velocity has a considerable influence on power calculations, for instance a 10% underestimation of velocity would result in almost 30% underestimation of power. As a result, the accuracy of a resource assessment is highly sensitive to the accuracy of the velocity data used.

Some of the earliest available resource assessments used tidal velocity data taken from navigational charts (e.g. Black & Veatch Consulting Ltd (2005); Energy Technology Support Unit (1993);

Fraenkel & Musgrove (1979); Grabbe et al. (2009); Tecnomare SpA & IT Power Ltd (1996); Wyman & Peachey (1979)). For such data, the means of measurements, whether collected from anchored rigs or estimated from visual observations, is usually unknown; consequentially, the accuracy of the data is also unknown. Better accuracy can be achieved by using measured velocity data (e.g. Blunden & Bahaj (2007); Cartwright et al. (1988); Marone et al. (2003)). Measured data should be seen as a rough indication of the size of the resource only; however, it is often the case that the measured data used in resource assessments are the only source of information on tidal streams. Long-term measurements of velocities at a site will give a more accurate assessment but still have the drawback that the assessment only applies to the measurement location and the available power may be quite different at a nearby location. This spatial variability problem may be addressed by using high frequency radars that record bay-scale flow fields at high temporal and spatial resolution (e.g. Barth et al. (2008); Liu et al. (2009); Paduan & Shulman (2004); Ren et al. (2015)). However, this method of data collection is very expensive and the radar records surface currents which may differ significantly to the sub-surface due to wind influence.

A more comprehensive approach to preliminary resource assessment is to use a numerical model to simulate tidal flow over the full extent of the area of interest, thus capturing both temporal and spatial variations in velocities and, by extension, available power. The accuracy of a resource assessment based on numerical model results is dependent on the accuracy of the model itself, which is highly sensitive to the spatial resolution of the computational grid. Model validation is also an important factor in simulating accurate tidal flow. Validation should involve comparison of modelled water surface levels and current velocities with measured data. There are numerous examples of published studies in which numerical models are used to simulate tidal flow and carry out resource assessments

(e.g. Adcock & Draper (2014); Bryden et al. (2007); Carballo et al. (2009); Divett et al. (2009); Draper et al. (2014); Lewis et al. (2015); Rachmayani et al. (2006); Rourke & Reynolds (2010); SEI (2004)).

#### 2.4.4.2 Formulation of available power equation

The Fraenkel formula is an established first step approach for estimating available tidal power. Proposed by Fraenkel (2002), it is a modified version of equation (2.3) which accounts for temporal variations in current speeds. Assuming a spring-neap tidal cycle that is sinusoidal in nature, the mean available power is estimated as:

$$P_{\text{mean}} = 0.5\rho AK_s K_n u_{\text{peak}}^3 \quad (2.4)$$

where  $u_{\text{peak}}$  is the maximum spring velocity,  $K_s$  is the velocity shape factor which accounts for the nature of the variation in velocities over a tidal cycle and  $K_n$  is the neap/spring factor which accounts for the nature of the difference in spring and neap peak velocities. For a sinusoidal flow,  $K_s$  is typically assumed as 0.424 while  $K_n$  is typically taken as 0.57 for a 60% reduction in peak currents between spring and neap tides (Fraenkel, 2002). Examples of studies using this formula include (Fraenkel & Musgrove (1979); Fraenkel (2002); Rachmayani et al. (2006); Rourke & Reynolds (2010); SEI (2004)).

Fraenkel's assumptions of a sinusoidal tidal cycle and 60% spring-neap variation may not always be the case, which will result in an inaccurate assessment of  $P_{\text{mean}}$  in equation (2.4). If time-varying velocity data are available, a more accurate quantification of the mean power available for tidal energy extraction can be determined using equation (2.3) as:

$$P_{\text{mean}} = \frac{\sum_{n=1}^{n_{\text{max}}} 0.5\rho A u_n^3}{n_{\text{max}}} \quad (2.5)$$

where  $n_{\text{max}}$  is the number of timesteps and  $u_n$  is the magnitude of the current velocity at time-step  $n$ .

At present the majority of devices tested at field scale have been horizontal axis turbines. Many of these turbines are designed with a fixed orientation, preventing the turbine blades from rotating into the tidal stream as it changes direction during different stages of the tide. Traditional approaches to quantify available tidal power (equation (2.4) and (2.5)) employ the total velocity vector. For a fixed-orientation horizontal axis turbine, this introduces inaccuracies in the resource assessment as the direction of current flow is ignored. A more sophisticated approach to a tidal resource assessment should incorporate the prevailing flow direction into the available power equation. This concept is further developed in this research and is discussed in detail in Chapter 4.

Equations (2.4) and (2.5) estimate the theoretical available resource, however, in practise energy losses and physical limits will restrict all of the theoretical resource from being extracted by a tidal turbine device. The proportion of the theoretical resource that a turbine can extract is a function of the power coefficient,  $C_p$ , which is dependent on both turbine design and physical limits. In theory, the maximum power coefficient of a single horizontal axis turbine is typically assumed to be equal to the Betz limit of  $C_p = 0.59$  (Rourke & Reynolds, 2010). However, the actual power coefficient will be lower due to energy losses, such as turbulence and structural drag, occurring during the extraction process. The power that can be extracted by an array of  $N$  turbines, each with a turbine swept area  $A_T$  and power coefficient,  $C_p$ , is defined as the technical resource and is determined as:

$$P_{\text{ext}} = \sum_1^N P_{\text{mean}} A_T C_p \quad (2.6)$$

where  $N$  is the number of turbines in the array.

#### **2.4.4.3 Turbine Impacts**

Another important consideration for resource assessment is the effect of energy extraction by one turbine on the power available to another. In the traditional farm method of resource assessment,  $P_{mean}$  is the mean undisturbed theoretical resource and does not take account of the impacts of turbines on the available resource. Deployment of a tidal turbine will alter the prevailing hydrodynamics of a water body. The resulting hydrodynamic impact of each turbine will influence the power available to the other turbines, and hence, the overall power output from the array. The placement of individual turbines within an array is therefore crucial to extracting the maximum power possible; this is a major aspect of the present research. A fundamental consideration is the spatial extents of the turbine wake, as the placement of a turbine in the downstream wake of another will reduce the potential power capture of the downstream turbine. Blockage effects will also be crucial as devices can be positioned to take advantage of the accelerated flows caused by blockages from other turbines.

### **2.5 Approaches to Numerical Modelling of Tidal Turbines**

When determining the potential power output from tidal turbines using hydrodynamic models, one should account for the changes to the available resource as a result of turbines extracting energy. With this in mind, a review of approaches to numerical modelling of tidal energy extraction was undertaken. A list of the modelling studies reviewed is given in Table 2.2 (Section 2.6.3).

Computational fluid dynamics (CFD) model studies of tidal turbines have typically used either near-field or far-field modelling approaches, and almost exclusively model horizontal axis turbines. Near field models (e.g. Javaherchi et al. (2013); Mozafari (2014); Sun et al. (2008)) are highly resolved in three dimensions with mesh elements typically orders of magnitudes smaller than the turbine rotor

diameter. They are computationally expensive and therefore largely limited to modelling single turbines in idealised channels under steady flow conditions. In contrast, far-field models (e.g. Ahmadian et al. (2012); Fallon et al. (2014); Funke et al. (2014); Nash et al. (2015); Neill et al. (2009); Ramos et al. (2013)), whether 2D or 3D, use much coarser spatial resolutions, typically an order of magnitude greater than the turbine rotor diameter. Consequently, far-field models cannot accurately capture flow through, and around, individual turbines and are most suited to modelling large arrays of turbines. More recently, multi-scale models have been developed to model turbine arrays using a range of scales with low resolutions outside the array and high resolutions within the array so as to simulate the flow around individual turbines (e.g. Divett et al. (2011); Funke et al. (2014); Nash et al. (2015); Ramos et al. (2013)). Both unstructured and nested structured mesh approaches can be used for this.

### **2.5.1 Turbine Representation**

In addition to spatial resolution, the other main difference between CFD models is the representation of the turbines. Some high resolution studies include the physical structure of the turbine, but for reasons of computational efficiency and ease of implementation it is more common to represent the turbine by including the mechanics of the energy extraction process rather than the structure itself. Energy extraction can be incorporated in CFD modelling studies by modifying the governing equations of flow. The various approaches to CFD modelling of tidal turbines are shown in Figure 2.5 and are summarised briefly as follows:

- *Sliding mesh model (SMM)*: simulates a rotating turbine. A sliding mesh interface is used to enable a region of cells to rotate within a larger static grid. It is the most computationally expensive approach as it enables detailed simulation of the rotor motion and the resulting complex flows (e.g. McNaughton et al. 2014).

- *Rotating reference frame (RRF)*: enables the simulation of rotating flows and uses detailed blade geometry to simulate the hydrodynamics, including the downstream wake, around the turbine rotor. The governing equations of flow are solved in a reference frame which rotates at the turbine speed by including Coriolis and centripetal force terms in the momentum equation (e.g. Javaherchi et al. (2013); Mozafari (2014)).
- *Blade element model (BEM)*: models the time-averaged aerodynamic effects of the rotating blades. The effects are simulated using a moment source term placed inside a rotor disk fluid zone that depends on the chord length, angle of attack, and lift and drag coefficients for different sections along the turbine blade (e.g. Masters et al. (2013); Masters et al. (2015); Mozafari (2010); Turnock et al. (2011)).
- *Actuator disc model (ADM)*: the ADM represents the turbine rotor as an infinitely thin porous disc, with an area equal to the swept area of the rotor. The influence of energy extraction is incorporated into the momentum equations as an extraction-related momentum sink (e.g. Batten et al. (2013); Churchfield et al. (2011); Harrison et al. (2010); Sun et al. (2008)).
- *Momentum sink model (MSM)*: here, the mechanics of energy extraction are simulated by momentum sinks introduced in the momentum equations which represent the axial thrust induced by the turbine and the drag induced by the turbine support structure. This is the most common approach in far-field models (e.g. Ahmadian et al. (2012); Fallon et al. (2014); Nash et al. (2015); Ramos et al. (2013)).
- *Bed roughness model (BRM)*: bed roughness is increased to simulate the wake effects of tidal turbines on the flow (e.g. Funke et al. (2014); Karsten et al. (2008); Molen et al. (2016); Sutherland et al. (2007)). A disadvantage of the approach is that energy is always captured from the flow regardless of flow

direction, which is unrealistic in the case of horizontal axis turbines whose orientations are typically fixed.

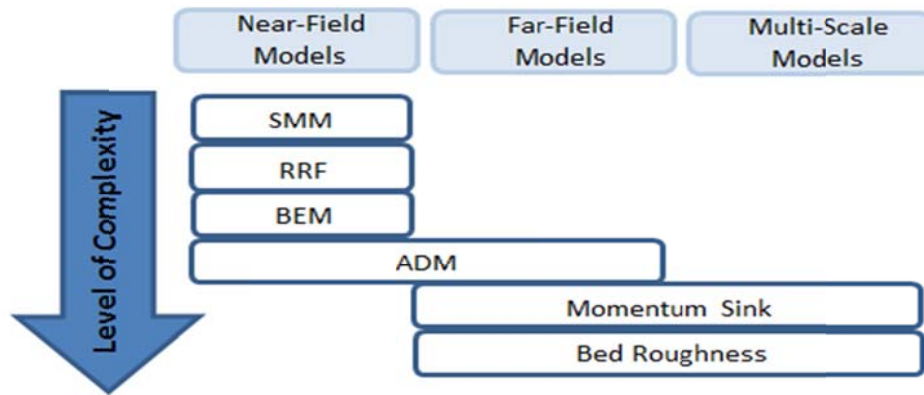


**Figure 2.5: Numerical approaches to representation of tidal turbines in CFD models.**

The majority of model studies used the Reynolds-averaged Navier-Stokes (RANS) CFD modelling approach in which all turbulent scales are modelled. Churchfield et al. (2011) used a large eddy simulation approach where larger turbulent scales are directly resolved while smaller turbulent scales are modelled. While the large-eddy simulation (LES) approach produces more detailed flow physics, it is much more computationally expensive than the more commonly used RANS approach.

### 2.5.2 Momentum Sink Approach

As seen from Table 2.2, tidal turbine impacts are commonly simulated in far-field hydrodynamic models using the momentum sink model, in which the induced turbine thrust is included in the momentum equations as a momentum sink. The turbine thrust can be determined from linear momentum actuator disc theory (LMADT) as (Houlsby et al. 2008):

$$T = 0.5\rho u^2 A_T C_T \quad (2.7)$$

where  $u$  is the undisturbed upstream current velocity,  $A_T$  is the swept area of the turbine represented as an actuator disc, and  $C_T$  is the dimensionless thrust coefficient.

The turbine thrust determines the level of power extracted from the flow and  $C_T$  is therefore a function of turbine design and flow speed. Through application of LMADT to a tidal turbine in an infinite medium Housby et al. (2008) showed that the theoretical maximum power coefficient,  $C_p$  (i.e. the proportion of available power that a turbine can extract) is 0.59 (called the Betz limit), and that this occurs when  $C_T$  is at an optimum value of  $C_T = 0.9$ . Similar findings were observed experimentally by Bahaj et al. (2007) who determined power and thrust coefficients for various design conditions. Tests were carried out on a single 800mm diameter model turbine deployed in a 2.4m x 1.2m cavitation tunnel and 60m towing tank. The results determined a maximum,  $C_p$  of 0.49 which occurred at a  $C_T$  of 0.8. Far-field modelling studies of tidal turbine arrays using a turbine thrust-based momentum sink approach have therefore typically assumed a thrust coefficient in the range of 0.8-1.0 as such values are assumed to correspond to peak turbine efficiency, typically in the range of  $C_p = 0.4$  (e.g. Ahmadian et al. (2012); Fallon et al. (2014); Nash et al. (2014); Plew & Stevens (2013); Ramos et al. (2014)).

The assumption of a  $C_T$  value close to 1 is based on the relationship between turbine thrust and undisturbed free-stream flow, as illustrated in equation (2.7). However, implementation of the momentum sink approach usually means that the thrust is calculated using the flow at the turbine itself as opposed to the undisturbed upstream flow speed. Since the velocity at the turbine will be lower as a result of the turbine's inclusion via the momentum sink,  $C_T$  values in the range of 0.8-1.0 may not be appropriate. Indeed, Housby et al. (2008) recommends a thrust coefficient of 2.0 based

on localised velocity. A challenge in applying the momentum sink approach to accurately model tidal energy extraction is therefore selection of suitable values of  $u$  and/or  $C_T$  in equation (2.7). This problem becomes more significant at higher resolutions since the disparity in free-stream and turbine velocities will be larger.

Gillibrand et al. (2016) and Kramer & Piggott (2016) have studied this problem of selecting suitable values of  $u$  and/or  $C_T$  for use in hydrodynamic models. In the 3-dimensional study by Gillibrand et al. (2016) a large averaging volume is applied at the turbine location with the aim being that the volume-averaged velocity is a close approximation to the undisturbed upstream velocity. Kramer & Piggott (2016) developed a relationship between the upstream velocity and the local velocity at the turbine, enabling a correction factor to be formulated and applied to the thrust resulting in a force close to the theoretical thrust to be applied.

### **2.5.3 Array Optimisation**

Divett et al. (2011) and Funke et al. (2014) have both modelled the hydrodynamic impacts of turbines with the aim of determining optimised turbine configurations. Both studies utilised high resolution, 2D, depth-averaged models. The model developed by Divett et al. (2011) was used to compare the energy capture from different array configurations. Whilst Funke et al. (2014) combined a gradient-based optimisation algorithm with a shallow water flow model to carry out optimisation in a single simulation, in which turbines are repositioned and flows recalculated in iterative steps until an optimised array is reached. An important aspect of the present research was the development of an optimisation algorithm which enabled an optimum turbine array to be determined considering both energy capture and hydrodynamic impacts. This is discussed in further detail in Chapter 6.

## **2.6 Hydro-environmental Impacts of Tidal Turbines**

In order to understand the likely impacts of energy removal by tidal turbines and how they might be incorporated in a resource assessment a review of the available literature was conducted. A 2010 scientific workshop comprising both academic researchers and industry professionals from the tidal energy sector identified the following primary environmental stressors arising from tidal turbine developments (Polagye et al. 2011):

- Presence of devices (static effects): include near-field changes to current velocities, sediment dynamics, habitat and ecosystem interactions due to physical structures (turbines, support structures, moorings, cables, etc.).
- Presence of devices (dynamic effects): include effects on marine life of rotating turbine blades and pressure and velocity gradients around the device.
- Chemical effects: include effects on water quality and marine life of leaks/spills of lubricants, hydraulic fluids, etc. and release of toxic contaminants from anti-fouling coatings.
- Acoustic effects: include effects on marine life of generation of underwater sound during installation and operation.
- Electromagnetic effects: include effects on marine life of electromagnetic fields resulting from the generation and transmission of electricity.
- Energy removal effects: include far-field changes to current velocities, tidal range, transport, water quality.

Despite the apparent readiness of the industry for commercial-scale deployments, the certainty and significance of the impacts to the marine environment described above are still relatively unknown. Due to the limited number of deployments to date, there is very little available measured data on the environmental impacts of tidal turbines operating at sea. The pilot nature of any marine deployments to date coupled with the expense of data collection, has

also meant there has been an understandable bias towards collection of performance, over environmental, data, and that developers have been slow to release data to the public domain. In the absence of field data, researchers have attempted to investigate the potential environmental impacts of tidal turbines through laboratory and numerical model studies.

It is generally thought that energy removal effects of tidal turbines are likely to be the most significant effect, particularly for commercial-scale arrays. In their study of the significance of environmental stressors, Polagye et al. (2011) noted that while energy removal was not considered a high priority issue at the pilot scale (i.e. single device or small array installations), it emerged as the priority area of concern for commercial-scale arrays. Various numerical modelling studies have shown that large-scale arrays have the potential to significantly impact hydrodynamics and transport processes at large scales e.g. a bay. For example, Karsten et al. (2008) estimate that extracting 7GW of power from the Bay of Fundy via tidal turbines would change the tidal range by more than 30%. It is most likely for this reason that much of the research to date has focussed on the effects of energy removal. A further contributing factor may be that energy removal by every device will produce a turbine wake and accelerated by-pass flows, while many of the other effects (i.e. chemical, acoustic and electromagnetic) will be device specific.

### **2.6.1 Summary of Environment Impact Studies**

Three relevant reports from sea tests of tidal turbines were found (Corren et al. (2013); Keenan et al. (2011); Schmitt et al. (2015)) that made reference to observed environmental impacts. Twelve relevant publications from laboratory studies of scaled tidal turbines were identified (see Table 2.1). The relatively small volume of meaningful laboratory test data is likely due to some of the following factors:

- Paucity of suitable test facilities: large towing tanks and/or recirculating flumes are required.

- Financial cost: fabricating scale turbines and accessing test facilities can be expensive.
- Focus on performance: similar to pilot studies, the focus of many laboratory studies has been on quantifying the energy and structural performances of turbines rather than environmental effects.
- Scale issues: accurately scaling turbines and flow properties can be problematic.
- IP issues: many laboratory studies have been commissioned by developers who are, understandably, slow to publically release data that has valuable IP and was collected at considerable expense.

CFD model studies of tidal turbines are the most abundant; primarily because they are cheaper and more flexible than physical testing. Thirty six modelling studies were found that reported on energy removal effects, these are summarised in Table 2.2. The approaches used in physical and numerical model studies vary in many ways; most obviously in the method used to represent the turbine(s) (whether physically or numerically), but also in the numbers and arrangements of turbines studied, the types of impacts investigated, and the quantification of said impacts.

### **2.6.2 Pilot Studies**

All of the pilot study literature reviewed was from deployments of horizontal axis turbines in shallow (< 30m) coastal waters. The studies included:

- MCT's 1.2MW SeaGen turbine deployed in Strangford Lough, Northern Ireland, which comprises two, 16m diameter, two-bladed rotors mounted each side of a cross arm attached to a supporting 3m diameter monopile (Figure 2.6 (a)) (Keenan et al. 2011). Maximum power is reached at flow speeds of 2.4m/s.

- Verdant Power's 35kW Dyno turbine deployed at the RITE project site in New York, USA, which comprises a single 5m diameter, 3-bladed rotor where the nacelle sits atop a support pylon (Figure 2.6 (b)). Maximum power is achieved at flow speeds of 2.1m/s (Corren et al. 2013).
- SCHOTTEL's 50kW Tidal Generator (STG) deployed at the Queen's University tidal test centre in Strangford Lough, Northern Ireland, which is a 4m diameter, 3-bladed turbine designed to reach maximum power at 2.75m/s (Figure 2.6 (c)) (Schmitt et al. 2015).

The SeaGen environmental monitoring report (Keenan et al. 2011) is the only dedicated environmental study of in-situ tidal turbines identified. The programme was aimed at monitoring effects of the device on tidal flows, marine mammals and benthic ecology. The published environmental data from the Verdant Power and SCHOTTEL turbine studies only relate to the effects of energy extraction on current velocities and the data are quite limited.

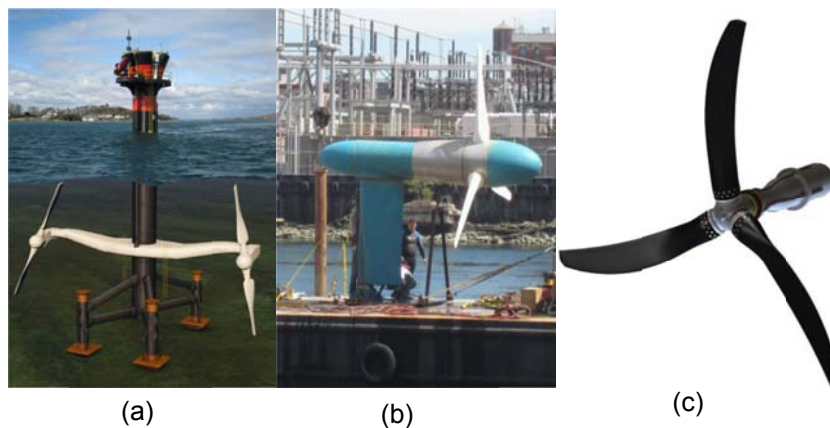


**Figure 2.6: In-situ turbines for which some environmental impact data are available: (a) MCT's SeaGen turbine, (b) Verdant Power's Dyno turbine (c) the SCHOTTEL tidal generator.**

### 2.6.3 Laboratory and Numerical Model Studies

Laboratory studies (e.g. Chamorro et al. (2013); Myers & Bahaj (2007); Myers & Bahaj (2012); Stallard et al. (2015)) of flow through scaled turbines have generally focussed on assessment of hydrodynamic impacts, which are a result primarily of energy removal but also of the static effect of the turbine structure. Due to the dimensional constraints of test tanks, laboratory studies have been mostly limited to single turbines.

Laboratory studies can be divided in two groups: (1) those using scale model rotors and (2) those using porous mesh discs as pseudo-turbines (see Figure 2.7). The reduction in fluid speed downstream of a turbine, the *turbine wake*, is primarily the result of the change in momentum caused by the thrust exerted by the fluid on the turbine rotor. By controlling the porosity of mesh discs, one can generate similar thrusts to scaled rotors and can thus use the discs to study wake properties. Using porous discs avoids some of the challenges of modelling turbines at small scales. Accurately scaling turbine properties can be technically difficult and can cause exaggerated changes in the flow downstream of the turbine, e.g. Bahaj et al. (2007) note that accurate scaling of turbine tip speed for a 0.1m diameter rotor requires a scaled rotation speed in the range of 1,500rpm which is unachievable and would create large amounts of swirl and large pressure gradients in the wake. Compared to scaled rotor testing, the porous disc method is quite cost-effective and has previously been extensively used for wind turbine wake studies (Bultjes (1978); Vermeulen & Bultjes (1982)), but it does have some limitations. The static discs do not extract energy from the flow (they instead convert it to small-scale downstream turbulence) (Bahaj et al. 2007) and they cannot create the downstream swirl of a rotating turbine. Compared to the flow fields generated by rotors, these principal differences have been shown to disappear in the near-wake region, generally less than 4 rotor diameters (RD)

downstream (Connel & George (1982); Vermeulen (1979)), and according to Bahaj et al. (2007) once the thrust and flow properties have been accurately scaled the far-wake properties compare well with those of a full-scale rotor.

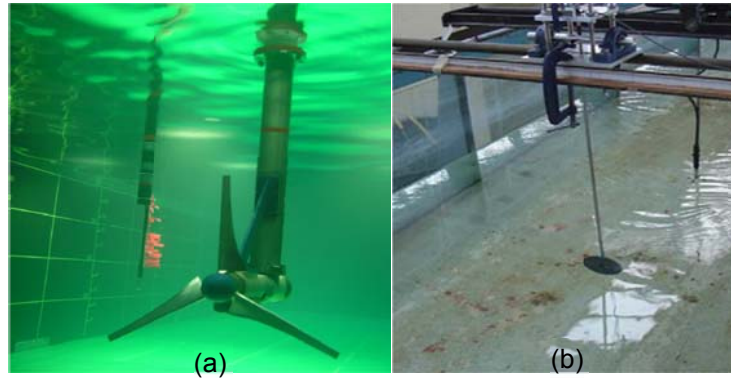


**Figure 2.7: (a) 0.8m diameter scaled rotor (Myers & Bahaj, 2009) and (b) mesh disc rotor simulator (Myers & Bahaj, 2010) used in laboratory studies of turbine impacts.**

A summary of the reviewed laboratory studies is provided in Table 2.1. All were conducted in steady flow conditions in circulating flumes and were based on horizontal axis turbines. The scaled rotor studies all involved three-bladed horizontal axis rotors which varied in size from 0.27 - 0.8m diameter and were either attached to the tank bed or suspended from above the water surface. The porous disc experiments all used 0.1 m diameter discs which were suspended from above the water surface. Ten of the studies investigated flow through a single turbine/disc while Myers & Bahaj (2012) investigated flow through a single row array of 2 turbines and a two-row array of 3 turbines, and Stallard et al. (2013) looked at a range of small arrays comprising different numbers (1, 2, 3, 5, 6, 7 and 10), arrangements and spacings of turbines. The studies covered a broad range of flow conditions as follows:

- channel (tank) depth,  $d$ : 0.3-2.0m
- channel (tank) width,  $w$ : 1.35-4.0m
- free-stream velocity,  $U_0$ : 0.25-2.35m/s

Reynolds numbers based on water depth ( $Re_d$ ) ranged from  $7.5 \times 10^4$  -  $3.0 \times 10^6$  and were thus all well within the turbulent flow regime ( $Re_d > 2 \times 10^3$ ); typical  $Re$  values at real deployment sites might be in the order of  $10^7$  (Myers & Bahaj, 2007). When testing scale model turbines, it is recommended that the channel blockage ratio, BR, (rotor swept area to channel cross-sectional area) be less than 20% (Department of Energy and Climate Change, 2008); this was the case for all of the studies.

Studies focussed solely on the hydrodynamic impacts of the turbines with most making some attempt at characterisation of the turbine wake by measuring velocities and turbulence at various points downstream. Measurements included both the near-field wake region (0-5/6RD downstream) and the far-field region (>5/6RD downstream). Changes in water levels were only investigated in two of the studies.

The CFD model studies discussed in Section 2.5 are also summarised, and are presented in Table 2.2.

**Table 2.1: Details of laboratory studies of energy removal impacts (w = tank width, d = water depth,  $v_0$  = velocity, I = turbulence, h = water surface elevation) (\*d not given, taken as max operating depth)**

| Study                  | Turbine Type   | Number of Turbines |        | Flow Cross-section<br>w x d [m] | Freestream Velocity<br>$v_0$ [m/s] | $Re_d$                | Rotor Diameter [m] | Channel Blockage Ratio | Impacts Assessed |   |   |
|------------------------|----------------|--------------------|--------|---------------------------------|------------------------------------|-----------------------|--------------------|------------------------|------------------|---|---|
|                        |                | Single             | Arrays |                                 |                                    |                       |                    |                        | h                | v | I |
| (Myers & Bahaj 2007)   | 3-bladed rotor | X                  |        | 1.4 x 0.78                      | 1.55-2.35                          | $1.2-1.8 \times 10^6$ | 0.4                | 11.5                   | X                |   |   |
| (A. Bahaj et al. 2007) | Mesh disc      | X                  |        | 1.35 x 0.3                      | 0.61-0.94                          | $1.8-2.8 \times 10^5$ | 0.1                | 1.9                    |                  | X | X |
| (Myers & Bahaj 2008)   | Mesh disc      | X                  |        | 1.35 x 0.3                      | Not given                          | ---                   | 0.1                | 1.9                    |                  | X |   |
| (Myers et al. 2008)    | Mesh disc      | X                  |        | 1.35 x 0.3*                     | Not given                          | ---                   | 0.1                | 1.5                    |                  | X |   |
|                        |                |                    |        | 4.0 x 2.0*                      | Not given                          | ---                   | 0.1                | 0.1                    |                  | X |   |
| (Myers & Bahaj 2009)   | 3-bladed rotor | X                  |        | 4.0 x 2.0                       | 0.8                                | $1.6 \times 10^6$     | 0.8                | 6.3                    |                  | X | X |
| (Myers & Bahaj 2010)   | Mesh disc      | X                  |        | 1.35 x 0.3                      | 0.25                               | $7.5 \times 10^4$     | 0.1                | 1.9                    |                  | X | X |
| (Maganga et al. 2010)  | 3-bladed rotor | X                  |        | 4.0 x 2.0                       | 0.5-1.5                            | $1.0-3.0 \times 10^6$ | 0.7                | 4.8                    |                  | X |   |
| (Gunawan et al. 2012)  | 3-bladed rotor | X                  |        | 2.8 x 1.16                      | Not given                          | ---                   | 0.5                | 6.0                    |                  | X |   |
| (Myers & Bahaj 2012)   | Mesh disc      |                    | X      | 1.35 x 0.3                      | Not given                          | ---                   | 0.1                | 0.2                    |                  | X |   |
| (Chamorro et al. 2013) | 3-bladed rotor | X                  |        | 2.75 x 1.15                     | 0.4                                | $4.6 \times 10^5$     | 0.5                | 6.2                    | X                | X | X |
| (Stallard et al. 2013) | 3-bladed rotor | X                  | X      | 5.0 x 0.45                      | 0.47                               | $2.1 \times 10^5$     | 0.27               | 2.5                    |                  | X | X |
| (Stallard et al. 2015) | 3-bladed rotor | X                  |        | 5.0 x 0.45                      | 0.46                               | $2.1 \times 10^5$     | 0.27               | 2.5                    |                  | X | X |

**Table 2.2: Details of CFD model impact studies (WL = water level, V = velocity, ST = suspended sediment, Oth = other).**

| Study                              | Spatial Approach |           | Turbine Arrangement |       | Modelling Approach | Turbine Representation * |     |     |     |     | Impacts Assessed |   |    |     |
|------------------------------------|------------------|-----------|---------------------|-------|--------------------|--------------------------|-----|-----|-----|-----|------------------|---|----|-----|
|                                    | Near Field       | Far Field | Single              | Array |                    | SMM/RRF                  | BEM | ADM | MSM | BRM | WL               | V | ST | Oth |
| (Couch & Bryden 2007)              |                  | X         | X                   | X     | 2D                 |                          |     |     | X   |     | X                | X |    |     |
| (Sutherland et al. 2007)           |                  | X         |                     | X     | 2D                 |                          |     |     |     | X   |                  | X |    |     |
| (Sun et al. 2008)                  | X                |           | X                   |       | 3D                 |                          |     | X   |     |     | X                | X |    |     |
| (Karsten et al. 2008)              |                  | X         |                     | X     | 2D                 |                          |     |     |     | X   |                  | X |    |     |
| (Neill et al. 2009)                |                  | X         |                     | X     | 1D                 |                          |     |     | X   |     |                  |   | X  |     |
| (Mozafari 2010)                    | X                |           | X                   | X     | 3D                 | X                        | X   | X   |     |     |                  | X |    |     |
| (Harrison et al. 2010)             | X                |           | X                   |       | 3D                 |                          |     | X   |     |     |                  | X |    |     |
| (Turnock et al. 2011)              | X                |           |                     | X     | 3D                 |                          | X   |     |     |     |                  | X |    |     |
| (Churchfield et al. 2011)          | X                | X         | X                   | X     | 3D                 |                          |     | X   |     |     |                  | X |    |     |
| (Hasegawa et al. 2011)             |                  | X         |                     | X     | 3D                 |                          |     |     | X   |     | X                | X |    |     |
| (Neill & Couch 2011)               |                  | X         |                     | X     | 3D                 |                          |     |     | X   |     |                  | X | X  |     |
| (Divett et al. 2011)               |                  | X         | X                   | X     | 2D                 |                          |     |     |     | X   | X                | X |    |     |
| (Ahmadian et al. 2012)             |                  | X         |                     | X     | 2D                 |                          |     |     | X   |     | X                | X | X  | X   |
| (Sheng et al. 2012)                |                  | X         | X                   | X     | 3D                 |                          |     |     | X   |     |                  | X | X  |     |
| (University of Massachusetts 2012) |                  | X         |                     | X     | 3D                 |                          |     |     | X   |     | X                | X | X  |     |
| (Neill et al. 2012)                |                  | X         |                     | X     | 3D                 |                          |     |     | X   |     |                  | X | X  |     |

|                            |   |   |   |   |          |   |   |   |   |   |   |   |   |   |
|----------------------------|---|---|---|---|----------|---|---|---|---|---|---|---|---|---|
| (Ahmadian & Falconer 2012) |   | X |   | X | 2D       |   |   |   | X | X | X | X | X | X |
| (Javaherchi et al. 2013)   | X |   | X |   | 3D       | X |   |   |   |   |   | X |   |   |
| (Masters et al. 2013)      | X |   | X | X | 3D       |   | X |   |   |   |   | X |   |   |
| (Batten et al. 2013)       | X |   | X |   | 3D       |   | X | X |   |   |   | X |   |   |
| (Smith et al. 2013)        |   | X |   | X | 3D       |   |   |   | X |   | X | X | X |   |
| (Ramos et al. 2013)        |   | X |   | X | 2D       |   |   |   | X |   | X | X |   |   |
| (Yang et al. 2013)         |   | X |   | X | 1D,2D,3D |   |   |   | X |   |   |   |   | X |
| (Plew & Stevens 2013)      |   | X |   | X | 2D       |   |   |   | X | X | X | X |   |   |
| (McNaughton et al. 2014)   | X |   | X |   | 3D       | X |   |   |   |   |   | X |   |   |
| (Funke et al. 2014)        |   | X |   | X | 2D       |   |   |   |   | X | X | X |   |   |
| (Mozafari 2014)            | X |   | X | X | 3D       | X | X |   |   |   |   | X | X |   |
| (Fallon et al. 2014)       |   | X |   | X | 2D       |   |   |   | X |   | X | X |   |   |
| (Robins et al. 2014)       |   | X |   | X | 2D       |   |   |   | X |   |   | X | X |   |
| (Nash 2014)                |   | X |   | X | 2D       |   |   |   | X |   | X | X |   | X |
| (Masters et al. 2015)      | X | X | X | X | 3D       | X | X |   | X |   |   | X |   |   |
| (Fairley et al. 2015)      |   | X |   | X | 3D       |   |   |   | X |   |   |   | X |   |
| (Martin-Short et al. 2015) |   | X |   | X | 2D       |   |   |   | X |   |   | X | X |   |
| (Thiebot et al. 2015)      |   | X |   | X | 2D       |   |   |   | X |   |   | X | X |   |
| (Nash et al. 2015)         | X | X | X | X | 2D       |   |   |   | X |   |   | X |   |   |
| (Gillibrand et al. 2016)   |   | X |   | X | 3D       |   |   |   | X |   |   | X | X |   |
| (Molen et al. 2016)        |   | X |   | X | 3D       |   |   |   |   | X | X | X | X | X |

\* SSM: Sliding mesh model  
RRF: Rotating reference frame  
BEM: Blade element model

ADM: Actuator disc model  
MSM: Momentum sink model  
BRM: Bed roughness model

## 2.7 Hydrodynamic Impacts of Tidal Turbines

### 2.7.1 Hydrodynamic Effects: Single Turbine

Extraction of energy from a fluid via a tidal stream turbine will cause a reduction in momentum (and by extension velocity) in the downstream flow known as the turbine wake. The hydrodynamic effects of a single tidal turbine include:

1. reduced wake velocities,  $U_w$ , downstream of the turbine due to energy removal
2. accelerated bypass velocities,  $U_b$ , around the turbine due to blockage
3. elevated turbulence levels and turbulent mixing of the wake with bypass flows
4. a drop in water level across the turbine

#### 2.7.1.1 Reduced Wake Velocities

Reduced wake velocities are the most obvious and significant impact of tidal turbines and are thus the most widely-studied to date.

Wakes are complicated features; however, their structures are typically characterised by:

- Wake length: downstream distance where wake velocities return to free-stream levels.
- Wake width: lateral extents of the wake.
- Depth profile: variation in wake velocities through the water column.

#### ***Wake length***

Velocity changes from experiments are generally reported as velocity deficits ( $U_d$ ) where:

$$U_d = 1 - (U_w / U_0) \quad (2.8)$$

Wake length is governed by the rate of wake recovery and is typically assessed by measuring and plotting  $U_d$  along the downstream longitudinal turbine centreline, i.e. the longitudinal  $U_d$ . Figure 2.8 (a) compares longitudinal  $U_d$  from six different laboratory studies of singular scaled turbines. Despite the differences in experimental setups (see Table 2.1), the shapes of the deficit curves are quite similar. As would be expected, deficits are highest adjacent to the turbine and decrease with distance downstream as velocities recover to free-stream levels. In the near-wake region (immediately downstream of the turbine) wake velocities are reduced to 60-90% of free-stream levels while in the far wake region turbulent mixing dissipates the wake, for example at 10RDs downstream wake velocities recover to between 10-25% of free-stream levels and at 20RD they further recover to within 5-10%.

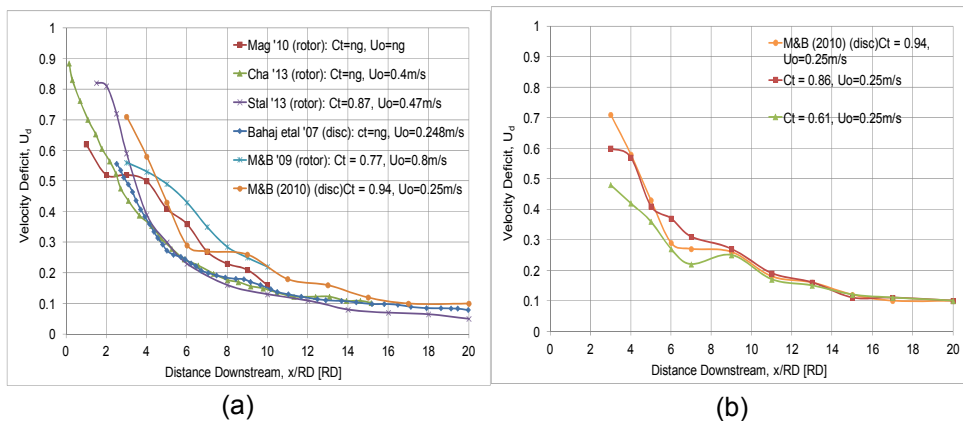


**Figure 2.8: Longitudinal variation in  $U_d$  for (a) single scaled rotors (reproduced from: Bahaj et al. (2007); Myers & Bahaj (2009); Myers & Bahaj (2010); Stallard et al. (2013)) and (b) 3 porous discs of different  $C_T$  values (reproduced from: Bahaj et al. (2007); Myers & Bahaj (2009); Myers & Bahaj (2010); Stallard et al. (2013)).**

Laboratory measurements of velocity deficits beyond 20RD are not available, most likely due to test tank sizes and the time needed to collect data. Numerical models have no such limitation and have been shown to be capable of accurately capturing turbine wake dynamics when compared with experimental data (e.g. Batten et al.

(2013); Harrison et al. (2010); Masters et al. (2013); Nash et al. (2015)). When simulating the wake of a single turbine, Nash et al. (2015) found that velocity deficits of approximately 2% still persisted at 40RD and full recovery to free-stream levels did not occur until approximately 70RD.

### ***Wake width and vertical profile***

The wake immediately downstream of a turbine will have approximately the same width as the turbine but will undergo lateral and vertical expansion with distance downstream due to turbulent mixing of the lower-velocity wake flow with the higher-velocity flow outside it. For example the scale model studies of Stallard et al. (2013) and Stallard et al. (2015) recorded wake widths of approximately 1.5RD at 1.5RD downstream, 2RD at 4RD downstream and 3RD at 8RD downstream. In addition, they observed that the lateral wake profile was approximately symmetric and followed a nearly Gaussian profile, particularly from 4RD downstream (see Figure 2.9 (a)). Nash et al. (2015) modelled the wake of a single turbine and their findings were generally in agreement with Stallard et al. (2013) and Stallard et al. (2015). They also observed that beyond 5RD, the wake width did not undergo any further expansion before it had almost fully dissipated by about 40RD.

The vertical velocity profile of a single turbine (Figure 2.9 (b)) has been shown to be asymmetrical about the wake centreline for the near-wake, with greater velocities occurring slightly above the centreline than below it (Maganga et al. (2010); Myers & Bahaj (2009); Stallard et al. (2013)). As the wake transitions between the near- and far-wake regions, the vertical profile becomes more symmetric and the profile becomes much flatter so that by 12RD (Stallard et al. 2013) to 15RD (Myers & Bahaj, 2009) downstream, the deficit is nearly constant over the wake depth.

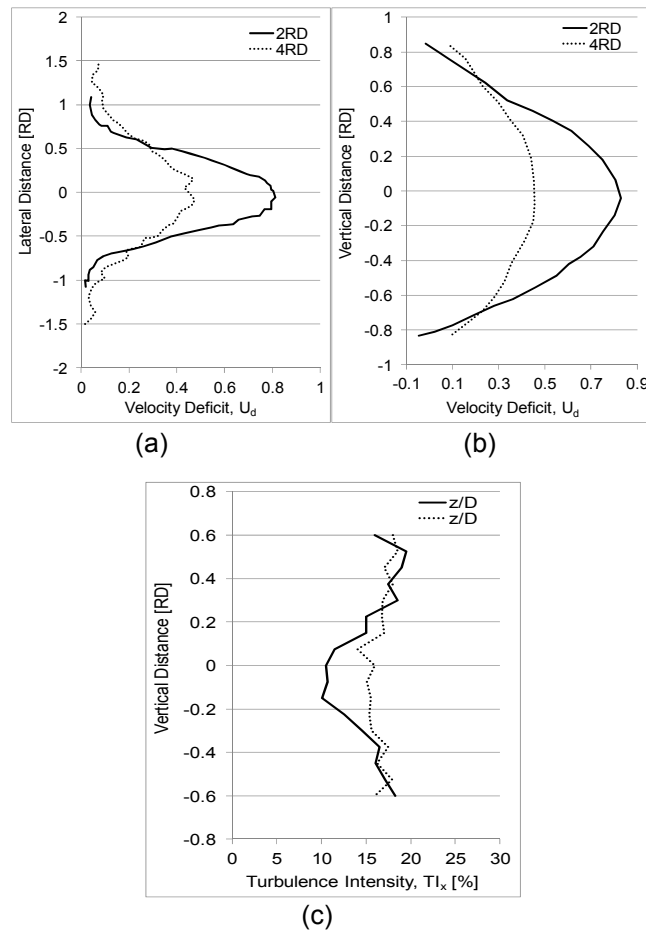


**Figure 2.9: (a) Lateral profiles of  $U_d$ , (b) vertical profiles of  $U_d$  and (c) vertical profiles of  $TI_x$  at 2RD and 4RD downstream of a single scaled rotor (reproduced from Stallard et al. 2013).**

### 2.7.1.2 Accelerated Bypass Velocities

The blockage to flow presented by the physical structure of a turbine and its support structure, and the slowing of water as it passes across the device, means that some flow will be diverted around the device, to the sides and/or possibly above/below. The 2RD velocity deficits in Figure 2.9 (b) recorded by Stallard et al. (2013) show acceleration of flows above and below the scaled rotor in the range of 6-8%.

### 2.7.1.3 Turbulence

Tidal turbine wakes are typically characterised by elevated turbulence levels. Turbulence levels are typically expressed as turbulence intensity,  $TI$ , defined as:

$$TI = \frac{\sigma}{\bar{U}_0} \quad (2.9)$$

where  $\sigma$  is the root-mean square of the turbulent velocity fluctuations and  $\bar{U}_0$  is the mean free-stream velocity.

Experiment results show that turbulence profiles are quite different in the near- and far-wakes. In the near-wake, turbulence levels are highest at the outsides of the wake due to the strong shear layer, whilst, further downstream, turbulent mixing of the wake and bypass flows mean that  $TI$  levels within the wake become more uniform (Figure 2.9 (c)). Stallard et al. (2015) showed that uniformity of turbulence levels throughout the wake had occurred by 10-12RD downstream and that  $TI$  levels had returned to background levels (approximately 12%) by 12RD from initial highs in the near-wake of 22-23%.

#### **2.7.1.4 Water Levels**

In accordance with the theoretical model of **Error! Reference source not found.**, experimental (Myers & Bahaj, 2007) and numerical (Divett et al., 2011) studies have showed that water levels will be affected by an increase in level upstream of a turbine and a decrease in level downstream of a turbine. However, in relation to total water depth, these changes are generally deemed negligible.

#### **2.7.2 Hydrodynamic Effects: Arrays**

The recorded hydrodynamic effects of a single turbine described above are unlikely to have any significant large-scale environmental effects beyond those in their immediate vicinity. However, the cumulative hydrodynamic effects of large numbers of turbines packed relatively closely together have the potential to be much greater than those of a single device and could therefore have greater environmental consequences. The most significant cumulative impacts are the greater levels of energy extraction and merging of individual turbine wakes resulting in greater potential for

velocity and water level changes. The following sections summarise the findings of laboratory studies which have examined merging of turbines using small numbers (<10) of scaled turbines and, subsequently, numerical modelling studies that have examined the potential effects of much larger arrays.

### **2.7.2.1 Wake Merging**

Studies of interactions between wakes of a single turbine row (e.g., . Myers & Bahaj (2012); Stallard et al. (2013); Nash et al. (2015)) found that if the spacing between adjacent turbines is large enough the wake of each rotor will be similar to that of an isolated rotor. For smaller spacings the isolated wakes form in the immediate near-field but will merge to form a single expanded wake. For example, an experimental study by Stallard et al. (2013) found wake merging to occur for lateral spacings of 2RD or less and at about 2RDS downstream. Myers & Bahaj (2012) investigated wake interactions for a two row array of porous discs and found inclusion of the third disc resulted in merging of the three wakes creating a much stronger far-field wake than for a single disc. The merged wake had an increased width, resulting in a longer wake recovery. Myers & Bahaj (2012) also observed that the lateral spacing between adjacent rotor discs could be optimised to achieve acceleration of the bypass flow between them. For example, a centre-to-centre spacing of 2.5RDs achieved a 22% increase in available kinetic energy.

### **2.7.2.2 Array Effects on Velocities**

The general findings from the far-field models of tidal turbine arrays studied (see Table 2.2) are that current velocities will be substantially reduced within the array and in the array wakes that will form upstream and downstream of the array. For example, a 2D modelling study of a 2000 x 10m turbine array by Ahmadian & Falconer (2012) observed peak spring velocities being reduced from 2.0m/s to 1.5m/s. The resulting array wakes are found to exist several kilometres from the point of energy extraction (Ramos et al. 2013).

Bypass flows will be accelerated around the array due to the blockage effects of the turbines and the slow moving water within the array and its wakes. The magnitude of these impacts is dependent on the array configuration; with higher velocity deficits occurring for inline configurations compared with staggered layouts (Nash et al. 2015). Impacts on current velocities are also found to increase with increasing density (Fallon et al. 2014) and capacity arrays (Plew & Stevens 2013).

### **2.7.2.3 Array Effects on Water Levels**

Similarly to single turbines, deployment of arrays will result in increased water levels upstream and decreased water levels downstream of an array. However, unless overly small turbine spacings are used, impacts on water levels are generally considered negligible.

## **2.8 Environmental Impacts of Tidal Turbines**

The previous section showed that energy removal by tidal stream turbine arrays has the potential to considerably alter the existing velocities and water levels of tidal flows. Any changes to the prevailing hydrodynamics may in turn have consequential environmental impacts such as changes to mixing and transport processes which may affect water quality, or impacts on flora and fauna. Numerical models have been used to study the water quality impacts of tidal turbine arrays, primarily sediment transport impacts (Ahmadian et al. (2012); Ahmadian & Falconer (2012); Fairley et al. (2015); Gillibrand et al. (2016); Martin-Short et al. (2015); Mozafari (2014); Neill et al. (2009); Neill & Couch (2011); Neill et al. (2012); Robins et al. (2014); Sheng et al. (2012); Smith et al. (2013); Thiebot et al. (2015); University of Massachusetts (2012)) but also impacts on bacteria levels (Ahmadian et al. (2012); Ahmadian & Falconer (2012)), salinity and temperature levels (Sheng et al. 2012), flushing times (Nash et al. (2014); Yang et al. (2013)) and primary production (Sanderse 2009).

Sediment transport (bed load + suspended load) is a high order function of velocity ( $\sim U^{3.4}$ ) (Robins et al. 2014), and bed shear stress which plays an important role in sediment transport is a function of  $U^2$ ; therefore, even relatively small changes to current velocities could have a measureable impact on sediment transport processes. In turn, changes to erosion/deposition patterns and bed levels may have consequential impacts on bed ecosystems. Changes to sediment transport are thus similar to changes in velocities with transport rates, suspended sediment levels and bed shear stresses decreasing where velocities reduced within an array and in the array wakes and increased in areas of accelerated bypass flows.

Tidal flushing is defined as the repeated exchange of inter-tidal water between a bay or an estuary and its receiving water body due to tidal flow. A flushing study is a time-scale analysis which enables assessment of the exchange of water and sediment transport within a particular body of water. It can therefore be used to combine assessment of the impacts of energy extraction on hydrodynamics and water quality parameters. Yang et al. (2013) and Nash et al. (2014) have investigated the potential effects of tidal arrays on flushing within estuaries dominated by strong tidal currents. They showed that the flushing time of the waters immediate to the array was increased as a result of the array and that the increase in flushing time was greater for higher numbers of turbines. However, Nash et al. (2014) showed that using a relatively large spacing between turbines (5RD) significantly reduced the increase in flushing time even for very large numbers (1000s) of turbines.

The majority of bacteria living in tidal stream waters will become attached to sediments in the water body; thus, a direct interaction between the levels of suspended sediment and bacterial concentrations might be expected. According to Kadiri et al. (2012), since water quality parameters such as salinity, nutrient levels and bacterial concentrations are all inter-connected, then an alteration to

one will have a consequential effect on another. Thus, the modelling of the impacts of tidal turbines on water quality parameters in isolation of each other, as many studies have done to date, cannot provide a complete picture and should be accompanied by full hydrodynamic-biogeochemical modelling.

## **2.9 Summary and Conclusions**

The review of published literature identified traditional approaches to resource assessments and highlighted the importance of considering the effects of tidal energy extraction on the tidal regime, and thus on the power available for extraction.

Reviewing established methods of available power quantification showed accuracy of estimates relied on the accuracy of the velocity data used and on the formulation of the available power equation. Numerical models are commonly used to simulate current flows for resource assessment studies; however, accuracy of the power estimates is dependent on the accuracy of the model itself. In regards to quantifying power available for extraction by a fixed orientation horizontal axis turbine, estimates are more accurate if they account for the direction of current flow relative to the device. Considering this, a methodology has been developed which utilises harmonic analysis and tidal ellipse theory to determine the prevailing direction of current flow and the rectilinearity of the flow. The developed approach is applied to the Shannon estuary case study site and compared to available resource estimates based on two traditional approaches. Based on the results suitable turbine deployment sites are identified and assessed in greater detail. This research is detailed in Chapter 4.

An important consideration when determining the available resource to turbines in an array is to account for the impacts of energy extraction on current velocities. Following on from this the best means of modelling these impacts must be identified. The review of

approaches for modelling tidal energy extraction identified that a common method for simulating tidal turbines in far-field numerical coastal models is the momentum sink approach, where the thrust induced by a tidal turbine is included as an additional external force in the momentum equations. A tidal energy extraction model has been developed based on this method; the details of this model development are discussed in Chapter 5.

Incorporation of tidal turbines into a hydrodynamic model via the momentum sink approach requires parameterisation of the turbine thrust coefficient,  $C_T$ , which is theoretically defined based on the undisturbed velocity upstream of a turbine, but is usually specified in a far-field hydrodynamic model based on the local current velocity at the turbine location. This presents a problem since the local velocity will be reduced from the undisturbed velocity due to the presence of the turbine. A major focus of this research is optimisation of a turbine array based on power output and the resulting hydro-environmental impacts, it is therefore of vital importance to this work that tidal energy extraction is accurately modelled. To ensure this, development of the tidal energy extraction model in this research included assessment of the sensitivity of an energy extraction model (based on the momentum sink approach) to specification of the thrust coefficient, and in particular the appropriateness of adopting the typical value of  $C_T$  in the range of 0.8 – 1.0. A methodology has been determined for identifying a localised thrust coefficient that can be used in conjunction with the local turbine velocity to result in accurate representation of tidal energy extraction and the resulting hydro-environmental impacts. This work, which is particularly important for high resolution far-field modelling, is presented in Chapter 5. Initial tests are carried out on an idealised channel, and one-way nesting is then employed to simulate tidal energy extraction in the Shannon estuary.

It is clear from the literature that energy removal by tidal turbines will undoubtedly result in some hydro-environmental impacts and that the magnitudes of those impacts will increase (non-linearly) with increased energy removal. The amount of energy captured by an array and the hydro-environmental impact of the array are therefore inextricably linked. The literature suggests that energy removal by a single turbine deployment will have negligible hydro-environmental impact with some localised changes to velocities, and by extension material transport, but very little far-field effects. In contrast, modelling studies have shown that large arrays can result in large changes in velocities, water levels, sediment transport and flushing times and that those impacts can exist many kilometres from the array. Most significantly changes are to velocities and most of the environmental impacts result from these. Changes to velocities are also the quickest to determine - water quality impacts require longer simulation times thus changes to velocities were identified as the impact factor of significance for determining optimum array layouts. Use of change in residence times as an impact factor was also explored.

The main aim of this research was to develop a model which could determine optimised turbine array configurations. To achieve this the energy extraction model was further developed to include an optimisation algorithm which can be used to determine optimum tidal turbine arrays, first, based on maximising power output and, second, based on minimising impacts on current velocities. The model development and results from its application to the Shannon estuary site are presented in Chapter 6.

The major novel contribution of this research is the development of an automated optimisation model, which has the ability to optimise array configurations considering both power extracted and the resulting impact on current velocities. The optimisation model has been successfully applied to a number of idealised cases and the

Shannon estuary case study site at both coarse resolutions and turbine scale. To date the only other automated approach found in literature is the gradient-based optimisation algorithm developed by Funke et al. (2014), however, their study, whilst applied to an idealised representation of the Pentland Firth, is not developed at estuary scale level, it also does not consider the resulting impacts of turbine deployment. A second novel contribution of this research is a detailed resource assessment of the Shannon estuary, in which potential deployment sites are determined based on a developed sophisticated assessment approach, A further novel contribution is the development of the localised thrust coefficient, through which accurate simulation of tidal energy extraction via the momentum sink approach is achieved.

## 3 Numerical Modelling Theory

### 3.1 Introduction

The models used for this research are DIVAST (Depth Integrated Velocities and Solute Transport) and MSN (multi-scale nested model). DIVAST was originally developed by Professor R.A. Falconer at the University of Bradford, UK. It is a two-dimensional, finite difference, depth integrated and time-variant model, and is written in the FORTRAN 77 programming language. The model has been developed to simulate distribution of currents, water surface elevations and water quality parameters in shallow estuarine and coastal waters. The model consists of two main sections: a hydrodynamic module which computes the currents and water surface elevations and a solute transport module which computes the transport of water quality parameters, incorporating up to twelve user specified water quality constituents.

The hydrodynamic module is based on the depth integrated solution of the Navier-Stokes equations. The module incorporates the effects of local and advective accelerations, the earth's rotation, barotropic and free surface pressure gradients, the effect of wind, bed friction and turbulent mixing. The solute transport and water quality module is based on the depth integrated advection-diffusion equations and takes account of turbulent dispersion and diffusion, source and sink inputs and decay and kinetic transformation processes.

DIVAST is a comprehensive and versatile model that has since been extensively used in many coastal and estuarine modelling studies (e.g. Ahmadian et al. (2012); Ahmadian & Falconer (2012); Dabrowski (2005); Fallon et al. (2014); Nash et al. (2014); Nash & Hartnett (2009); Nece (1989); Willis et al. (2010)).

MSN is a nested version of the DIVAST model developed by Dr S Nash and Prof M Hartnett at National University of Ireland, Galway. It has been applied to a number idealised domains and Irish estuaries (e.g. Cork Harbour, Galway Bay and Dublin Bay) and has been extensively validated (e.g. Nash & Hartnett (2010); Nash & Hartnett (2014)). MSN allows one to achieve computational savings through selective mesh refinement in areas of interest (i.e. the nested regions). Since MSN is based on the DIVAST model, it uses the same governing equations and solution procedures, thus the following model description is based on the DIVAST model.

### **3.1.1 Model Description**

DIVAST is a two-dimensional numerical model used for the prediction of time-varying water surface elevations, depth averaged velocities and water quality parameters in water bodies that are dominated by horizontal, unsteady flows which do not display significant vertical stratification (Falconer et al. 2001). The water quality parameters which can be simulated include: temperature, salinity, total and faecal coliforms, biochemical oxygen demand (BOD), nitrogen (organic, ammoniacal and nitrate), phosphorus (organic and inorganic), algal biomass and sediments.

The governing differential equations for the hydrodynamic and solute transport processes are solved using a finite difference (FD) scheme based upon an Alternating-Direction Implicit (ADI) technique. The ADI method enables the time-step to be divided into two half time-steps, allowing a two-dimensional implicit scheme to be applied, considering only one dimension implicitly for each half time-step, thus removing the need for the solution of a full two-dimensional matrix (Falconer et al. 2001). Computations are performed on a uniform rectilinear grid structure, with equal grid spacings in the x- and y-directions. The model grid is discretised on an I-J plane in which I and J axes correspond to the x- and y-directions (see Figure 3.1). The solution scheme solves in the x-direction during the first half

time-step, solving water surface elevation (measured above mean water level),  $\zeta$ , the x-direction velocity component,  $U$ , and solute concentrations,  $S$ , implicitly. The solution process is repeated in the y-direction for the second half time-step, computing water surface elevation,  $\zeta$ , the y-direction velocity component,  $V$ , and the solute concentrations,  $S$ . Once initial boundary conditions are generated, the resulting FD equations are solved for each half time-step using the Gauss elimination and back substitution method (Falconer et al. 2001).

The model utilises a space-staggered orthogonal grid system (Figure 3.1). Water elevations and solute concentrations are specified at the centre of each grid cell, while velocity components, volumetric flux and water depths are specified at the centre of each grid cell interface. There are two main advantages of the staggered grid system: one advantage is that for each variable solved, centrally located spatial derivatives are available for each other variable. A second advantage is that in most estuarine modelling scenarios, the boundary conditions are in the form of water elevations at the seaward boundary and velocities (zero in land cases) at the landward boundary.

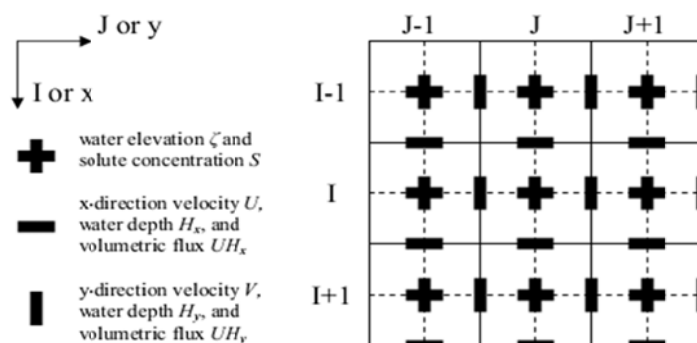


**Figure 3.1: The space-staggered grid scheme and (I, J) coordinate system (Nash, 2010).**

### **3.1.2 Justification of Model Choice**

The DIVAST (and MSN) model has been developed by researchers in the Marine Modelling Group (MMG), NUI Galway of which I am a part of. The model had been well validated for the Shannon estuary and other sites by the MMG and the level of accuracy has been found to be high. In addition, the model is written in FORTRAN, a code which the author was familiar with, this aided the ease of model implementation. This, along with the collective experience within the MMG of using the DIVAST model, and its extensive validation, made it a good model choice for this research.

3D models are capable of simulating current velocities over the depth of the water column and so can accurately reproduce velocities at turbine depth. Whilst this makes them advantageous in simulating tidal energy extraction they have high computational costs and processing times which limits their applications; in contrast, 2D models have relatively low computational costs. DIVAST, and by extension MSN, are depth-averaged and so are appropriate for modelling well-mixed water bodies which do not exhibit large-scale vertical stratification. They were therefore deemed suitable for this research as the majority of estuaries in Ireland, including the Shannon estuary, where tidal turbines might be deployed are predominantly well-mixed (Nash et al. 2005). A disadvantage of the 2D model is that the effects of turbines will also be depth-averaged and thus velocity changes at the turbine-centreline will be less than those measured at the turbine-centreline, or indeed modelled. This is important when assessing the near-field impacts but the present research is focussed on assessing far-field impacts and, based on the computational savings, a 2D model was deemed sufficient.

### **3.2 Governing Equations**

Numerical modelling of fluid flow is based on the theory of conservation of mass and momentum in the body of fluid to be

modelled. In shallow, well-mixed water bodies (see Figure 3.2) the vertical velocity component,  $w$ , is generally small compared to the horizontal velocity components,  $u$  and  $v$ . This allows the horizontal velocity components to be integrated over depth, resulting in depth-integrated velocities  $U$  and  $V$ :

$$U = \frac{1}{H} \int_{-h}^{\zeta} u dz; \quad V = \frac{1}{H} \int_{-h}^{\zeta} v dz \quad (3.1)$$

where  $U$  and  $V$  are the depth integrated velocity components in the  $x$ - and  $y$ -directions respectively,  $H$  is the total water depth and  $h$  is water depth below mean water level, i.e.  $H = h + \zeta$ . This integration reduces the model environment from a complex three-dimensional problem (in  $x, y, z$ ) to a simpler two-dimensional problem (in  $x, y$ ) and is illustrated graphically in Figure 3.3.

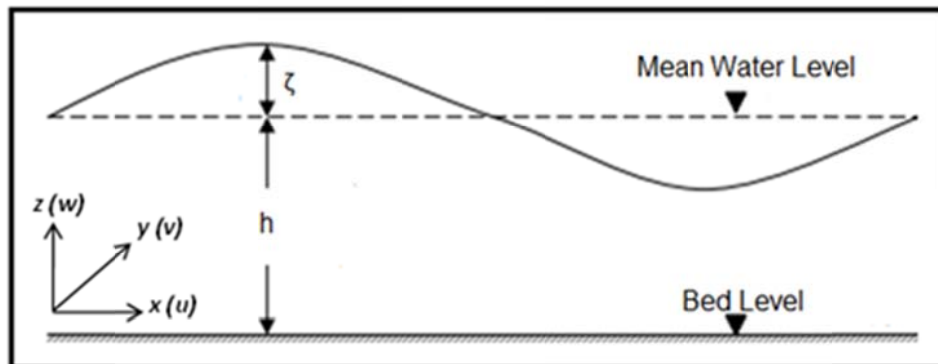


Figure 3.2: A shallow, well-mixed water body.

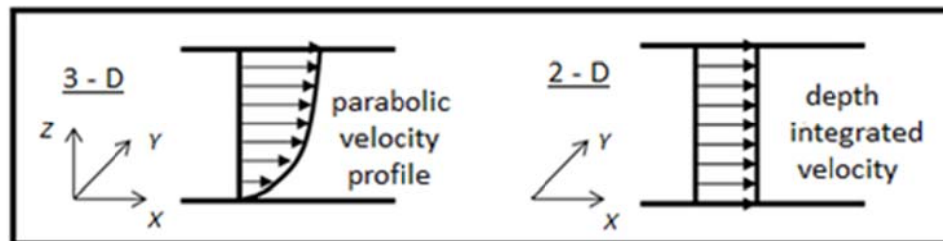


Figure 3.3: Principle of the two-dimensional model (Nash, 2010).

The governing differential equations employed to determine water surface elevations and depth integrated velocities in the horizontal plane are deduced through integration of the three-dimensional continuity and Navier-Stokes equations over the water column depth. Assuming that vertical accelerations are negligible in comparison to gravity, and that the Reynolds stresses in the vertical plane can be represented by a Boussinesq approximation, the depth integrated continuity and x- and y-direction momentum equations can be expressed as (Falconer et al. 2001):

Continuity equation:

$$\frac{\partial \zeta}{\partial t} + \frac{\partial q_x}{\partial x} + \frac{\partial q_y}{\partial y} = 0 \quad (3.2)$$

x-direction momentum equation:

$$\begin{aligned} \frac{\partial q_x}{\partial t} + \beta \left[ \frac{\partial U q_x}{\partial x} + \frac{\partial U q_y}{\partial y} \right] = f q_y - g H \frac{\partial \zeta}{\partial x} + \frac{\rho_a C^* W_x (W_x^2 + W_y^2)^{\frac{1}{2}}}{\rho} - \frac{g U (U^2 + V^2)^{\frac{1}{2}}}{C^2} \\ + 2 \frac{\partial}{\partial x} \left[ \epsilon H \frac{\partial U}{\partial x} \right] + \frac{\partial}{\partial y} \left[ \epsilon H \left[ \frac{\partial U}{\partial y} + \frac{\partial V}{\partial x} \right] \right] \end{aligned} \quad (3.3)$$

y-direction momentum equation:

$$\begin{aligned} \frac{\partial q_y}{\partial t} + \beta \left[ \frac{\partial V q_x}{\partial x} + \frac{\partial V q_y}{\partial y} \right] = f q_x - g H \frac{\partial \zeta}{\partial y} + \frac{\rho_a C^* W_y (W_x^2 + W_y^2)^{\frac{1}{2}}}{\rho} - \frac{g V (U^2 + V^2)^{\frac{1}{2}}}{C^2} \\ + 2 \frac{\partial}{\partial y} \left[ \epsilon H \frac{\partial V}{\partial y} \right] + \frac{\partial}{\partial x} \left[ \epsilon H \left[ \frac{\partial V}{\partial x} + \frac{\partial U}{\partial y} \right] \right] \end{aligned} \quad (3.4)$$

where  $q_x$  ( $=UH$ ) and  $q_y$  ( $=VH$ ) are the discharges per unit width in the x- and y-directions respectively,  $\beta$  is the momentum correction factor for a non-uniform vertical velocity profile,  $f$  is the Coriolis parameter due to the earth's rotation,  $g$  is gravitational acceleration,  $\rho_a$  and  $\rho$  are the densities of air and fluid respectively,  $C^*$  is the air/fluid resistance coefficient,  $W_x$  and  $W_y$  are the wind velocity components

in the x- and y- directions, C is the Chezy bed roughness coefficient and  $\varepsilon$  is the depth averaged turbulent eddy viscosity.

The individual terms within the momentum equations (3.3) and (3.4) from left to right, refer to the depth integrated local acceleration, advective accelerations, Coriolis force, pressure gradient, wind shear force, bed shear resistance and turbulence induced shear force.

Solute transport processes are incorporated into the model based on the two-dimensional, depth integrated, advective-diffusion equation (Falconer et al. 2001):

$$\begin{aligned} & \text{(1)} \qquad \qquad \qquad \text{(2)} \\ & \frac{\partial SH}{\partial t} + \beta \left[ \frac{\partial Sq_x}{\partial x} + \frac{\partial Sq_y}{\partial y} \right] = \\ & \frac{\partial}{\partial x} \left[ HD_{xx} \frac{\partial S}{\partial x} + HD_{xy} \frac{\partial S}{\partial y} \right] + \frac{\partial}{\partial y} \left[ HD_{yx} \frac{\partial S}{\partial x} + HD_{yy} \frac{\partial S}{\partial y} \right] \end{aligned} \quad \text{(3)} \quad (3.5)$$

where  $D_{xx}$ ,  $D_{xy}$ ,  $D_{yx}$ ,  $D_{yy}$  are the depth averaged dispersion diffusion coefficients in the x- and y-directions respectively. Each term in equation (3.5) (from left to right) represents the depth integrated solute variations within the model due to (1) local effects, (2) advective effects, (3) turbulent diffusion and dispersion.

### 3.2.1 Finite Difference Formulations

The governing differential equations (3.2) – (3.5) are expressed in FD form and solved using an ADI scheme. Further details on the finite difference formulations and their solution scheme can be found in Nash, (2010).

### 3.3 Model Accuracy, Stability and Resolution

The accuracy of the hydrodynamic model is dependent on the ability of the applied FD scheme to correctly solve the models governing equations. The success of a FD scheme can be analysed based on

consistency, convergency, stability and accuracy. These characteristics are significant as they will influence the model resolution.

The developed finite difference equations are employed to solve the models governing differential equations; if they are to describe the same physical phenomena they must be consistent. However, the FD equations are approximations of the exact solution of the differential equations, and so will contain some error. This is known as the truncation error. For any FD scheme it is desirable for the time-step,  $\Delta t$ , and spatial distance step,  $\Delta x$ ,  $\Delta y$ , to converge to zero, at which point the FD equation converges to the original differential equation and the truncation error is negligible. If this condition is met, the FD scheme is assumed consistent with the differential equation.

The stability of the model is dependent on the round off errors generated during calculation of the FD equations. A limitation of a numerical model is its inability to generate the solution of a FD equation to an infinite number of decimal places. Instead solutions are determined to a finite number of decimal places and a round off error is generated for each individual calculation. A FD scheme will only be deemed stable if the cumulative effects of the round off errors, at any point of the computation, are negligible. This results in a computed solution that differs only very slightly from the exact solution of the FD equations.

Numerical models can be defined as explicit or implicit. In explicit models, a direct computation is carried out in which the dependent variables are expressed in terms of known parameters. In implicit models the dependent variables are defined by coupled sets of equations involving unknown parameters (i.e. at the next time-step), and the solution is determined using an iterative technique or matrix. The stability of the FD solutions in an explicit computational model is governed by the Courant condition (Nash, 2010). DIVAST is an implicit model and is therefore inherently stable regardless of time-

step. As such, the choice of model resolution is not constrained by the Courant stability criteria.

Although a FD scheme may be both consistent (convergent) and stable, truncation errors can become aggregated during the computation process, resulting in an inaccurate model solution. To ensure sufficient accuracy, the model is subjected to a constraint based on the acceptable degree of truncation error for a FD scheme. This constraint is applied to the model by restricting the time-step using Courant stability criteria. The Courant number,  $C_n$ , can be expressed mathematically as:

$$C_n = \sqrt{gH} \frac{\Delta t}{\Delta x} \quad (3.6)$$

Falconer et al. (2001) determined that DIVAST model accuracy begins to decline when the Courant number exceeds 8 ( $C_n > 8$ ). Based on this, the model time-step is restricted by employing the Courant equation in the form:

$$\Delta t \leq 8 \frac{\Delta x}{\sqrt{gH}} \quad (3.7)$$

This equation can then be used to determine the maximum time-step,  $\Delta t_{max}$ , allowable for a selected spatial resolution,  $\Delta x$ .

### **3.4 Model Architecture**

The model consists of a main program and a number of subroutines each with a different function. The main program calls the subroutines for execution as they are required. Figure 3.4 illustrates a flowchart of the model architecture and describes the function of each subroutine. Input and output data files are opened in subroutines 1 and 2. The input data including boundary conditions, land/sea values and water depth data within the domain are read in and stored in subroutines 3, 4 and 6. Subroutine 5 establishes the x- and y-direction integration sections. All variables are initialised in

subroutine 7. The hydrodynamics in the x-direction are computed during the first time-step in subroutines 8-11, whilst subroutines 12-15 compute the hydrodynamics in the y-direction during the second half time-step. Subroutines 8-15 are executed at every time-step for the entire model simulation. The chezy values and eddy viscosities are recalculated in subroutines 16 and 17, which are called based on a recalculation time-step specified in the input data file. Any specified output parameters are written to output files in subroutine 18.

| MAIN PROGRAM |  |
|--------------|--|
| 1. FILINP    | •Opens input data file   |
| 2. FILOUT    | •Opens file for data output                                      |
| 3. BOUND     | •Reads open boundary (OB) data                                   |
| 4. FIELD     | •Reads computational domain                                      |
| 5. FIND      | •Establishes the integration sections                            |
| 6. DEPTH     | •Reads water depths  |
| 7. INITL     | •Initialises depths, elevations, concentrations and chezy values |
| 8. HYDBND    | •Assigns hydrodynamic data at OB                                 |
| 9. HYDMODX   | •Solves hydrodynamics in x-direction                             |
| 10. SIDEH    | •Recalculates water depths                                       |
| 11. FLDRY    | •Checks for flooding and drying of cells                         |
| 12. HYDBND   | •Assigns hydrodynamic data at OB                                 |
| 13. HYDMODY  | •Solves hydrodynamics in y-direction                             |
| 14. SIDEH    | •Recalculates water depths                                       |
| 15. FLDRY    | •Checks for flooding and drying of cells                         |
| 16. CHEZY    | •Recalculates chezy values                                       |
| 17. EDDY     | •Recalculates eddy viscosities                                   |
| 18. PRINT    | •Outputs time series and snapshots                               |

**Figure 3.4: Flowchart of model subroutines.**

### **3.5 The Nested Model**

The accuracy of a numerical coastal model increases with increasing spatial resolution. High resolution models improve the precision of simulation of the hydrodynamics and sediment transport within a water body, which results in enhanced representation of local features. Open boundaries within a model must be positioned such that they do not adversely impact on simulations in an area of interest, therefore the model domain is generally much larger than the area of interest. As a result models of high resolution can have overly large computational domains, leading to long processing times and high computational costs. However, it is not necessary to apply high spatial resolutions throughout an entire domain, only in the area of interest. Nested models involve embedding of a fine resolution grid(s) into a larger grid of coarse resolution allowing simulation of a specified area in high resolution, thus keeping down processing times and associated computational expenses.

#### **3.5.1 Nested Model Grids**

Of particular interest in this research was modelling the hydro-environmental impacts of tidal turbines deployed in an array. To simulate interactions between individual turbines a high resolution model of grid spacing similar to the physical size of the turbine (e.g. the turbine rotor diameter) was required. In order to achieve these high resolutions of the order of 1-20 m, a nested model was employed which enabled flow between neighbouring turbines to be resolved whilst still capturing impacts at a bay/estuary-scale at a relatively low computational cost.

Nested models can be described as one-way (passive) (Anthes, 1974) or two-way (interactive) (Zhang et al. 1986) depending on the interaction between the parent and child grid. In one-way nesting, the parent grid provides boundary data to the child grid, i.e. the interaction occurs in one direction only, in a two-way nested model

there is a two-way interaction as the fine grid data is then fed back from child to parent grid and the parent grid solution is updated. One-way nesting is an established technique used in a number of hydrodynamic studies (e.g. Korres & Lascaratos (2003); Nash (2010); Staneva et al. (2009)), it was deemed appropriate for this research as the nested model is used for down-scaling applications; hence the nested grid solution is of sole interest.

The Multi-Scale Nested model (MSN) used for this research was developed from the DIVAST model described in the previous section and is therefore also a 2D finite difference model (Nash & Hartnett (2010); Nash & Hartnett (2014)). The MSN model uses an overlapping grid structure in which a single coarse grid contains one or more fine grids within its boundary limits; this is illustrated in Figure 3.5. The coarse grid is known as the parent grid (PG) and the fine grids are known as child grids (CG). Throughout this thesis parent grids refer to coarse, low resolution models while child grids refer to fine, high resolution models. MSN is capable of multiple levels of nesting, in which child grids can also be parents, parents can have one or more child grids and several children may have the same parent at the same level of nesting. Figure 3.5 illustrates a multiple nested model, in this example the parent grid, G.1.1, contains three children, G.2.1, G.2.2 and G.2.3, and the nested grid, G.2.1, contains further levels of nesting.

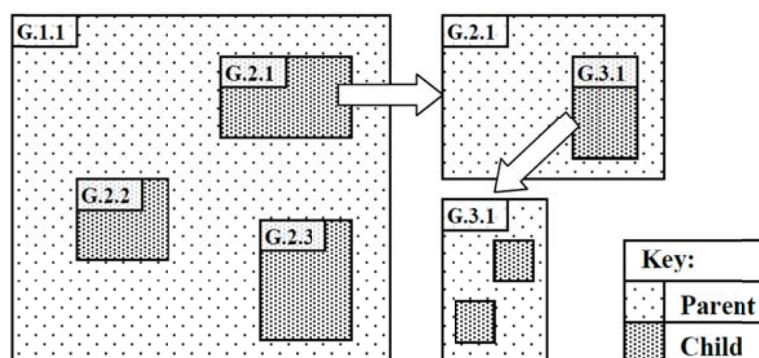
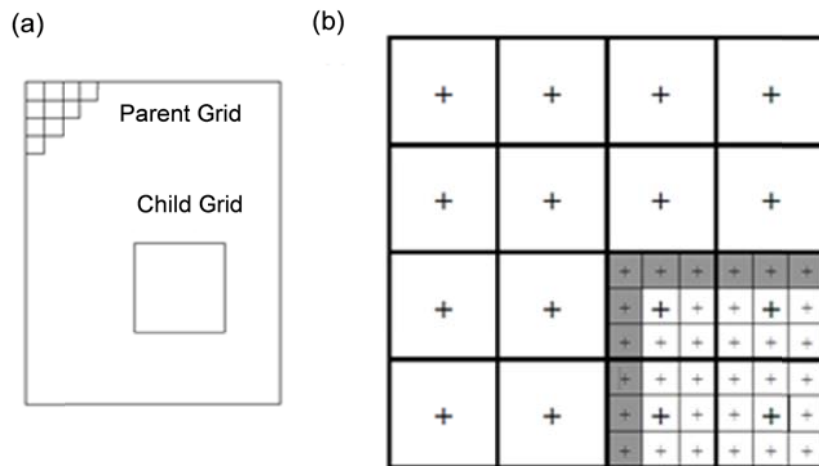


Figure 3.5: Nested model grid structure (Nash, 2010).

The relationship between parent and child grids in space and time are known as the spatial ( $\Delta X_{Parent} / \Delta X_{Child}$ ) and temporal ( $\Delta t_{Parent} / \Delta t_{Child}$ ) nesting ratios, respectively. Generally they are integers and they are usually set to the same value, although this is not a necessity.

### 3.6 MSN One-way Nested Model

In a one way nested model the parent model solution is used to generate hydrodynamics within the child model. The parent model is temporally integrated and the boundary data for the child grid are obtained by interpolating the required data from the adjacent parent grid cells temporally and spatially. The child model is then integrated temporally and spatially. The child model is then integrated temporally. An example of a one-way nested model grid with a 3:1 spatial nesting ratio is shown in Figure 3.6.



**Figure 3.6: Schematic of a one-way nested model grids with a 3:1 spatial nesting ratio: (a) the parent and child grids, (b) a detail of the child grid interface (shaded cells represent child grid boundary) (Nash, 2010).**

The parent and child grid models in MSN are coupled, meaning the coarse and nested grids are dynamically linked. The parent grid is simulated for a full time-step, at the end of which the open boundary data for the child grid is assigned and integrated with respect to the current parent time-step. The parent grid can then proceed to the

next time-step and the process is repeated. It is possible for a one-way nested model to be uncoupled, in which case the parent model must be run for the entire simulation and the data stored before the child model can use this data and begin to run; however, this method requires large amounts of storage space and boundary data is often averaged to reduce storage requirements. It is therefore more accurate and efficient to use a coupled model.

The nesting procedure for a single level nesting MSN simulation is presented graphically in Figure 3.7 and is described as follows:

1. Integrate parent grid by one time-step to time  $t + \Delta t_p$
2. Interpolate (time-wise) the required parent grid data along the child grid boundary to the current time-step of the child grid ( $t + \Delta t_c$ )
3. Interpolate (spatially) the child grid open boundary data from the parent grid data at the current time-step of the child grid ( $t + \Delta t_c$ )
4. Integrate child grid by one time-step to time  $t + \Delta t_c$
5. Repeat steps 2 – 4 so the child grid is synchronised to the current time-step of the parent grid ( $t + \Delta t_p$ )
6. Return to step one and proceed.

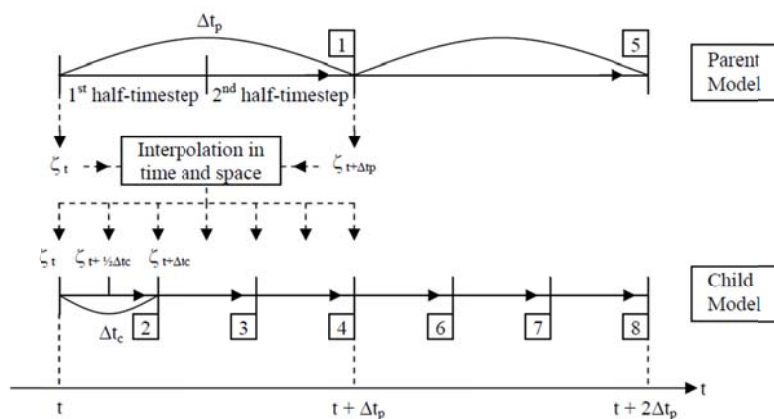


**Figure 3.7: The nesting procedure. Subscripts  $p$  and  $c$  denote parent and child grids (Nash, 2010).**

Figure 3.7 illustrates the order of time integration within the model, which proceeds from the outer parent grid to the inner child grid. All child grids must be integrated up to the time-level of the parent grid before the integration of the parent grid can proceed. The ADI solution method employed to solve the models governing differential equations does not impact on the time integration as each parent grid is integrated by one complete time-step before the child grid is integrated. It does, however, impact on the temporal interpolation process as the child grid requires boundary data at each half time-step.

The accuracy of a nested model is dependent on the conservation of mass and momentum between the boundaries of the coarse (parent) and fine (child) models. If conservation is not achieved noise and, consequently, errors will be generated in the child model. The choice of boundary condition is therefore vital when simulating nested models.

### 3.7 The Open Boundary Problem

A nested model uses the boundary conditions of the parent grid to force hydrodynamics within the nested child grid. The resulting simulation of the fine resolution child domain,  $\Omega_C$ , over a time period  $[0, T]$  with initial conditions  $t=0$  can be initially described mathematically as:

$$L_C \phi_C = f_C \quad \text{in } \Omega_C \times [0, T] \quad (3.8)$$

where  $L_C$  is the partial differential operator,  $\phi_C$  is the child grid solution,  $f_C$  is the child model forcing. In a coastal model,  $\Omega_C$  will never be completely enclosed by a solid boundary, but will be connected to the open ocean through an open boundary,  $\Gamma$ . The open boundary problem exists in accurately computing the interaction between nested grid and the open boundary and can therefore be expressed as:

$$B\phi_C = e \quad \text{on } \Gamma \times [0, T] \quad (3.9)$$

where  $B$  is the open boundary operator, typically in linear differential form, known as the open boundary condition (OBC), and  $e$  represents the behaviour of the open ocean on the open boundary,  $\Gamma$ .

The one-way nested problem can therefore be expressed in terms of the parent model as:

$$L_P \phi_P = f_P \quad \text{in } \Omega_P \times [0, T] \quad (3.10)$$

where  $L_P$  is the partial differential operator,  $\phi_P$  is the parent grid solution,  $f_P$  is the parent model forcing and  $\Omega_P$  is the parent domain.

Since  $\Omega_C \cup \Omega_P$ , the parent solution can be used to force the child open boundary solution and equation 3.21 can be expressed as:

$$B_C \phi_C = B_P \phi_P \quad \text{on } \Gamma \times [0, T] \quad (3.11)$$

Due to the different resolutions of the parent and child grids, the open boundary operators,  $B$ , in equation (3.11) are not equal; the parent boundary operator,  $B_P$ , must incorporate the interpolation of  $\phi_P$  from the spatial resolution of the parent grid to the child grid resolution. The accuracy of the nested model solution is therefore dependent on the choice of open boundary operator and the accuracy of the data specified at the parent boundary.

Inconsistencies between the parent and child boundary solutions can lead to wave reflection and noise generation, and create inaccuracies due to loss of mass and momentum, generating errors within the child model. An appropriate boundary operator will reduce these errors as they suitably blend the parent and child solutions, limiting the distortion of waves. Selection of  $B$  is often referred to as the open boundary problem. Specification of incorrect boundary data can lead to simulation errors in the parent model which will transfer into the

child grid through the boundary specification. These errors can be minimised through suitable positioning of the nested grid's open boundaries.

### 3.7.1 Specification of the Open Boundary

MSN employs the Dirichlet, or 'clamped', boundary condition. It is a relaxation, or nudging, method which attempts to nudge the child grid solution to the solution of the parent grid. Whilst there are a number of relaxation methods, this is considered the most severe as the parent grid solution is directly imposed onto the boundary,  $\Gamma$ , of the child grid such that:

$$\phi_C|_{i,j}^{n+\frac{1}{2}} = \phi_P|_{i,j}^{n+\frac{1}{2}} \quad \text{on } \Gamma \quad (3.12)$$

where  $i$  and  $j$  are the nested grid coordinates. The parent grid solution  $\phi_P|_{i,j}^{n+\frac{1}{2}}$  on  $\Gamma$  is determined by interpolation in space and time to the child grid resolution.

Simplification of boundary formulations can also lead to errors in data transfer between parent and child models. To resolve this ghost cells are incorporated into the child grid just outside the open boundary, allowing the boundary grid cells to behave as internal cells thus creating an internal boundary. This eliminates the need for simplification of the boundary formulations, preserving mass and momentum and improving accuracy of the model (Nash (2010); Nash & Hartnett (2014)). The incorporation of the ghost cells into child grid is shown

Figure 3.8. This example is a schematic of the grid configuration for a 3:1 spatial nested ratio.

The nature of a nested model means the parent and child grids will possess different spatial resolutions, therefore, for accurate data transfer, the parent grid data must be interpolated to the resolution of

the child grid. Use of an appropriate interpolation technique will ensure accurate boundary data is transferred from parent to child grid, thereby minimising noise generation and errors. MSN uses a linear interpolation scheme in which the coarse boundary data is interpolated linearly in both time and space.

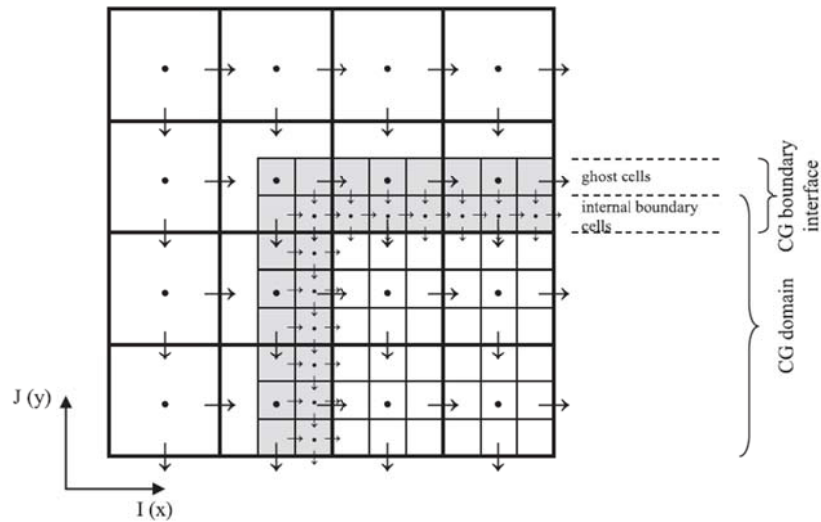


**Figure 3.8: Schematic of the internal boundary configuration for a 3:1 nesting ratio (Nash & Hartnett, 2014).**

### 3.7.2 Model Architecture

The original MSN model is modified to include energy extraction.. The main 'DO loop' for the nested model is found within the NEST subroutine, which allows interaction with the coarse resolution code, enabling information to be passed from the coarse domain to the fine nested domain which is used to specify the boundary conditions. Figure 3.9 shows the MSN model architecture with the child grid subroutines shaded blue.

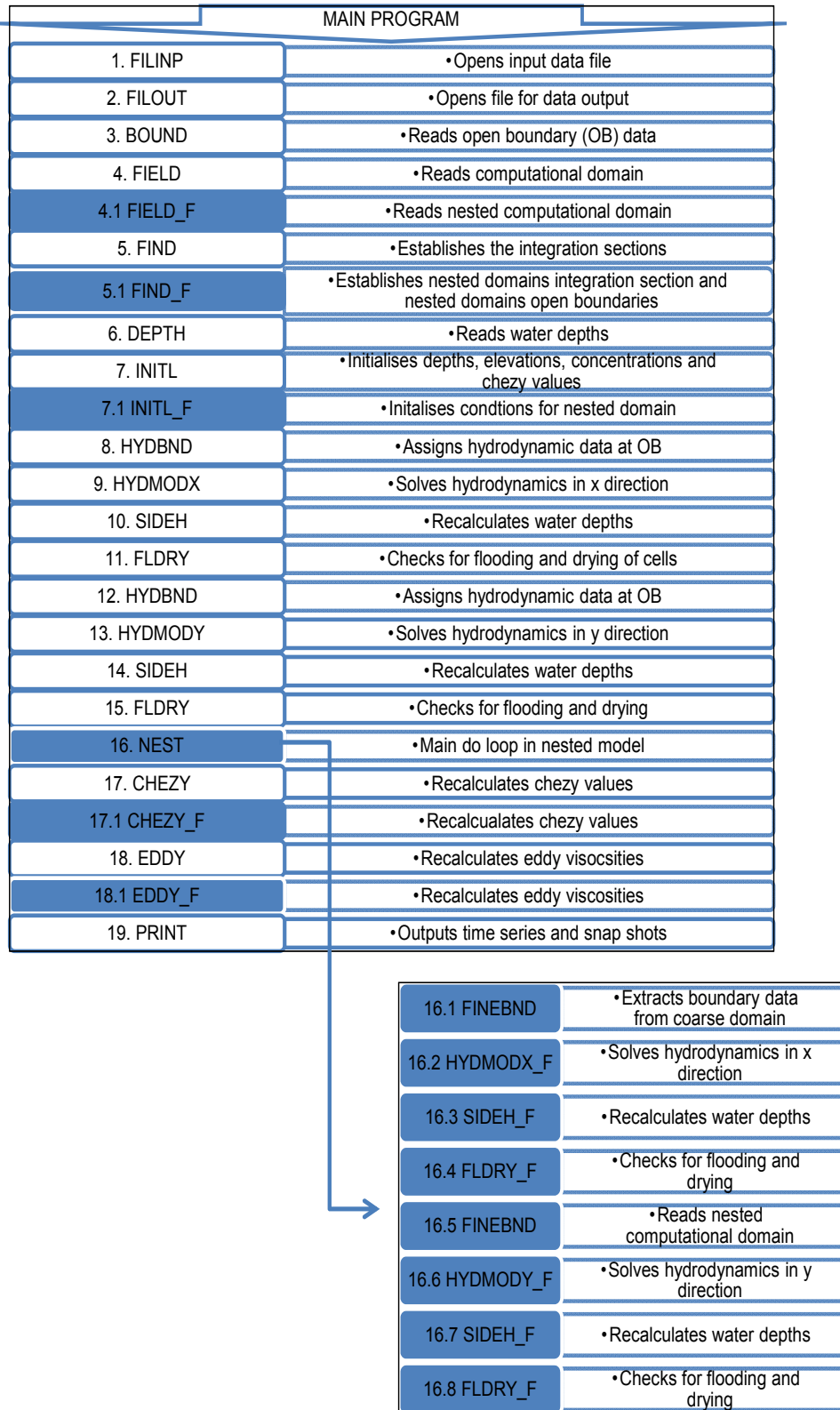


**Figure 3.9: Flowchart of model subroutines including amendments for one-way nesting.**

### **3.8 Tidal Flushing**

In this research the solute transport module of DIVAST is used in conjunction with data computed in the hydrodynamic module to undertake a flushing analysis. The advective-diffusion equation (3.5) is used to describe mass transport and the effect of energy extraction there-on, allowing prediction of changes in a water body's flushing capabilities due to turbine deployment.

The average residence time,  $\tau_r$ , is defined as the expected amount of time a material stays in a particular area. Residence time has been acknowledged as the most appropriate concept for describing tidal exchange characteristics (Takeoka,1984). A common method for assessing residence times in a water body is through a dye decay study, in which a known dye concentration is instantaneously injected into the fluid and its movement and dissipation is examined. In this research  $\tau_r$  is defined as the time taken for the dye level in a particular grid cell/region to fall below a user specified cut-off value.

### **3.9 Tidal Harmonics and Tidal Ellipse Analysis**

A tidal resource assessment of a case study site was carried out to compare different methodologies of quantifying available tidal power and to identify potential tidal energy berths within the site. Tidal harmonic analysis was employed along with tidal ellipse theory to analyse current flow and determine the prevailing flow direction. Available power could then be quantified using only the velocity vectors aligned with this prevailing flow direction. A weakness of traditional approaches to resource assessment is that they fail to consider current flow directionality. The approach developed in this research therefore has a higher level of sophistication and so is expected to achieve a greater level of accuracy.

The DIVAST model was developed to include harmonic analysis software, described in Section 3.9.2, which is used to analyse the

hydrodynamics to produce tidal constituents and ellipse parameters. This section explains tidal harmonic and ellipse theory in further detail and presents the modifications performed to incorporate harmonic analysis into the existing numerical model.

A sample plot of water surface variation due to tides is shown in Figure 3.10; the data was recorded at Inishmore, County Galway, Ireland, on 20<sup>th</sup> of January, 2008. Numerical methods can be used to deconstruct observed or modelled tidal heights and currents into component signals resulting from the different forcing factors; this process is called tidal harmonic analysis.

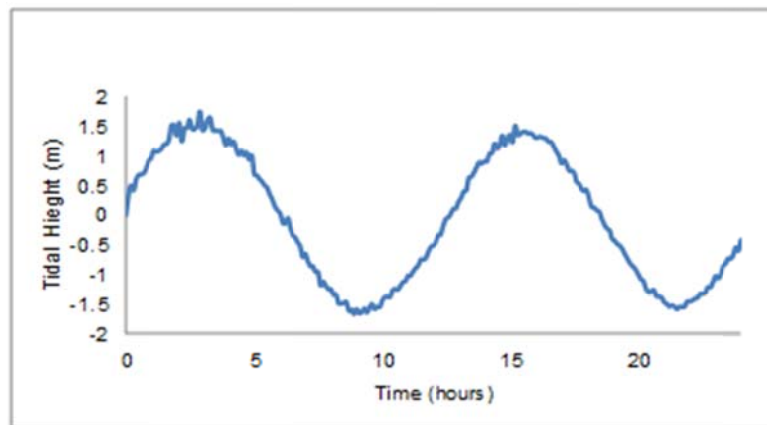


Figure 3.10: Example of tidal gauge data plot (Marine Institute, 2017).

### 3.9.1 Tidal Harmonic Analysis

The basis of tidal analysis and prediction methods originates from Doodson's tidal potential model (Doodson, 1941). Doodson developed the idea that the position of the sun or moon, and thus the tide generating forces, could be determined based on a number of astronomical variables, namely:

- $L$  = mean lunar time
- $S(t)$  = mean longitude of the moon,
- $H(t)$  = mean longitude of the sun,
- $P(t)$  = mean longitude of the lunar perigee,
- $N'(t)$  = negative of the longitude of the mean ascending node,
- $P'(t)$  = mean longitude of the solar perigee.

Tidal harmonic analysis is based on the principle that each tide generating force is represented by a harmonic cosine curve, with the same period of oscillation as the astronomic force producing it; these are known as harmonic or tidal constituents. Each constituent is dependent on a different astronomical phenomena, for instance the principal lunar,  $M_2$ , and solar,  $S_2$ , constituents result from the earth spinning relative to the moon and sun, respectively, whereas the lunar elliptic constituents,  $N_2$  and  $L_2$ , are a consequence of the nearest and furthest distances between the earth and moon. The nature of a tide will be dependent on the distribution of the tidal constituents generating it; for instance, a characteristic the  $M_2$  and  $S_2$  constituents have in common is that they are semi-diurnal in nature, and so if they are dominant relative to the major diurnal constituents,  $K_1$  and  $O_1$ , the resulting tides will be semi-diurnal.

Based on Doodson's theory, the frequency of each tidal constituent can be defined by its 'Doodson number', which consists of a set of six integers that identify both the speed and phase of a tidal constituent. The frequency of each constituent is known, and so, if tidal measurements exist for a sufficiently long time-series the signal can be decomposed into its comprising constituents. Each tidal constituent is designated by a letter, representing the acting astronomical force, and symbol, denoting the number of tidal cycles per astronomical cycle, for example consider the Principal Lunar Semidiurnal constituent,  $M_2$ : the M refers to the moon and the subscript 2 means there are two complete tidal cycles for each astronomical tide. Tidal constituents are generally grouped according to their defining subscript number and can be classed in one of three main categories (Mann & Lazier, 2013):

1. Diurnal: have tidal periods of approximately 24 hours, equating to one full tidal cycle per solar day, and so their symbols are accompanied by subscript 1,

2. Semidiurnal: have tidal periods close to 12 hours, with two full tidal cycles per solar day; their symbols are therefore accompanied by subscript 2,
3. Long period/frequency: have tidal periods of days to years, their symbols have no general pattern.

A further category of tidal constituents is defined as ‘overtides’. These constituents are caused by the nonlinear interactions of other constituents and bathymetry and are common to estuaries and shallow waters. Their tidal periods are less than 9 hours and generally have subscripts of 4 or 6 equating to around four or six tidal cycles per solar day.

There are a large number of tidal constituents; 37 of these are listed in Table 3.1 along with a description of the causative astronomical phenomena and the nature of the tide they produce. Not every constituent will contribute to tidal flow in every water body; with more complex tidal variations resulting from the combined effect of a large number of tidal constituents.

Harmonic analysis is developed on the principal that tidal characteristics such as water height and current velocity at a given location can be represented by the sum of a finite number,  $M$ , of harmonic constituents, with each constituent consisting of a unique pair of amplitude and phase parameters, oscillating at a certain frequency, that are determined by the astronomical tide generating forces (Marone et al. 2003). These unique values of amplitude and phase are referred to as the tidal harmonic constants (Boon, 2017). The purpose of any tidal harmonic analysis is to determine the constants at a given location for each individual tidal constituent, thereby enabling the astronomical tide to be forecast. The resulting tidal height can be represented in the form:

$$h(t) = \sum_{j=1}^M A_j \cos[2\pi(\delta_j t - \theta_j)] \quad (3.13)$$

where  $h(t)$  is the tidal height at time  $t$ ,  $M$  is the number of harmonic constituents chosen for the analysis,  $j$  is the individual constituent,  $A_j$  and  $\delta_j$  are the amplitudes and frequencies of the constituent respectively, and  $\Theta_j$  is the constituent phase, measured in radians. An example of the resulting tidal curve due to a combination of its individual tidal constituents is presented in Figure 3.11.

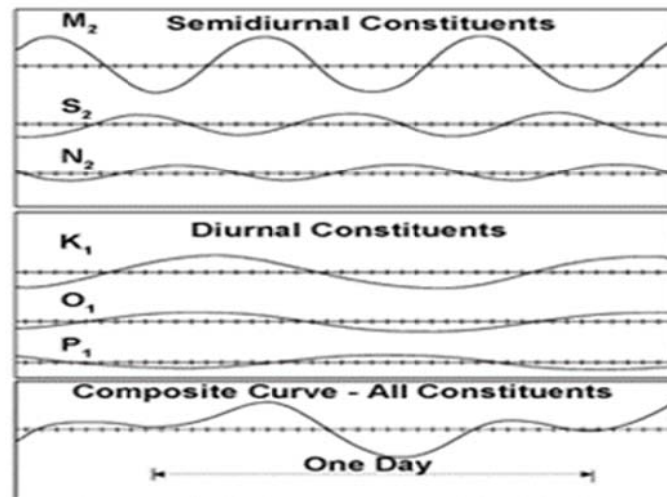


Figure 3.11: A tidal curve resulting from its individual constituents (Naval Postgraduate School (Department of Oceanography), 2015).

**Table 3.1: Tidal harmonic constituents (NOAA, 2017).**

| Tidal constituent | Period (hour) | Speed ( $^{\circ}$ /hour) | Description  | Tidal constituent | Period (hour) | Speed ( $^{\circ}$ /hour) | Description                     |
|-------------------|---------------|---------------------------|--|-------------------|---------------|---------------------------|---------------------------------|
| $M_2$             | 12.4206012    | 28.984104                 | Principal lunar semidiurnal                            | $M_M$             | 661.3111655   | 0.544375                  | Lunar monthly                   |
| $S_2$             | 12            | 30                        | Principal solar semidiurnal                            | $S_{SA}$          | 4383.076325   | 0.082137                  | Solar semiannual                |
| $N_2$             | 12.65834751   | 28.43973                  | Larger lunar elliptic semidiurnal                      | $S_A$             | 8766.15265    | 0.041069                  | Solar annual                    |
| $K_1$             | 23.93447213   | 15.041069                 | Lunar diurnal  | $M_{SF}$          | 354.3670666   | 1.015896                  | Lunisolar synodic fortnightly   |
| $M_4$             | 6.210300601   | 57.96821                  | Shallow water overtides of principal lunar constituent | $M_F$             | 327.8599387   | 1.098033                  | Lunisolar fortnightly           |
| $O_1$             | 25.81933871   | 13.943035                 | Lunar diurnal  | $RHO_1$           | 26.72304239   | 13.47152                  | Larger lunar evectional diurnal |
| $M_6$             | 4.140200401   | 86.95232                  | Shallow water overtides of principal lunar constituent | $Q_1$             | 26.868350     | 13.39866                  | Larger lunar elliptic diurnal   |
| $MK_3$            | 8.177140247   | 44.025173                 | Shallow water terdiurnal                               | $T_2$             | 12.01644934   | 29.95893                  | Larger solar elliptic           |
| $S_4$             | 6             | 60                        | Shallow water overtides of principal solar constituent | $R_2$             | 11.98359564   | 30.04107                  | Smaller solar elliptic          |
| $MN_4$            | 6.269173724   | 57.423832                 | Shallow water quarter diurnal                          | $2Q_1$            | 28.00621204   | 12.85429                  | Larger elliptic diurnal         |

| Tidal constituent | Period (hour) | Speed (°/hour) | Description  | Tidal constituent | Period (hour) | Speed (°/hour) | Description                        |
|-------------------|---------------|----------------|--|-------------------|---------------|----------------|------------------------------------|
| MU <sub>2</sub>   | 12.62600446   | 28.512583      | Larger lunar evectional                                | P <sub>1</sub>    | 24.06588766   | 14.95893       | Solar diurnal                      |
| S <sub>6</sub>    | 4             | 90             | Shallow water overtides of principal solar constituent | 2SM <sub>2</sub>  | 11.60695157   | 31.0159        | Shallow water semidiurnal          |
| MU <sub>2</sub>   | 12.8717576    | 27.968208      | Variational  | M <sub>3</sub>    | 8.280400802   | 43.47616       | Lunar terdiurnal                   |
| 2N <sub>2</sub>   | 12.90537439   | 27.895355      | Lunar elliptical semidiurnal second-order              | L <sub>2</sub>    | 12.19162085   | 29.52848       | Smaller lunar elliptic semidiurnal |
| OO <sub>1</sub>   | 22.30608083   | 16.139101      | Lunar diurnal  | 2MK <sub>3</sub>  | 8.386302931   | 42.92714       | Shallow water terdiurnal           |
| LAM <sub>2</sub>  | 12.22177386   | 29.455626      | Smaller lunar evectional                               | K <sub>2</sub>    | 11.96723606   | 30.08214       | Lunisolar semidiurnal              |
| S <sub>1</sub>    | 24            | 15             | Solar diurnal  | M <sub>8</sub>    | 3.105150301   | 115.9364       | Shallow water eighth diurnal       |
| M <sub>1</sub>    | 24.84120241   | 14.496694      | Smaller lunar elliptic diurnal                         | MS <sub>4</sub>   | 6.103339275   | 58.9841        | Shallow water quarter diurnal      |
| J <sub>1</sub>    | 23.09848146   | 15.5854435     | Smaller lunar elliptic diurnal                         | SK <sub>3</sub>   | 7.992705324   | 45.04107       | Shallow water terdiurnal           |
| 2SM <sub>6</sub>  | 4.045666131   | 88.98411       | Shallow water sixth-diurnal                            |                   |               |                |                                    |

### **3.9.2 Tidal Harmonic Analysis Software**

Classic harmonic analysis involves employing a least squares fit technique to separate the observed tide or tidal current into harmonic constituents. Advancement on this traditional method involves performing nodal corrections and interference to heighten the sophistication of the analysis. A number of tools are available to perform harmonic analysis, examples of available software packages include T\_Tide, which is designed for implementation into MATLAB, TAPPY (tidal analysis program in python), TASK (tidal analysis software kit) which is developed by the National Oceanography Centre and written to run in Microsoft windows, GEOTIDE which is another window-based program, and a MIKE 21 tidal analysis and prediction module.

The software chosen to perform tidal analysis in this research is the harmonic tidal analysis software, henceforth called HTAS, developed at the Institute of Ocean Sciences, Fisheries and Oceans Canada, Sidney, British Columbia, Canada (Foreman & Bay 1996). HTAS permits greater accuracy and versatility in the harmonic analysis of a tidal time-series than was accessible in traditional software. A specific improvement to traditional methods is its ability to analyse randomly sampled and multiyear data, as older codes were restrictive, requiring regularly sampled input time-series data. A further advancement is the manner in which adjustments to the results from the least squares fitting procedure are made. This more versatile software allows more accurate nodal correction, inference calculations and astronomical argument adjustments to be made as they are directly incorporated into the least squares matrix. The program allows one or two dimensional time-series data to be analysed, eliminating the need for separate programs to analyse tidal heights and currents. Furthermore, HTAS has the ability to produce tidal current ellipse parameters from the results of the harmonic analysis of tidal currents (Foreman et al. 2009). Producing current

ellipses is necessary in this research for determining the prevailing direction of current flow. Perhaps most importantly, the HTAS software is free and it is written in FORTRAN meaning it could be relatively easily implemented into the DIVAST model. A cohesive and user-friendly manual is available with details on how to correctly utilise the software (Foreman & Bay, 1996) and literature is available discussing its improvements and applications (Foreman et al. 2009). For all of these reasons, HTAS was deemed suitable for use in this research.

HTAS consists of a number of subroutines which are called as required from the main program. A flowchart of the model architecture including descriptions of the function of each subroutine is shown in Figure 3.12. The program has been validated at the Institute of Ocean Sciences (Foreman & Bay, 1996). The main program reads input data and controls the output. Specific inputs are required to perform an analysis, these consist of input files containing tidal constituent information including constituent name, frequency, the constituent with which they are compared with under the Rayleigh criterion and the six Doodson numbers, phase correction and number of satellite constituents for each main constituent. Details on the tidal station (station name, number and position), analysis time and time period of the analysis are also required along with the observed tidal heights, current velocities and their times of occurrence. The resulting output data consists of the constituents included in the analysis, their frequencies, amplitudes and phase lags. A current analysis determines and outputs ellipse parameters for each constituent, including the major and minor axis lengths, the angle of inclination and the Greenwich phase angles for the current vector.

Once initial constituent data is read in and stored, subroutine 1 is called to read in the astronomical information and re-calculate the constituent frequencies. Subroutines 2–6 are contained within the

main DO-loop and so are called depending on the user specified analysis type, with computations carried out once for a tidal height analysis only and twice for a height and current analysis. They are executed for each selected (I, J) location in the domain. Subroutine 2 converts any given date in day/month/year/century format to the day number based on the universal Gregorian calendar, and it is called after any input date data is read in. The main analysis computations occur in subroutines 3-6, which are executed for each constituent included in the analysis. If current analysis has been specified, once the over-determined matrix has been solved, the ellipse parameters are computed within the main program and any specified output parameters are written to output files at the end of the main program.

| 'HTAS' MAIN PROGRAM   |   |
|-----------------------|---|
| Input Data            | • Input hourly height and current data for specified time period read in and stored in main program |
| Included Constituents | • Constituents to be included in analysis selected in the main program                              |
| 1. Opnvuf             | • Reads required information to preform nodal corrections   |
| 2. Gday               | • Returns consecutive day number from a known origin for any date                                   |
| 3. Setvuf             | • Sets-up the over-determined matrix system   |
| 4. Astr               | • Calculates position of sun and moon   |
| 5. Vuf                | • Calculates nodal corrections for all constituents   |
| 6. Svd                | • Solves least squares fit matrix   |
| Ellipse               | • If current analysis flag is on tidal ellipse parameters are computed in main program              |
| Output                | • Analysed hourly height and current data output in main program                                    |

**Figure 3.12: Flowchart of the HTAS model implemented in DIVAST.**

The specific tidal constituents employed in any analysis will be particular to each study, dependent on the length of time of the tidal data used. The Rayleigh criterion determines the minimum length of time required to separate two neighbouring constituents based on the assumption that separation requires a phase change of  $360^{\circ}$  to occur between the constituents during the recorded period. This separation

can be expressed mathematically as (Permanent Service for Mean Sea Level, 2017):

$$(n_1 - n_2)T \geq 360^0 \quad (3.14)$$

where  $n_1$  and  $n_2$  are the constituents' angular speeds in degrees per hour and  $T$  is the record length in hours. The analysis program uses the Rayleigh criterion to determine if a specific constituent should be included in the analysis. Take  $F_0$  to be the frequency of a main constituent,  $F_1$  to be the frequency of its Reyleigh comparison constituent and  $T$  to be the time period of observed data, then the constituent will be included in the analysis if  $|F_0 - F_1|T \geq RAY$ , where  $RAY$  is the comparison between the two frequencies, signifying if the particular frequency in question is large enough to include the constituent in question, it is commonly specified as 1 but can be altered within the program by the user (Foreman & Bay 1996).

The initial stage of the analysis is the mathematical breakdown of the input data to determine the amplitude and phase of each individual harmonic constituent included in the analysis. This involves determining the amplitude,  $A_j$ , and phase,  $\theta_j$ , values, of a constituent, with frequency  $\delta_j$  for the tidal signal  $\sum_{j=1}^M A_j \cos[2\pi(\delta_j t - \theta_j)]$  that best fit the series of input data observations,  $y(t_i)$  for  $i = 1, N$ , for the specified length of time. The system  $y(t_i) = \sum_{j=1}^M A_j \cos[2\pi(\delta_j t - \theta_j)]$  is over-determined and so cannot be solved exactly. Therefore, it is necessary for the analysis to adopt a criterion to allow optimum values of amplitude and phase to be determined, the optimisation criterion adopted by HTAS is the least squares fit technique. There are a number of techniques for performing the least squares fit. The method employed within HTAS is the singular value decomposition (SVD) technique (Foreman & Henry (1989); Foreman et al. (2009)). The derivation of the least squares matrix equation is presented in Appendix B.

Doodson's development of tidal potential comprises over four hundred tidal constituents (Kowalik & Luick, 2013). Separation of all four hundred constituents would require an impractical length of tidal observations; as a result, groups of constituents containing the same first three Doodson numbers are formed. The main contributor to the tidal potential is the main constituent and the remaining constituents are referred to as satellites. Analysis of a main constituent will therefore determine the amplitude and phase due to the cumulative effect of all constituents included in that group. To determine the tidal parameters due to only the main constituent, an adjustment is made, known as the nodal modulation. Due to these nodal corrections the actual contribution of the constituent group to the tidal signal  $A_j \cos[2\pi(\delta_j t - \theta_j)]$  is  $f_j a_j \cos[2\pi(V_j + u_j - g_j)]$  where  $A_j$  and  $\delta_j$  are the optimal amplitude and phase value for the tidal signal respectively,  $V_j$  is the astronomical argument,  $a_j$  and  $g_j$  are the amplitude and Greenwich phase lag of the tidal constituent,  $j$  respectively, and  $f_j$  and  $u_j$  are the nodal modulation corrections in amplitude and phase, respectively. Hence, the amplitude and Greenwich phase lag of the constituent of frequency  $\delta_j$  can be calculated as follows:

$$a_j = \frac{A_j}{f_j} \qquad g_j = V_j + u_j + \theta_j \qquad (3.15)$$

The tidal analysis software was incorporated into the DIVAST model of the case study Shannon estuary site, the resulting current heights and velocities computed by the developed model were utilised as time series data in the harmonic analysis. The modified model architecture is shown in Figure 3.13 in which the additional subroutine 'HTAS', included to perform the harmonic analysis is shaded in blue.

| MAIN PROGRAM   |   |
|----------------|---|
| 1. FILINP      | • Opens input data file   |
| 2. FILOUT      | • Opens file for data output  |
| 3. BOUND       | • Reads open boundary (OB) data                                     |
| 4. FIELD       | • Reads computational domain  |
| 5. FIND        | • Establishes the integration sections                              |
| 6. DEPTH       | • Reads water depths  |
| 7. INITL       | • Initialises depths, elevations, concentrations and chezy values   |
| 8. MARTURBINIT | • Calculates turbine area and cells that modification is applied to |
| 9. HYDBND      | • Assigns hydrodynamic data at OB                                   |
| 10. MARTURB    | • Calculates parameters for momentum sink term                      |
| 11. HYDMODX    | • Solves hydrodynamics in x direction                               |
| 12. SIDEH      | • Recalculates water depths   |
| 13. FLDRY      | • Checks for flooding and drying of cells                           |
| 14. HYDBND     | • Assigns hydrodynamic data at OB                                   |
| 15. HYDMODY    | • Solves hydrodynamics in y direction                               |
| 16. SIDEH      | • Recalculates water depths   |
| 17. FLDRY      | • Checks for flooding and drying of cells                           |
| 18. CHEZY      | • Recalculates chezy values   |
| 19. EDDY       | • Recalculates eddy viscosities                                     |
| 20. HTAS       | • Carries out tidal harmonic analysis                               |
| 21. PRINT      | • Outputs time series and snapshots                                 |

Figure 3.13 Flowchart of modified DIVAST model to include HTAS.

### 3.9.3 Tidal Ellipse Theory

Tidal currents are more difficult to analyse in comparison to tidal heights as they are vector quantities, and so both speed and direction have to be accounted for. Currents can be resolved into positive east and north direction components,  $U$  and  $V$ , which can be expressed as follows:

$$U = q \sin\theta \quad (3.16)$$

$$V = q \cos\theta \quad (3.17)$$

where  $q$  is the current speed and  $\theta$  is the direction of flow, measured clockwise from North.

The  $U$  and  $V$  vector components can undergo separate harmonic analysis by least squares fitting:

$$U(t) = \sum_{j=1}^M A_{uj} \cos[2\pi(\delta_j t - \theta_{uj})] \quad (3.18)$$

$$V(t) = \sum_{j=1}^M A_{vj} \cos[2\pi(\delta_j t - \theta_{vj})] \quad (3.19)$$

where the unknown parameters to be determined are the two amplitude values,  $A_{uj}$  and  $A_{vj}$ , and two phase values,  $\theta_{uj}$  and  $\theta_{vj}$ , for each velocity component  $U$  and  $V$ , corresponding to each individual harmonic constituent,  $j$ , chosen for inclusion in the analysis. Once the components are analysed their separate solutions are then recombined, therefore, each harmonic constituent is represented by four parameters, namely two amplitudes and two phases, which define a tidal current ellipse. The harmonic constituents for tidal currents are therefore expressed in terms of ellipse parameters.

Tidal harmonic analysis will determine a separate ellipse for each constituent included in the analysis, each individual ellipse is described by its major and minor axes as well as its angle of inclination, these properties are derived directly from the velocity component parameters and are illustrated in Figure 3.14.

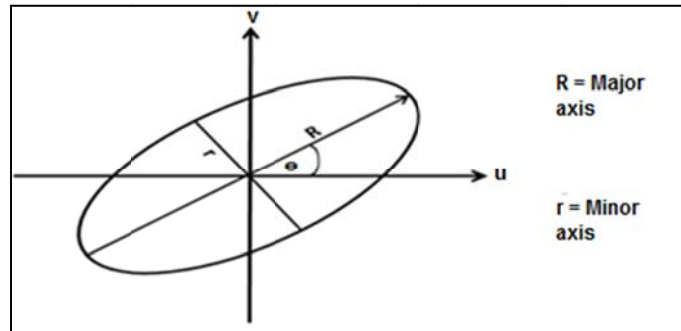


**Figure 3.14: Basic parameters of a current ellipse.**

The major axis represents the maximum current speed and can be expressed as follows:

$$R = \left( \frac{U^2 + V^2 + a^2}{2} \right)^{\frac{1}{2}} \quad (3.20)$$

Similarly, the minor axis represents the minimum current speed and is defined as:

$$r = \left( \frac{U^2 + V^2 - \alpha^2}{2} \right)^{\frac{1}{2}} \quad (3.21)$$

where  $U$  and  $V$  are the maximum amplitudes of the east and north velocity components, respectively, and  $\alpha$  is a parameter related to the velocity components and their corresponding phases.

Tidal current ellipses describe the characteristics of a tidal velocity. The angle of inclination,  $\theta$ , of the tidal ellipse indicates the primary direction of flow. The ratio of the minor and major axes is defined as:

$$ER = \left| \frac{r}{R} \right| \quad (3.22)$$

$ER$  describes the variability in flow direction over the course of a tidal cycle. Long narrow ellipses (e.g. Figure 3.15 (a)) indicate rectilinear flow and will yield low ellipse ratios (close to 0) while shorter, fatter ellipses (Figure 3.15 (b)) indicate rotary flows and will yield higher ratios (close to 1).

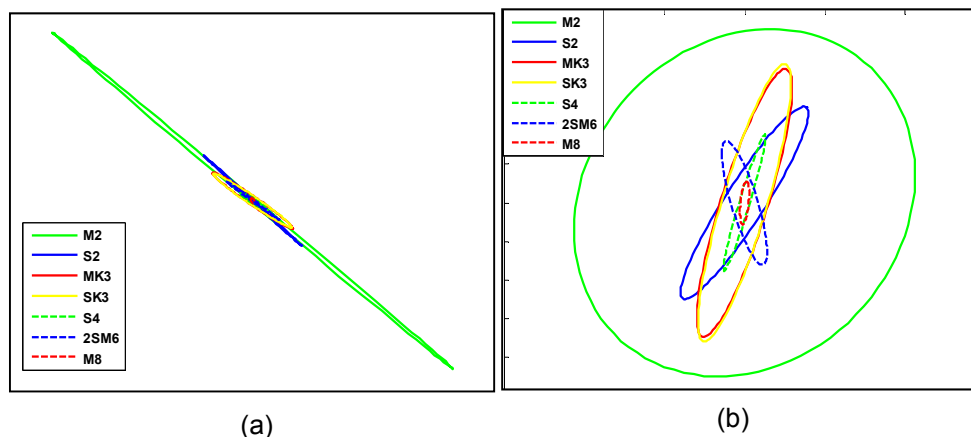


**Figure 3.15: Examples of tidal current ellipses indicating (a) rectilinear, (b) rotary flow.**

## 4 Resource Assessment

### 4.1 Introduction

Selection of suitable sites for tidal energy extraction is largely dependent on the available tidal resource. Given that tidal stream power is a function of the current velocity cubed (e.g. equation (4.1)), resource assessments are highly sensitive to the accuracy of the velocities used. Traditional methods for calculating the power that is available from tidal currents involve using either peak or time-varying current velocities but, in both cases, the total velocity magnitude is employed. At present the most common tidal turbine designs are horizontal axis turbines whose fixed orientation means they cannot rotate with changing current direction. HATS can however be bi-directional (e.g., SeaGen), meaning they are capable of extracting energy from both flood and ebb tides. For the purpose of this research simulated turbines are assumed to be bi-directional HATs. For optimum performance, horizontal axis turbines should be oriented with their swept area perpendicular to the flow direction. A weakness of adopting the total velocity vector in resource assessments is that the directionality of tidal flows is ignored.

This chapter presents the development and application of an assessment methodology which incorporates the direction of flow at a potential site. Two-dimensional numerical modelling is employed along with tidal harmonic analysis and tidal ellipse theory to facilitate long-term forecasts of current velocities, allowing for a more accurate assessment of the mean available power at a location of interest. Two traditional methods of resource assessment are applied to a case study site - the Shannon estuary, on the west coast of Ireland - and the results compared with those using the author's developed methodology. A more detailed resource assessment of Shannon estuary is then carried out at specifically chosen locations designated

by the Shannon Framework Plan (SIFP, 2013) as tidal energy berths (see Figure 4.2).

## 4.2 Tidal Resource Assessment

Blunden & Bahaj's (2007) description of a tidal energy resource assessment, discussed in Chapter 2, consists of four fundamental stages. The first stage in the assessment process i.e. 'selection of sites suitable for placing arrays of tidal stream generators' is the focus of this chapter. Suitability is largely dependent on the power available for extraction (which in turn is dependent on the flow speed); hence, the primary aim of this first stage is quantification of the tidal stream power available at a particular site, i.e. the available resource. To date, this has typically been determined as the kinetic energy flux available for extraction by a turbine, expressed mathematically as:

$$P = 0.5\rho Au^3 \quad (4.1)$$

### 4.2.1 Traditional Methodologies for Available Resource Assessment

The two traditional approaches used in this investigation are the Fraenkel approach (which uses equation (4.2)) and the time-varying velocity approach (which uses equation (4.3)). The theory behind these approaches is discussed in detail in Chapter 2.

$$P_{\text{mean}} = 0.5\rho AK_s K_n u_{\text{peak}}^3 \quad (4.2)$$

$$P_{\text{mean}} = \frac{\sum_{n_1}^{n_{\text{max}}} 0.5\rho Au_t^3}{n_{\text{max}}} \quad (4.3)$$

### 4.2.2 New Methodology for Available Resource Assessment

A weakness of the traditional methods for calculating the available power from tidal currents is that they fail to consider flow direction. The resource assessment methodology presented here was developed so as to consider the prevailing direction of current flow. Tidal harmonic analysis is performed to compute tidal current ellipses

which are used to identify the primary flow direction. The mean available power is then determined using only the velocity vectors aligned with the primary direction of flow as follows:

$$P_{\text{mean}} = \left( \frac{\sum_{n_1}^{n_{\text{max}}} 0.5\rho A u_{p,t}^3}{n_{\text{max}}} \right) \quad (4.4)$$

where  $u_{p,t}$  is the component of velocity in the primary direction of flow at time  $t$ . The development of this direction-based methodology is described in further detail in Section 4.4.

### 4.3 The Shannon Estuary Model

A 2D hydrodynamic model of the Shannon estuary was used to develop the author's direction-based resource assessment methodology and to compare its resource estimates with those from the more traditional resource assessment methodologies.

#### 4.3.1 General Description of the Shannon Estuary

The Shannon estuary is located on the west coast of Ireland and is one of the longest estuarine systems in the British Isles. It has been rightly identified as a potential location for tidal energy extraction (SEI, 2006) (see Figure 4.2) but with the exception of Fallon et al. (2014) little detailed analysis has been carried out to accurately determine its tidal energy potential. The estuary (see Figure 4.1(b)) measures approximately 87km from its head at the River Shannon to its mouth at the Atlantic Ocean and has a surface area of circa 500km<sup>2</sup> (Fallon et al. 2014). The estuary is a highly dynamic system, possessing a large tidal range and strong peak currents. The tidal ranges at the mouth and head of the estuary are approximately 5m and 6.5m, respectively, during normal spring tides, inducing peak currents of up to 3m/s in water depths of 35m.



**Figure 4.1: (a) Potential current energy sites in Ireland (estimated practical energy resource is shown in GWh/y) (SEI, 2006) (b) Map of the Shannon estuary (Source: Google Maps).**

A Strategic Integrated Framework Plan (SIFP) for the Shannon estuary has identified potential areas for tidal energy extraction taking account of the flow regime and other uses of the estuary (illustrated in Figure 4.2) (SIFP, 2013). Preferred berths would be within the outside of the commercial shipping lanes. In the present assessment, the resource in the estuary as a whole was first assessed. This was followed by more detailed resource assessment at selected locations within the identified tidal energy berths.

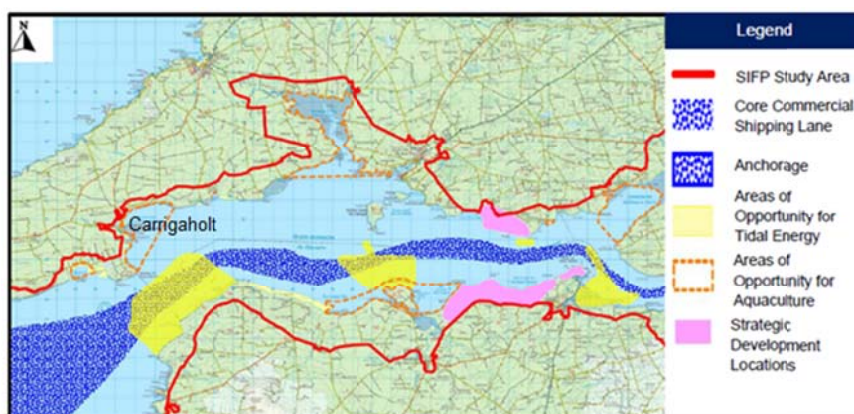


**Figure 4.2: Composite map of SIFP study area (Source: SIFP, 2013).**

### 4.3.2 Model Description

The 2D model of the Shannon estuary was created using bathymetry data obtained from digitised Admiralty Charts No. 1819, 1547, 1549 and 1540 and interpolated onto a finite difference grid at a spatial resolution of 189m x 189m. For the domain extents (shown in Figure 4.3) this resulted in a computational domain of 507 x 217 computational cells. Flow boundaries were specified at the north-eastern river boundaries for the Shannon (east) and Fergus (north), and at the northern and southern open sea boundaries. Tidal elevations were specified at the western open sea boundary. Boundary elevation data were specified using tidal constituent data obtained from analysis of measured tidal elevation data at Carrigaholt (shown in Figure 4.3) for a one-year period (2006). Monthly average flow data was obtained from the Office of Public Works (OPW) for a 10 year period and used to specify flow boundary data for the Shannon and Fergus rivers. River Shannon flow data was taken from the Banagher station (no. 25017) and River Fergus flow data was taken from the Ballycorey station (number 27002). The data is read into the model as a volumetric flow rate ( $\text{m}^3/\text{s}$ ) and was converted to velocities ( $\text{m}/\text{s}$ ) internally in the model by dividing by the area of the grid cells each river flows through. The average monthly river data is presented in Figure 4.4. A 2D bathymetry plot of the Shannon model domain is shown in Figure 4.3. A summary of the Shannon model parameters are presented in Table 4.1 and validation of the model is presented in Section 4.3.3.

The hydrodynamic model has been modified to include harmonic analysis allowing the model to compute current ellipse parameters (such as ellipse axes lengths and ellipse inclination). The model was then utilised to calculate the available tidal stream resource across the estuary using the three different assessment approaches. The development of the resource assessment model is discussed in Section 4.4 and the case study results are presented in Section 4.5.

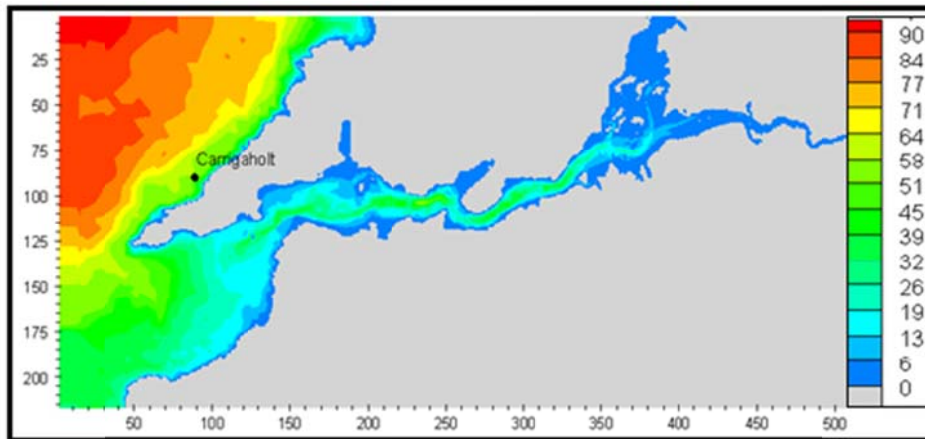
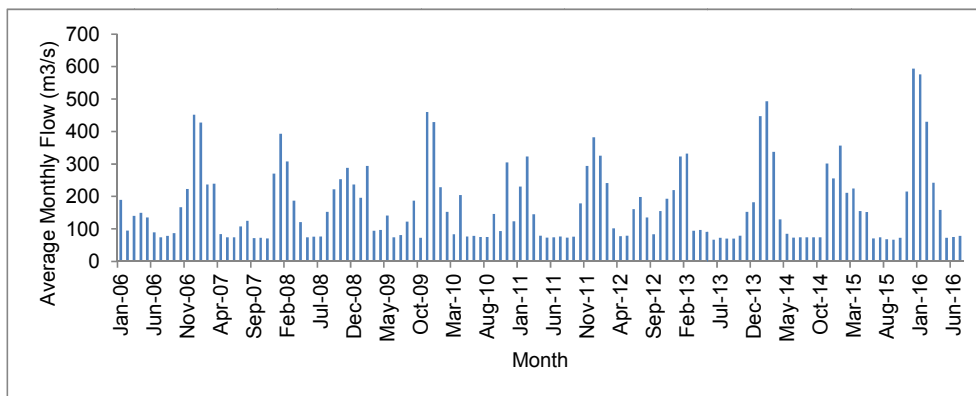
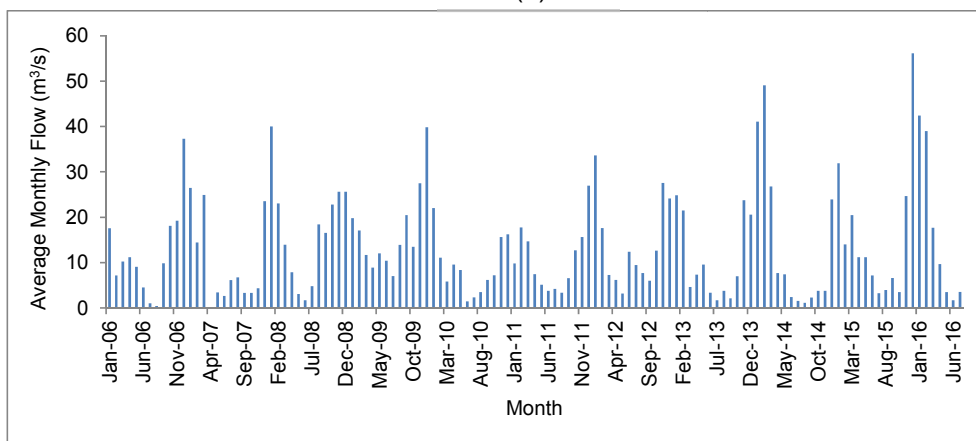


Figure 4.3 Bathymetry plot of Shannon estuary (legend shows mean water depth in m).



(a)



(b)

Figure 4.4: River flow data for (a) Shannon, (b) Fergus rivers (Source: OPW)

**Table 4.1: Principal Model Parameters.**

| Parameters                  | Value                 | Parameters                    | Value  |
|-----------------------------|-----------------------|-------------------------------|--------|
| Boundaries<br>(x-direction) | 2                     | Eddy viscosity coeff.         | 0.1    |
| Boundaries<br>(y-direction) | 3                     | Momentum correction<br>coeff. | 1.016  |
| Spatial resolution          | 189 m                 | Angle of latitude             | 52.58° |
| Bed Roughness               | 200mm                 | Time-step                     | 40s    |
| Fluid density               | 1026kg/m <sup>3</sup> |                               |        |

### 4.3.3 Model validation

The Shannon estuary model has been validated against measured tidal elevations at six locations (T1-T6) and tidal current velocities at two locations (C1 & C2) shown in Figure 4.5. Figure 4.6 illustrates the performance at T5 for the 4 week period from May 2<sup>nd</sup> to May 31<sup>st</sup>, 2013. The modelled water levels show excellent agreement with the measured data; the  $R^2$  is 0.98 and the RMSE is 0.17m. Significant natural tidal distortion occurs in the Shannon estuary with amplification of the tidal range as one moves from the head to the mouth. This contributes to the generation of higher velocities. It is important that the model captures this tidal distortion. Figure 4.7 compares measured and modelled water levels at T2 and T5 over a spring tide and shows that the model does reproduce the amplification of the tidal range. It can also be seen that high tide at T5 occurs approximately one hour after high tide at T2 which the model also captures. Correlation values of  $R^2 = 0.97$  and RMSE values of 0.23m were determined for locations T2, and again confirm the model accuracy.

The accuracy of the model in relation to current velocities is shown in Figure 4.8 and Figure 4.9 which compare modelled and measured depth-averaged velocities at C1 and C2, respectively. Good correlation between measured and modelled values was achieved at

both sites. At C1 correlation values of  $R^2=0.92$  and  $0.9$  and  $RMSE=0.1m/s$  and  $0.06m/s$  were achieved for spring and neap velocities respectively. At C2  $R^2=0.98$  and  $0.97$  and  $RMSE=0.08m/s$  and  $0.05m/s$  for spring and neap tides respectively. Due to the long, narrow shape of the Shannon estuary, the trough of the ebb tidal wave travels faster than crest of the flood tide, resulting in an ebb tide with shorter duration than the flood tide (Fallon et al. 2014). As the same volume of water is flowing through each stage of the tide, this induces larger ebb tide velocities than flood tide velocities. This is known as ebb-domination and is clearly demonstrated in Figure 4.9.

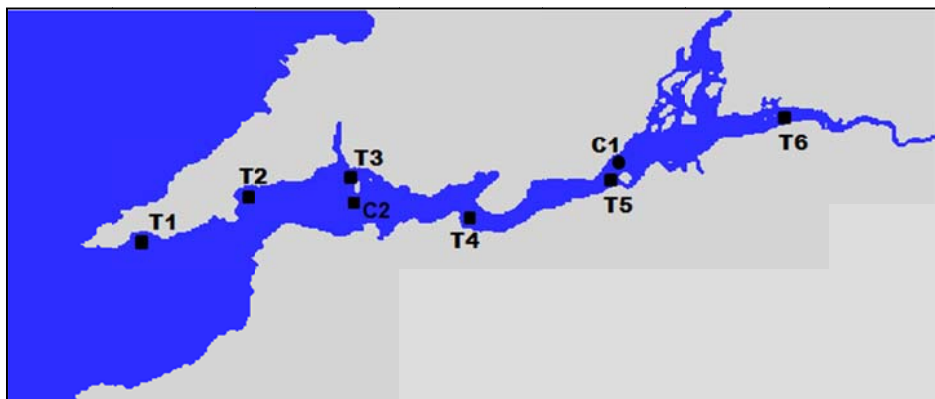


**Figure 4.5: Extent of model domain and locations of measured data for tidal elevations (T1-T6) and tidal current velocities (C1 & C2) used to validate the model.**

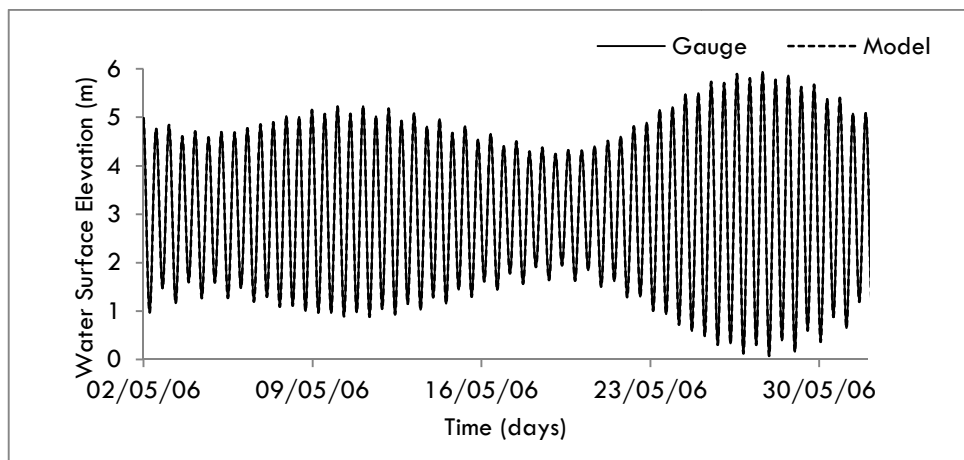


**Figure 4.6: Measured and modelled water surface elevations at T5 for May 2<sup>nd</sup> to May 31<sup>st</sup> (Data courtesy:Shannon Foynes Port Company).**

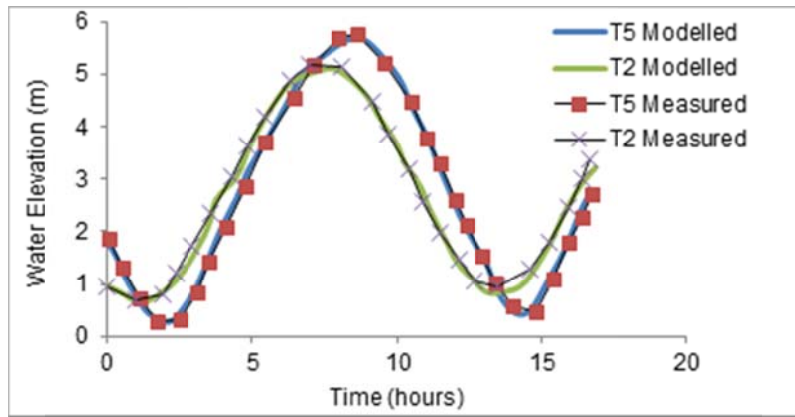


**Figure 4.7: Comparison of measured water elevation data against the predicted model elevation data at T2 and T5 (Data courtesy: Shannon Foynes Port Company).**

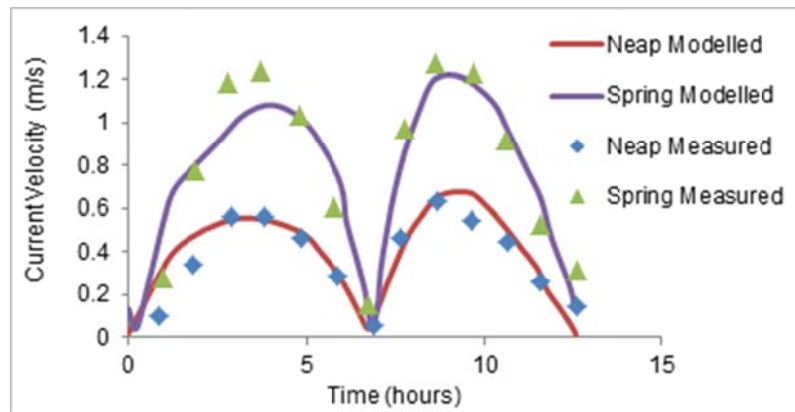


**Figure 4.8: Comparison of measured current velocity data against the predicted model current data at C1 (Data courtesy: Fallon et al. 2014)**

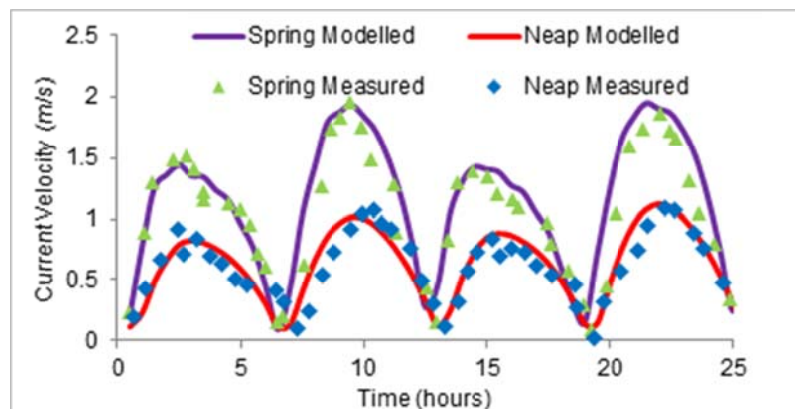


**Figure 4.9: Comparison of measured current velocity data against the predicted model current data at C2 for 4th January 2003 (Data courtesy: SEI, 2004).**

## 4.4 Development of Model to Implement New resource Assessment

### 4.4.1 Importance of Considering Flow Direction

The majority of HATS have fixed orientation meaning they extract most energy from those flows travelling perpendicular to the turbine swept area. Assuming a bi-directional HAT these perpendicular flows will occur during both flood and ebb tides. For maximum energy extraction, HAT's should therefore ideally be orientated with their swept area perpendicular to flow direction (illustrated in Figure 4.10 (a)). Optimum deployment locations are those where there is a  $180^{\circ}$  shift in current direction between flood and ebb tide (as illustrated in Figure 4.10 (b)); this flow type is known as rectilinear flow.

Tidal current ellipses (illustrated in Figure 3.14 **Error! Reference source not found.**) describe the characteristics of current flow and so are useful in determining both device orientation and identifying suitable deployment locations. First, the angle of inclination,  $\theta$ , indicates the primary flow direction. Second, it is shown in this research that the ellipse ratio,  $ER$ , defined in equation (3.22), is a useful indicator of the nature of a flow. In the proposed assessment methodology, both  $\theta$  and  $ER$  are determined in order to assess the available resource and identify suitable turbine deployment sites.

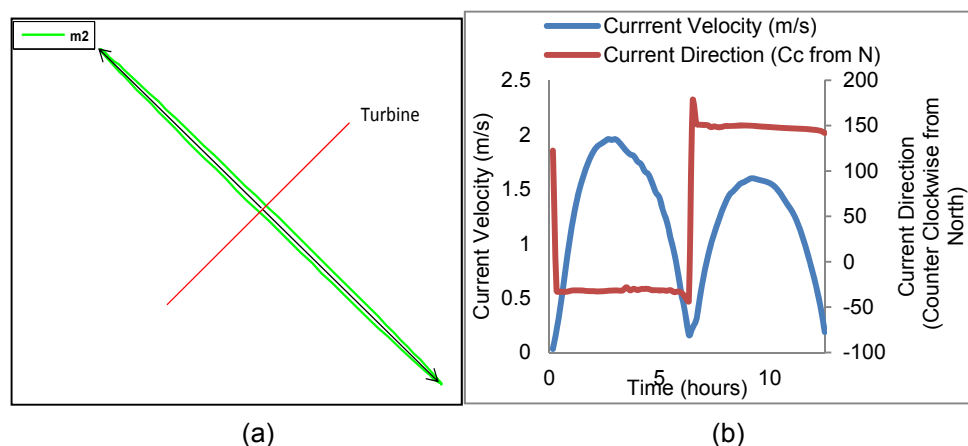


**Figure 4.10: Example analysis of flow data at a site exhibiting rectilinear flow showing (a)  $M_2$  ellipse and optimum HAT orientation and (b) variation in speed and direction over a tidal cycle.**

#### 4.4.2 Development of Resource Assessment Model

The tidal harmonic analysis software (HTAS), described in Section 3.9.2, was integrated into the existing two-dimensional flow model to compute the ellipse parameters described above. These parameters were then used in a new resource assessment methodology which accounts for the prevailing direction of current flow. The main stages in the developed resource assessment methodology and the required modifications to the model source code to implement them are outlined in Figure 4.11 and discussed thereafter.

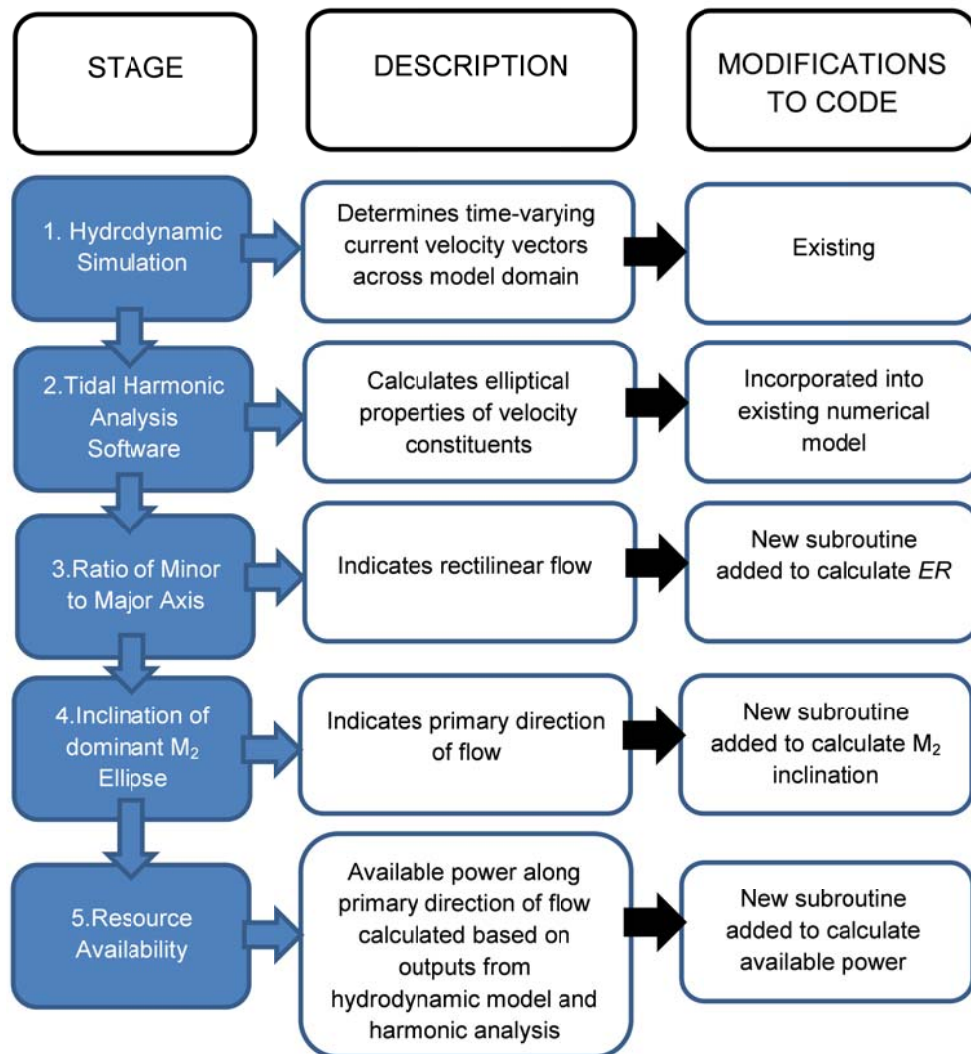


**Figure 4.11: Flow chart outlining main steps in resource assessment methodology.**

1. *Hydrodynamic Simulation*: the two-dimensional, depth-averaged numerical model simulates the hydrodynamic regime of a tidal model domain. The model determines time-varying current velocity vectors across the domain which are then used to facilitate tidal current analysis and resource assessment.
  
2. *Tidal Harmonic Analysis Software*: as detailed in Section 3.9.2, the numerical model has been developed to include HTAS. HTAS separates the current velocities computed by the hydrodynamic model into harmonic constituents and calculates elliptical properties of the velocities, including the angle of inclination ( $\theta$ ) and major and minor ellipse axes ( $ER$ ). A list of the primary constituents included in the analysis is given in Table 4.2. A full description of each ellipse including their period and speed can be found in Chapter 3 Table 3.1.

**Table 4.2: Tidal constituents included in analysis.**

| Tidal Constituent |
|-------------------|
| $M_2$             |
| $S_2$             |
| $MK_3$            |
| $SK_3$            |
| $S_4$             |
| $2SM_6$           |
| $M_8$             |

3. *Ratio of Minor to Major Axis*: the ratio of the minor to major axis of a tidal current ellipse,  $ER$ , determines the type of current flow. The numerical model was developed to include a subroutine in which  $ER$  is calculated at each (I, J) grid cell in the model domain. The results can then be used to illustrate the nature of flow across the domain and for closer examination of the flow at a particular site. An ideal location to deploy tidal turbines is one in which flow is predominantly rectilinear, therefore a low minor-to major axis ratio is desired when determining deployment locations.

4. *Inclination of the Dominant  $M_2$  Ellipse*: the  $M_2$  constituent is generally the dominant constituent at semi-diurnal sites (Polagye 2009; Pugh 1996). Irish coastal waters are all semi-diurnal. As such, it was concluded that the  $M_2$  constituent will be the main contributor to the primary direction of current flow. The current velocities computed by the hydrodynamic model undergo harmonic analysis and the  $M_2$  angle of inclination,  $\theta$ , is determined and used to indicate the primary direction of flow at a particular location. Using the  $M_2$  constituent alone means that the primary direction of flow can be determined from a simulation of a few tidal cycles rather than a few months or more, thus reducing the computational overhead.
5. *Resource Availability*: The primary flow directions are read back into the hydrodynamic model and the velocity vectors aligned with the primary flow directions,  $V_{p, t}$ , are calculated and used in equation (4.4) to quantify the available tidal energy resource. This process is carried out for each wet grid cell within the model domain.

#### **4.5 Shannon Estuary Case Study Results**

The Fraenkal approach, the time-varying velocity and the author's new direction-based approach to resource assessment were applied to the Shannon estuary model to quantify the available tidal stream resource. Further detailed analysis of the resource was also carried out at sites of interest identified by the resource assessment. The analysis presented is based on a simulation of one full year (2006). Harmonic analysis was performed on measured water level data from Carrigaholt to determine the tidal constituents given in Table 4.3. These parameters were then used in equation (4.5) to generate water elevation boundary data specified at the western open sea boundary (see Figure 4.12).

**Table 4.3: Tidal Constituent Data**

| Constituent      | Frequency (Radians/hour) | Amplitude (m) | Phase (degrees) |
|------------------|--------------------------|---------------|-----------------|
| M <sub>2</sub>   | 0.0805114                | 1.50723       | 140.997         |
| S <sub>2</sub>   | 0.08333334               | 0.52557       | 174.536         |
| MK <sub>3</sub>  | 0.1222921                | 0.00513       | 354.437         |
| SK <sub>3</sub>  | 0.1251141                | 0.01233       | 104.209         |
| S <sub>4</sub>   | 0.1666667                | 0.00369       | 262.986         |
| 2SM <sub>6</sub> | 0.2471781                | 0.00372       | 68.037          |
| M <sub>8</sub>   | 0.3220456                | 0.00479       | 168.014         |

$$h(t) = \sum_{j=1}^M A_j \cos[2\pi(\delta_j t - \theta_j)] \quad (4.5)$$

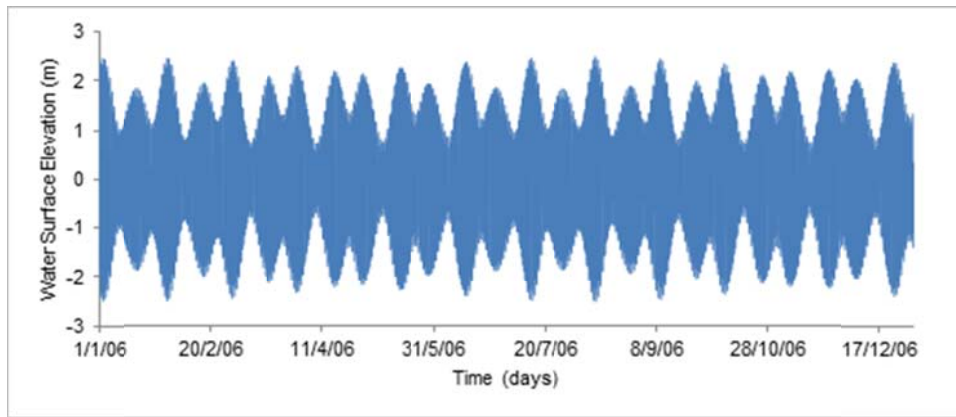


**Figure 4.12: Water elevation boundary data resulting from tidal constituent data.**

#### 4.5.1 Testing of the Ellipse Code

The author's assessment approach uses tidal elliptical data. Before the approach was applied the ellipse code was tested to ensure the constructed ellipses were accurate. A short simulation time of five tidal cycles (62.5 hours) around spring tide was used and harmonic analysis was conducted over the last 3 tidal cycles after cold start effects had dissipated. The Cahercon location (see Figure 4.13) is used for illustration. Modelled velocity data plotted first as a scatter plot using x- and y-direction components, and second as a stick plot using speed and direction at half-hourly intervals over a single spring tidal cycle were used to compare with the constructed tidal current

ellipses. This comparison is presented in Figure 4.14 (a-c). The directions and magnitudes of the velocity data in the scatter and stick plots show very good agreement with the ellipse properties confirming that the harmonic analysis software is able to correctly compute ellipse properties.

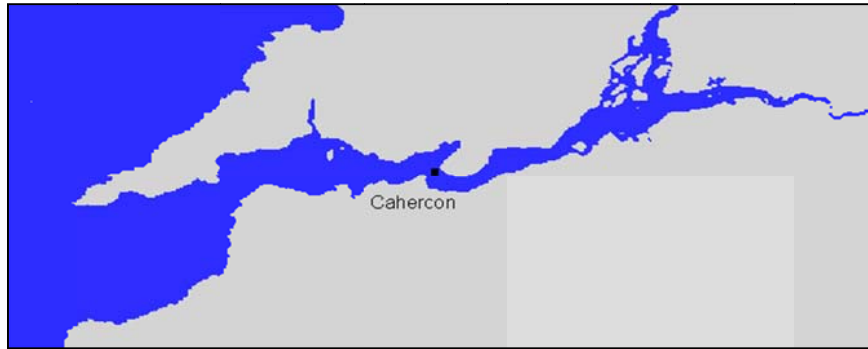


**Figure 4.13: Cahercon ellipse validation location.**

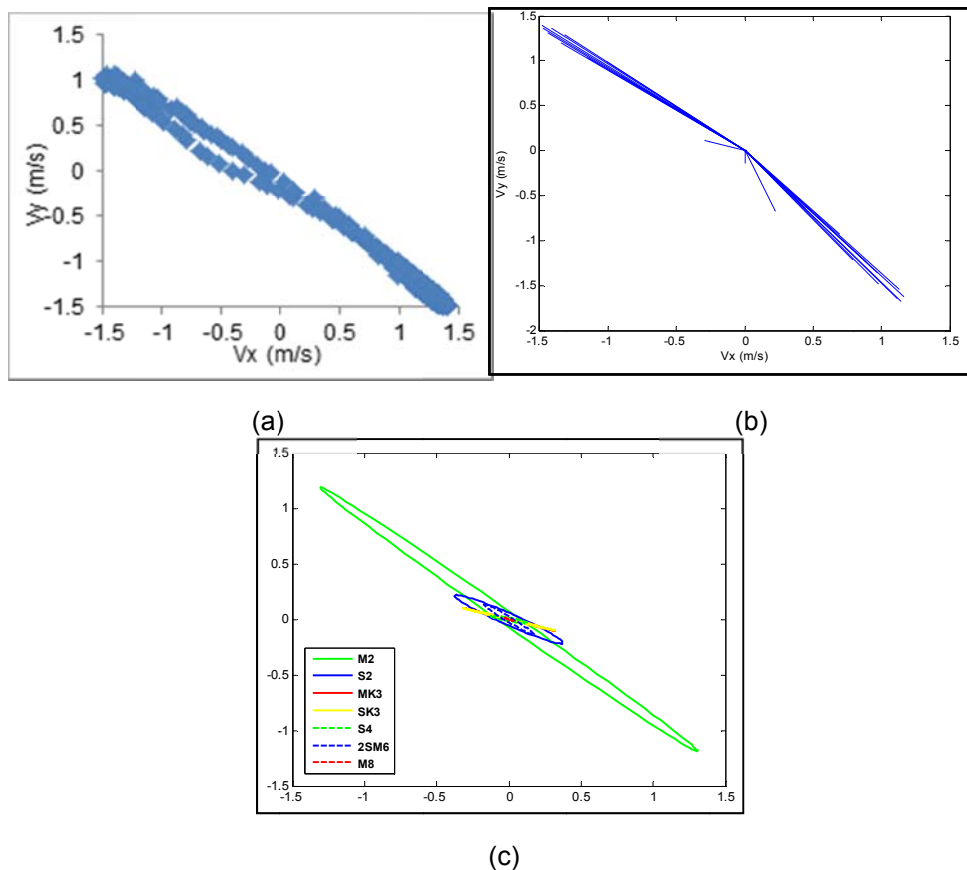


**Figure 4.14: Model outputs at Cahercon: (a) Direction of flow over 3 tidal cycles (b) total velocity vectors at 0.5 hour intervals over 1 tidal cycle (c) tidal current ellipses for relevant harmonic constituents determined for a period of 3 tidal cycles.**

Implementation of the author's resource assessment approach in the array optimisation model required require swift recalculation of the available resource after turbines are iteratively deployed. To save computational time it would be desirable to be able to determine the primary flow direction from a short simulation of a few tidal cycles rather than a full year, A run of 400 hours (32 tidal cycles) covering a full spring-neap tidal cycle was conducted to check the validity of using just three spring tidal cycles to determine primary flow direction. The direction of flow is compared by way of velocity component scatter plots illustrated for an arbitrary location in Figure 4.15 (a) and (b) respectively. It can be seen that the direction of the flows are very similar for both the 400 hour and 37.5 hour runs, this is highlighted by the resulting linear trend-lines for each case, with both runs having gradients of approximately -0.861. Similar comparisons at a number of other locations along the estuary agreed with this finding. It was therefore conclude that utilising the 37.5 hour run to construct ellipses was an appropriate time-saving approach.

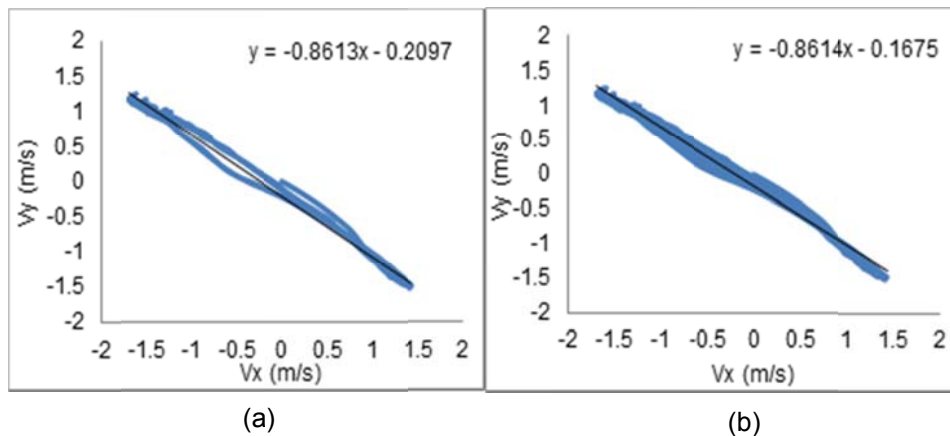


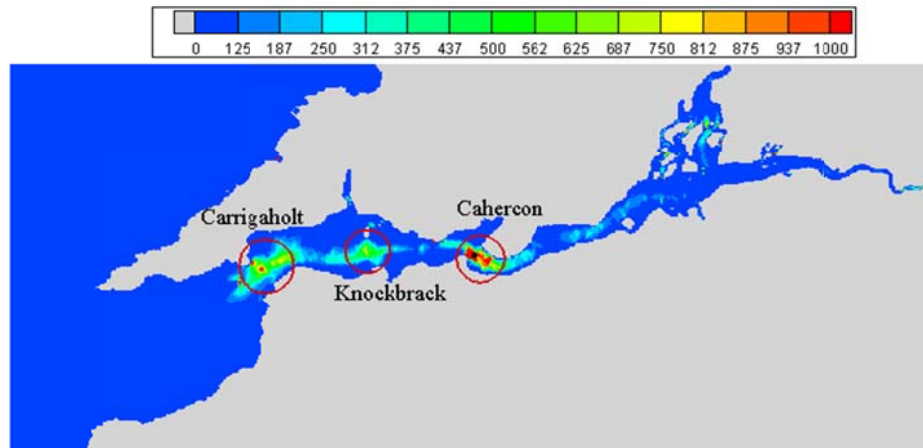
**Figure 4.15: Velocity component scatter plots for (a) 37.5 hours model data and (b) 400 hours model data.**

#### 4.5.2 Available Resource Assessments

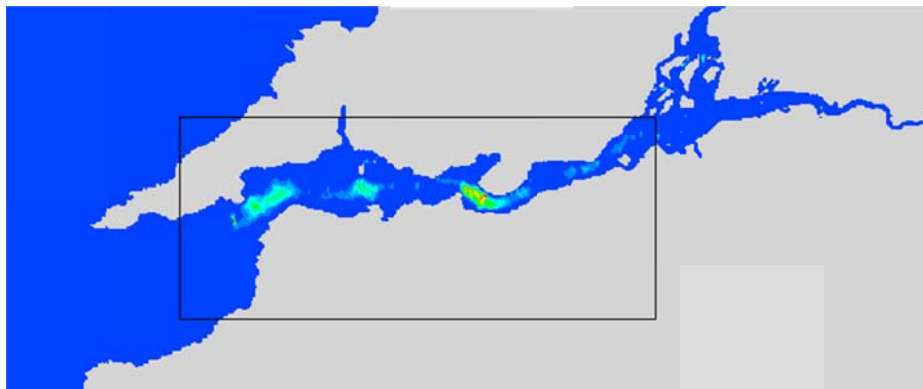
The available power across the entire estuary was calculated for the year 2006 using:

- (1) the peak velocity Fraenkel formula approach (denoted FFA)
- (2) the time-varying total velocity approach (denoted TVA)
- (3) the time-varying primary direction velocity approach (denoted PDA)

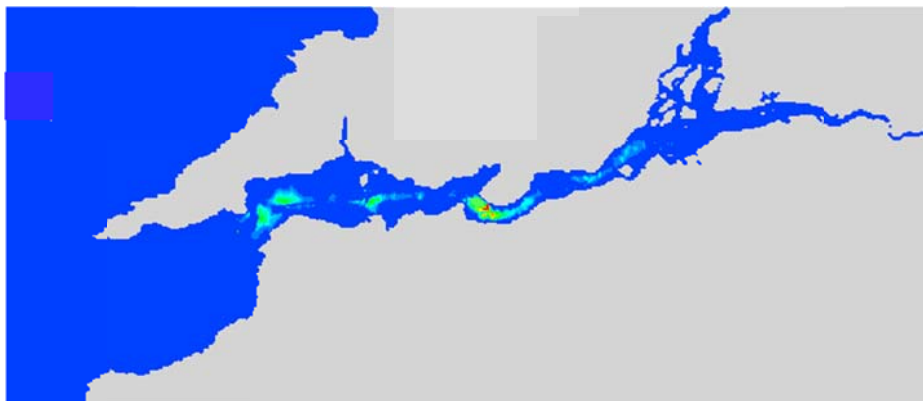
Whilst the many assumptions made by the FFA make it a crude approach, it is used in many published resource assessment studies (as discussed in Section 2.4.4.2) and so is included in this assessment. The resulting annual mean available power maps are presented in Figure 4.16 (a-c) respectively.  $P_{mean}$  is the mean power per  $m^2$  cross-section of flow, i.e. the swept area of the turbine in equations (4.2), (4.3) and (4.4) is omitted from the calculation. There is significant variation in the  $P_{mean}$  values cross the estuary. For the majority of the estuary, mean available power levels are less than  $125W/m^2$ . In areas where stronger velocities occur, the  $P_{mean}$  values range from approximately  $125W/m^2$  to  $2500W/m^2$ . All three assessments indicate the greatest available resource lies in three main areas: Carrigaholt, Knockbrack and Cahercon (illustrated in red in Figure 4.16 (a)), where the estuary narrows. This is a result of the conservation of mass; for mass flow to remain constant, when the area in which fluid flows is decreased, current velocities are forced to increase resulting in greater power availability at that location. This is demonstrated in Figure 4.17 which shows total currents and velocity vectors at peak flood and peak ebb spring tides (vectors are shown at intervals of 5 grid cells).



(a)



(b)



(c)

**Figure 4.16: Mean available power for the Shannon estuary determined using the (a) FFA (b) TVA and (c) PDA (Units of legend:  $W/m^2$ ).**

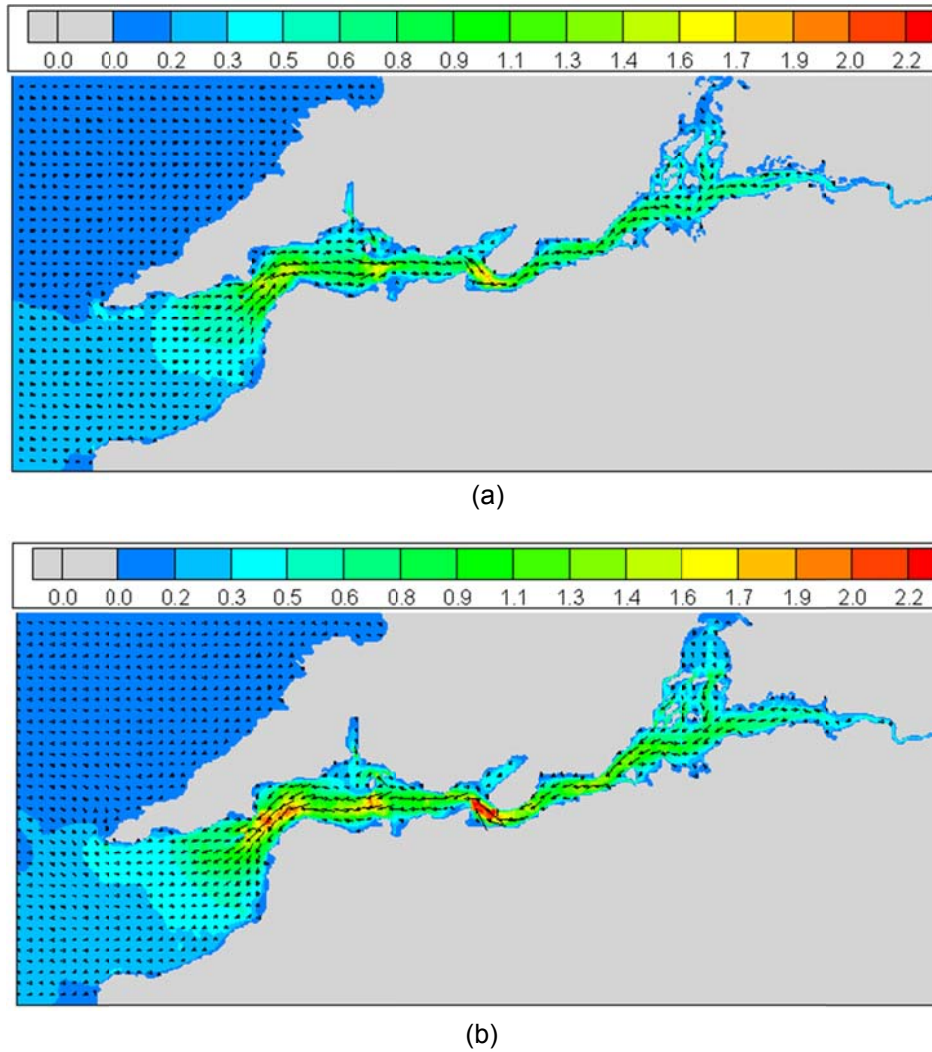


**Figure 4.17: Spring tide currents at (a) peak flood and (b) peak ebb (legend shows current speed in m/s).**

Whilst all three assessment approaches identify the same areas of high tidal resource (Figure 4.16), there are substantial differences in the magnitudes of the resource estimates calculated at the three sites. Comparing the three assessments shows the FFA estimates a higher tidal resource than TVA and PDA. For example, for a location taken in the Cahercon region (shown by the black square in Figure 4.16 (a)) available power is estimated as  $1276\text{W/m}^2$ ,  $931\text{ W/m}^2$  and  $700\text{ W/m}^2$  by FFA, TVA and PDA respectively.

To further demonstrate the differences in the assessment approaches, the percentage difference between  $P_{mean}$  values determined by each approach have been calculated as follows:

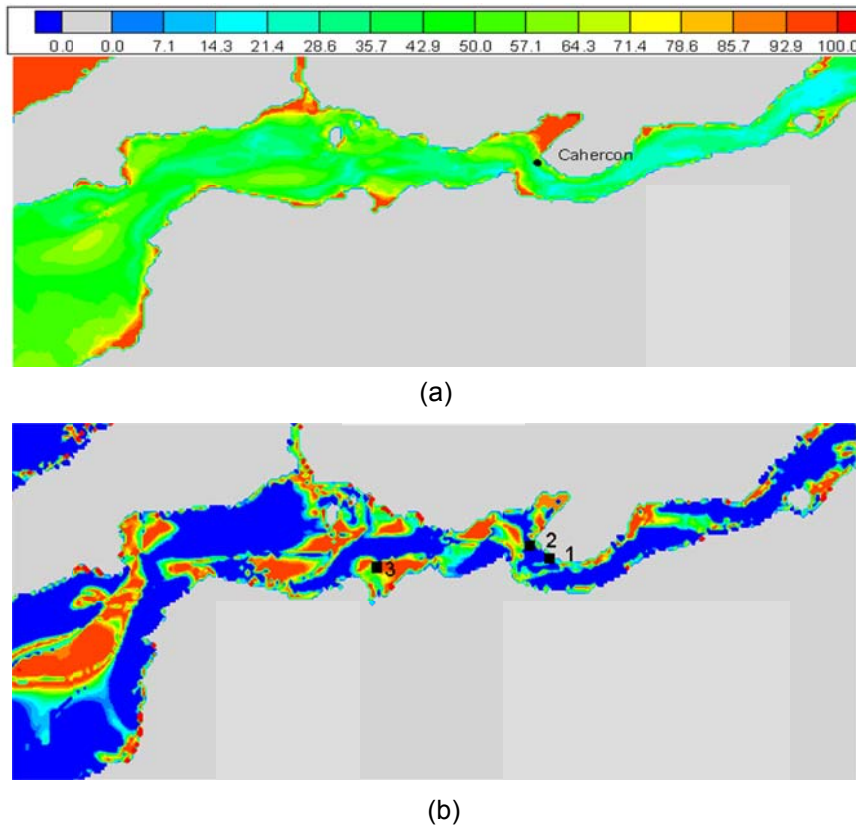
*% Diff TVA vs FFA:*

$$\left( \frac{(P_{\text{mean FFA}} - P_{\text{mean TVA}})}{P_{\text{mean FFA}}} \right) \cdot 100\% \quad (4.6)$$

*% Diff PDA vs TVA:*

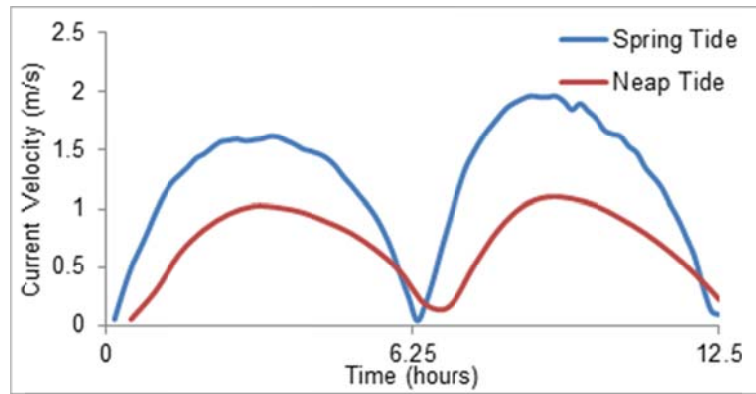
$$\left( \frac{(P_{\text{mean TVA}} - P_{\text{mean PDA}})}{P_{\text{mean TVA}}} \right) \cdot 100\% \quad (4.7)$$

Figure 4.18 shows the % power differences for the portion of the domain containing the three areas of highest power (the areal extent is shown by the black rectangle in Figure 4.16 (b)). Considering firstly the differences between FFA and TVA (Figure 4.18 (a)); a percentage difference ranging between 20-60% is noted across most of the the area. This variance between the two approaches is due to the nature of the methodologies. The FFA is a rather crude approach. At any location, the available power is defined as a function of the maximum spring tide velocity and two shape factors, one which accounts for variations in velocities over a tidal cycle and the other which accounts for variations in velocities over a spring-neap cycle. The approach assumes that peak neap velocities are 60% of peak springs. The shape factor values used assume (1) flows are sinusoidal and thus peak flood velocities are similar to peak ebb velocities, and (2) peak neap velocities are 60% of peak springs. However, these are highly idealised conditions that may not always persist and will definitely not persist everywhere in a study area. This can be demonstrated using a location in the Cahercon area (shown in Figure 4.18 (a)). Modelled spring and neap current velocities at this location (see Figure 4.19) show that the neap/spring peak velocity ratio is approximately 50% and that peak ebb velocities are greater than peak floods, particularly on spring tides.



**Figure 4.18: Percentage difference between available powers calculated using (a) FFA and TVA, (b) TVA and PDA (legend shows percentage differences in %).**

The assumption of sinusoidal flow is actually particularly problematic in the case of the Shannon estuary. Fallon et al. (2014) noted that the estuary is an ebb-dominated system, meaning peak ebb velocities are typically higher than peak flood velocities. To further investigate this, the model was used to output the ratio of peak ebb to peak flood velocities for a spring tide. The resulting ratio map is shown in Figure 4.20 where values greater than 1 indicate ebb-dominance. It can be seen that this is the case for most of the estuary, with ratios of more than 1.5 prevailing in large areas meaning the peak ebb velocities are more than 50% greater. Since power is a function of velocity cubed - this is likely accounting for much of the difference between the FFA and TVA estimates. Incorporating time-varying velocities, as the TVA does, should improve the accuracy of the resource assessment.



**Figure 4.19: Spring and neap current velocities over one tidal cycle at Cahercon location.**

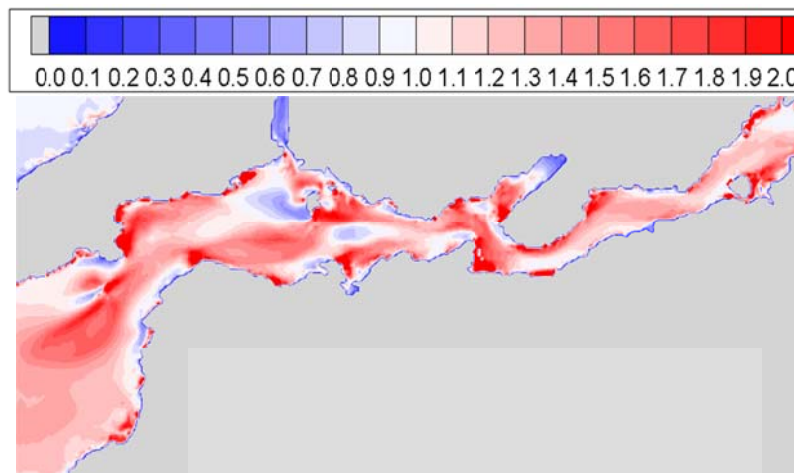


**Figure 4.20: Ratios of peak ebb velocities to peak flood velocities. Value > 1 indicates larger peak ebb velocities.**

Figure 4.18 (b) shows the PDA estimates are further reduced from the TVA. This is a direct result of flow directionality. PDA, incorporating flow direction, is a more sophisticated approach than TVA which ignores directionality. As a result one would expect the difference between the two approaches to be minimal in areas where flow is primarily rectilinear and greatest in areas where flow is more rotary. To examine the difference more closely

Figure 4.21 shows available power as determined by TVA and PDA at three locations (1 - 3) across the estuary. The locations (see Figure 4.18 (b)) represent sites of minimal percentage difference in resource estimates (1, 2) and large differences (3).

Flow at locations 1 and 2 is found to be predominantly rectilinear, (see Figure 4.21 (a1) and (a2)), hence, as expected, there is a minimal difference between the available power determined using TVA and PDA (Figure 4.21 (b1) and (b2)). For location 3, flow is seen to be more rotary (Figure 4.21 (a3)), hence a larger difference in TVA and PDA results is observed (Figure 4.21 (b3)).

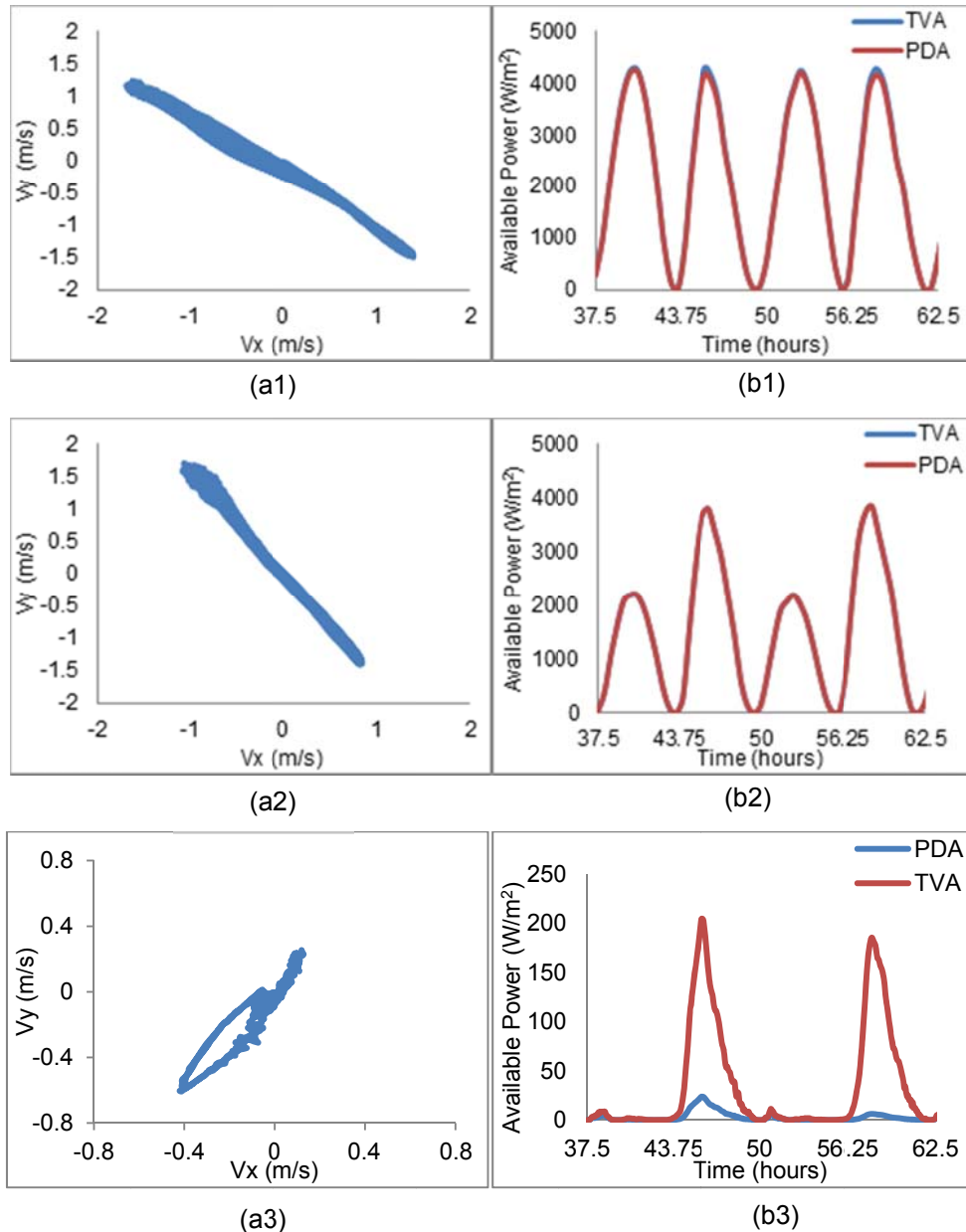


**Figure 4.21: (a) Flow direction, (b) Available power ( $W/m^2$ ) over 2 tidal cycles as determined using TVA and PDA at locations (a) 1, (b) 2, (c) 3.**

One would expect the accuracy of a resource assessment to increase with the level of sophistication of the approach. Comparing the three resource assessments it can be concluded that whilst the TVA is no doubt more precise than the cruder FFA, it still contains simplifications as it utilises the total velocity vector. The PDA is the most sophisticated approach as it considers the proportion of energy a fixed orientation horizontal axis turbine can extract from the flow by considering the prevailing current direction.

#### **4.5.3 Site Identification and Device Orientation**

As discussed in Section 4.4.1, identifying suitable sites for turbine deployment will involve considering both resource availability and flow type, with desired locations possessing a high resource and rectilinear flow. Device orientation depends on flow directionality, with optimum orientation of a HAT being perpendicular to current flow.

As previously discussed,  $M_2$  is the dominant constituent across the estuary; hence the prevailing direction of current flow is determined based on the  $M_2$  angle of inclination. The dominance of  $M_2$  is demonstrated in Figure 4.22, which illustrates a spatial map of the ratio of the  $M_2$  major axis to the sum of the major axes of all the constituents included in the analysis. It can be seen that the  $M_2$  major axis accounts for approximately 0.6 - 0.8 of the summed major axes of all constituents included in the analysis and is therefore by far the dominant constituent. An additional reason for basing this analysis solely on  $M_2$  data was to reduce the model run time, as to include other constituent data would require a substantially longer time period. The final objective of this research is the development of an array optimisation model which involves calculating a new resource assessment after each individual turbine is deployed, hence creating the need for efficiency in model simulation time.

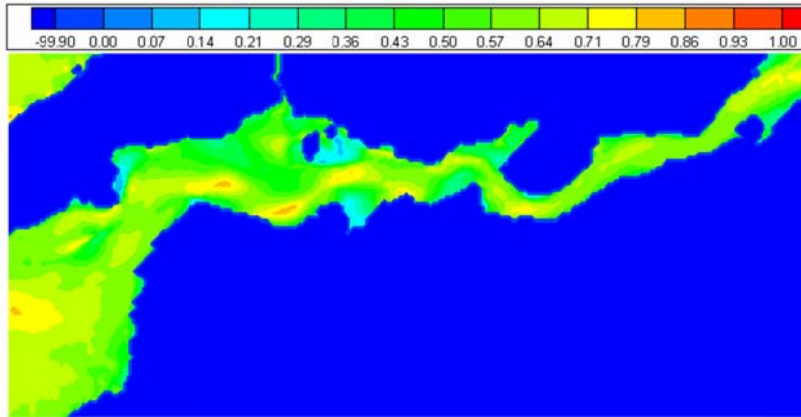


**Figure 4.22: Ratio of  $M_2$  major axis to the sum of all constituent's major axis.**

To illustrate the flow type and prevailing direction of flow across the estuary, the author's assessment approach uses contour plots of the minor-to-major axis ratio and the angle of inclination of the  $M_2$  ellipse. These are presented in Figure 4.23 and Figure 4.24, respectively. To identify suitable turbine deployment locations, criteria for both power availability and flow type are considered. As rectilinear flow moving perpendicular to the turbine is desired, site selection criteria of  $ER \leq 0.2$  and  $P_{mean} \geq 350W/m^2$  are employed. These values were selected by the author to represent areas of high resource and rectilinear flow; however they can be altered to any value deemed suitable by the user. These are conditional criteria which both must be satisfied. Using the criteria and associated maps, the model selects locations within the estuary that possess both high available tidal resource and rectilinear flow. The results are presented in Figure 4.25, with potential deployment sites shown in red. Device orientation at any suitable location can subsequently be determined using the ellipse inclination map in Figure 4.24.

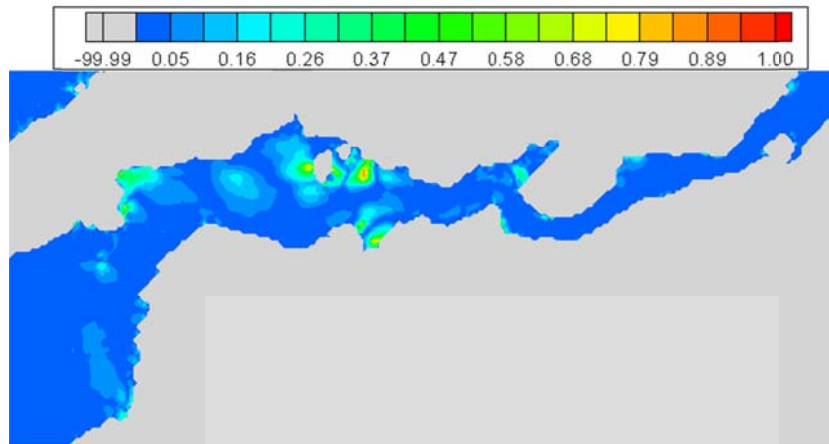


**Figure 4.23: Ratio of minor to major axis (ER) of  $M_2$  ellipses across the Shannon estuary.**

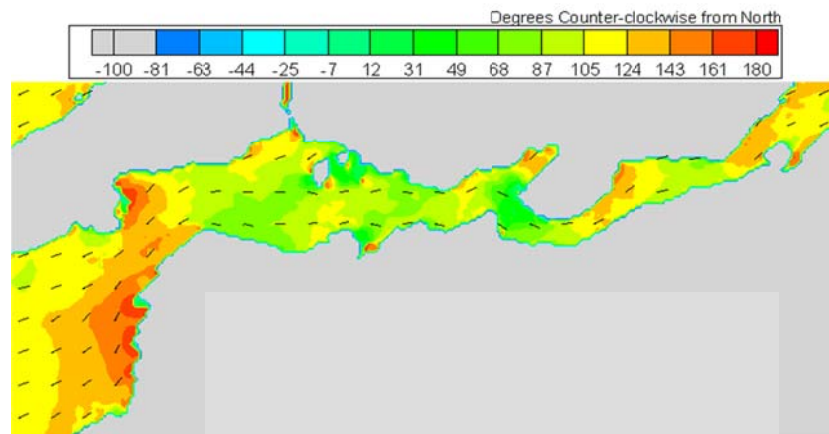


**Figure 4.24: Angle of inclination of  $M_2$  ellipse across the Shannon estuary, measured counter-clockwise from North.**

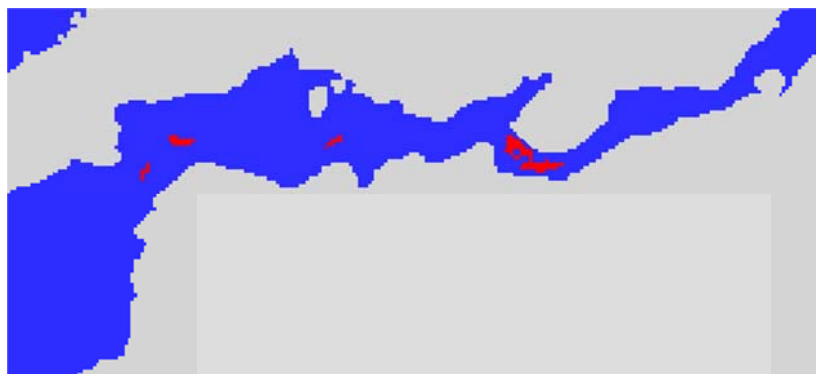


**Figure 4.25: Suitable deployment locations based on power availability and flow direction.**

#### 4.5.4 Preferred Berths

Resource estimates of the Shannon estuary indicated greatest power potential in three specific areas, which corresponded closely to the tidal energy berths identified by the Shannon Framework Plan (Figure 4.2). To further characterise these sites, six locations were selected based on available resource and the Framework Plans preferred option of turbine deployment outside of the shipping lanes shown in Figure 4.2. The six locations of interest (A-F) are shown in Figure 4.26.

Assessment of the tidal parameters at each location showed that each preferred berth was considerably different, with a varying range of flows and, hence, potential available power found across the sites.

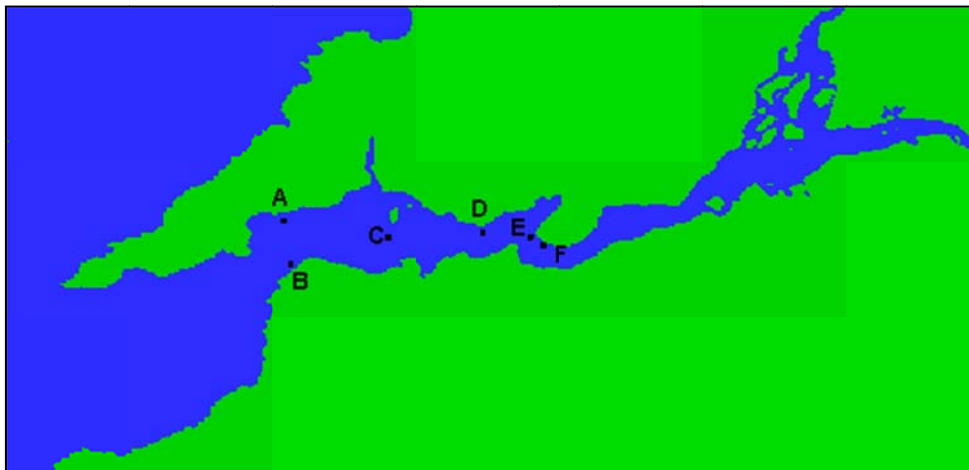


Figure 4.26: Locations of interest (A-F).

#### 4.5.5 Tidal Current Analysis

Tidal current ellipses were constructed for the locations of interest (A-F). The resulting ellipses along with the current velocities used by TVA and PDA are presented in Figure 4.27 - Figure 4.32 (a) and (b), respectively.

Total current velocities at A reach a peak of 1.1m/s, which may not be strong enough for turbine operation. The dominant  $M_2$  ellipse ratio

at A indicates a moderate-to-strong rectilinear flow ( $ER = 0.09$ ). The ellipse ratio at B indicates very strongly rectilinear flow ( $ER = 0.009$ ) but peak velocities reach only 0.9m/s, which, similar to A, are too low for efficient tidal energy extraction. The shape of the  $M_2$  ellipse at C suggests that flow is nearly all resulting from the  $V$  velocity component, with  $U$  velocities being significantly smaller, if present at all. The ellipse ratio ( $ER=0.17$ ) indicates more rotary flow than at A or B, this is also observed in the comparison of TVA and PDA velocities. Based on the PDA, location C would not be a suitable deployment site as power availability would be considerably low during the ebb tide. Considering flow directionality location C, having a relatively high  $ER$  compared to the other locations, is the only site deemed unsuitable for deployment. This suggests selecting a criterion of  $ER \leq 0.2$  for suitable deployment locations (see Figure 4.25) may be too high, an improvement would be to reduce this criteria to 0.1.  $ER$  at D suggests flow is primarily rectilinear ( $ER = 0.02$ ). However, considering the relatively low peak velocities of 1.0m/s it can be concluded that it is not suitable for turbine siting. Comparing all six locations, flow at E is seen to be the most rectilinear ( $ER = 0.008$ ). High current velocities, reaching peaks of 2.0m/s, are also noted at E. Currents at F show similar characteristics to those at E, having strong peak velocities of 2.0m/s and being predominantly rectilinear ( $ER = 0.03$ ). The strong currents along with the rectilinear nature of the flow indicate locations E and F to be the most appropriate deployment sites.

Analysis of the resource potential of a possible turbine deployment site depends on both flow speed and direction. Strong currents result in a high power potential, but the proportion of available power that a horizontal axis turbine will be able to extract is dependent on the direction of current flow. Considering the direction of flow as well as the current speed will result in less over-prediction of tidal power potential and improve the sophistication of resource assessments.

Analysis of tidal current ellipses constructed at the selected tidal energy berths indicates that locations E and F have the greatest potential for energy extraction. Locations A, B and D, based on flow directionality, may also be suitable deployment sites, however most operational devices require peak current velocities of 2.0-2.5m/s which are not reached at A, B or D. Flows at location C were seen to be low in strength and more rotary than the other locations, indicating it is not a suitable turbine deployment site.

#### **4.5.6 Frequency of Resource Availability**

Further assessment of the potential resource at the areas of interest involved determining the frequency of power availability using TVA and PDA and comparing results from both approaches. Results from this assessment are presented in Figure 4.27 - Figure 4.32 (c). These types of frequency analyses can be used to determine the most suitable type of tidal turbine (e.g. power rating and performance characteristics) to be deployed at a site.

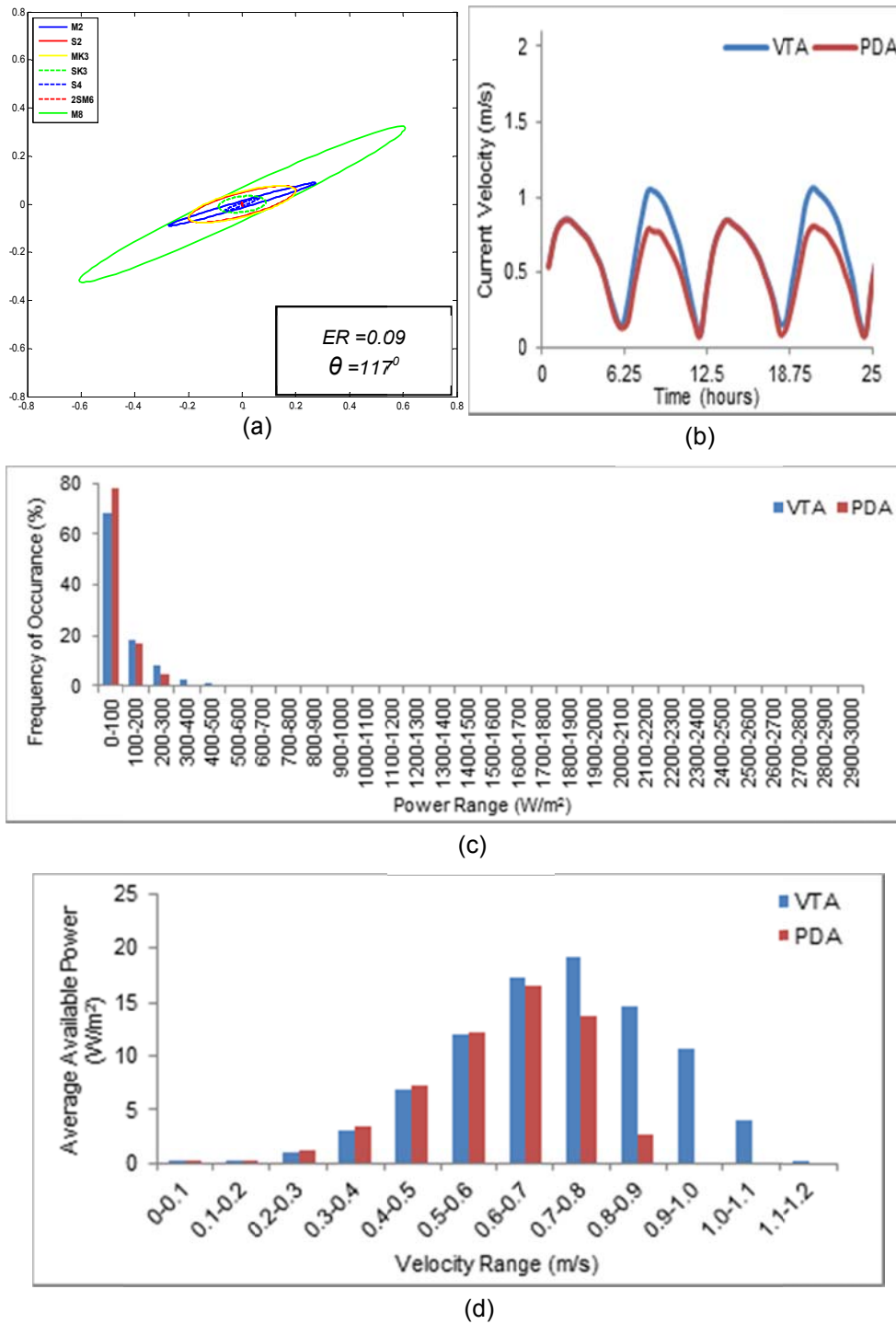


Figure 4.27: (a) Tidal current ellipses and (b-d) comparison of VTA and PDA assessments at location A for (b) current velocity data, (c) frequency of power availability and (d) available power in each velocity range.

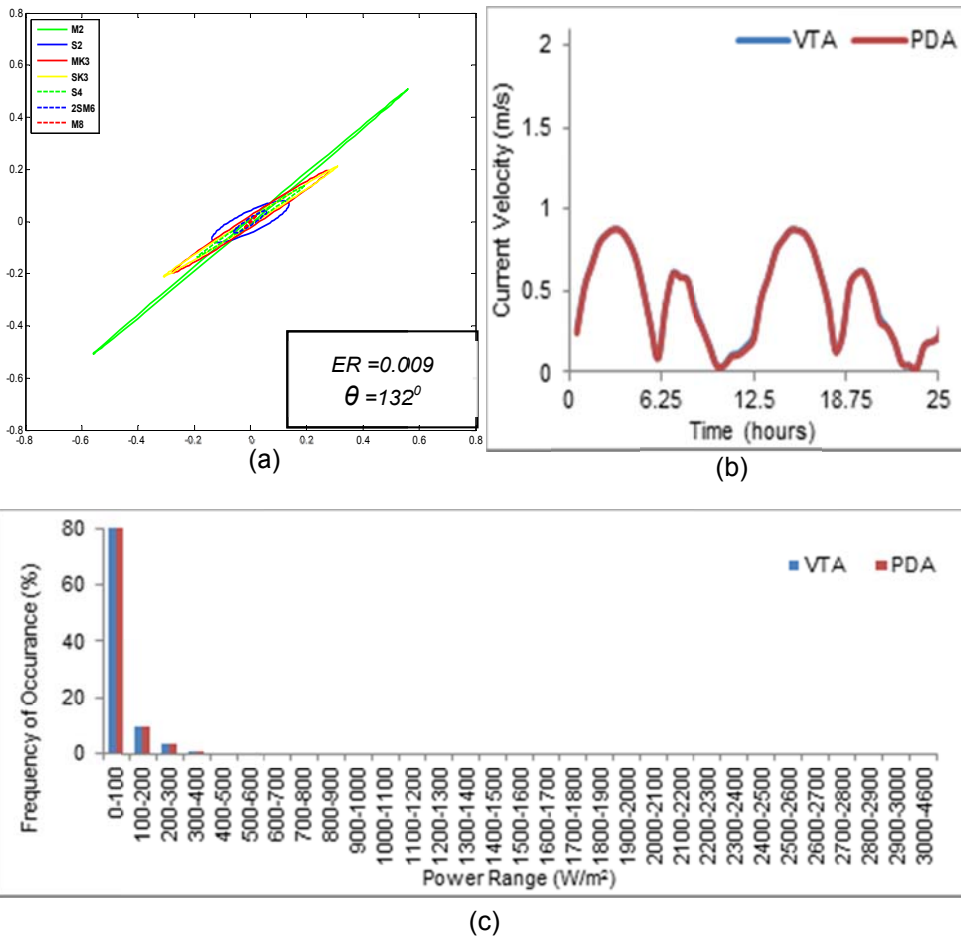
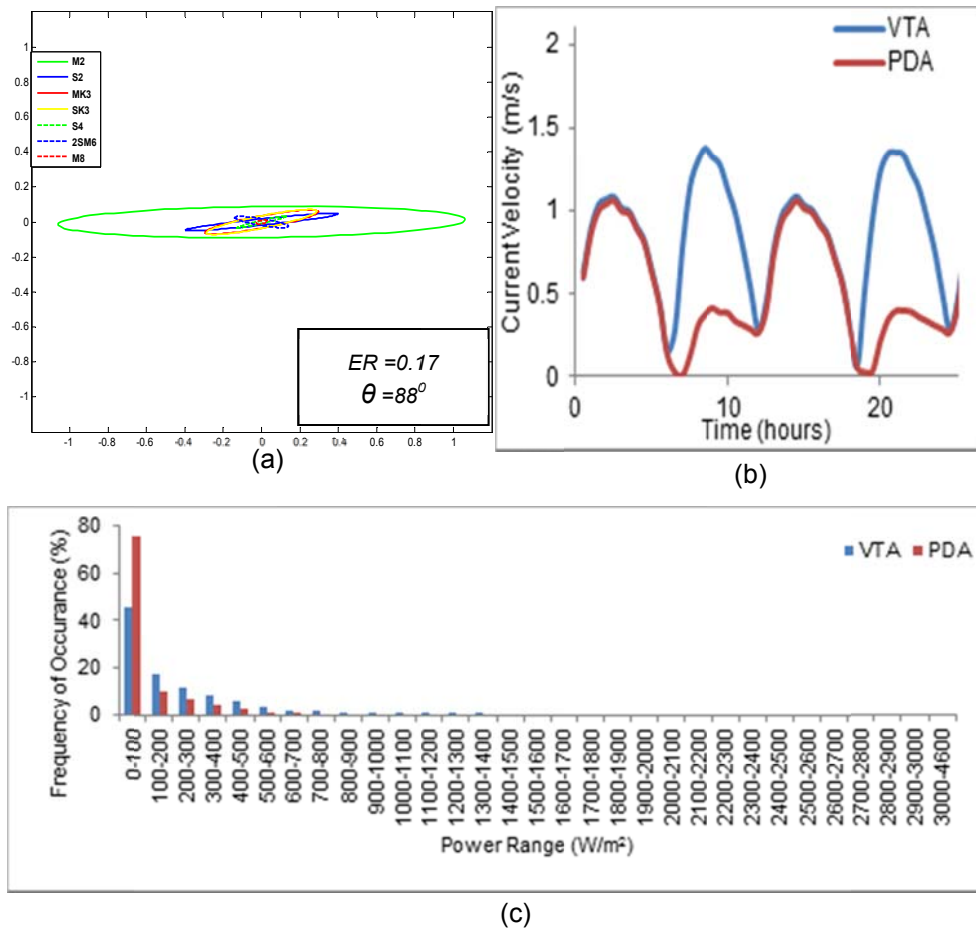
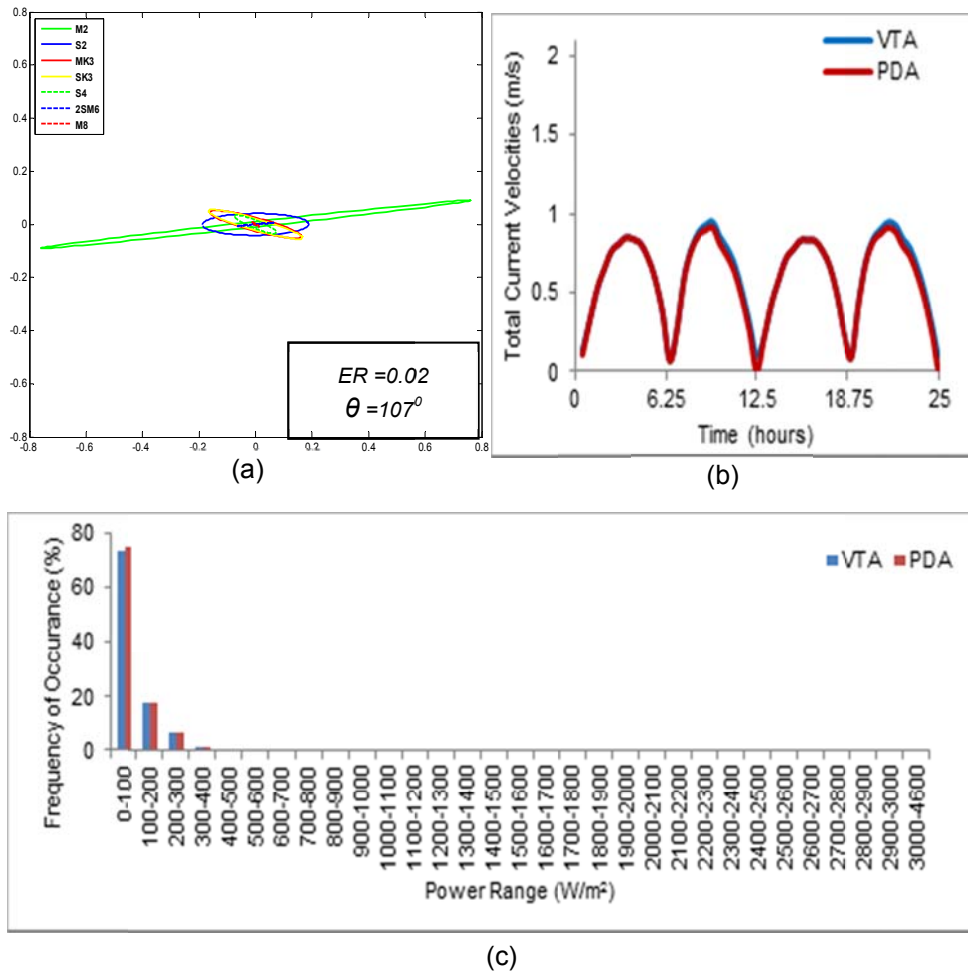


Figure 4.28: (a) Tidal current ellipses and (b-c) comparison of VTA and PDA assessments at location B for (b) current velocity data and (c) frequency of power availability.



**Figure 4.29: (a) Tidal current ellipses and (b-c) comparison of VTA and PDA assessments at location C for (b) current velocity data and (c) frequency of power availability.**



**Figure 4.30: (a) Tidal current ellipses and (b-c) comparison of VTA and PDA assessments at location D for (b) current velocity data and (c) frequency of power availability.**

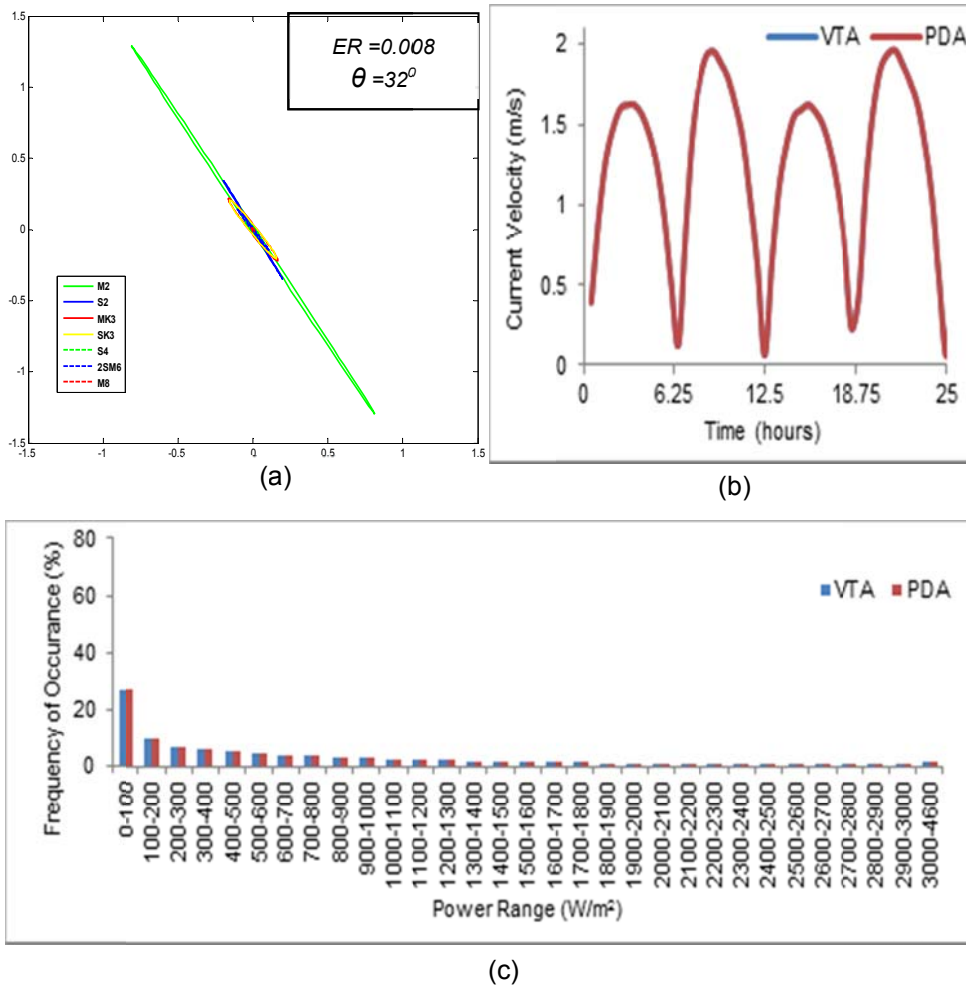


**Figure 4.31: (a) Tidal current ellipses and (b-c) comparison of VTA and PDA assessments at location E for (b) current velocity data and (c) frequency of power availability.**

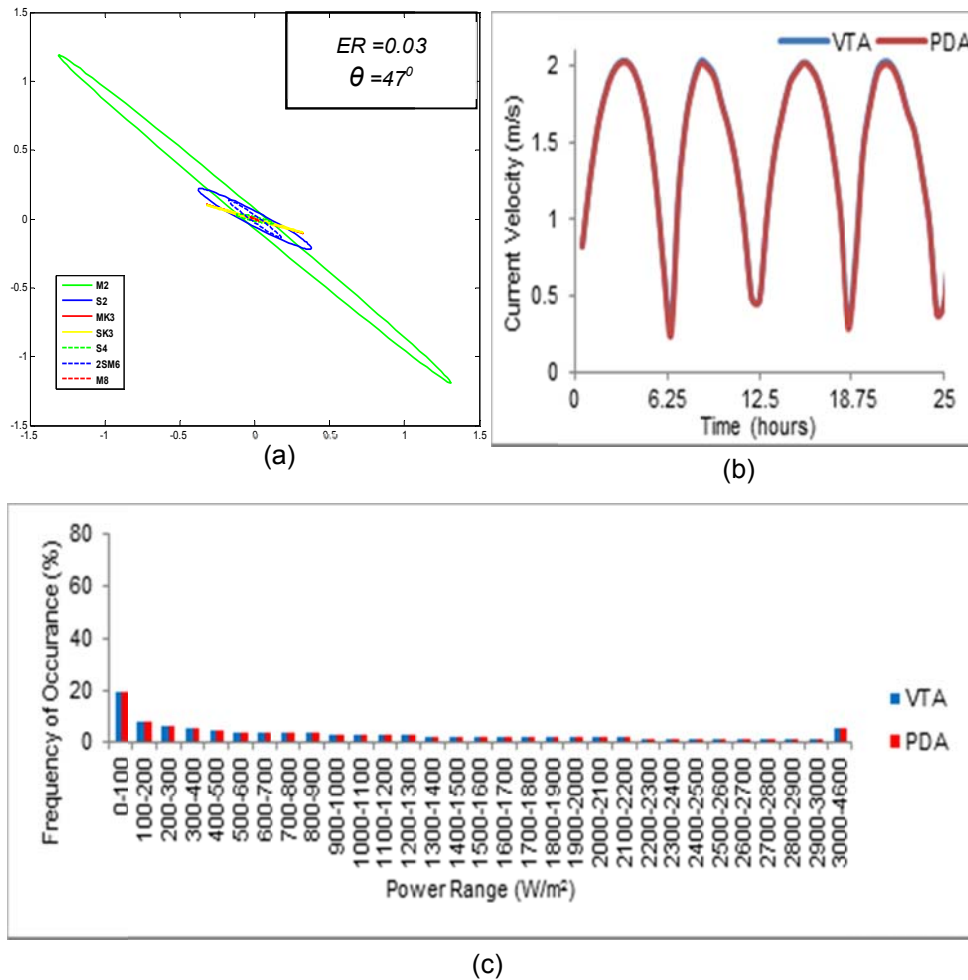


**Figure 4.32: (a) Tidal current ellipses and (b-c) comparison of VTA and PDA assessments at location F for (b) current velocity data and (c) frequency of power availability.**

The velocity data used in the two different assessment approaches at location A show a reduction in current velocities when only the velocity components parallel to the primary direction of flow are considered (see Figure 4.27 (b)). This is further demonstrated when assessing the average power available in each velocity range Figure 4.27 (d)). At lower velocities, taking the 0.2-0.3m/s range for illustration, available power is estimated using the TVA as  $0.96\text{W/m}^2$ , whilst a higher estimate of  $1.097\text{W/m}^2$  is determined using the PDA. For higher velocity ranges, for example 0.8-0.9m/s, the TVA estimates a considerably higher power of  $14.65\text{W/m}^2$  compared to the  $2.64\text{W/m}^2$  calculated using the PDA. This is mirrored in the power frequency graph Figure 4.27 (c)) which shows the PDA resulting in

greater frequencies of lower powers and lower frequencies of higher powers.

Looking in more detail at the frequency of power availability determined using both methods at location A, (Figure 4.27(c)), the TVA indicated a maximum available power in the range of 700-800W/m<sup>2</sup>; however, this power is available for extraction for less than 0.01% in a year. In contrast, power levels between 0W/m<sup>2</sup> and 100W/m<sup>2</sup> can be obtained for approximately 68% of the year. For the PDA, frequencies are higher for lower power ranges, as is expected due to the decreased velocities. For powers greater than 100W/m<sup>2</sup>, the frequency of all power availability is reduced, with maximum available power estimated to lie between 300-400W/m<sup>2</sup>, a reduction of around 50% from the maximum available power range calculated using the TVA.

Reductions in PDA velocities compared to TVA velocities at location B were minimal (see Figure 4.28 (b)). This is not surprising as the M<sub>2</sub> ellipse at B indicates predominantly rectilinear flow, hence the majority of flow will be moving in the primary direction (see Figure 4.28 (a)). Overall, current velocities were substantially lower at location B compared to those at A, therefore the estimated resources were considerably less (see Figure 4.28 (c)). Results at location B determined using the TVA estimated a maximum power in the 300-400W/m<sup>2</sup> range, available for 0.5% of the total time. Lower powers, such as those in the 0-100W/m<sup>2</sup> range, were available for approximately 86% of the year. Similarly, the PDA estimated a maximum power value in the range 300-400W/m<sup>2</sup>, and indicated that powers in the range of 0-100W/m<sup>2</sup> were available for 86% of the time. The similarities in results at location B are due to the rectilinear nature of flow found at this site.

Tidal current ellipses indicated dominance of the  $V$  velocity component at C (Figure 4.29 (a)); this is further demonstrated in Figure 4.29 (b). Investigating current velocities at this site in more detail shows that the magnitude of the total velocity and velocity aligned only with the primary direction of flow are relatively equal during the flood tide, in contrast the magnitude of the velocity aligned with the primary flow direction is substantially lower during the ebb tide, this is likely a result of bathymetric/topographic steering causing non-rectilinearity of flood and ebb flows. As one would expect, the changing direction of flow has a significant impact on the resulting frequency of power availability, as illustrated in Figure 4.29 (c). Maximum powers calculated using the TVA lie in the 900-1000 W/m<sup>2</sup> range, whereas the maximum power determined using the PDA are considerably lower falling in the 600-700W/m<sup>2</sup> range. In both cases, these peak powers are only available for extraction for an extremely small percentage of time. The difference in the frequency of power availabilities determined using both methods is substantial, for instance; resource estimates decrease from just over 11% to around 6% in the 200-300W/m<sup>2</sup> range and increase from 45% to 75% in the 0-100W/m<sup>2</sup> range when the flow direction is considered. This is a direct result of the reduced currents during the ebb tide. Due to the nature of flow at C it was assumed that PDA results are more accurate than those determined by TVA.

Tidal current ellipses at location D (see Figure 4.30 (a)) indicate that flow due to the dominant  $M_2$  constituent is primarily rectilinear, this is further demonstrated in Figure 4.30 (b). As a result, the frequencies of power availability determined using the two methods are quite similar (see Figure 4.30 (c)). In the 0-100W/m<sup>2</sup> range, percentages of occurrence are marginally lower when the TVA is employed; however, this is to be expected due to the slightly reduced current velocities determined by using the PDA. The maximum available

power estimated by both approaches is also similar, with both estimates of maximum power in the 400-500W/m<sup>2</sup> range.

Considering the six selected locations, E and F were seen to have the highest current velocities and their M2 tidal ellipses indicated rectilinear flow, this suggests they have high potential to be suitable sites for tidal energy extraction. This is further confirmed when looking in more detail at both locations; current speeds are relatively similar even when only the primary direction of flow is considered, illustrated in Figure 4.31 (b) and Figure 4.32 (b).

Due to the high velocities, high levels of power available for extraction are estimated. At location E (see Figure 4.31(c)) maximum available powers in the range 4100-4200W/m<sup>2</sup> are determined using both methods; however, in both cases this power range is available for extraction for less than 0.006% of the time. As the powers decrease their extraction availability period increases, this is a trend seen throughout assessment of all six locations. Power estimations at location F (see Figure 4.32 (c)) show a maximum power availability in the range of 4400-4500W/m<sup>2</sup> and 4300-4400W/m<sup>2</sup> determined using the TVA and PDA, respectively. The 4400-4500W/m<sup>2</sup> range is available for a minimal 0.016% of the time when determined using the TVA and the 4300-4400W/m<sup>2</sup> range is available for less than 0.005% of the time when using the PDA. At lower power ranges frequencies determined based on the TVA are slightly lower than those estimated by the PDA, however this difference is marginal again due the similar velocities and rectilinear nature of flow at this site.

#### **4.5.7 Recommended Deployment Sites**

A further detailed resource assessment was carried out based on available power alone, i.e. ignoring any spatial constraints such as the presence of shipping lanes. Figure 4.33 illustrates resource availability across the estuary determined using the PDA approach

and the five locations of interest (G-K). All three assessment approaches determined location I as the site of maximum power availability while the other locations were selected to demonstrate the benefits of using the direction-based PDA over the TVA and FFA assessments. Figure 4.34 shows the selected locations superimposed on the 'suitable deployment areas' map produced in in Section 4.5.3. Locations G and H were specifically chosen to be outside of the suitable areas - these are examples of locations that one might choose for turbine deployment based on an assessment by TVA alone.

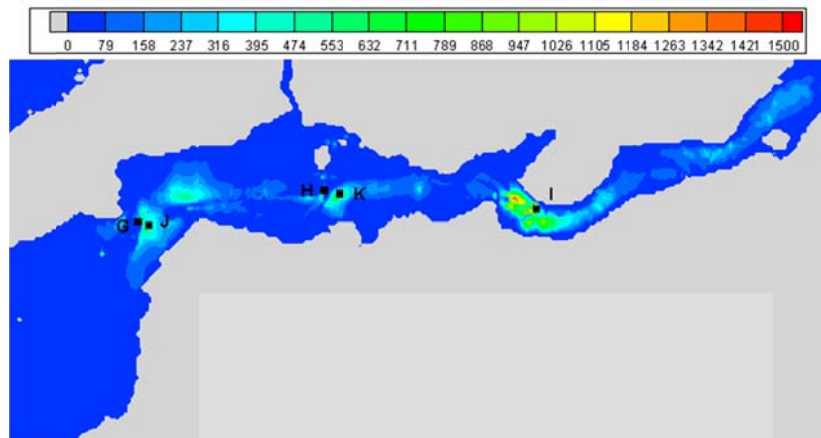


Figure 4.33: Locations of interest (G-K) and available power as determined using PDA (Units of legend:  $W/m^2$ ).

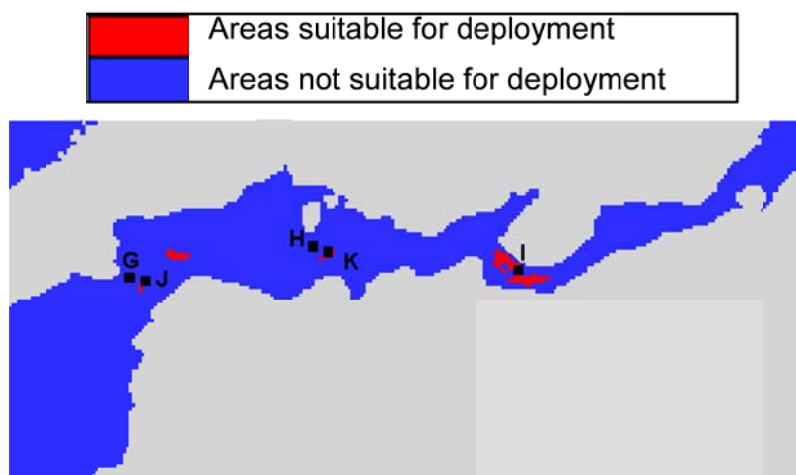
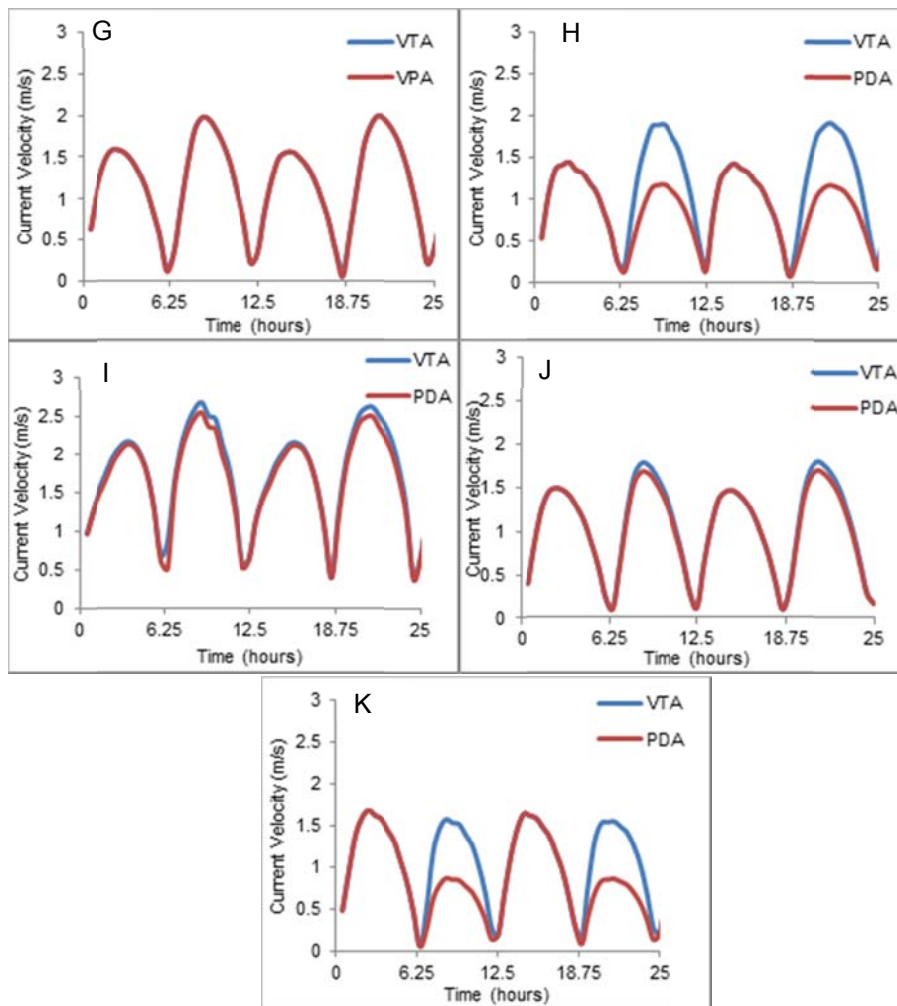
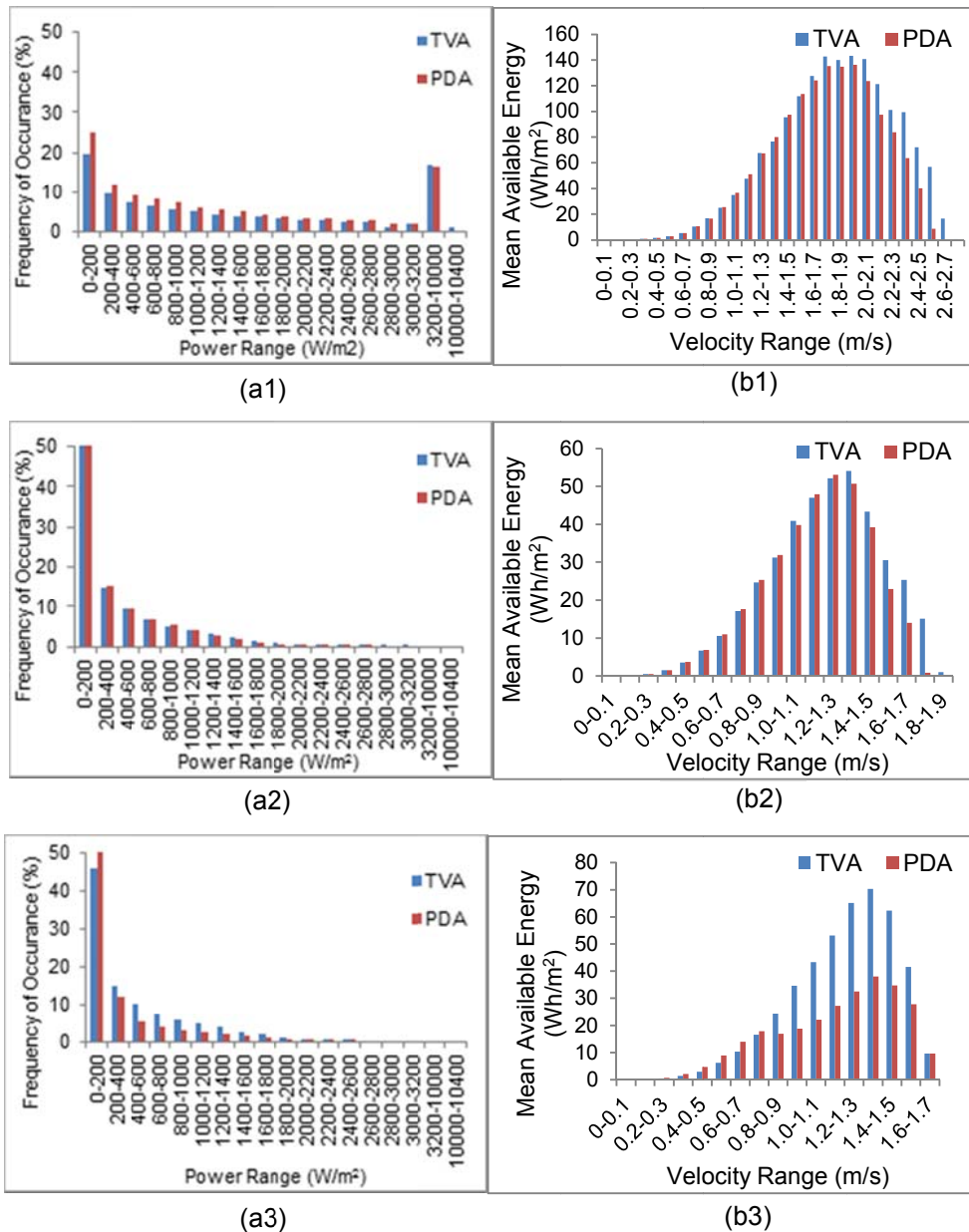


Figure 4.34: Locations of interest (G-K) shown with suitable deployment locations based on power availability and flow direction.

A comparison of the total and primary current velocities at locations G-K are presented in Figure 4.35. Since they were chosen as high resource sites they all exhibit strong currents with peaks in the region of 2-2.5m/s. However, while rectilinear flow is present at locations G, I and J, locations H and K possess a more rotary flow. Locations G and H were selected based on the FFA assessment. This is the crudest approach and so is likely to be the least accurate. Figure 4.34 shows G and H fall outside of the suitable deployment sites. These locations were therefore not selected for further assessment. Locations I, J and K were all identified by the PDA as suitable deployment sites and proceeded to a more detailed assessment, the results of which are presented in Figure 4.36.



**Figure 4.35: Comparison of time-varying total and primary direction velocities at locations of interest (G-K).**



**Figure 4.36: Comparison of (a) frequency of power availability and (b) available power in each velocity range at locations (1) I, (2) J and (3) K determined using both methods.**

Location I has strong rectilinear flows, with velocities reaching peaks of over 2.5m/s, leading to high power potential. TVA estimates a maximum power availability of approximately 10,400W/m<sup>2</sup> whilst PDA estimates a slightly lower maximum power of just under 10,000W/m<sup>2</sup>. Location J also has rectilinear flows reaching peaks of 2m/s. High power estimates are also found at this location with maximum powers in the range 3,000-3,200 W/m<sup>2</sup> and 2,600-2,700 W/m<sup>2</sup> determined using the TVA and PDA, respectively. However,

these very high power ranges are only available for a small percentage of time. Currents at location K are less rectilinear and hence a more notable difference is found in power estimates.

The available power in each velocity range is also an important factor to consider when determining suitable deployment sites. The turbines' cut-in speed is the lowest speed at which it is economical to extract power. The average cut-in speed for a horizontal axis turbine, for example SeaGen, is around 0.8m/s (MacEnri et al. 2011). Results (Figure 4.36 (b)) show high available powers for velocities greater than 0.8m/s for each location. However at location K there is a substantial decrease between available powers calculated using the PDA compared with the TVA, and it may be less suitable for turbine deployment than locations I and J.

To summarise the differences between assessment approaches for the potential tidal energy berths, the average annual available power was determined using each approach at each of the 11 locations - these are presented in Table 4.4. For all locations, estimates based on the FFA are considerably greater than those determined by the TVA and PDA. It can therefore be concluded that, due to its many assumptions, FFA significantly over-predicts the available resource, particularly in an estuary where ebb-dominance exists. Comparing results from TVA and PDA, considerable differences in resource estimates will occur in areas which have been identified as possessing non-rectilinear flow, for example the relative difference in available powers at location H is 53%. Differences in power estimates at locations where rectilinear flow prevails will be minimal, for instance, at location E the difference in resource estimates is just 0.08%.

**Table 4.4: Average annual available power at preferred berths using different assessment approaches.**

| Location | Average Annual Available Power (W/m <sup>2</sup> ) |                                     |                                       |
|----------|--|-------------------------------------|---------------------------------------|
|          | Fraenkel Formula (FFA)                             | Time-Varying (Total) Velocity (TVA) | Time-Varying (Primary) Velocity (PDA) |
| A        | 204.14   | 88.94                               | 56.96                                 |
| B        | 126.53   | 43.88                               | 34.27                                 |
| C        | 350.20   | 210.12                              | 74.74                                 |
| D        | 120.77   | 69.62                               | 65.53                                 |
| E        | 1048.84  | 670.46                              | 669.96                                |
| F        | 1161.03  | 969.93                              | 951.80                                |
| G        | 1088.81  | 543.54                              | 540.81                                |
| H        | 950.27   | 508.30                              | 241.61                                |
| I        | 3058.50  | 1659.92                             | 1465.25                               |
| J        | 783.41   | 405.70                              | 367.16                                |
| K        | 612.64   | 442.75                              | 276.81                                |

#### **4.6 Effect of River Flow on Resource Assessment**

The Shannon model used throughout this assessment included hydrodynamic river flow data from the Shannon and Fergus rivers. To examine the effect of river flows on available resource assessment, the model was run again for the year 2006 with zero flow for both rivers and the available power was recalculated and compared with the original assessment. Figure 4.37 shows the relative percentage difference in the resulting resource determined by the FFA (i.e.  $\%Diff = ((P_{\text{mean (with rivers)}} - P_{\text{mean (no rivers)}}) / P_{\text{mean (with rivers)}}) \cdot 100\%$ ). it can be seen that across the majority of the estuary, the % difference is less than 3%. Similar levels of difference were found for all three approaches. It can therefore be concluded that in this case tidal stream energy resource assessments are not hugely sensitive to accurate prescription of river flows.

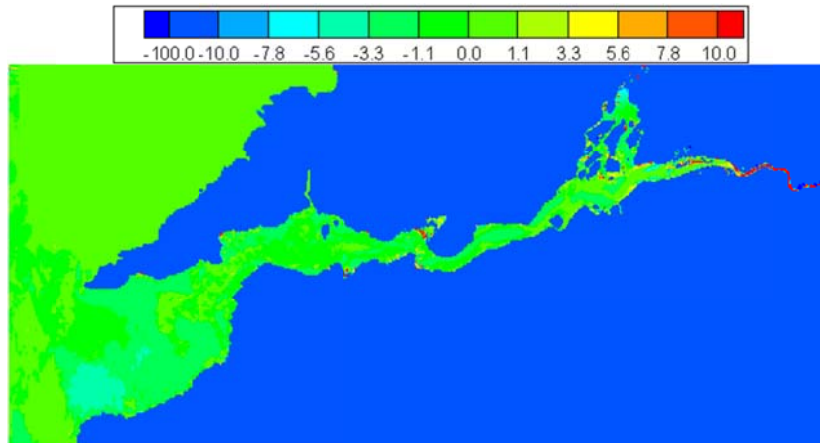


**Figure 4.37: Change in available powers calculated with and without river flow based on FFA.**

#### **4.7 Summary and Conclusions**

This chapter presents the development of a resource assessment methodology which utilises a 2D hydrodynamic flow model along with tidal harmonic analysis and ellipse theory to incorporate the prevailing direction of current flow into the power calculation. The main conclusions from this assessment are as follows:

- HTAS was incorporated into the existing numerical model to deconstruct current velocities and produce elliptical parameters which were used to indicate current flow direction. Comparison of the resulting ellipses to measured current data validated the developed model, showing the constructed ellipses correctly captured velocities across the domain. As measured data for the Shannon estuary was available an alternative method to determine the primary flow direction would have been to use velocity time-series data directly. However, as previously discussed, the estuary possessed strong variations between spring and neap currents which are better captured through use of tidal ellipses.
- Available resource in the estuary was quantified based on two traditional approaches and the author's developed approach.

All three approaches indicated a similar trend in the resource potential across the estuary. However, differences in the magnitude of available resource were observed due to the varying levels of sophistication of each approach. The traditional methods were found to over-predict the tidal energy potential compared to the more sophisticated approach developed by the author which incorporates flow direction. Accuracy of the assessment is assumed to increase with the increasing level of sophistication of the approach.

- Initial assessment of the available tidal resource across the Shannon estuary indicated greatest potential in three regions. Based on this, locations within the regions were selected for a more detailed resource assessment to determine if they are in fact suitable sites for turbine deployment. Six locations (A-F) were selected considering resource and shipping lane restrictions, five further locations (G-K) were selected considering only potential resource. Results highlighted similarities in approaches in regions where rectilinear flow prevails, while a considerable difference between resource estimates was found in areas where flow was multi-directional.
- Locations G and H were selected based on the FFA, however, as this methodology has proven to over-predict the tidal resource these locations are not recommended. Locations I, J and K were chosen based on the authors' methodology, whilst these sites are found to be more accurate location K possesses rotary flow and so it is not a recommended site. Assuming no restrictions are in place, the author would recommend locations I and J as turbine deployment sites. However considering both flow regime and shipping lane restrictions locations E and F are found to be the most promising tidal energy berths.

- Selection of suitable turbine deployment sites based on the available resource is the first step in Blunden & Bahaj's (2007) definition of a tidal stream energy resource assessment. The subsequent steps consider energy extracted by a turbine(s) and the associated impact on both the hydrodynamics of a water body and on the available power. Available power is a measure of the undisturbed resource; however, deployment of tidal turbines will alter the undisturbed current flow, and therefore impact on the available resource. Of particular interest in this research is capturing the hydrodynamic impacts and effect on available power of tidal energy extraction. This concept is developed, discussed and applied in the next chapter.

## 5 Energy Extraction Model

### 5.1 Introduction

A primary aim of this research was the modification of the depth-averaged hydrodynamic model to incorporate the effects of tidal energy extraction. The developed model can then be used to facilitate quantification of the power output from a turbine array and determination of an optimum array configuration for maximum energy extraction with minimal hydro-environmental impacts.

Energy removal by tidal turbines was incorporated in the numerical model using the momentum sink approach, in which the thrust induced by a tidal turbine is included as an additional external force in the momentum equations. A method to quantify the extracted power based on the turbine thrust was also developed and implemented in the model. The standard thrust and power equations were formulated using the free-stream velocity; however, determining this velocity in a simulation where turbines have been included can be problematic since the turbines will alter the velocities. This problem is a primary focus of the attempts to implement energy extraction and power quantification in the model.

This chapter details the theory behind the energy extraction process within the model and describes how it was incorporated into the model, namely through alterations to the governing momentum equations. The free-stream velocity issue with regard to calculation of turbine thrust is then discussed. A sophisticated approach to thrust calculation and quantification of energy extracted is developed and the methodology is tested and validated using an idealised channel and the Shannon estuary case study site. Finally, using two idealised domains (flow around an island and flow around a headland and island), the model is used to investigate the impacts of tidal arrays on

residence times with a view to using residence time as an indicator of both hydrodynamic and environmental impact.

## **5.2 Development of the Energy Extraction Model**

### **5.2.1 Turbine Representation within the Model**

Tidal energy extraction is simulated in the hydrodynamic model using the momentum sink approach, in which a retarding force, representing the turbine thrust, is incorporated into the model through inclusion of a negative sink term in the momentum equations. This approach is a common method used in far-field models (e.g. Ahmadian & Falconer (2012); Plew & Stevens (2013); Fallon et al. (2014); Adcock & Draper (2014)).

The turbine thrust is derived using the Linear Momentum Actuator Disc Theory (LMADT) which was first introduced by Betz in the 1920's (Burton et al. 2001), with initial applications based on wind turbine analysis. The concept was further developed by Houlby et al. (2008) for tidal turbines, considering a stream tube enclosing a turbine rotor in a flow of constant cross section, bounded by parallel channel walls and a constant depth free surface. The turbine rotor is simulated as a porous actuator disc which takes momentum from the flow in an open channel, enabling the thrust for a horizontal axis turbine to be derived. Figure 5.1 graphically explains the LMADT theory based on five stations: (1) far upstream of the turbine, (2) immediately upstream of the turbine, (3) immediately downstream of the turbine, (4) region in which slower moving flow from the turbine's wake merges with free-stream fluid from the by-pass flow and (5) far enough downstream from the turbine that pressure returns to free-stream levels. Flow passing through the turbine is denoted  $t$ , whilst by-pass flow is denoted  $b$ .

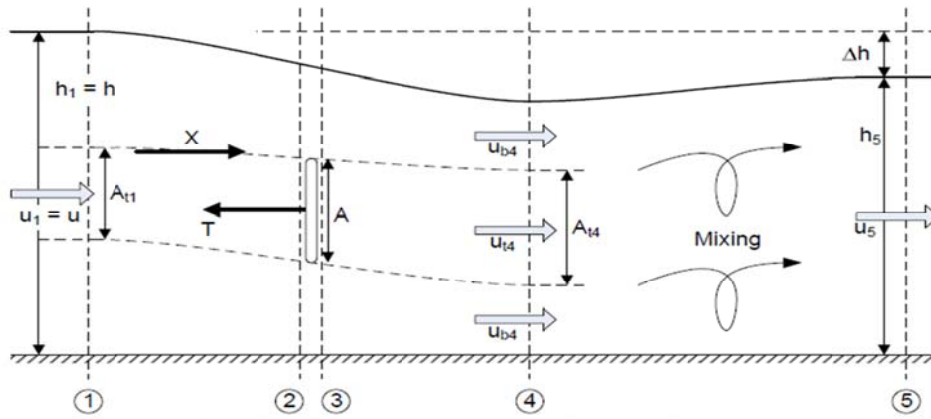


**Figure 5.1: One dimensional linear momentum actuator disc theory in open channel flow (Houlsby et al. 2008).**

As the undisturbed flow at (1) passes through the porous disc (2-3) a continuous reduction in velocity occurs as the disc takes momentum from the flow. Consequently, immediately downstream of the disc (3-4) flow passing through the disc is slower than the by-pass flow diverted around it and so must expand to satisfy conservation of momentum. This action generates the wake (an area of reduced velocity downstream of the disc) and turbulent mixing. As flow travels away from the disc (5) the wake gradually dissipates and flow returns to free-stream conditions. Along with altering current flow, tidal energy extraction is also found to cause a drop in water depth,  $\Delta h$ , across the turbine.

As the undisturbed flow at (1) moves through the stream tube and passes through the turbine it exerts a force on the turbine rotor. Due to Newton's third law the turbine exerts an equal and opposite force on the flow, this force is known as the thrust,  $T$ , has been previously defined in Section 2.5.2 as:

$$T = \frac{1}{2} \rho u^2 A_T C_T \quad (5.1)$$

$C_T$  (the dimensionless thrust coefficient) is further defined as:

$$C_T = (\beta_4^2 - \alpha_4^2) \quad (5.2)$$

where  $\beta_4$  is the bypass flow velocity coefficient and  $\alpha_4$  is the turbine wake flow velocity coefficient which represent the acceleration and reduction in the bypass and wake flows respectively.

The effects of tidal energy extraction are represented within the numerical model by adding a momentum sink term ( $F_{Tx}$  in equation (5.3)) to the momentum equations which represents the thrust exerted by the turbine on the flow. The x-direction (and similarly the y-direction) momentum equations are hence amended as follows:

$$\begin{aligned} \frac{\partial q_x}{\partial t} + \beta \left[ \frac{\partial U q_x}{\partial x} + \frac{\partial V q_y}{\partial y} \right] = & f q_y - g H \frac{\partial \zeta}{\partial x} + \frac{T_{xw}}{\rho} + \frac{T_{xb}}{\rho} \\ & + 2 \frac{\partial}{\partial x} \left[ \epsilon H \frac{\partial U}{\partial x} \right] + \frac{\partial}{\partial y} \left[ \epsilon H \left[ \frac{\partial U}{\partial y} + \frac{\partial V}{\partial x} \right] \right] - \frac{F_{Tx}}{\rho} \end{aligned} \quad (5.3)$$

The axial thrust induced by the turbine(s) on the flow in the x- and y-directions respectively is distributed across a grid cell such that  $F_{Tx}$  and  $F_{Ty}$  may be calculated as:

$$F_{Tx} = \frac{T}{\Delta x \Delta y} \cdot |\sin \theta| \cdot \left( \frac{U}{|U|} \right) \quad (5.4)$$

$$F_{Ty} = \frac{T}{\Delta x \Delta y} \cdot |\cos \theta| \cdot \left( \frac{V}{|V|} \right) \quad (5.5)$$

where  $U / |U|$  and  $V / |V|$  are a sign convention that ensure that the thrust is always a momentum sink irrespective of the reversing of tidal flows; these functions equate +1 if  $U$  and  $V$  are acting in the positive x- and y-directions and -1 if  $U$  and  $V$  are acting in the negative x- and y-directions.

Horizontal axis turbines are usually designed to have a fixed orientation but a small number can swivel around their vertical axis. An advantage of having the ability to swivel is that the turbine can re-orientate so its swept area always faces the direction of flow, thereby maximising the energy extracted. In contrast, a fixed turbine cannot

swivel into the flow direction, potentially reducing the amount of energy extracted. For the purpose of model development the turbine was always assumed to be perpendicular to the flow but in the later optimisation model turbine orientation is fixed perpendicular to the predominant flow direction. The symbol  $\theta$  in equation (5.4) and (5.5) represents the angle the turbine makes with the positive y-axis.

## 5.2.2 Development of Model Architecture

Development of the energy extraction model involved extending the existing model architecture by amending existing subroutines and adding new subroutines to the original DIVAST model. Figure 5.2 shows a flow chart of the modified model architecture, illustrating all subroutines called in the main program and highlighting the sections developed for inclusion of energy extraction. Similar modifications were made to incorporate energy extraction in the MSN; this is illustrated in Figure 5.3.

As with the original DIVAST model described in Chapter 3, the main program consists of a number of subroutines, each with a different task, which are called as required. Subroutines 1 – 7 deal with input data, establishing integration sections and initialising variables. Subroutines 10 - 13 compute the x-direction hydrodynamics during the first half time-step, whilst the y-direction hydrodynamics are computed during the second half time-step in subroutines 14 – 17, each of these subroutines are executed for every time-step for the complete model simulation. Subroutines 18 and 19 recalculate the chezy and eddy parameters. Outputs are printed in subroutine 20. The sections of code that have been modified or added to incorporate energy extraction are listed in Table 5.1

The subroutine TURB\_DATA was added to read the input data relating to turbine modelling such as the turbine rotor diameter and turbine spacings (nested values are read in if required). This subroutine is executed once at the beginning of the model simulation.

The subroutine MARTURBINIT (and MARTURBINIT\_F in the nested model) was added to implement the energy extraction code. The purpose of this subroutine is to calculate the turbine(s) swept area, and identify the grid cells in which turbines are to be placed. The turbine thrust components,  $F_{Tx}$  and  $F_{Ty}$  of equations (5.4) and (5.5), used to simulate the effects of tidal turbines are calculated in subroutines HYDMODX and HYDMODY (and similarly HYDMODX\_F and HYDMODY\_F in the nested model) and subsequently incorporated in the momentum equations. These subroutines are executed at every time-step during the entire model simulation.

Two new sections of code were also added to the main program. The first utilises a method developed by the author to quantify energy extracted by the turbine(s) and is discussed in further detail in this chapter. The second is an optimisation algorithm which determines optimal turbine array configurations based on power availability and the hydrodynamic impacts of turbine deployment; this is discussed in Chapter 6.

| MAIN PROGRAM   |  |
|----------------|--|
| 1. FILINP      | •Opens input data file &   |
| 2. FILOUT      | •Opens file for data output  |
| 3. BOUND       | •Reads open boundary (OB) data                                     |
| 4. FIELD       | •Reads computational domain  |
| 5. FIND        | •Establishes the integration sections                              |
| 6. DEPTH       | •Reads water depths  |
| 7. INITL       | •Initialises depths, elevations, concentrations and chezy values   |
| 8. TURB_DATA   | •Reads input turbine data  |
| 9. MARTURBINIT | •Calculates turbine area and cells that modification is applied to |
| 10. HYDBND     | •Assigns hydrodynamic data at OB                                   |
| 11. HYDMODX    | •Solves hydrodynamics in x-direction                               |
| 12. SIDEH      | •Recalculates water depths   |
| 13. FLDRY      | •Checks for flooding and drying of cells                           |
| 14. HYDBND     | •Assigns hydrodynamic data at OB                                   |
| 15. HYDMODY    | •Solves hydrodynamics in y-direction                               |
| 16. SIDEH      | •Recalculates water depths   |
| 17. FLDRY      | •Checks for flooding and drying of cells                           |
| 18. CHEZY      | •Recalculates chezy values   |
| 19. EDDY       | •Recalculates eddy viscosities                                     |
| 20. PRINT      | •Outputs time series and snapshots                                 |

**Figure 5.2: Flowchart of coarse model subroutines, including the energy extraction code (subroutines which have been modified/ added to include energy extraction are shaded blue).**

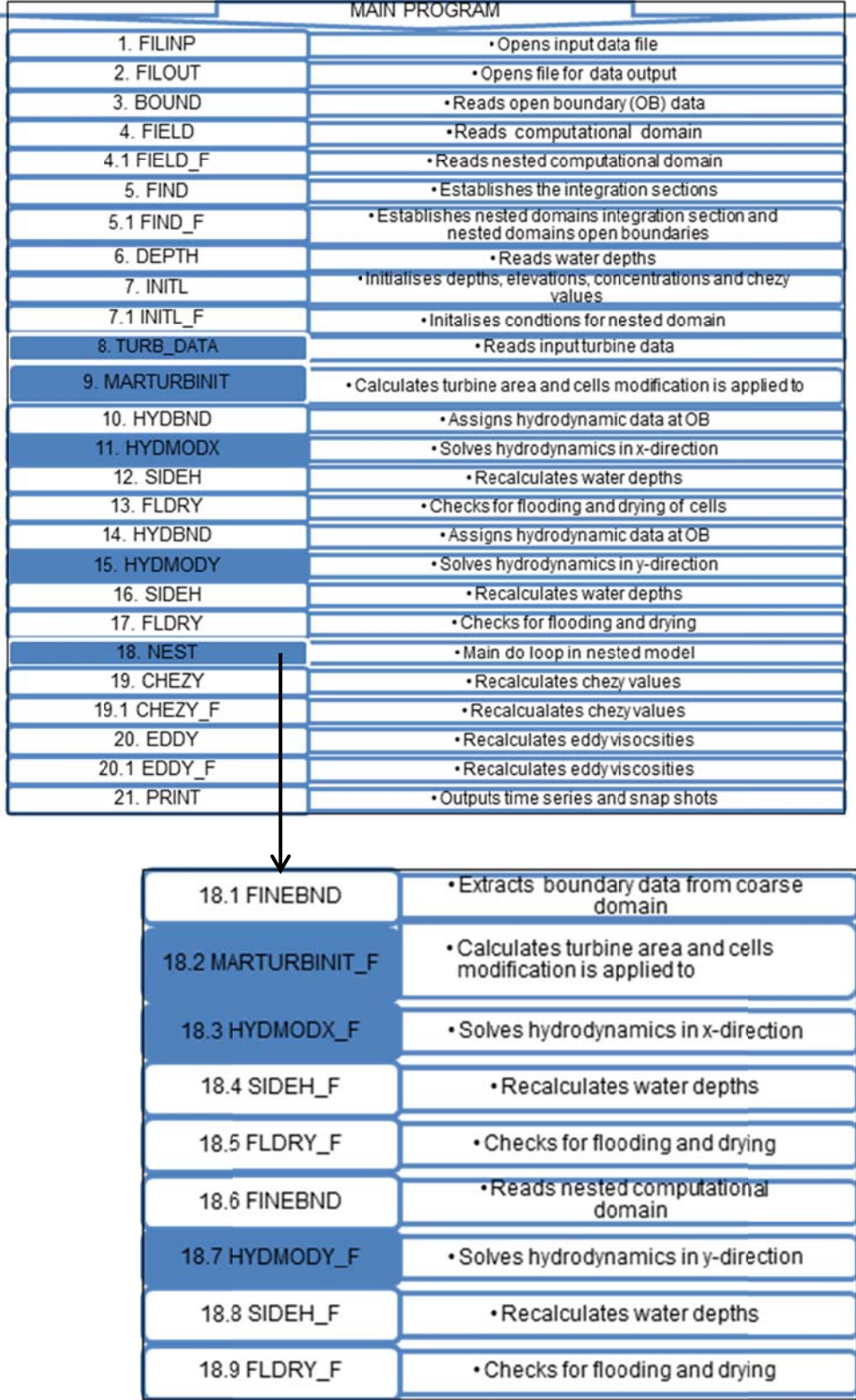


Figure 5.3: Flowchart of nested MSN model subroutines, including the energy extraction code (subroutines which have been modified/ added to include energy extraction are shaded blue).

**Table 5.1: Sections of code modified or added to incorporate tidal energy extraction.**

| <b>Program Section</b> | <b>Function and Modification</b>   |
|------------------------|--|
| <b>FILINP</b>          | Open input turbine data file   |
| <b>TURB_DATA</b>       | Read input turbine data  |
| <b>MARTURBINIT</b>     | Identify grid cell location of energy extraction and calculate turbine swept area in coarse domain                         |
| <b>HYDMODX</b>         | Calculation of turbine thrust and incorporation of momentum sink term into x-direction momentum equation in coarse domain  |
| <b>HYDMODY</b>         | Calculation of turbine thrust and incorporation of momentum sink term into y-direction momentum equation in coarse domain  |
| <b>MARTURBINIT_F</b>   | Identify grid cell location of energy extraction and calculate turbine swept area  |
| <b>HYDMODX_F</b>       | Calculation of turbine thrust and incorporation of momentum sink term into x-direction momentum equation in nested domains |
| <b>HYDMODY_F</b>       | Calculation of turbine thrust and incorporation of momentum sink term into y-direction momentum equation in nested domains |

### **5.2.3 Incorporation of Energy Extraction into Source Code**

The modified x -and y-direction momentum equations calculated in subroutines HYDMODX and HYDMODY (and similarity in HYDMODX\_F and HYDMODY\_F) are expressed in equation (5.6):

$$\begin{aligned}
 B_i^n = & (1)\text{depth averaged volumetric flux} - (2)\text{advective accelerations} \\
 & + (3)\text{Coriolis force} - (4)\text{bed shear resistance} - (5)\text{momentum sink} \\
 & + (6)\text{wind shear force} - (7)\text{pressure gradient} \\
 & + (8)\text{turbulence induced shear force}
 \end{aligned}
 \tag{5.6}$$

where  $B_i^n$  is the recursion term resulting from a combination of known variables from the partial difference x- and y-direction momentum equations (see Appendix A for derivation).

Table 5.2 lists the model representations of the parameters used in the energy extraction equation (5.6).

**Table 5.2: Model representation of energy extraction variables.**

| Variable   | Type                                       | Model representation |
|--|--|----------------------|
| $H$  | Depth (x-direction)                        | DEPX                 |
| $\Delta t$   | Time-step                                  | DT                   |
| $\Delta x$   | Grid spacing                               | DELX                 |
| $\zeta_{i,j}^{n+\frac{1}{2}}, \zeta_{i,j}^{n-}, \zeta_{i,j}^{n-\frac{1}{2}}$                               | Water elevation                            | EU, EM, EL           |
| $U_{i+\frac{1}{2},j}^n$  | Velocity (x-direction)                     | UM                   |
| $V_{i,j+\frac{1}{2}}^n$  | Velocity (y-direction)                     | VM                   |
| $q_x _{i+\frac{1}{2},j}^{n-\frac{1}{2}}, q_x _{i+\frac{1}{2},j}^n, q_x _{i+\frac{1}{2},j}^{n+\frac{1}{2}}$ | Volumetric flux (x-direction)              | QXL; QXM; QXU        |
| $q_y _{i,j+\frac{1}{2}}^{n-\frac{1}{2}}, q_y _{i,j+\frac{1}{2}}^n, q_y _{i,j+\frac{1}{2}}^{n+\frac{1}{2}}$ | Volumetric flux (y-direction)              | QYL; QYM; QYU        |
| $q_y _{i+\frac{1}{2},j}^n$   | Volumetric flux (averaged)(y-direction)    | QYMAV                |
| $f$  | Coriolis parameter                         | CORI                 |
| $g$  | Gravity                                    | GRAV                 |
| $C$  | Chezy coefficient                          | C                    |
| $f_i$  | Air-water interfacial friction coefficient | CRSURF               |
| $\rho_a$   | Density of air                             | DENAIR               |
| $\rho_w$   | Density of water                           | DENWAT               |
| $m/s$  | Wind speed                                 | WINSPD               |
| $\beta$  | Momentum correction factor                 | BETA                 |
| $V_e$  | Coefficient of eddy viscosity              | COED                 |
| $g^{1/2}$  | Square root of gravity                     | ROOTG                |
| $mm^2/s$   | Kinematic viscosity                        | VISCMM               |

The mathematical expressions and the corresponding model code representations for the terms in equation (5.6) are defined as follows in the x-direction (similar expressions are used for the y-direction):

(1) *Depth-averaged volumetric flux:*

$$q_x|_{i+\frac{1}{2},j}^{n-\frac{1}{2}} = QXL(I,J) = (U \cdot H) \text{ i.e. velocity} \cdot \text{water depth} \quad (5.7)$$

(2) *Advective accelerations*

$$\frac{\beta \Delta t}{\Delta x} \left[ U' q_x|_{i+1,j}^n - U' q_x|_{i,j}^n + U' q_y|_{i+\frac{1}{2},j+\frac{1}{2}}^n - U' q_y|_{i+\frac{1}{2},j-\frac{1}{2}}^n \right] = D2BETA \cdot (DUUHDX + DUVHDI) \quad (5.8)$$

$$\text{where } D2BETA = (BETA) \cdot (DT)/DELX \quad (5.9)$$

$$DUUHDX = U' q_x|_{i+1,j}^n - U' q_x|_{i,j}^n \quad (5.10)$$

$$= ([UM(I+1,J) + UM(I,J)]/2) \cdot ([QXM(I+1,J) + QXM(I,J)]/2) \\ - ([UM(I,J) + UM(I-1,J)]/2) \cdot ([QXM(I,J) + QXM(I-1,J)]/2)$$

$$DUVHDI = U' q_y|_{i+\frac{1}{2},j+\frac{1}{2}}^n - U' q_y|_{i+\frac{1}{2},j-\frac{1}{2}}^n \quad (5.11)$$

$$= ([UM(I,J) \cdot QXL(I,J)] - [UM(I,J) \cdot QXL(I,J-1)])/2$$

(3) *Coriolis force*

$$\Delta t f_y|_{i+\frac{1}{2},j}^n = + D3CORI \cdot QYMAV \quad (5.12)$$

$$\text{where } D3CORI = DT \cdot CORI \quad (5.13)$$

$$QYMAV = VMAV(I,J) \cdot DEPX(I,J)$$

$$VMAV(I,J) = [VM(I,J) + VM(I+1,J) + VM(I,J-1) + VM(I+1,J-1)]/4$$

(4) *Bed shear resistance*

$$- \frac{g \Delta t (q_x'^2 + q_y'^2)^{\frac{1}{2}}}{2(HC)^2} |_{i+\frac{1}{2},j}^n q_x'^{n-\frac{1}{2}} = - D4BDFR \cdot QYL(I,J) \quad (5.14)$$

where

$$D4BDFR = (D4) \cdot (DIVMAG) [(DEPX(I,J)) \cdot CHZVAL]^2 \quad (5.15)$$

$$D4 = ((DT) \cdot (GRAV)) / 2 \quad (5.16)$$

$$DIVMAG = [(QXM(I,J))^2 + QYMAV^2]^{1/2} \quad (5.17)$$

$$CHZVAL = (C(I,J) + C(IP1,J)) / 2 \quad (5.18)$$

(5) *Momentum sink*

$$-\frac{0.5 \Delta t C_T (NA_T) \left( U'_{i+\frac{1}{2},j} \right)^2}{\text{Delx}^2} \left( \frac{|U'_{i+\frac{1}{2},j}|}{U'_{i+\frac{1}{2},j}} \right) = -D3MARTURB \quad (5.19)$$

(6) *Wind shear force*

$$+ \frac{\rho_a \Delta t C^* W_x (W_x^2 + W_y^2)^{\frac{1}{2}}}{\rho} = +WSTRESS \quad (5.20)$$

where

$$WSTRESS = D3WINC \cdot WINVX \quad (5.21)$$

$$D3WINC = DT \cdot WINCON \quad (5.22)$$

$$WINCON = CFSURF \cdot DENRAT \cdot WINSPD \quad (5.23)$$

$$DENRAT = DENAIR / DENWAT \quad (5.24)$$

$$CFSURF = 1.25 \times 10^{-3} / WINSPD^{1/5} \quad \text{FOR } (WINSPD < 1.0) \quad (5.25)$$

$$CFSURF = 0.5 \times 10^{-3} / WINSPD^{1/2} \quad \text{FOR } (1.0 \leq WINSPD \leq 15.0) \quad (5.26)$$

$$CFSURF = 2.6 \times 10^{-3} \quad \text{FOR } (WINSPD \geq 15.0) \quad (5.27)$$

(7) *Pressure gradient*

$$-\frac{g \Delta t}{2 \Delta x} H_{i+\frac{1}{2},j}^n \left[ \zeta_{i+1,j}^{n-\frac{1}{2}} - \zeta_{i,j}^{n-\frac{1}{2}} \right] = -D1DPC \cdot [EU(I+1,J) + EL(I+1,J) - EU(I,J) - EL(I,J)] \quad (5.28)$$

where

$$D1DPC = D1 \cdot DEPX(I,J) \quad (5.29)$$

$$D1 = DT/2 \cdot GRAV/DELX \quad (5.30)$$

(8) *Turbulence induced shear force*

$$+ \frac{\Delta t}{\Delta x^2} \varepsilon H_{i+\frac{1}{2},j}^n \left[ \begin{array}{l} 2 \left( U'_{i+\frac{3}{2},j} + U'_{i-\frac{1}{2},j} \right) + U'_{i+\frac{1}{2},j+1} + U'_{i+\frac{1}{2},j-1} - 6U'_{i+\frac{1}{2},j} - V_{i,j+\frac{1}{2}} \\ + V_{i,j-\frac{1}{2}} - V_{i+1,j-\frac{1}{2}} + V_{i+1,j+\frac{1}{2}} \end{array} \right] \quad (5.31)$$

$$= + D5 \cdot EDDVAL \cdot \{ UM(I+1,J) + UM(I-1,J) \\ + UM(I,J+1) + UM(I,J-1) - 4 \cdot UM(I,J) \} \quad (5.32)$$

where

$$D5 = DT/DELX^2 \quad (5.33)$$

$$EDDVAL = EDDYH(I,J) + EDDYH(I+1,J)/2 \quad (5.34)$$

$$EDDYH(I,J) = [(((COEDRG) \cdot (QMAG))/C(I,J)) + VISLAM] \cdot DEPCEN \quad (5.35)$$

$$COEDRG = (COED) \cdot (ROOTG) \quad (5.36)$$

$$QMAG = (VELMAG) \cdot (DEPCEN) \quad (5.37)$$

$$VELMAG = (UCEN^2 + VCEN^2)^{1/2} \quad (5.38)$$

$$UCEN = (UM(I,J) + UM(IM1,J))/2; VCEN = (VM(I,J) + VM(I,JM1))/2 \quad (5.39)$$

$$DEPCEN = HCEN(I,J) + EU(I,J) \quad (5.40)$$

$$VISLAM = VISCMM \times 10^{-6} \quad (5.41)$$

The turbine thrust momentum sink term is included in the momentum equations as term 5 and defined in the model source code as D3MARTURB (see equation (5.19)). D3MARTURB is expressed in subroutine HYDMODX (and similarly in HYDMODY, HYDMODX\_F, HYDMODY\_F) as follows:

$$D3MARTURB = \frac{(0.5 \cdot (D3 \cdot THRUSTC \cdot (N(I, J) \cdot TURBAREA) \cdot (VELMAG)^2))}{DELX^2} \cdot UMSIGN \quad (5.42)$$

where:

- *D3* is the model time step,  $\Delta t$
- *THRUSTC* is the localised turbine thrust coefficient,  $C'_T$ , which can be user-specified in the input data file, or calculated in the main program.  $C'_T$  is a new parameter defined during this research and is dependent on the model set-up.  $C'_T$  is discussed in further detail in the next section.
- $N(I, J)$  is the number of turbines present in a grid cell (I, J)
- *TURBAREA* is the swept area of a single turbine
- *VELMAG* is the magnitude of the current velocity,  $U'_{i+\frac{1}{2}, j}$ , at the middle time step at the I, J grid cell and is calculated as follows:

$$U'_{i+\frac{1}{2}, j} = \frac{q_{x, i+\frac{1}{2}, j}^n}{H} \quad (5.43)$$

where  $q_{x, i+\frac{1}{2}, j}^n$  is the volumetric flux and  $H$  is the water depth.

- *DELX* is the model grid spacing
- *UMSIGN* accounts the direction of flow and is equal to  $U / |U|$

The input data file and source code required to read it were amended to incorporate input data relating to tidal energy extraction. The additional input parameters are:

- *NFLTURB*: Flag for including (or excluding) turbine deployment calculations ( 1 = yes, 0 = no)
- *TURBDIAM*: Diameter of turbines being simulated
- *THRUSTC*: default turbine thrust coefficient
- Turbine Locations: included by editing the land-sea mask which uses 1's and 0's to identify wet and dry cells,

respectively. The '1' values of wet cells in which turbines are to be deployed are changed to a '7'.

It should be noted that both THRUSTC and the land-sea map to indicate turbine deployment can also be set within the model source code; this is discussed later in this chapter.

### **5.3 Thrust and Power Calculation**

Once the model code had been modified to simulate tidal energy extraction the next step was to assess the accuracy of the momentum sink approach and determine a means of quantifying the power output from a modelled turbine or array.

#### **5.3.1 Turbine Thrust Coefficient**

The amount of power extracted from a current flow is determined by the turbine thrust, which is in turn dependent on the thrust coefficient,  $C_T$  (as per equation (5.1)).  $C_T$  will vary with changes in velocity, however in far-field hydrodynamic models where a momentum sink approach is used to include the turbine thrust a constant  $C_T$  value - close to 1- is commonly used. This value is based on the relationship between turbine thrust and undisturbed free-stream flow as defined in equation (5.1). In far-field models the physical structure of the turbine is not modelled and it is therefore not possible to directly calculate  $C_T$ . A challenge in applying the momentum sink approach to turbine modelling in a hydrodynamic model is selecting suitable values of  $u$  and/or  $C_T$ . Tidal energy extraction will alter the water body's hydrodynamics, making it difficult to identify the location of free-stream flow. In modelling studies based on the momentum sink approach, challenges in identifying the location and magnitude of the upstream undisturbed velocity has meant the thrust has generally been calculated using the localised velocity at the turbine grid cell ( $u_t$ ) as follows:

$$T = \frac{1}{2} \rho u_t^2 A_T C_T \quad (5.44)$$

Since  $u_t$  will be lower than  $u$  as a result of the turbine's inclusion via the momentum sink, using  $C_T$  values in the range of 0.8-1.0 which are based on calculation of thrust using  $u$  will result in underestimation of the thrust.

Adopting a  $C_T$  value which is based on the undisturbed upstream velocity may be suitable for low resolution models where the grid cell spacing is much larger than the turbine. In such applications, the reduced local turbine velocity may not be too dissimilar to the undisturbed velocity. The problem becomes more significant as one uses finer spatial resolutions since the local velocity will then be significantly reduced from the undisturbed velocity. It can even be a problem for low resolution models where multiple turbines are located in the same grid cell.

In this research, a localised thrust coefficient,  $C'_T$ , is introduced which can be used in combination with the velocity at the turbine,  $u_t$ , to calculate the turbine thrust as follows:

$$T = \frac{1}{2} \rho u_t^2 A_T C'_T \quad (5.45)$$

This was expected to result in more accurate representation of power extraction, particularly at finer spatial resolutions.

### 5.3.2 Power Output

The power available from a tidal flow has previously been defined as:

$$P_{ava} = 0.5 \rho A_T u^3 \quad (5.46)$$

Equation (5.46) determines the total available resource; however, in practice, energy losses and physical limits mean that a tidal turbine can only convert a fraction of the total available energy into useable

power. The proportion of the available resource that a turbine can extract is dependent on the turbine power coefficient,  $C_P$ , which is a measure of the efficiency with which the turbine converts available tidal stream power into usable electrical power. The theoretical extracted power can therefore be calculated as:

$$P_{E(th)} = 0.5 \rho A_T u^3 C_P \quad (5.47)$$

Applying LMADT to a tidal turbine placed in an infinite medium, one can determine the theoretical maximum  $C_P$  of 0.59, which is known as the Betz limit. However, due to mechanical losses this theoretical value will be reduced. Experimental tests of scaled horizontal-axis turbines by Bahaj et al. (2007) determined a maximum  $C_P$  of 0.46, whilst the SeaGen turbine has a  $C_P$  of 0.48 (Renewable Energy Focus, 2017). These are maximum values but  $C_P$  will change over a tidal cycle as velocity and  $C_T$  changes. In this research  $C_T$  is assumed to be constant over a tidal cycle, therefore a slightly lower turbine efficiency of  $C_P = 0.4$  has been adopted to reflect a tidal average. Turbines of varying performance can be simulated in the model by selecting a desired  $C_P$  and tuning  $C_T$  accordingly.

In this research,  $P_{E(th)}$  represents the power one would expect a turbine to extract from the available resource, based on a turbine  $C_P$  of 0.4. The free-stream velocity value is taken as the velocity at the proposed turbine location without the turbine being present.

In this research a methodology was developed to quantify the modelled extracted power by a turbine, denoted  $P_{E(mod)}$ .  $P_{E(mod)}$  is calculated as follows:

$$P_{E(mod)} = T \cdot u_t \quad (5.48)$$

where  $u_t$  is the velocity at the turbine grid cell and  $T$  is calculated according to equation (5.45).

As the modelled turbines are intended to have a  $C_p$  of 0.4, appropriate values for the localised thrust coefficient can be found through satisfaction of the following condition:

$$P_{E(\text{mod})} = P_{E(\text{th})} \quad (5.49)$$

#### **5.4 Model Application: Idealised Domain**

This research was particularly interested in determining appropriate  $C_T$  values for higher spatially-resolved grids, at scales similar to the physical dimensions of the tidal turbines. Using the developed energy extraction model, an idealised channel was used to investigate the sensitivity of model predictions of energy extraction and resulting hydrodynamic impacts to specification of the thrust coefficient. Appropriate localised thrust coefficients were determined for different model resolutions and water depths based on the desired turbine  $C_p$  of 0.4.

##### **5.4.1 Model Set-up**

Assessment of the validity of adopting a  $C_T$  value in the range 0.8-1.0 when determining thrust based on the local turbine velocity was conducted using an idealised channel model.

A 4km long x 1.6km wide model domain was subjected to tidal flows. The model was set-up for initial assessment with a spatial resolution of 16m x 16m resulting in a computational domain of 250 x 100 grid cells. A resolution of 16m was employed to match the rotor diameter of the utility scale SeaGen turbine (Fraenkel, 2007). The western and eastern sea boundaries were specified as tidal elevation boundaries, with an idealised repeating tide of 8m amplitude, whilst this tidal amplitude is quite large it was necessary to produce peak velocities in the turbine operating range.

A 6.25 hour period was specified at the open sea boundaries. Although a typical diurnal tidal cycle period is approximately equal to

12.5 hours, a 6.25 hour period was selected to speed up the model runs. A phase difference of 10 minutes was specified between the two tidal boundaries to induce larger tidal currents of the order of 2m/s peak velocity. The northern and southern boundaries were set as land. A constant water depth of 50m was specified across the channel and fluid density was set at 1026kg/m<sup>3</sup>. The peak flow speeds reached approximately 2.0m/s. Simulations were conducted with a single turbine deployed in the centre of the channel. The model was executed for a simulation period of 50 hours (8 tidal cycles) with a half time-step of 2.5 seconds and a Chezy bed roughness of 200mm. Model results were analysed for the last tidal cycle.

#### 5.4.2 Model Sensitivity to the Thrust Coefficient

To investigate the sensitivity of the energy extraction model to  $C_T$  a number of different model scenarios were assessed. In addition to model runs with typical  $C_T$  values of 0.8 and 1, runs with values ranging from  $1.0 \leq C_T \leq 3.0$  were also conducted. A single turbine with 16m rotor diameter was modelled in all runs. For all model scenarios the results of the final tidal cycle were used to compare the extracted power and changes in current velocity.

Figure 5.4(a) shows a comparison of modelled extracted power with the expected theoretical extracted power calculated using a  $C_P$  of 0.4. As expected Figure 5.4(a) shows that the modelled extracted power ( $P_{E(mod)}$ ) is quite sensitive to the  $C_T$  value and that more power is extracted as  $C_T$  is increased. A  $C_T$  value of 1 can be seen to underestimate the extracted power relative to the theoretical value ( $P_{E(th)}$ ). For this particular model setup a value of  $C_T = 1.3$  gives closest agreement between modelled and theoretical extracted powers and is therefore deemed the optimum value for this case.

Figure 5.4(b) compares current velocities at the turbine grid cell for a no turbine scenario (NT) and each turbine scenario. Significant

changes in hydrodynamics were found for different  $C_T$  values, and thus different levels of power extraction. For instance; reductions in peak current velocities of approximately 4.2%, 4.7% and 5.2% occurred for  $C_T$  specifications of 0.8, 0.9 and 1.0, respectively. Selecting  $C_T=3.0$  resulted in a higher impact, with a reduction in peak currents of 13.6% relative to the no turbine case. This connection between the magnitude of power extracted and associated hydrodynamic impacts is to be expected, and highlights the importance of specification of an appropriate  $C_T$  value.

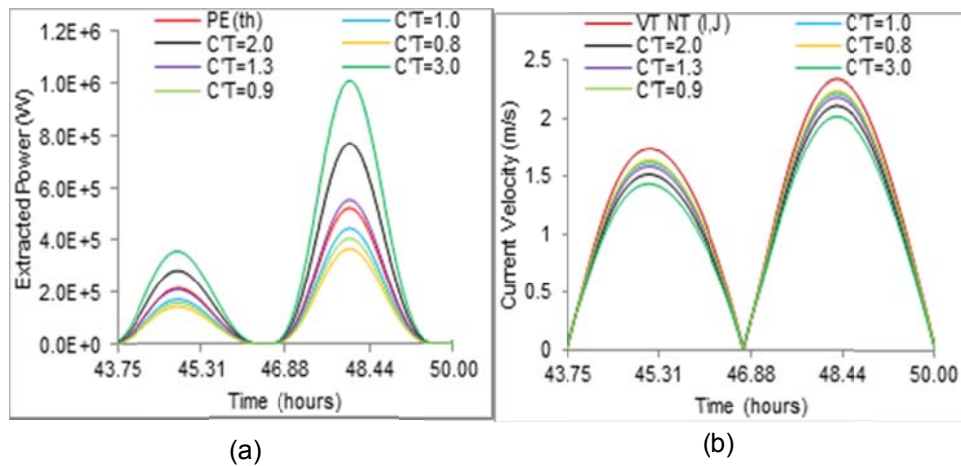


**Figure 5.4: (a) Comparison of  $P_{E(th)}$  to  $P_{E(mod)}$  for each model scenario, (b) comparison of total current velocities at turbine grid cell (I, J).**

Assessment of the far-field hydrodynamic impacts involved calculating the percentage different in peak-ebb velocities for the single turbine scenario relative to the no turbine case, i.e.  $\%Diff = ((V_{turb} - V_{no\ turb})/V_{no\ turb}) \cdot 100\%$ , Results (presented in Figure 5.5) indicate that the far-field impacts are strongly affected by  $C_T$  specification, with both the extent of the wake and the magnitude of the velocity deficits increasing considerably with increasing  $C_T$ , further stressing the importance of identifying optimal  $C_T$  values.

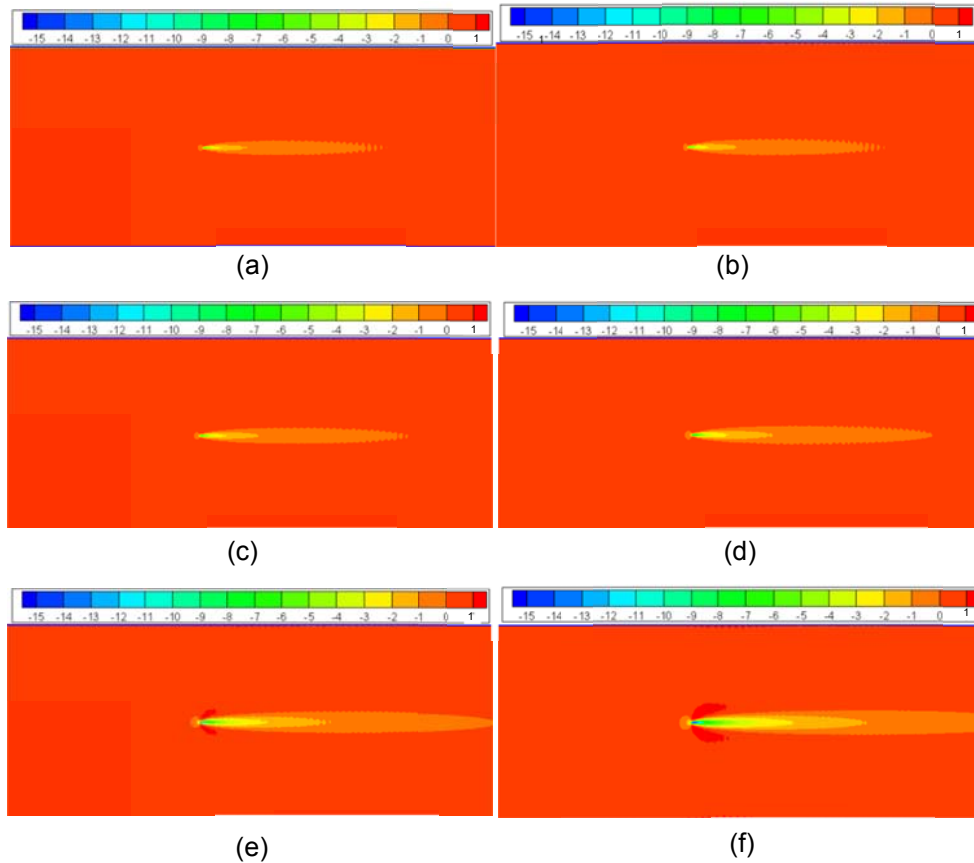


**Figure 5.5: Percentage differences in peak velocities for a single turbine scenario relative to a no turbine scenario using  $C_T$  values of (a) 0.8, (b) 0.9, (c) 1.0, (d) 1.3, (e) 2.0, (f) 3.0.**

Changes in velocities along the longitudinal wake centreline for each  $C_T$  value are shown in Figure 5.6. Adopting the commonly-used value of  $C_T = 1.0$  resulted in peak reductions in current velocities of approximately 7%, whilst the optimum  $C_T$  value of 1.3 results in a velocity deficit of 9%. Further increasing  $C_T$  to 2.0 increases velocity deficit to 13%, whilst the higher  $C_T$  value of 3.0 results in a deficit of approximately 18%.

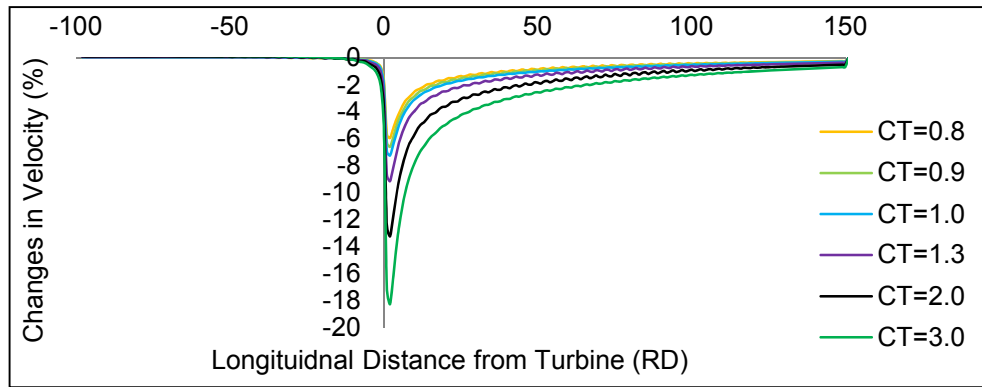


**Figure 5.6: Changes in current speed (%) along the longitudinal wake centreline for a range of  $C_T$  values.**

As a final summary of the analysis, Table 5.3 lists the peak power output, modelled power extraction efficiency,  $\varepsilon$  (ratio of  $P_{E(mod)}$  to  $P_{ava}$ ) and peak % change in velocity for all of the modelled energy extraction cases ( $C_T = 0.8, 1.0, 1.3$  and  $3.0$ ).  $P_{E(th)}$  and the power coefficient for the turbine are also given for comparison. It can be seen that for the optimum value of  $C_T = 1.3$ ,  $P_{E(mod)} = P_{E(th)}$  and  $\varepsilon = C_P$ .

**Table 5.3: Peak power output (MW) and velocity deficit at turbine (%) determined for varying  $C_T$  specifications.**

| $C_T$       | Peak Power (MW) | $\varepsilon$ | Velocity Deficit at Turbine (%) |
|-------------|-----------------|---------------|---------------------------------|
| 0.8         | 0.38            | 0.28          | 5.5                             |
| 1.0         | 0.46            | 0.33          | 7                               |
| 1.3         | 0.55            | 0.40          | 9                               |
| 3.0         | 1.02            | 0.74          | 18                              |
| Theoretical | 0.55            | 0.40          | 9                               |

This initial analysis was undertaken to assess the accuracy of modelled extracted power when  $C_T = 0.8-1.0$  is used in a high resolution model. Results showed that using such  $C_T$  values result in under-prediction of extracted power and that more accurate

predictions of extracted power are achieved when a value  $>1$  is employed. This is in line with the findings of Housby et al. (2008) who recommended a thrust coefficient of 2.0 based on localised velocity. This is logical when the thrust is being calculated with a local turbine velocity that is lower than the free-stream velocity (due to energy extraction). It was therefore concluded that accurate calculation of the turbine thrust whilst using the local turbine velocity requires the use of a 'localised thrust', henceforth termed  $C'_T$ . For the particular operating condition modelled here, the optimum value determined for  $C'_T$  was 1.3.

### 5.4.3 Operating Conditions

Further analysis was undertaken to determine optimum  $C'_T$  values for different operating conditions based on a desired turbine  $C_p = 0.4$ . The 4km x 1.6km model domain was employed keeping the same boundary conditions. A total of 40 model scenarios were simulated, with grid spacings ranging from 16m to 100m and mean water depth varying from 30m to 100m, for a run time of 50.0 hours. A turbine diameter of 16m was again selected. Model time-step, bed roughness and fluid density were unchanged from the initial scenario runs of the previous section. Analysis of the resulting impact on power output and current velocities was carried out to determine appropriate  $C'_T$  values for each of the 40 scenarios. The optimum  $C'_T$  values were determined by comparing  $P_{E(th)}$  and  $P_{E(mod)}$ . Details of each model set-up and the resulting optimum  $C'_T$  values are tabulated in Table 5.4.

Results from each model run were combined to produce a thrust sensitivity chart (Figure 5.7) from which the optimum  $C'_T$  value for a modelled site of any depth and grid spacing ( $\Delta x$ ) within the range can be determined. The results were also related to the turbine grid cell blockage ratio (i.e. the fraction of the channel occupied by the

turbines calculated as the ratio of the swept area of turbine to the cross-sectional area of the grid cell containing the turbine) (see Figure 5.8). The best-fit trend line for all data points was a polynomial one with  $R^2$  values of 0.98. This relationship can then be applied to determine optimum  $C'_T$  values for model scenarios in which the grid resolution or water depths fall outside of those modelled.

**Table 5.4: Model details and optimum  $C'_T$  values.**

|           |     | Grid Spacing ( $\Delta x$ ) (m) |      |      |      |      |      |      |      |
|-----------|-----|---------------------------------|------|------|------|------|------|------|------|
|           |     | 16                              | 20   | 25   | 35   | 40   | 50   | 80   | 100  |
| Depth (m) | 30  | 1.63                            | 1.40 | 1.30 | 1.20 | 1.18 | 1.14 | 1.08 | 1.07 |
|           | 40  | 1.40                            | 1.26 | 1.20 | 1.15 | 1.13 | 1.10 | 1.06 | 1.05 |
|           | 50  | 1.30                            | 1.20 | 1.15 | 1.12 | 1.10 | 1.08 | 1.05 | 1.04 |
|           | 70  | 1.19                            | 1.14 | 1.10 | 1.08 | 1.07 | 1.05 | 1.03 | 1.02 |
|           | 100 | 1.10                            | 1.09 | 1.07 | 1.05 | 1.04 | 1.03 | 1.02 | 1.01 |

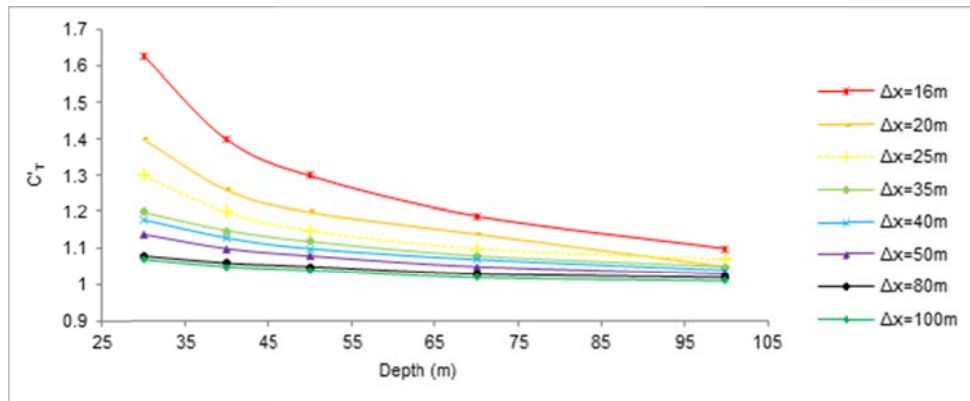


**Figure 5.7: Thrust sensitivity chart.**

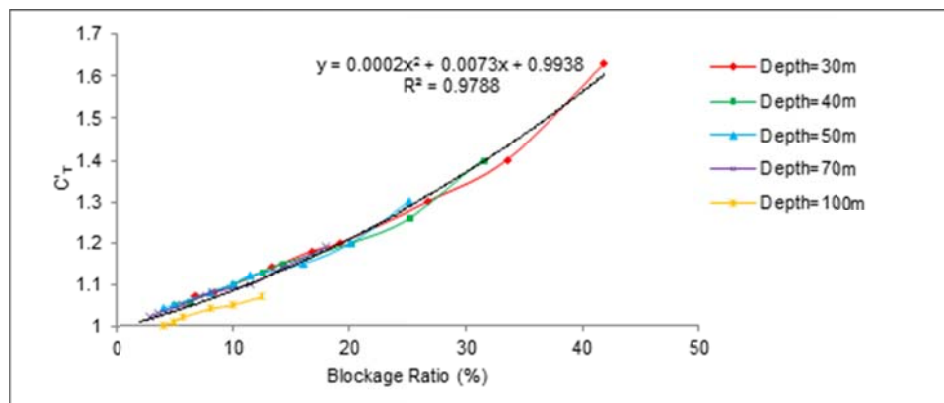


**Figure 5.8: Relationship of thrust sensitivity to grid cell blockage ratio.**

Results show that appropriate specification of  $C'_T$  is highly affected by the model set-up, with optimum values varying considerably for each model scenario.  $C'_T$  decreases with increasing water depth; this is a result of velocity deficits. Deployment of a turbine in deeper water will have a reduced impact on depth-averaged current velocities than deployment of the same turbine in shallower water, therefore the resulting velocities in deeper waters are closer to free-stream velocities; hence, the optimum  $C'_T$  will be closer to the typical  $C_T$  range of 0.8-1.0). For shallower waters, in order to maintain the desired turbine efficiency, in this case of 40%, a higher  $C'_T$  value is required.

$C'_T$  decreases with increasing grid spacing. As  $\Delta x$  is increased the same level of power extraction will result in smaller velocity deficits compared to model set-ups of smaller  $\Delta x$ ; hence, for coarser resolution models the velocity at the turbine site becomes closer to free-stream velocity, resulting in a lower  $C'_T$  compared to higher resolution models.

The resulting power output and impact on the along-stream current velocity component, denoted  $V_m$ , are shown for two different model set-ups in Figure 5.9 and Figure 5.10. Extraction of peak levels of power (0.55MW) resulted in a change in peak velocities of approximately 7%. The average percentage differences in  $P_{E(mod)}$  relative to  $P_{E(th)}$  over a full tidal cycle (calculated at each time-step as  $\%Diff = ((P_{E(TH)} - P_{E(Mod)}) / P_{E(TH)}) \cdot 100\%$ ), are presented for each model scenario in Table 5.5. Results show minimal difference ( $\leq 1\%$ ) between power outputs, demonstrating that the selected  $C'_T$  values are appropriate. Similar results were found for all the modelled scenarios depicted in Table 5.4.

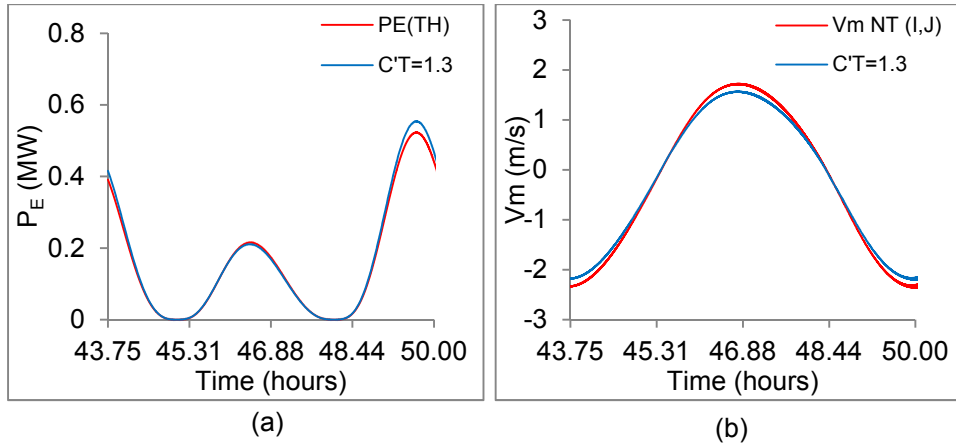


**Figure 5.9: (a) Comparison of  $P_{E(th)}$  and  $P_{E(mod)}$ , (b) impact of turbine deployment on  $V_m$  for a single turbine model scenario of grid spacing 16m and depth 50m.**

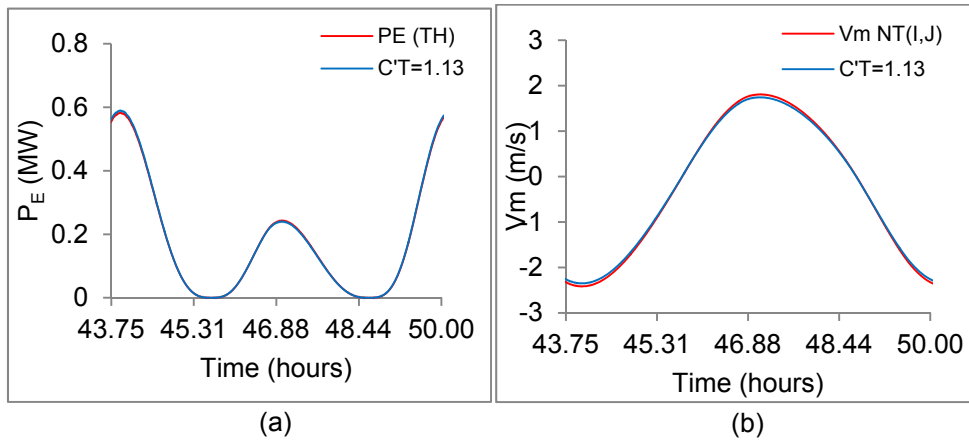


**Figure 5.10: (a) Comparison of  $P_{E(th)}$  and  $P_{E(mod)}$ , (b) impact of turbine deployment on  $V_m$  for a single turbine model scenario of grid spacing 40m and depth 40m.**

**Table 5.5: Resulting relative percentage differences (%) in  $P_{E(th)}$  and  $P_{E(mod)}$  estimates determined over 1 tidal cycle for each model scenario.**

|           |     | Grid Spacing (m) |       |       |       |       |       |       |       |
|-----------|-----|------------------|-------|-------|-------|-------|-------|-------|-------|
|           |     | 16               | 20    | 25    | 35    | 40    | 50    | 80    | 100   |
| Depth (m) | 30  | -1.05            | -0.10 | -0.05 | -0.05 | 1.16  | 1.06  | 0.24  | 1.02  |
|           | 40  | -0.57            | -0.42 | -0.52 | -0.52 | 0.82  | 0.49  | 0.34  | 0.46  |
|           | 50  | 0.51             | 0.22  | -0.54 | -0.54 | 0.53  | 0.50  | 0.59  | 0.44  |
|           | 70  | 1.11             | 1.12  | -0.28 | -0.28 | 0.64  | -0.05 | -0.19 | -0.30 |
|           | 100 | -0.15            | -0.13 | 0.37  | 0.37  | -0.22 | -0.46 | -0.16 | -0.72 |

#### 5.4.4 Model Validation

In an attempt to validate the changes in velocity due to energy extraction, longitudinal velocity deficits ( $1-u/u$ ) downstream of the turbine were calculated and compared with the experimental measurements of Stallard et al. (2013) who recorded velocity deficits due to a single scale model turbine. The mean water depth of the author's model set-up was reduced to 30m, to give a grid cell blockage ratio of 0.42, which was similar to the blockage ratio 0.47 of Stallard et al. (2013). The deficits recorded by Stallard et al. (2013) were measured along the turbine centreline. To allow comparisons with the modelled deficits, the measured data were depth-averaged. As mean water depth was reduced from 50m to 30m, a new optimum  $C'_T$  of 1.05 was determined. For comparison of results based on an optimum localised thrust and a value typically adopted in far-field studies the model was also run for  $C'_T=0.9$ . Figure 5.11 compares the resulting velocity deficits for the two  $C'_T$  values with the depth-averaged experimental results of Stallard et al. (2013). Due to factors such as the relative crudeness of the momentum sink approach (compared to higher fidelity approaches such as BEM) and the spatial resolution, one would not expect the model be able to reproduce the highest deficits in the turbine near-field (0-4RD). However, there is relatively good agreement between the measured observations and the author's model results from 5RD downstream which validates the momentum sink approach. It can also be seen that the velocity deficits based on  $C'_T = 0.9$  are lower than results based on the optimum  $C'_T$  run and the experimental data, which provides confirmation that the  $C'_T$  specification improves the model performance. Finally, it should be noted that the power coefficient of Stallard's scaled turbine was not reported and one would not therefore expect complete agreement between the modelled and measured data.

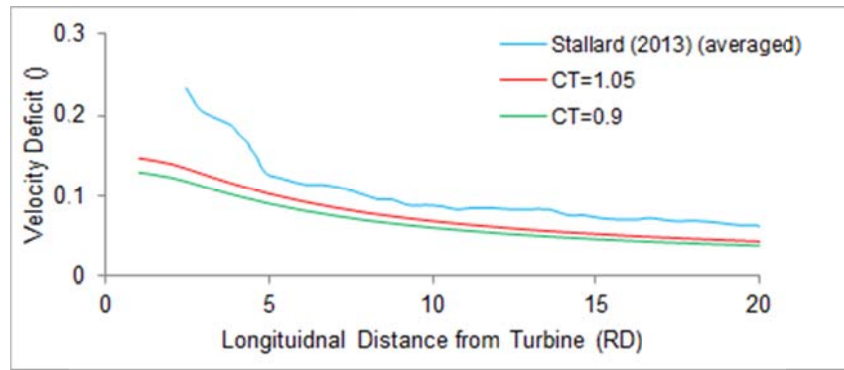


Figure 5.11: Velocity deficits due to a single turbine.

## 5.5 Case Study of the Shannon Estuary

After testing and validation of the energy extraction model in an idealised domain, it was then applied to the Shannon estuary case study site to demonstrate its applicability to real environments and to highlight the differences in predictions of energy capture and resulting hydrodynamic impacts when typical  $C_T$  and optimum  $C'_T$  values are employed.

### 5.5.1 Hydrodynamic Numerical Model

The numerical model used for this assessment is the 2D multi-scale nested model (MSN) described in Chapter 3.

Two levels of one-way nesting are applied to the Shannon estuary model to simulate the effects of tidal energy extraction at varying spatial resolutions. Details of the nested model are given in Section 3.6.

### 5.5.2 Model Details

The coarse model of the Shannon estuary is the same as that used for the resource assessment in Chapter 4 and has a spatial resolution of 189m x 189m, resulting in a computational domain of 507 x 217 grid cells in the x- and y- directions, respectively (see Figure 5.12). A 3:1 spatial nesting ratio was employed for two levels of nesting, resulting in fine grid spatial resolutions of 63m x 63m and

21m x 21m. To recap from Chapter 4, for the coarse grid model, flow boundaries were specified at the north-eastern river boundaries for the Shannon (east) and Fergus (north), and at the northern and southern open sea boundaries. Tidal elevations were specified along the western open sea boundary (see Figure 5.12) and the tidal period was set to 12.5 hours. The model was run for a typical spring-neap tidal cycle with tidal amplitudes of 2.325m and 1.125m for spring and neap tides, respectively. Further details of the model parameters are presented in Table 5.6.

**Table 5.6: Principal Model Parameters.**

| Model | Grid   | Grid Spacing (m) | No Cells (x-direction) | No Cells (y-direction) | Time -step (s) | Bed Roughness (mm) | Eddy Viscosity Coeff. |
|-------|--------|------------------|------------------------|------------------------|----------------|--------------------|-----------------------|
| CG189 | Parent | 189              | 507                    | 217                    | 36             | 50                 | 0.1                   |
| NG63  | Child  | 63               | 1521                   | 651                    | 12             | 50                 | 0.1                   |
| NG21  | Child  | 21               | 4563                   | 1953                   | 4              | 50                 | 0.1                   |

### 5.5.3 Model Validation

The Shannon estuary model has been validated against measured tidal elevations and current velocities at locations T1-T6 and C1-C2 (shown in Figure 5.12). The performance of the coarse (CG189) model was assessed in Chapter 4. Good correlation between measured and modelled tidal elevations and current velocities was achieved. The accuracy of the model in relation to depth-averaged current velocities at location C1 is shown in Figure 5.13. Modelled and measured data are seen to be in close agreement. The nesting technique was found to improve model accuracy at C1, correlation values of  $R^2 = 0.92$  and  $0.93$  were attained for spring tides for models CG189 and NG63 respectively, indicating the fine resolution model solution is closer to measured values than the coarser resolution model.

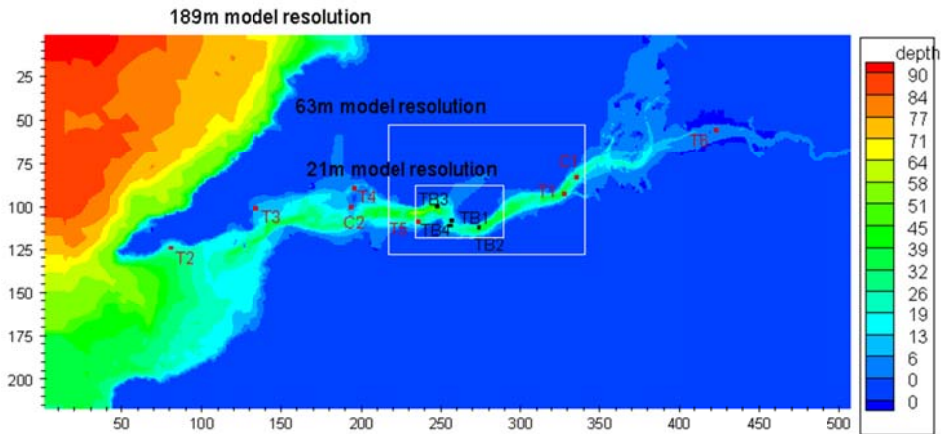


**Figure 5.12: Extent of domains, mean water depths and turbine locations (denoted TB) for Shannon model.**

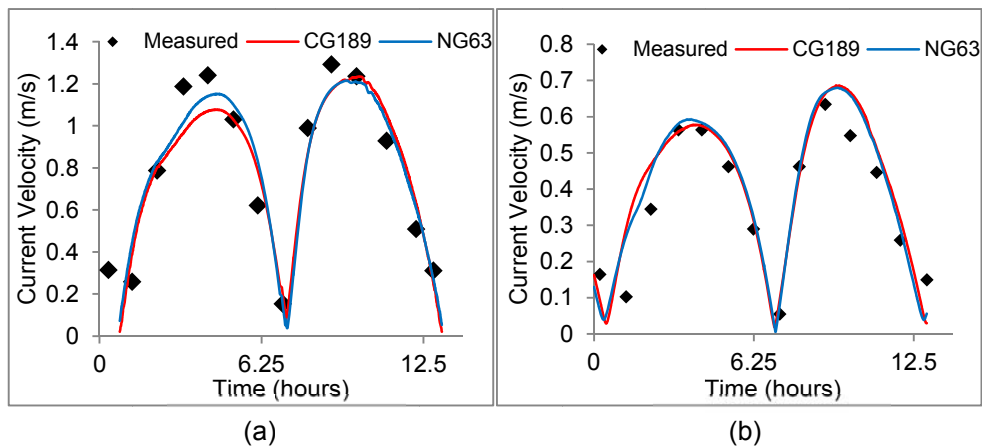


**Figure 5.13: Comparison of (a) spring (b) neap measured and modelled current velocities at C1 (Source: Fallon et al. (2014)).**

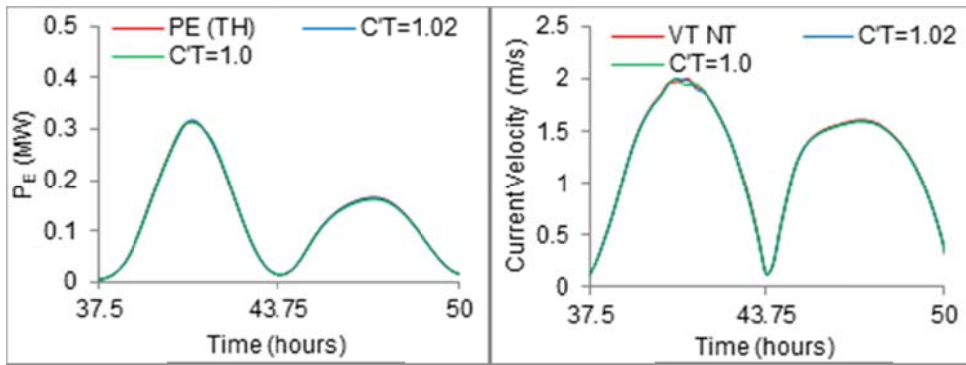
#### 5.5.4 Impact of $C'_T$ Specification on Energy Capture

To validate the  $C'_T$  approach developed in Section 5.4, four 16m diameter turbines were deployed within the Shannon estuary model in locations of different water depths (see Figure 5.12 – turbines denoted TB1-4). The simulated turbines were assumed to have  $C_p$  of 0.4. The turbines were simulated in the coarse model domain and the two nested domains with appropriate  $C'_T$  values specified for each turbine using the thrust sensitivity chart (Figure 5.7). Where the grid resolution exceeded the chart's limits (e.g. for the coarse 189m model) the optimal  $C'_T$  value was determined using the best-fit relationship developed between  $C'_T$  and the turbine grid cell blockage

ratio (see Figure 5.8). The details of the simulated turbine operating conditions are summarised in Table 5.7. Each modelled scenario was also run for  $C'_T=1.0$ , to compare with the more common far-field approach for specification of the thrust coefficient. The resulting energy capture and change in current velocities were compared. The results for each turbine are presented in Figure 5.14 - Figure 5.17. The key findings from the study are summarised in Table 5.8.

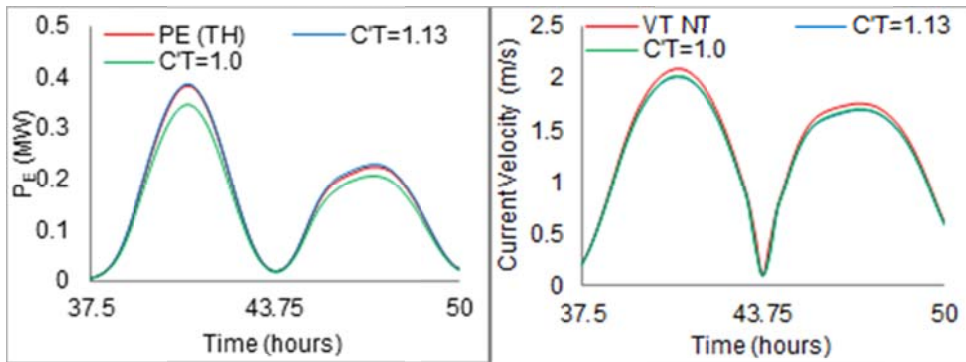
**Table 5.7: Individual Model Parameters**

| Turbine Number | Water Depth (m) | Spatial Resolution (m) | Turbine Grid Cell Blockage Ratio | $C'_T$ |
|----------------|-----------------|------------------------|----------------------------------|--------|
| 1              | 25.2            | 189                    | 0.04                             | 1.02   |
|                |                 | 63                     | 0.13                             | 1.13   |
|                |                 | 21                     | 0.38                             | 1.51   |
| 2              | 35.5            | 189                    | 0.03                             | 1.01   |
|                |                 | 63                     | 0.09                             | 1.08   |
|                |                 | 21                     | 0.27                             | 1.33   |
| 3              | 47.1            | 189                    | 0.02                             | 1.00   |
|                |                 | 63                     | 0.07                             | 1.05   |
|                |                 | 21                     | 0.20                             | 1.23   |
| 4              | 18.6            | 189                    | 0.06                             | 1.04   |
|                |                 | 63                     | 0.17                             | 1.18   |
|                |                 | 21                     | 0.51                             | 1.90   |



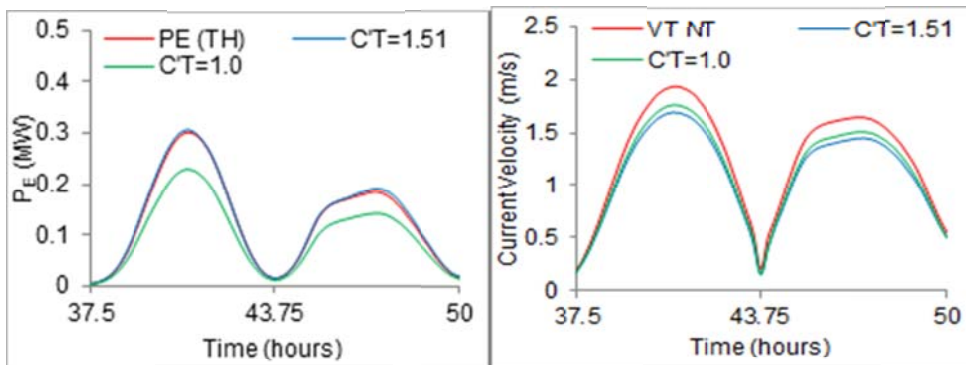
(a1)

(a2)



(b1)

(b2)



(c1)

(c2)

**Figure 5.14: Turbine 1: Comparison of (1) power capture and (2) velocity time-series over a spring tidal cycle for (a) CG189 model, (b) NG63 model and (c) NG21 model.**

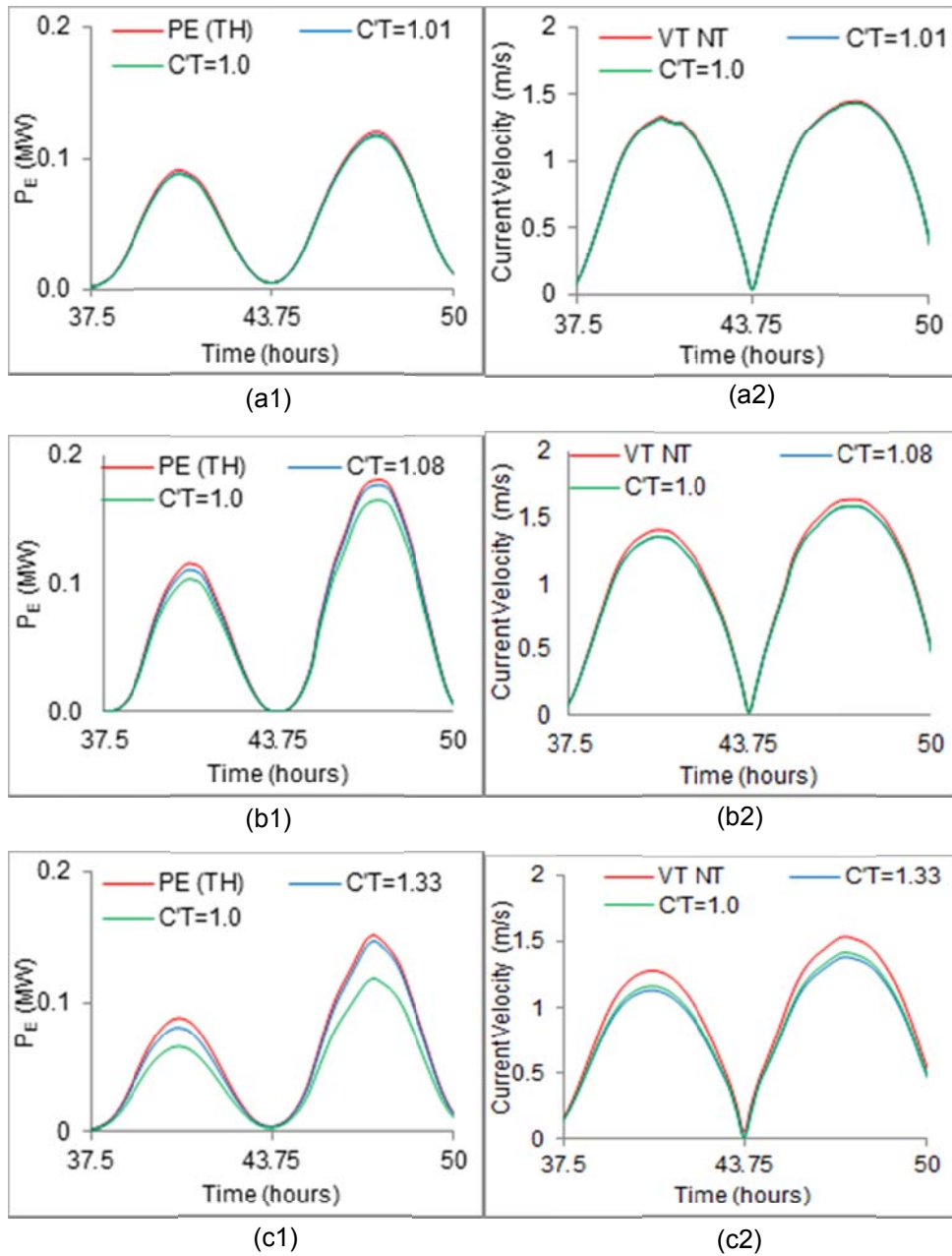


**Figure 5.15: Turbine 2: Comparison of (1) power capture and (2) velocity time-series over a spring tidal cycle for (a) CG189 model, (b) NG63 model and (c) NG21 model.**

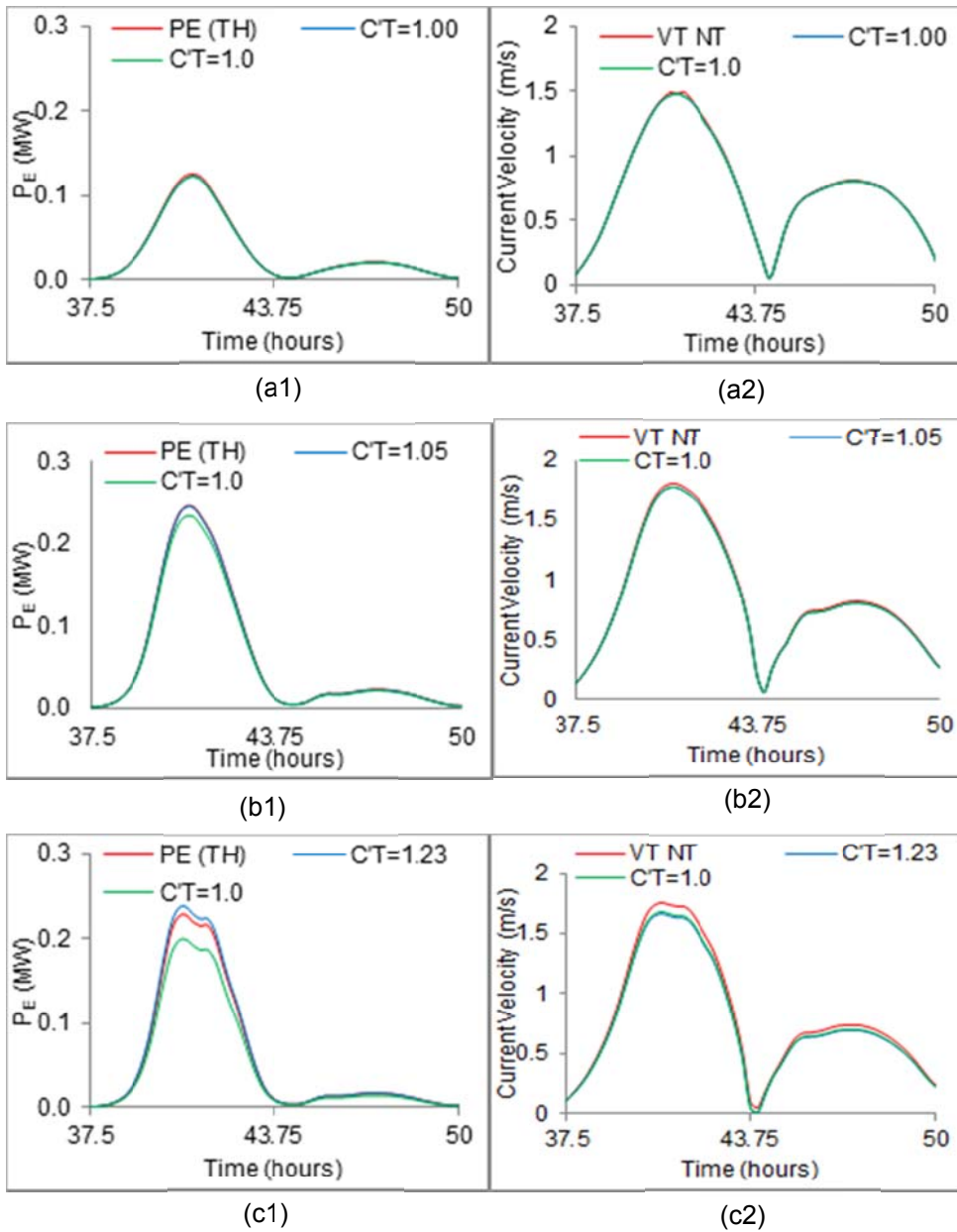


**Figure 5.16: Turbine 3: Comparison of (1) power capture and (2) velocity time-series over a spring tidal cycle for (a) CG189 model, (b) NG63 model and (c) NG21 model.**

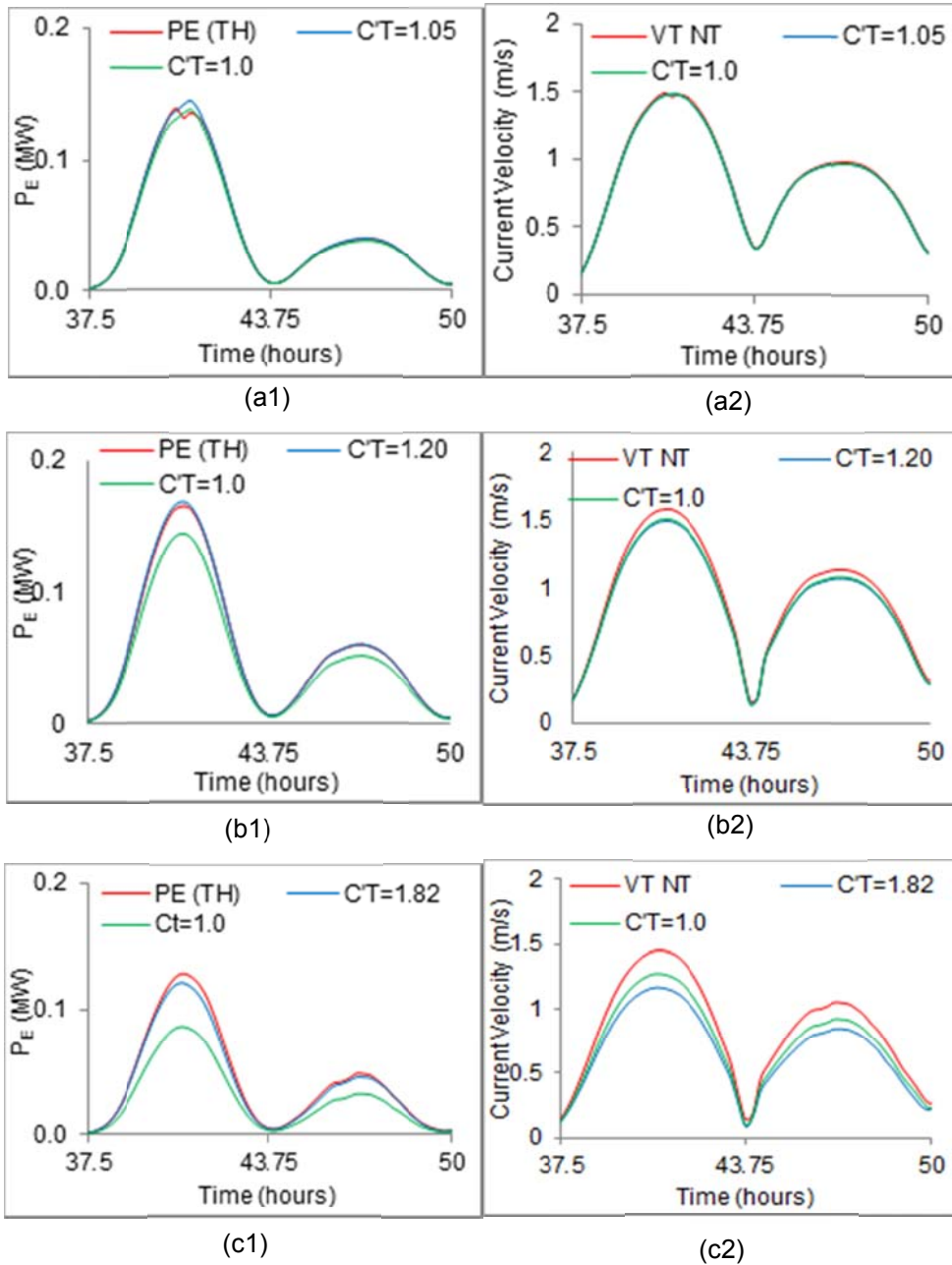


**Figure 5.17: Turbine 4: Comparison of (1) power capture and (2) velocity time-series over a spring tidal cycle for (a) CG189 model, (b) NG63 model and (c) NG21 model.**

**Table 5.8: Summary of Shannon Estuary Assessment showing optimum  $C'_T$  and modelled  $C_p$  values and the relative velocity deficit, due to turbine deployment, expressed as a percentage (%).**

| Turbine Number | Depth (m) |            | Model |      |      |      |      |      |
|----------------|-----------|------------|-------|------|------|------|------|------|
|                |           |            | CG189 |      | NG63 |      | NG21 |      |
| 1              | 25.2      | $C'_T$     | 1.02  | 1    | 1.13 | 1    | 1.51 | 1    |
|                |           | $C_p$      | 0.4   | 0.39 | 0.41 | 0.36 | 0.41 | 0.31 |
|                |           | $\Delta V$ | 1     | 0.8  | 4    | 3    | 13   | 8    |
| 2              | 35.5      | $C'_T$     | 1.01  | 1    | 1.08 | 1    | 1.33 | 1    |
|                |           | $C_p$      | 0.39  | 0.39 | 0.39 | 0.36 | 0.39 | 0.31 |
|                |           | $\Delta V$ | 1.2   | 1    | 4    | 3.5  | 12   | 9    |
| 3              | 47.1      | $C'_T$     | 1     | 1    | 1.05 | 1    | 1.23 | 1    |
|                |           | $C_p$      | 0.39  | 0.39 | 0.4  | 0.38 | 0.41 | 0.35 |
|                |           | $\Delta V$ | 0.9   | 0.9  | 2    | 1.9  | 6    | 5    |
| 4              | 18.6      | $C'_T$     | 1.04  | 1    | 1.18 | 1    | 1.9  | 1    |
|                |           | $C_p$      | 0.41  | 0.39 | 0.4  | 0.35 | 0.38 | 0.27 |
|                |           | $\Delta V$ | 1.5   | 1    | 6    | 5    | 20   | 13   |

The results verify the accuracy of the chosen  $C'_T$  values, and validate the use of the thrust sensitivity chart to select appropriate  $C'_T$  values for turbines in different operating conditions. When optimal  $C'_T$  values were specified each modelled scenario resulted in a turbine efficiency of approximately 0.4 matching the desired  $C_p$  of 0.4. Extraction of tidal energy from a single turbine is seen to reduce total velocities at the turbine location by 0.9-20%. The exact percentage difference depends on the modelled scenario, i.e. the combination of water depth and grid cell spacing (see Table 5.8) but in all cases the extent of the impact on current velocities is rational. Overall, the results convincingly demonstrate the accuracy of the selected  $C'_T$  values in reproducing tidal energy extraction in the numerical model. A comparison is drawn between the modelled effects of turbine deployment when specifying the optimal  $C'_T$  value and  $C'_T = 1.0$ . Using  $C'_T = 1.0$  resulted in power extraction, turbine efficiencies and velocity deficits being under-estimated in each model scenario

(unless the optimum  $C'_T$  value was equal to 1.0), with greater levels of under-estimation occurring in the finer resolution models.

Accurate representation of tidal energy extraction within a numerical model is of particular importance when assessing energy capture and associated hydro-environmental impacts of turbine deployment. This research has shown that accurate  $C'_T$  specification will be model specific, and that adopting  $C'_T$  in the range of 0.8-1.0 can lead to inaccuracies in predictions of energy capture and hydrodynamic impacts, particularly at higher grid cell blockage ratios which occurs for shallower water depths and/or higher spatial resolutions.

Accuracy in predicting the hydrodynamic impacts of tidal energy extraction is important as sediment transport (bed load + suspended load) is a high order function of velocity ( $\sim U^{3.4}$ ) (Robins et al. 2014), and bed shear stress which plays an important role in sediment transport is a function of  $U^2$ . therefore, even relatively small changes to current velocities could have a measureable impact on sediment transport processes (Nash & Phoenix 2017). This study has shown that accurate simulation of power extraction and changes in current velocities are directly linked, therefore, if energy capture, associated hydro-environmental impacts and optimal configurations of turbines within an array are to be accurately investigated it is essential that optimal  $C'_T$  values are employed.

## **5.6 Modelling Array Impacts on Residence Times**

With the energy extraction model fully validated, it was used to investigate the possibility of using impacts on residence times as an indicator of both the hydrodynamic and environmental impacts of turbine arrays. The energy extraction model was applied to two idealised domains which were resolved at turbine scale. Different turbine array configurations were simulated to investigate the relationship between the resulting hydrodynamic impacts,

environmental impacts and levels of energy extraction. Hydrodynamic impacts are examined through assessment of changes to current velocities while environmental impacts are investigated using a flushing study to examine the impact of the arrays on the water body's flushing capability.

To demonstrate the importance of the using the  $C'_T$  momentum sink approach, each modelled scenario was run using the optimal  $C'_T$  for the model set-up (determined from the results from Section 5.4 and Figure 5.7) and for the commonly assumed  $C'_T = 1.0$ . The resulting impacts on current velocities and flushing times were then compared.

### **5.6.1 Model Set-up**

Assessment of the influence of array configuration on the resulting hydro-environmental impacts was conducted using two idealised tidal domains; namely flow around a headland and flow between a headland and island. The model set-ups for each domain are discussed below and details of the model parameters common to both domains are presented in Table 5.9. The simulated turbines were 16m in diameters and the desired  $C_P$  was 0.4. All model simulations were run for four tidal cycles. In all instances, cold start effects had dissipated by the end of the first tidal cycle. All model results are presented for the final tidal cycle.

#### Flow around a headland

The headland model consists of an idealised channel with a headland in the centre to obstruct tidal flows, this increases velocities as the flow is diverted around the headland (see Figure 5.18 (a)). The 1.76km x 4km model domain uses a spatial resolution of 16m resulting in a computational domain of 110 x 250 grid cells. The western and eastern sea boundaries were specified as tidal elevation boundaries, with an idealised repeating tide of 1.5m amplitude, a

12.5 hour period and a phase difference of 5 minutes. The northern and southern boundaries were set as land. A constant mean water depth of 50m was specified across the domain. Peak current flows reach 1.2m/s

Flow around a headland and island

A 2.4km x 1.92km channel was created in which flow was constricted between an island and a near-by headland to induce accelerated currents. Grid resolution was 16m, producing a domain consisting of 150 x 120 computational grid cells. To induce flow between the two land masses northern and southern boundaries were specified as tidal elevation boundaries, with a repeating tide of 4m amplitude, a 12.5 hour period and a phase difference of 10 minutes specified. Again mean water depth was a constant 50m across the domain. The headland and island were set as land cells and the easterly boundary adjoining the headland was also set to land to simulate a coastline (see Figure 5.18 (b)). Peak current flows reached 1.7m/s.

**Table 5.9: Basic model parameters.**

| Simulation Time (hours) | Half time-step (s) | Bed Roughness (mm) | Water Density (kg/m <sup>3</sup> ) | Mean Depth(m) |
|-------------------------|--------------------|--------------------|------------------------------------|---------------|
| 50                      | 2.5                | 200                | 1026                               | 50            |

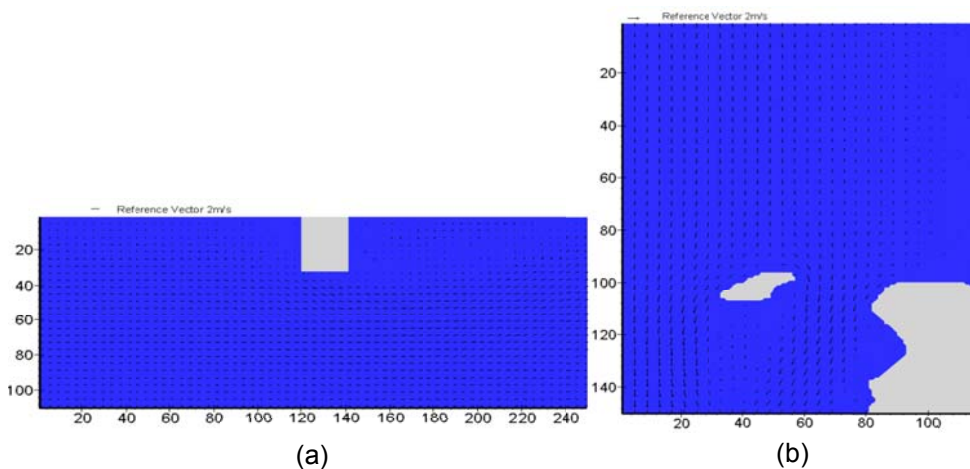


**Figure 5.18: Idealised tidal environments: (a) headland, (b) headland and island.**

### **5.6.2 Array Configurations**

A number of different array configurations were simulated in each domain. The number of turbines, shapes and densities of the arrays were varied to investigate the effect of array layouts on current velocities and residence times.

To compare the influence of turbine spacing, different array configurations were simulated with the same number of turbines deployed but with different spacings between adjacent turbines. For the headland domain, three arrays were simulated with 50 turbines deployed at spacings of 1 rotor diameter (RD), 3RD and 5RD in both the longitudinal and lateral directions. In the headland and island domain, 25 turbines were deployed at spacings of 1RD and 3RD.

The effect of array density was assessed by comparing configurations with the same array extent but different turbine numbers which were varied by using different spacings. For the headland domain, this assessment was based on the array extent of the 50 turbines at 5RD case, with the turbine spacing subsequently reduced to 3RD and 1RD, resulting in arrays of 84 and 364 turbines, respectively. For the headland and island domain, the array extent of the 25 turbines at 3RD spacing was used and turbine spacing was then reduced to 1RD producing an array of 81 turbines.

All modelled array configurations and their acronyms are listed in Table 5.10 while their positions in the headland and headland and island domains are illustrated in Figure 5.19 and Figure 5.20, respectively.

**Table 5.10: Array configurations and acronyms.**

| Scenario                   | Configuration               | Name     |
|----------------------------|-----------------------------|----------|
| Headland Domain            |                             |          |
| A                          | 50 turbines at 1RD spacing  | 50T_1RD  |
| B                          | 50 turbines at 3RD spacing  | 50T_3RD  |
| C                          | 50 turbines at 5RD spacing  | 50T_3RD  |
| D                          | 84 turbines at 3RD spacing  | 84T_3RD  |
| E                          | 364 turbines at 1RD spacing | 364T_1RD |
| Headland and Island Domain |                             |          |
| F                          | 25 turbines at 1RD spacing  | 25T_1RD  |
| G                          | 25 turbines at 3RD spacing  | 25T_3RD  |
| H                          | 81 turbines at 1RD spacing  | 81T_31D  |

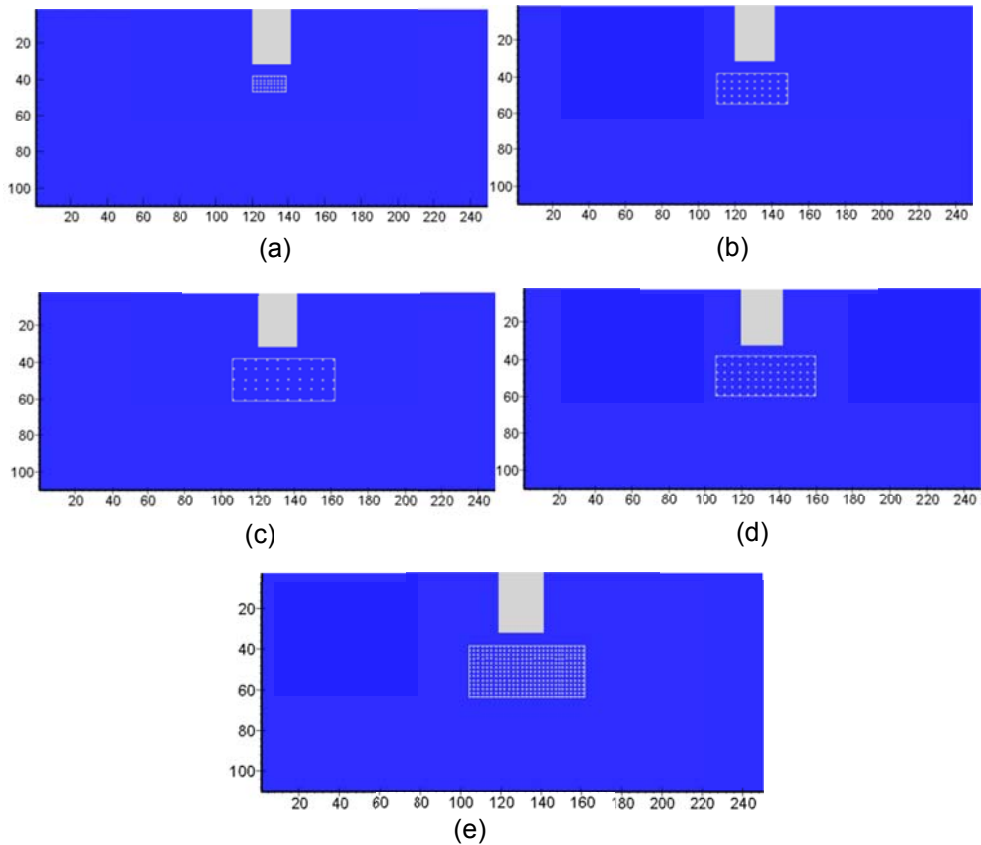


**Figure 5.19: Turbine arrays deployed in headland domain: (a) 50T\_1RD, (b) 50T\_3RD, (c) 50T\_5RD, (d) 84T\_3RD, (e) 364T\_1RD.**

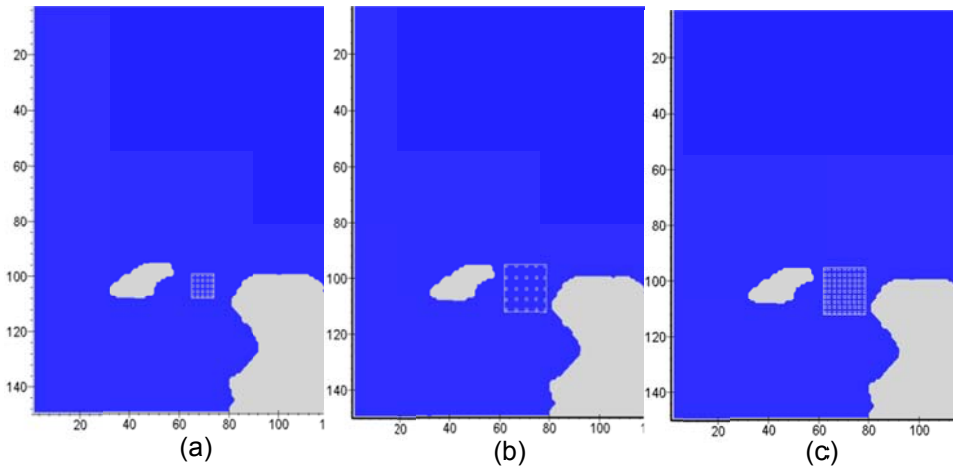


**Figure 5.20: Turbine arrays deployed in headland and island domain: (a) 25T\_1RD, (b) 25T\_3RD, (c) 81T\_1RD.**

### 5.6.3 Impact on Current Velocities

Based on the model set-up of grid resolution 16m and mean water depth 50m, an optimum  $C'_T$  value of 1.3 was determined using Figure 5.7. Tidal energy extraction was simulated for a no turbine case and turbine scenarios based on this optimum  $C'_T$  value as well as the commonly assumed  $C'_T = 1.0$ .

The impacts of each modelled array on peak current velocities across the domains are assessed. Comparisons are also drawn between the impacts due to the different configurations. The results for both domains are now discussed.

#### 5.6.3.1 Headland Domain

Figure 5.21 shows the current vectors and total current velocities at the time of peak ebb velocities (47.8 hours) for each of the modelled headland scenarios. The black rectangle indicates each array extent while the locations of each turbine are illustrated by the black squares. Grid units are measured in rotor diameters, a reference vector of 2m/s is shown for comparison with the peak ebb current vectors and the contour legend represents the magnitude of the total current velocity, expressed in m/s. One can see quite clearly that the deployment of each of the turbine arrays has a noticeable effect on

the flow; in particular, the wake (i.e. the area of reduced velocities downstream of the turbines/array) is clearly visible. A noted difference is the effect of each array configuration on the resulting wake.

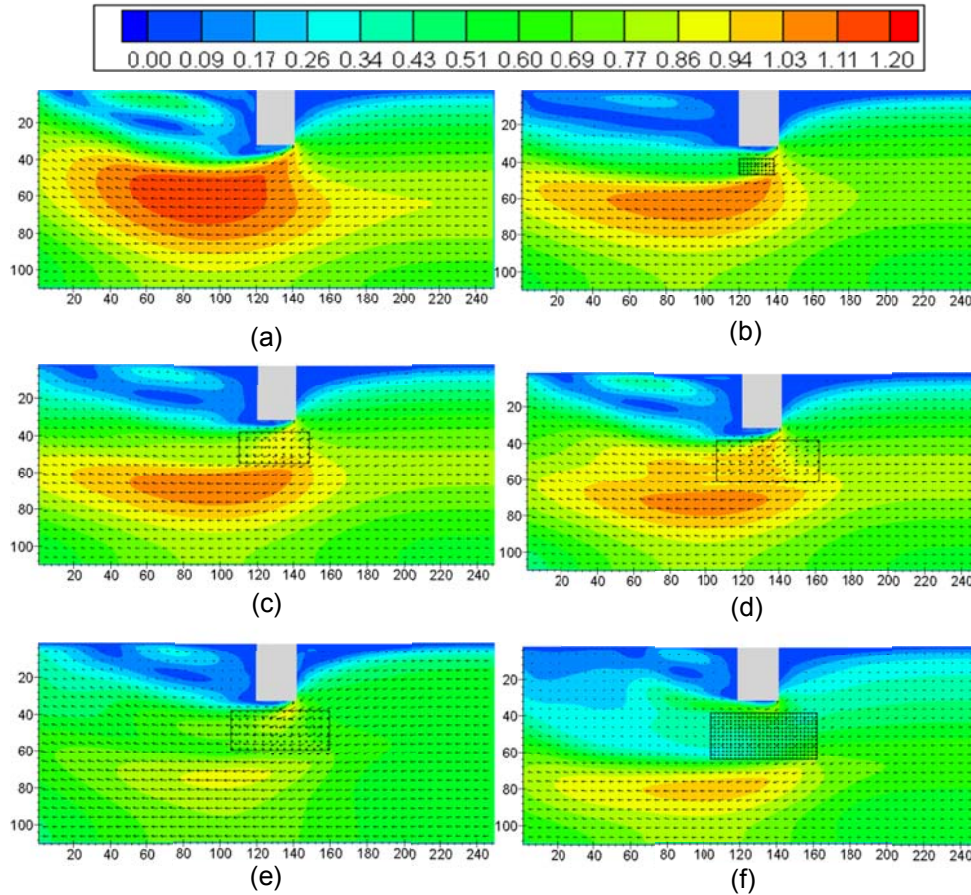


**Figure 5.21: Peak ebb current velocities for each model scenario: (a) No Turbine, (b) 50T\_1RD, (c) 50T\_3RD, (d) 50T\_5RD, (e) 84T\_3RD, (f) 364T\_1RD (legend shows total current velocities in m/s).**

**Effect of turbine spacings:**

To compare the influence of turbine spacing on array impacts, the three modelled scenarios with the same number of turbines (50) but different spacings, i.e. (A) 50T\_1RD, (B) 50T\_3RD and (C) 50T\_5RD are examined. In these scenarios, as turbine spacing is increased the resulting array increases in size and decreases in density. Percentage difference plots were calculated to better demonstrate and understand the difference between the impacts of the different arrays. Figure 5.22 shows the percentage difference in peak ebb

current velocities when a turbine array is included to those computed without any turbines (i.e. %DIFF = 100.  $((U_{turb} - U_{no\ turb}) / U_{no\ turb})$ ). Figure 5.22 (a-c) shows the hydrodynamic impacts are reduced as turbine spacing is increased. This is primarily a result of less merging of individual turbine wakes. For instance, scenario A, having the smallest spacing and extents, and therefore the highest array density, generates maximum changes in downstream currents of over 60%, whilst scenario C, with the largest spacing and thus least dense array, only generates maximum changes of around 25%. However, the width of the array wake does increase in proportion with increased array width.

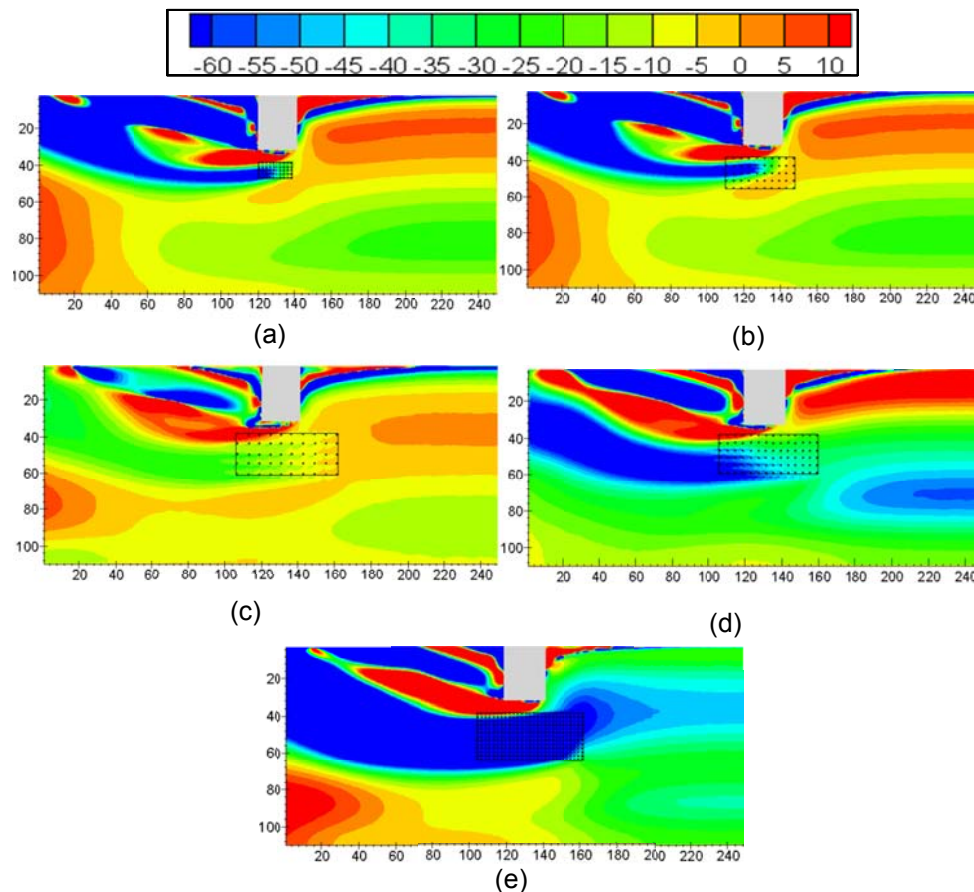


**Figure 5.22: Percentage change in peak ebb current velocities for each model scenario: (a) 50T\_1RD, (b) 50T\_3RD, (c) 50T\_5RD, (d) 84T\_3RD, (e) 364T\_1RD (legend % difference (%)).**

### **Effect of turbine numbers:**

To assess the influence of turbine numbers / density on array impacts, the array scenarios (C) 50T\_5RD, (D) 84T\_3RD and (E) 364T\_1RD are compared. Each scenario has the same array extent but different turbine numbers due to the different spacing employed. As would be expected, as turbine numbers are increased the impact on velocities is increased. This is illustrated in (Figure 5.22 (c-e)). Scenario C, being the least dense array, is found to have the smallest hydrodynamic impact. For both scenarios D and E, downstream current velocities are considerably lower compared to any of the other modelled scenarios (A-C). The most significant impacts were for scenario E, with maximum reductions in current velocities of over 70% occurring for a considerable distance and width downstream of the array, as well as inside the array, this result is expected as it is the highest capacity and most dense array scenario modelled.

It can be concluded that deployment of each array will result in velocity reductions due to energy extraction. The magnitude of the resulting wake is dependent on the array density, increasing with increasing density. As turbine numbers are increased more energy is extracted, resulting in a higher cumulative impact than that of a smaller turbine array. As turbine spacing is reduced, recovery of downstream wakes is less likely, and so adverse turbine interactions occur, resulting in greater wake effects. The extent of the wake depends on the array size, as a wake is produced downstream of the point of energy extraction, if turbines are placed over a greater area within the domain, naturally a larger wake width will be generated.

### Effect of Optimal $C'_T$ Versus $C'_T=1$

The results presented above are based on the optimum  $C'_T$  value for the model set-up of  $C'_T = 1.3$ . To demonstrate the importance of employing optimum  $C'_T$  specifications results are compared against those from runs using the commonly range of  $C'_T = 1.0$ . As the 364T\_1RD (scenario E) array was found to have the greatest impact on current velocities, the results for this model scenario based on  $C'_T = 1.3$ . and  $C'_T = 1.0$  are now presented and discussed.

Figure 5.23 shows the peak ebb flow for each scenario and Figure 5.24 shows the percentage difference between peak ebb results for both cases (i.e.  $\%DIFF = 100 \cdot ((U_{C'_T=1.3} - U_{C'_T=1.0}) / U_{C'_T=1.3})$ ). There is a noted difference in the resulting wakes, with the  $C'_T = 1.3$  model generating a stronger wake than the  $C'_T = 1.0$  model. This is demonstrated by differences of 10-20% in the modelled wake velocities in Figure 5.24. Similar findings were noted for each array scenario. This confirms the importance of employing optimum  $C'_T$  specifications for accurate energy extraction modelling and prediction of likely impacts.

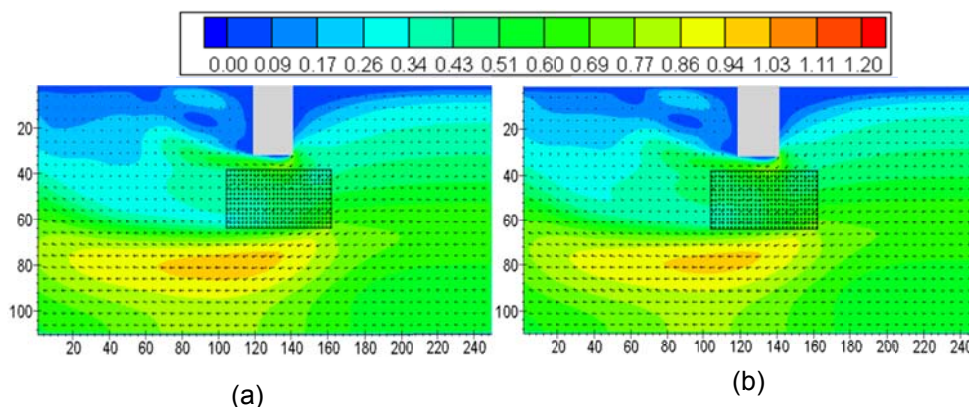


**Figure 5.23: Peak ebb current velocities for 364T\_1RD model scenario based on (a)  $C'_T = 1.3$  and (b)  $C'_T = 1.0$ .**

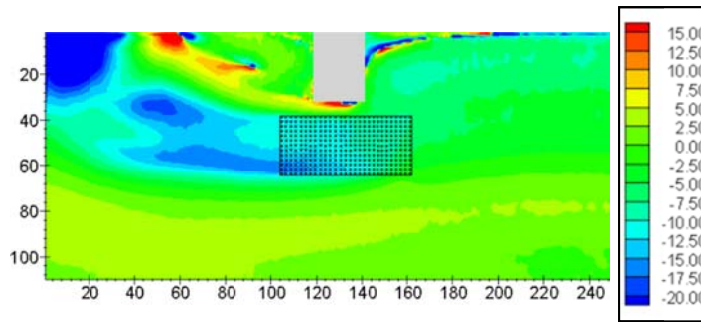


**Figure 5.24: Percentage change in peak ebb current velocities for 364T\_1RD model scenario based on  $C'_T = 1.3$  and  $C'_T = 1.0$ .**

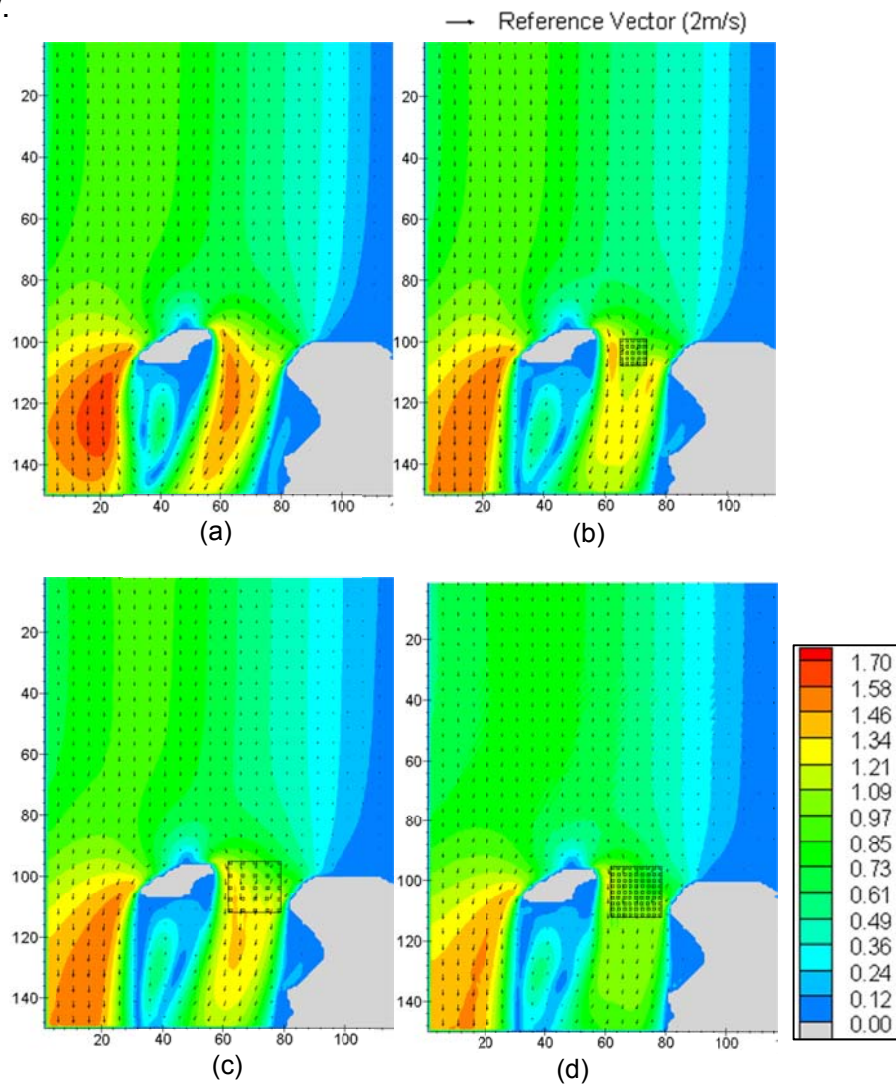
### 5.6.3.2 Headland and Island Domain

Figure 5.25 shows the current vectors and total current velocities at peak ebb for each of the modelled arrays in the headland and island domain. As with the headland scenarios, the black rectangle indicates each array extent while the locations of each turbine are illustrated by the black squares. Figure 5.26 shows the percentage difference in peak ebb current velocities when the turbines are included to those computed without any turbines.

#### **Effect of turbine spacings and numbers:**

Again results show that deployment of the tidal turbine array results in a reduction in current velocities downstream of, and inside, the array. The magnitude of the reductions is increased with increasing turbine density, as seen in Figure 5.26 (c), which shows results for the highest density 81T\_1RD array (scenario H). This is also found when comparing the two 21 turbine arrays (Figure 5.26 (b) and Figure 5.26 (c)) where a greater deficit is seen behind the 25T\_1RD array (scenario F). Even though it is smaller in size than the 21T\_3RD array (scenario G), the turbines are deployed closer together, hence the downstream wake deficit is greater. Again it is seen that the width of the wake is directly proportional to the array size. Comparing the 21T\_1RD and 81T\_1RD arrays, both scenarios have the same turbine spacing, but the 81T\_1RD array has more turbines and is larger in size. Looking at Figure 5.25 ((a) and (c))

Figure 5.26 ((a) and (c)) it is easily seen that the 81T\_1RD array has a substantially greater hydrodynamic impact than the 21T\_1RD array.



**Figure 5.25: Peak ebb current velocities for each model scenario: (a) No Turbine, (b) 25T\_1RD, (c) 25T\_3RD, (d) 81T\_1RD (legend shows total current velocities in m/s).**

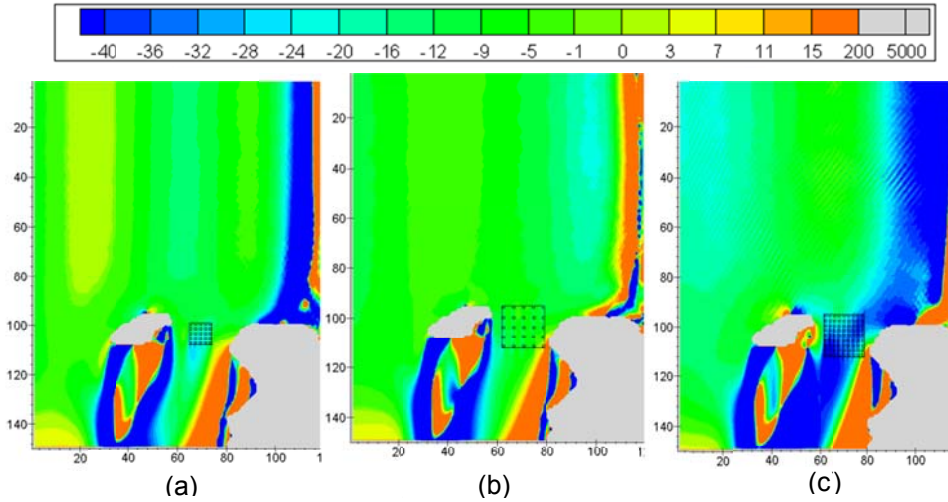


**Figure 5.26: Percentage change in peak ebb current velocities for each model scenario: (a) 25T\_1RD, (b) 25T\_3RD, (c) 81T\_1RD (legend % difference (%)).**

### ***Effect of Optimal $C'_T$ Versus $C'_T=1$***

A further demonstration of the importance of modelling tidal energy extraction based on a localised thrust is presented in Figure 5.27, which illustrates the lesser magnitude of impacts due to the  $C'^T=1.0$  scenario compared to the optimum  $C'^T=1.3$  run. This is due to the lower thrust coefficient effecting less energy removal and thus lower velocity impacts.

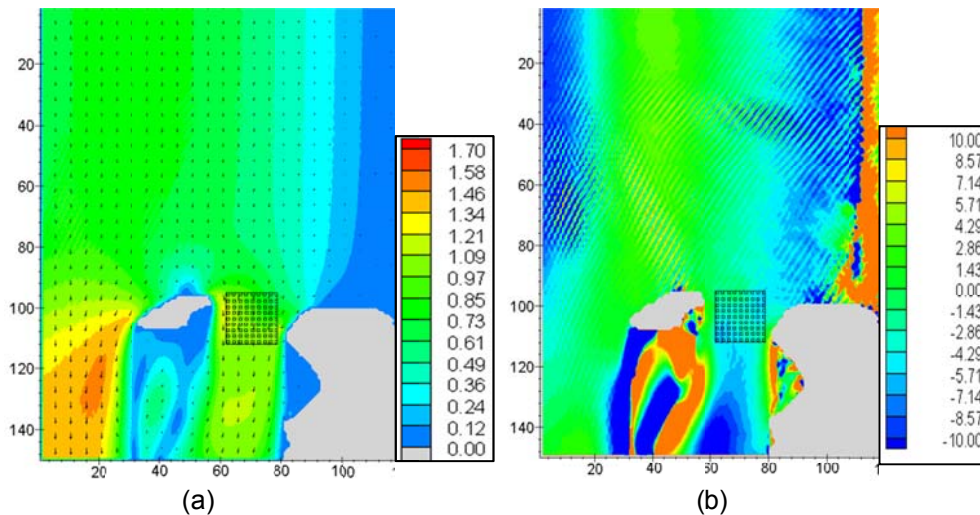


**Figure 5.27: (a) Peak ebb current velocities for 364T\_1RD model scenario based on  $C'_T=1.0$ , (b) percentage change in peak ebb current velocities for 364T\_1RD model scenario based on  $C'_T=1.3$  and  $C'_T=1.0$ .**

#### 5.6.4 Impact on Flushing

To assess the environmental impacts of the different arrays a flushing study was carried out on both domains. After tidal circulation reached steady state, a dye concentration of  $35\text{mg/m}^3$  was injected instantaneously and uniformly into regions in each domain. The regions chosen were representative of the areas of interest in each domain. For the headland domain dye was injected into the middle third section, dye was injected throughout the entire headland and island domain. Figure 5.28 and Figure 5.30 show the region of dye injection (in red) along with peak ebb velocity vectors within each dye region for the headland and headland and island domains respectively, vectors are shown for every 5<sup>th</sup> grid cell and a reference vector of 1m/s is shown. Solute concentrations are calculated based on the solute transport equation (3.5) as described in Section 3.2. Each model was run for a simulation time of 50 hours. Based on the works of The Florida Department of Environmental Protection (DEP) & Florida's five water management districts (WMDs) (2013) and Zhang & Tang (2009) the residence at each grid cell,  $\tau_r$ , is calculated as the time taken for the dye concentration in a grid cell to fall below 10% of the initial concentration, defined mathematically as.

$$\tau_r = t (C_N = 0.1C_0) \quad (5.50)$$

where  $C_0$  is the initial dye concentration at  $t=0$  (after steady state is reached) and  $C_N$  is the dye concentration at a time  $t$ . The residence time results were then used to assess the effect of each array scenario on the tidal environment's flushing rate.

##### 5.6.4.1 Headland Domain

The average residence times calculated for a no turbine scenario and each array scenario are shown in Figure 5.29. Due to velocity reductions inside the array and its wake, residence times are longer when the array is present. As solute transport is dependent on current flow, the impacts of the arrays on residence times follow a

similar pattern to the impacts on current velocities. The impact on  $\tau_r$  is less when a larger spacing is used for the same number of turbines while the impact is greater for greater turbine numbers/densities. However, changes in residence times are of a much lower order to changes in velocities. The most significant changes were observed for the largest and most dense turbine array (Figure 5.29 (f)). Compared to the no turbine case, residence times were found to be up to 10-15% longer downstream of the array. Overall, the results demonstrate that, with the exception of the largest turbine array, the impact of tidal energy extraction on residence times is insignificant.

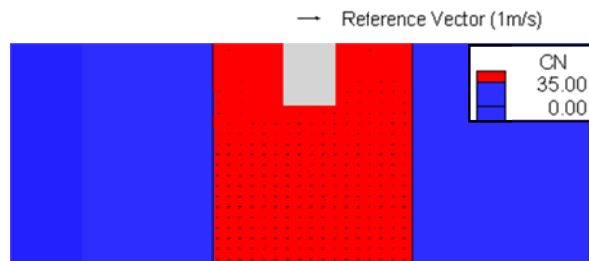


**Figure 5.28: Regions of dye injection in headland domain (legend shows dye concentration (CN) in  $\text{mg}/\text{m}^3$ ).**

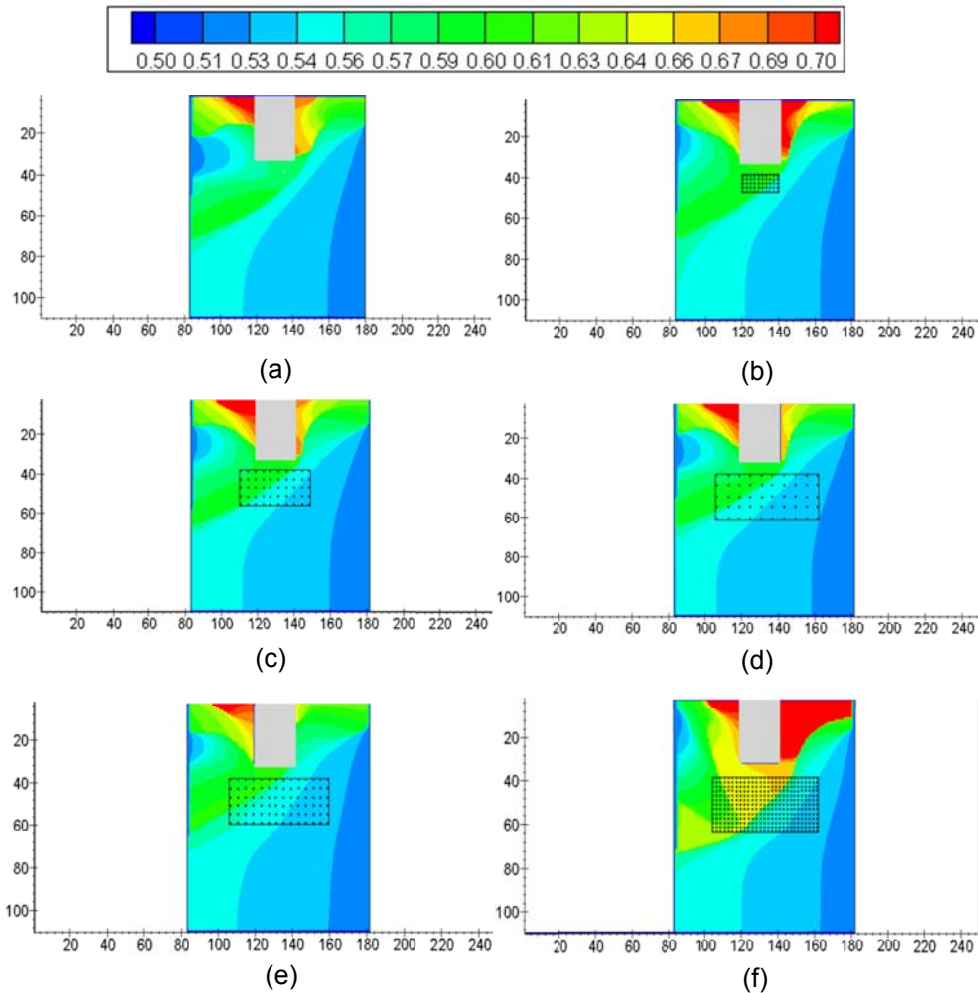


**Figure 5.29: Average residence times,  $\tau$ , for each model scenario: (a) No Turbine, (b) 50T\_1RD, (c) 50T\_3RD, (d) 50T\_5RD, (e) 84T\_3RD, (f) 364T\_1RD (legend shows residence time in days).**

#### 5.6.4.2 Headland and Island Domain

The average residence times for the no turbine and various array scenarios deployed in the headland and island domain are shown in Figure 5.31. As for the headland domain, it was found that array deployment does not substantially impact the domain's flushing capabilities, with little difference in residence times observed for each scenario. With a similar result to the headland domain, it can be concluded that residence time is not a suitable indicator of hydro-environmental impacts.

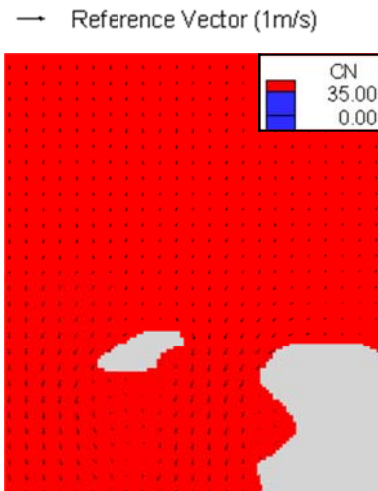


Figure 5.30: Regions of dye injection in headland and island domain (legend shows dye concentration (CN) in  $\text{mg/m}^3$ ).

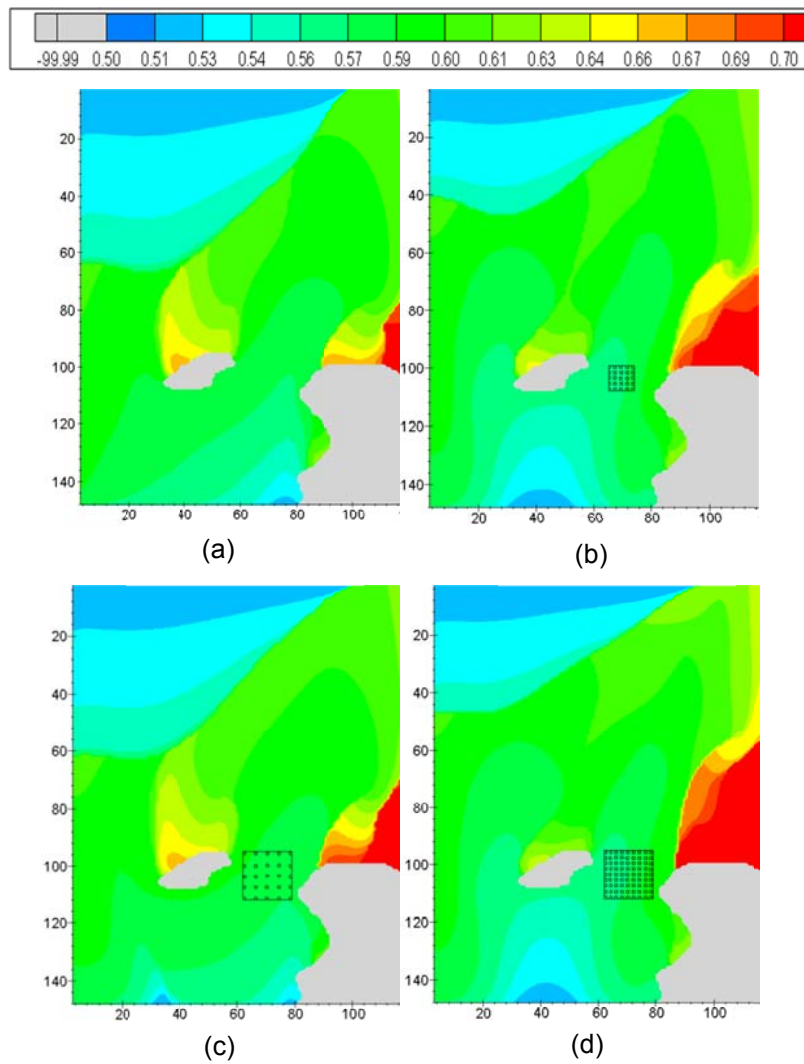


Figure 5.31: Average residence times,  $\tau$ , for each model scenario: (a) No Turbine, (b) 25T\_1RD, (c) 25T\_3RD, (d) 81T\_1RD (legend shows residence time in days).

## 5.7 Summary and Conclusions

A 2D hydrodynamic model was modified to enable simulation of tidal energy extraction and an idealised domain used to determine a means of identifying appropriate localised thrust coefficients to give desired turbine efficiencies of 40%. A model of a case study site, the Shannon estuary, was then used to validate the  $C'_T$  approach. Finally, two idealised tidal environments were developed at turbine scale and used to investigate the impact of turbine array configuration on current velocities and residence times. The following conclusions can be drawn from this study:

- Initial  $C_T$  sensitivity assessment found that employing  $C_T$  in the commonly-assumed range of 0.8-1.0 would under-predict both power capture and changes in velocities. To achieve 40% capture of available power required the use of a higher 'localised thrust' ( $C'_T$ ) of 1.3 for the modelled scenario.

The optimal value of  $C'_T$  (defined in this research as that which gives a turbine efficiency of 40%) is dependent on the model set-up (i.e. grid spacing and local water depths). A thrust sensitivity chart was constructed and a best-fit relationship developed to facilitate determination of optimal  $C'_T$  values for any model set-up.

- Application of the energy extraction model to the Shannon estuary validated both the  $C'_T$  approach for calculation of turbine thrust and the use of the  $C'_T$  sensitivity chart for calculating optimal  $C'_T$  values.
- Two idealised high resolution tidal domains were used to investigate the sensitivity of the array impacts to turbine spacings and numbers/densities. Whilst results found that both turbine spacing and number had substantial effects on the resulting

changes in velocity, minimal impacts on residence times were observed. It is therefore concluded that residence times/flushing would not make a very suitable environmental impact indicator.

## **6 Optimisation of Tidal Turbine Arrays**

### **6.1 Introduction**

The economic viability of tidal stream energy projects will likely require large-scale deployment, with hundreds of turbines positioned in an array. This leads to the question of how best to position these turbines for maximum energy capture with minimal associated hydro-environmental impacts. Application of the developed energy extraction model discussed in Chapter 5 indicated the resulting impacts of array deployment will depend on turbine configuration, with larger, denser arrays having a greater impact on the environment through changes in current velocities and, for example, flushing times.

This chapter details the final stage in the model development which involved development of an optimisation algorithm to facilitate determination of optimal array configurations, for maximum energy capture whilst employing spatial and environmental impact constraints. The effects of turbine spacing on energy capture and changes to the hydrodynamics are initially explored. The development of the optimisation algorithm, including its incorporation into the energy extraction model and testing of the fully developed model on an idealised domain along with its application to the Shannon estuary case study is then discussed in detail.

### **6.2 Turbine Spacing**

In order to inform the development of the array optimisation model, the influence of turbine spacing on changes to current velocities and energy capture was examined. Various scenarios were assessed; (1) looking at a single turbine, (2) a two turbine row (with turbines positioned along-stream) and (3) a two turbine column (with turbines positioned across-stream). Each configuration was deployed in an idealised model domain, the details of which are discussed below.

### 6.2.1 Model Set-up

The idealised channel model presented in Section 5.4 was also used for this assessment. The principal model parameters are summarised in Table 6.1 below. A constant depth of 50m was set across the model domain. The model resolution was set to 16m to match the turbine rotor diameter so that flows and hydrodynamic interactions between turbines could be captured. Based on results from the  $C'_T$  assessment undertaken in Chapter 5, the optimum  $C'_T$  value for the model set-up was 1.3.

**Table 6.1: Basic model parameters.**

| Simulation Time (hours) | Half time-step (s) | Bed Roughness (mm) | Density (kg/m <sup>3</sup> ) | Depth(m) |
|-------------------------|--------------------|--------------------|------------------------------|----------|
| 25                      | 2.5                | 200                | 1026                         | 50       |

All model simulations were run for four tidal cycles. In all instances, cold start effects had dissipated by the end of the first tidal cycle. All model results are presented for the final tidal cycle and for the ebb-tide. Where presented, the percentage change in velocities when a turbine is included relative to a no turbine scenario is calculated at the time of peak ebb tide (t=21.25 hours) as follows:

$$\%Diff = \left( (V_{turb} - V_{no\ turb}) / V_{no\ turb} \right) \cdot 100\% \quad (6.1)$$

Where a contour plot is shown, the turbine location is indicated with a black square and grid units are measured in rotor diameters (RD) from the turbine.

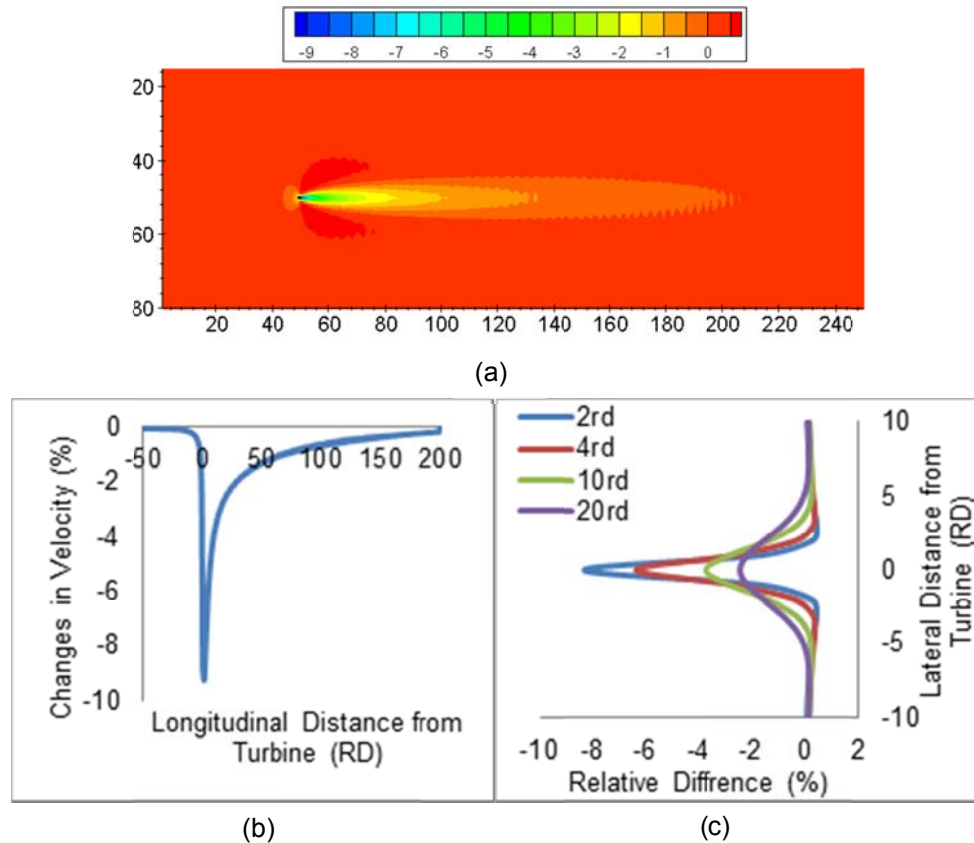
### 6.2.2 Numerical Simulations

#### Single Turbine:

For initial assessment a single turbine was deployed in the channel. The resulting impacts and energy capture could then be used as a reference point to compare changes due to deployment of additional

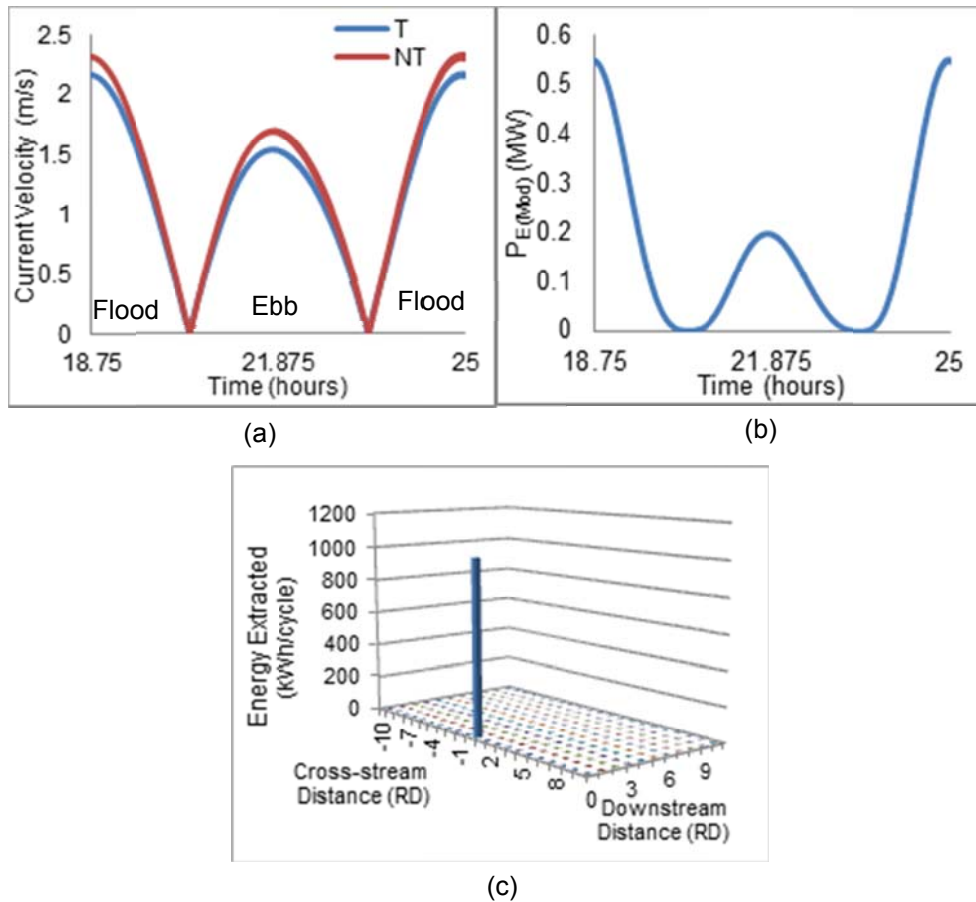
turbines. Figure 6.1(a) shows the percentage difference in peak velocities across the model domain. Results are as expected; with a clear wake downstream of the turbine and accelerated bypass flows observed either side of the wake. Figure 6.1(b) shows changes in peak velocities along the longitudinal wake centreline. The greatest reductions in velocities, with differences compared to the no turbine case of approximately 10%, occur immediately downstream of the turbine. The wake gradually recovers as flow moves further downstream, with differences reducing to 3% at 30RD downstream. However, the wake still persists a considerable distance away from the turbine, dissipating to around 1% difference at 70RD downstream.

Figure 6.1 (c) shows the percentage change in velocities at different lateral transects (2RD, 4RD, 10RD and 20RD downstream) through the turbine wake. Results show the wake is symmetrical about the turbine centre, with wake width increasing with downstream distance. Similar results were observed in an experimental simulation of a single rotor in a recirculating flume undertaken by Stallard et al. (2013). Their study indicted the resulting wake possessed a bell-shaped lateral velocity deficit profile, and observed the wake width increasing (i.e. wake expansion) as flow travels downstream.



**Figure 6.1: Percentage difference in velocities at peak ebb for a single turbine for (a) the full model domain (units: %) (b) along the longitudinal wake centreline, and (c) along a number of lateral transects at various distances downstream of the turbine.**

A comparison of current speeds at the turbine grid cell with and without turbine deployment is shown in Figure 6.2 (a) for a single tidal cycle. The power extracted by the single turbine over the same tidal cycle is presented in Figure 6.2 (b). Total energy capture per tidal cycle (shown in Figure 6.2 (c)) is determined by integrating this power curve over the tidal cycle giving 1006 kWh per cycle. Flood tide dominance is observed in Figure 6.2 (a) with peak undisturbed velocities reaching around 2.3m/s for the flood tide and 1.67m/s for the ebb tide. This flood-dominance generates considerable differences in the magnitude of power extracted over a tidal cycle, with substantially higher powers extracted during the flood tide compared to the ebb tide.



**Figure 6.2: (a) Current velocities over one tidal cycle before (NT) and after (T) turbine deployment, (b) power extracted by a single turbine over one tidal cycle, (c) energy capture per cycle of a single turbine.**

### Two Along-stream Turbines:

When considering the along-stream placement of turbines in an array it was important to consider the hydrodynamic impacts of each individual turbine. Since power is proportional to velocity cubed, placing a turbine in the downstream wake of a neighbouring turbine may significantly reduce the expected energy capture of the downstream turbine. To investigate turbine interactions, simulations were conducted of two adjacent turbines deployed at 0RD, 3RD and 5RD longitudinal spacings ( $\Delta S_{Long}$ ).

Figure 6.3 shows the percentage change in peak ebb velocities for the different scenarios. The single turbine wake plot is also included for comparison. It is noted that deployment of two inline turbines

resulted in greater velocity changes than a single turbine deployment, and that the magnitude of these changes decreased with increased turbine spacing. For instance maximum differences of 17%, 14.5% and 13.5% were found for the  $\Delta S_{Long} = 0RD$ , 3RD and 5RD scenarios, respectively, whilst a maximum change of 10% was observed for the single turbine case. Deployment of the second turbine resulted in a longer wake extent compared to the single turbine case, with changes in velocities of 2% still occurring at over 100RD away from the upstream turbine in each case.

These points are further demonstrated in Figure 6.4 which shows the percentage change in peak ebb current velocities along the longitudinal wake centreline for the different modelled scenarios. When 2 turbines are deployed at 0RD spacing, velocity changes increase by almost a factor of 2 compared to the single turbine scenario. For both cases, maximum changes occur immediately downstream of the turbine location. As the downstream distance between turbines is increased, changes in current velocities are reduced; however, even at  $\Delta S_{Long} = 5RD$  a maximum change of over 13% is observed. For both the  $\Delta S_{Long} = 3RD$  and 5RD cases, an initial peak reduction is seen immediately downstream of the first turbine and a second higher peak reduction occurs immediately downstream of the second turbine, due to the cumulative wake effects of both turbines.

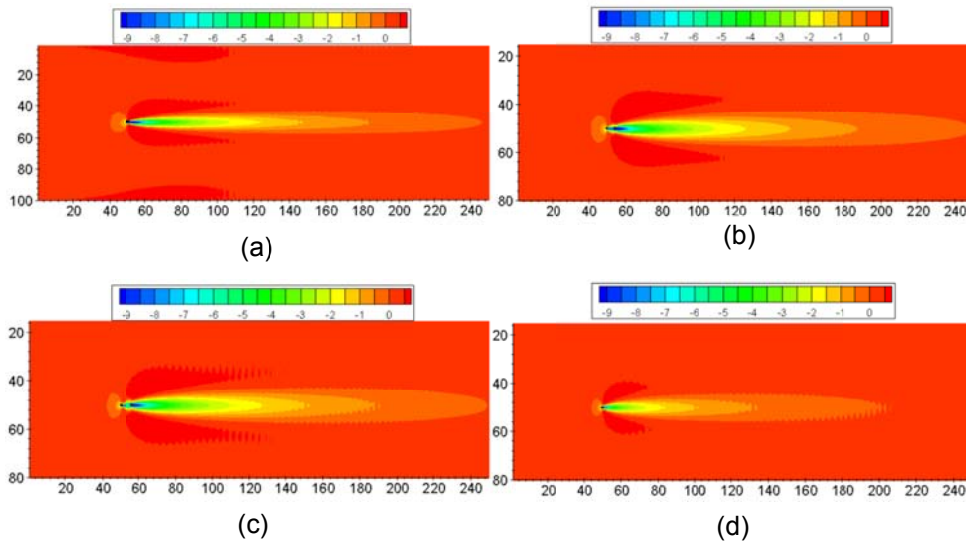


**Figure 6.3: Percentage difference in velocities at peak ebb for deployment of (a) 2 turbines with no downstream spacing (b) 2 turbines with 3rd downstream spacing (c) 2 turbines with 5rd downstream spacing (d) a single turbine (units of legend: %).**

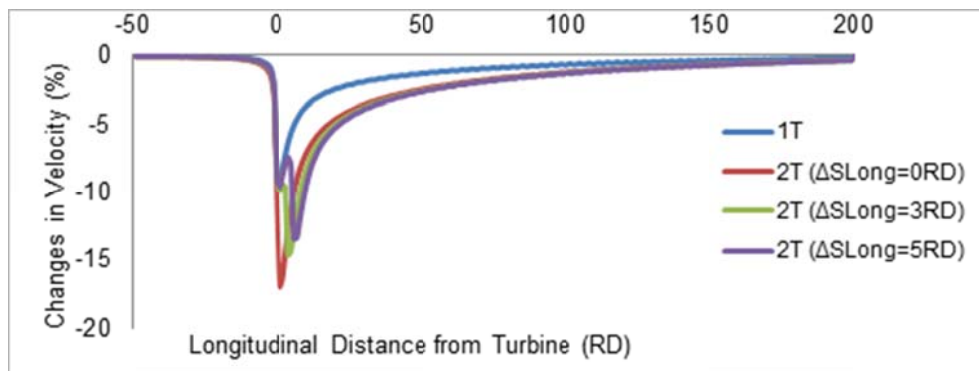


**Figure 6.4: Percentage difference in peak ebb velocities along longitudinal wake centreline for 1 turbine and 2 turbines deployed at 0RD, 3RD and 5RD downstream spacing.**

Figure 6.5 shows the power capture over a tidal cycle by each turbine placed at the different spacings. As would be expected, placing downstream turbines in the wakes of upstream turbines results in lower power capture compared to the case of singular deployments; power capture decreases with lower turbine spacing. This is illustrated through a comparison of the energy extraction levels for each turbine in the two turbine scenario with that from single turbine deployments in the same locations. For the 0RD spacing case, energy capture of T1 decreased from 1006kWh to

853kWh and of T2 decreased from 1006kWh to 900kWh, when the second turbine was deployed. For the 3RD spacing scenario reductions from 1006kWh to 908kWh and 1007kWh to 951kWh were found for T1 and T2 respectively. For the largest spacing of 5RD the impact is marginally less, with reductions of 1006kWh to 928kWh and 1008kWh to 964kWh determined for T1 and T2.

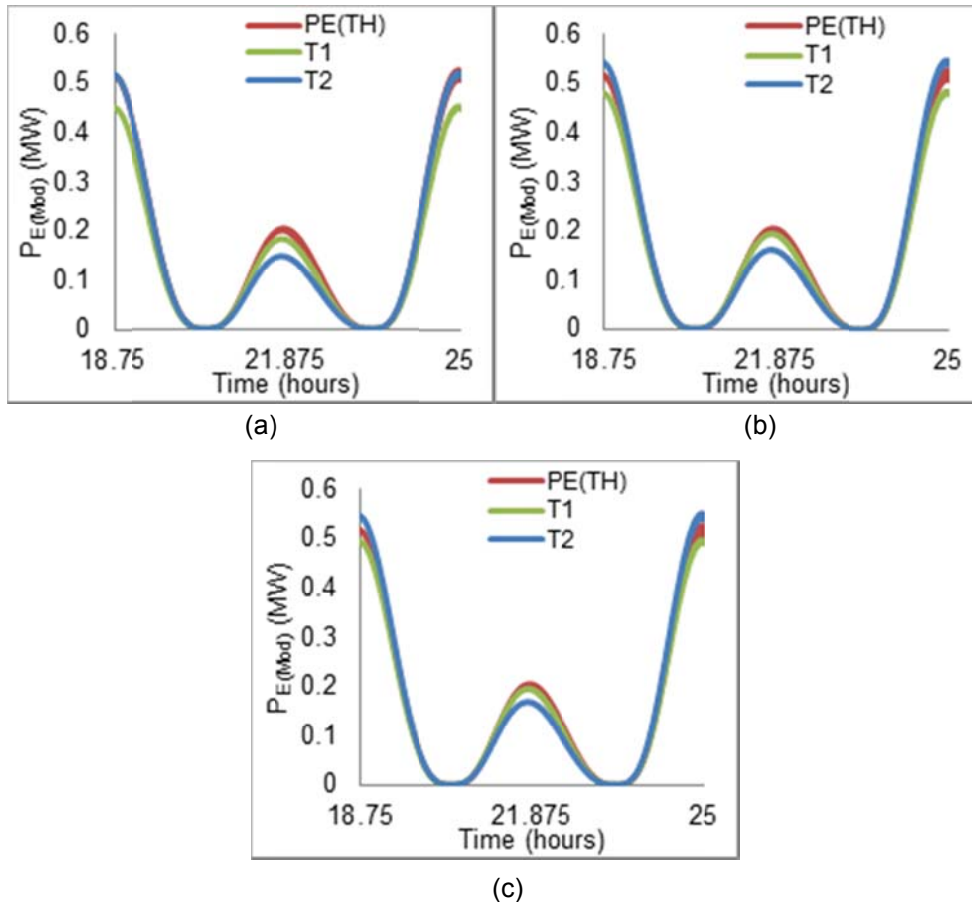


**Figure 6.5: Power extracted by each turbine (MW) at downstream spacings of (a) 0RD (b) 3RD and (c) 5RD.**

These reductions in energy capture only consider two turbines and the effects would be even greater for larger number of turbines placed in an inline array. This is illustrated by Nash et al. (2015) who utilised a 2D depth-averaged model to assess the energy captured by an inline array of turbines. Their results showed turbines positioned in the wakes of upstream turbines to perform poorly, capturing less energy than their upstream/downstream neighbours.

The farm method of resource estimate is based on the assumption that each turbine within an array will extract the same percentage of the undisturbed available resource. A major limitation of this approach is the assumption that the energy extraction by one turbine will be unaffected by the energy extraction of other turbines, however, published works (e.g., Black & Veatch (2005); Gebreslassie (2012); Nash et al. (2015)) as well as research throughout this thesis has demonstrated this is not the case.

The importance of incorporating the effects of energy extraction by one turbine in prediction of energy capture by another turbine is shown in Table 6.2. The table compares predictions of energy captured by the two along-stream turbines when placed at the different spacings as determined using the farm method and the author's model. Assuming a desired power coefficient of 0.4, the farm method calculates  $P_{ext}$  as 40% of the available resource, which results in approximately 2400kWh of energy being extracted by each turbine regardless of the spacing. Accounting for the impacts of energy extraction produces reduced estimates of energy capture, particularly at the smaller spacings.

Based on these results, it was important that the developed optimisation algorithm which is presented later incorporated the impact of the energy extraction process on available energy by recalculating the available resource after each turbine is deployed, essentially conducting a new resource assessment after each turbine is added.

**Table 6.2: Energy Capture (kWh) based on the Farm method and author's approach.**

| $\Delta S_{Long}$ | Approach | Energy Capture (kWh) |      |
|-------------------|----------|----------------------|------|
|                   |          | T1                   | T2   |
| 0RD               | Farm     | 2421                 | 2422 |
|                   | Model    | 853                  | 899  |
| 3RD               | Farm     | 2421                 | 2425 |
|                   | Model    | 908                  | 951  |
| 5RD               | Farm     | 2421                 | 2426 |
|                   | Model    | 927                  | 964  |

Results indicate that placing turbines in an inline configuration will result in adverse interactions between the turbines, resulting in larger velocity changes (and thus greater environmental impacts) and reduced power availability to downstream turbines. It is therefore considered likely that optimal turbine layouts will be staggered, placing downstream turbines in such a manner that they avoid the wakes of upstream turbines.

*Two Turbines Deployed Across-stream:*

The single turbine wake in Figure 6.1(a) shows accelerated flows to either side of the turbine. When considering the lateral placement of turbines in an array, optimal positioning might make use of these accelerated flows, generating greater levels of power. However, similar to downstream placement of turbines, lateral placement may also alter the turbine wake, reducing the potential energy capture of downstream turbines. To further investigate the effects of lateral spacing, simulations were modelled of two turbines positioned at lateral spacings ( $\Delta S_{Lat}$ ) of 1RD, 3RD, 5RD and 10RD.

Figure 6.6 compares the changes in peak ebb current speeds for the different  $\Delta S_{Lat}$ . For the 10RD spacing, two distinct wakes are formed, each with the same characteristics as that of the single turbine. For

$\Delta S_{Lat} = 1RD, 3RD$  and  $5RD$ , the wakes of each turbine merge at some point downstream of the turbines forming a single wake and the downstream merging distance increases with increasing  $\Delta S_{Lat}$ .

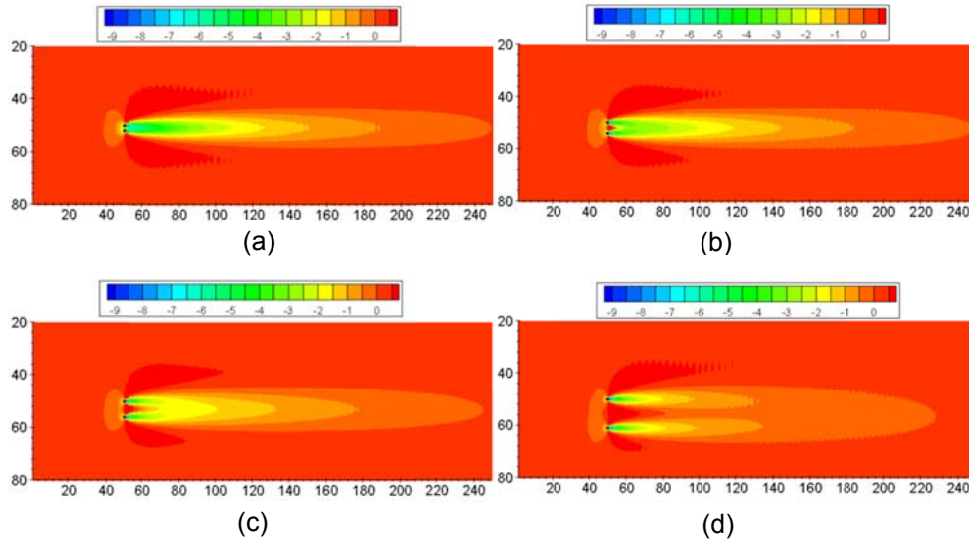


**Figure 6.6: Percentage difference in velocities at peak ebb for deployment of two turbines with lateral spacings of (a) 1RD (b) 3RD (c) 5RD (d) 10RD (units of legend: %).**

Figure 6.7 compares percentage differences in lateral velocities through the turbine wakes at distances of 2RD, 4RD, 10RD and 20RD downstream of the turbines for  $\Delta S_{Lat} = 1RD, 3RD, 5RD$  and  $10RD$ . For  $\Delta S_{Lat} = 1RD$ , the wakes have already begun to merge before 2RD downstream and have fully merged by 10RD - this is apparent by the bell-shaped profile at 10RD which is similar in shape to the lateral wake profile of a single turbine. For the 3RD spacing, the wakes merge somewhere between 2RD and 4RD downstream, while for the 5RD spacing merging does not occur until 10RD downstream. For  $\Delta S_{Lat} = 10RD$  wake merging does not occur and the resulting wakes mirror that of a single turbine. Stallard et al. (2013) investigated the impacts of different configurations of scale model turbines. Their results agree with the findings of this assessment, showing wake merging for  $\Delta S_{Lat} < 3RD$  only, and that the resulting wakes for larger spacings are similar to that of a single turbine.

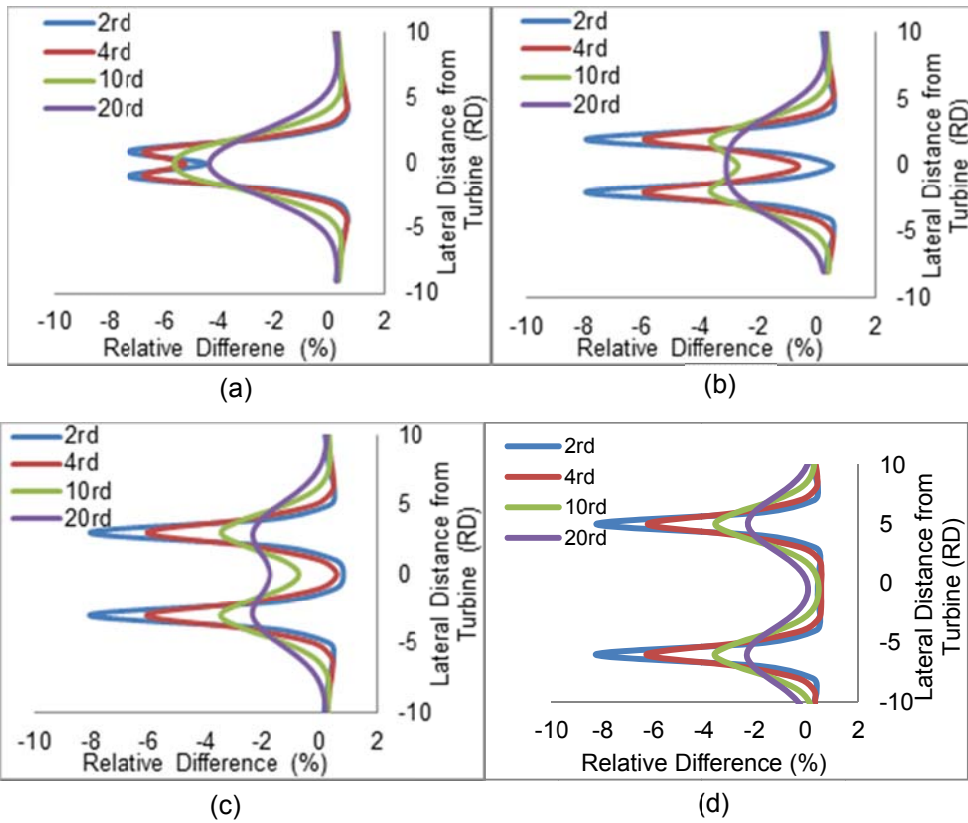


**Figure 6.7: Percentage difference (%) downstream of two turbines deployed at (a) 1RD (b) 3RD (c) 5RD (d) 10RD.**

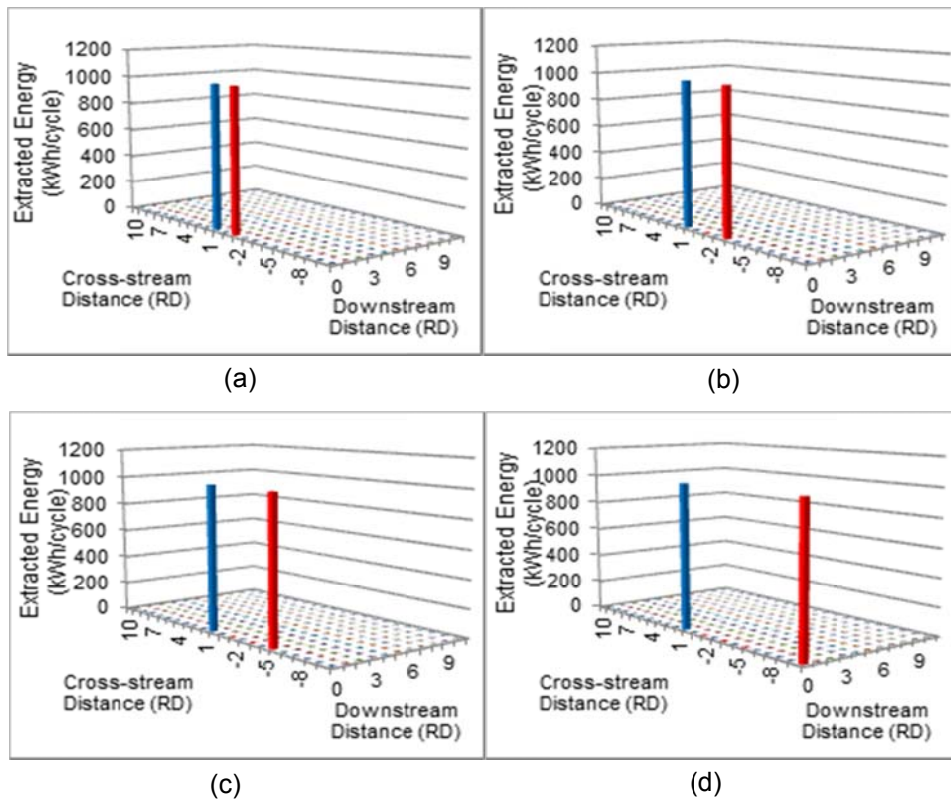


**Figure 6.8: Energy capture per cycle by each turbine at lateral spacings of (a) 1RD (b) 3RD and (c) 5RD (d) 10RD.**

Figure 6.8 shows the energy captured by each turbine positioned at the various lateral spacings; each turbine extracts between 1006-1012kWh. The results show, in contrast to downstream turbines, turbines placed laterally will not negatively impact on one another's energy capture. In fact, due to accelerated flows, energy captured in some cases is found to be very marginally increased from the single turbine case of 1006kWh. Figure 6.6 shows flow accelerations around and between the two turbines. This is due to blockage effects as flow is diverted around each individual turbine and to the spacings of the turbines, as the wakes of neighbouring devices induce a venturi effect on the flow.

This initial assessment has indicated that placement of inline turbines may lead to reduced energy capture by downstream turbines as the available power is reduced due to the upstream turbine wake. Results also show the potential for exploiting the accelerated flow around and between turbines to increase energy capture. Concluding from this, to optimise power output from a turbine array, optimal configuration is likely to be staggered, with along-stream turbines placed so they don't interact with the wakes of upstream turbines and with across-stream turbines spaced to induce flow acceleration for downstream turbines to intercept. An optimal configuration suggested by Nash et al. (2015) is a lateral spacing of between 3RD and 4RD and a longitudinal spacing of between 1RD and 4RD.

### **6.3 Development of Optimisation Model**

The results presented above demonstrate that the positioning of individual turbines within an array could significantly influence the total power output of the array. It is therefore desirable that array layouts are optimised so that power output will be maximised. The above assessment has also shown how turbines can impact on current velocities; with wake reductions and accelerations between and around the devices. The literature review of Chapter 2 and the research results presented thus far show that the quantity of energy

extracted by a turbine array and the resulting hydrodynamic impacts are inextricably linked. The literature review demonstrated that the most significant impact is to velocities and most other environmental impacts, such as changes to material transport and flushing times, result from this. It is therefore important to also consider the effects of turbine positioning on environmental impacts; this is done here by using changes in current velocities as a measure of impact.

To develop an array optimisation model, the energy extraction model (presented in Chapter 5) was further modified to include an automated optimisation model, which facilitates the determination of optimised array configurations, considering both extracted power and the resulting impact on current velocities. The optimisation model was incorporated into both the DIVAST and MSN models. Initially, the optimisation algorithm was developed solely for maximising power output. Once this was accomplished an approach to minimise the resulting impact on flow was developed and integrated into the model. The algorithms for (a) power maximisation and (b) impact minimisation are now presented and discussed. The parameters used in the optimisation algorithm are defined in Table 6.3.

**Table 6.3: Optimisation model parameters and symbols.**

| Naming Convention        | Parameter  |
|--------------------------|--|
| NFLTURB                  | Turbine flag (to identify inclusion or exclusion of turbines)          |
| $N_T$                    | Turbine number   |
| $P_{ava N_T}(I, J, N_T)$ | Available power at (I,J) location for turbine $N_T$                    |
| $(I, J)_T$               | Turbine location   |
| MARTURBINIT              | Marine turbine initialising subroutine (to incorporate turbine thrust) |
| $P_{ext N_T}(I, J, N_T)$ | Power extracted by turbine $N_T$                                       |
| $\Delta S_{Lat}$         | Lateral turbine spacing  |
| $\Delta S_{Long}$        | Longitudinal turbine spacing   |
| $H_{min}$                | Minimum mean water depth   |
| $V_{T N_T=0}$            | Undisturbed current velocity   |
| $V_{T N_T=N_T}$          | Current velocity after turbine deployed                                |
| SIF(I,J)                 | Significant impact factor  |
| Check2                   | Flag for 2 <sup>nd</sup> velocity impact check                         |

### 6.3.1 Power Maximisation

Figure 6.9 presents the power maximisation algorithm. It is implemented in the model as follows. The model is initially run for a no turbine scenario (i.e.  $N_T=0$ ) to calculate the mean undisturbed power available for extraction across the domain per tidal cycle ( $P_{ava N_T=0}$ ). Based on this mean, the location of maximum power is determined (defined in model grid coordinates (I,J)) and selected as the deployment site for the first turbine  $(I, J)_{T=1}$ . The marine turbine initialising subroutine (MARTURBINIT) is called to incorporate the presence of the turbine and to set the appropriate  $C'_T$  value for the

turbine. This is determined using the  $C'_T$  / grid cell blockage ratio relationship developed in Chapter 5 and expressed again here as:

$$C'_T = 0.0002BR^2 + 0.0073BR + 0.9938 \quad (6.2)$$

Additional turbines are then added in an iterative manner. After each new turbine is added, the model is run for two cycles to ensure that steady state conditions are achieved and the mean  $P_{ava N_T}$  per tidal cycle is recalculated. In other words, the available resource is reassessed taking account of the impacts of all turbines added to that point. A new turbine is added based on the resulting location of max power.

Limitations to sites in which turbines can be deployed are specified within the model, these include the following:

- Deployment domain: specifies the area within the model domain in which turbines can be deployed. The limits of this area are specified in the model input data file.
- Turbine spacing: lateral ( $\Delta S_{Lat}$ ) and longitudinal ( $\Delta S_{Long}$ ) spacing constraints are specified in the input data file. Based on  $\Delta S$  values, the model calculates how many turbines can be added to any one grid cell (if the turbine diameter is less than the model grid resolution)
- Minimum water depth ( $H_{min}$ ): limits turbines from being placed in locations where the water depth is less than a user specified minimum value.

The power extracted by each turbine,  $P_{ext N_T}$ , is calculated using equation (5.48) and written to an output file. This is done continually throughout the entire model simulation.

### 6.3.2 Power Maximisation and Impact Minimisation:

Figure 6.10 presents the power maximisation and impact minimisation algorithm. To incorporate minimisation of the impact of turbine deployment on current velocities, a significant impact factor (SIF) approach based on the work of Black & Veatch (2005) was employed. The SIF is defined as the maximum allowable change in peak velocity and is set here to 10% of the undisturbed peak current velocity i.e.  $SIF(I,J) = 0.1 \cdot V_{T N_T=0(Peak)}$ . This peak velocity is determined at each (I,J) location in the domain for  $N_T = 0$  and the resulting SIF is calculated. After each new turbine is added, the model determines the peak turbine velocities ( $V_{T N_T = N_T(Peak)}$ ) across the domain and the relative change in velocities is calculated as

$$Diff = ((V_{T N_T=0(Peak)} - V_{T N_T = N_T(Peak)}) / V_{T N_T=0(Peak)}) \quad (6.3)$$

After each turbine is deployed a check is carried out to assess the resulting hydrodynamic impact, if the change in velocities downstream of the turbine is greater than the SIF the turbine in question is removed, the next location of maximum mean  $P_{ava N_T}$  is determined and the turbine repositioned. This check is carried out until the user specified numbers of turbines,  $N_{T Max}$ , have been deployed. Once  $N_{T Max}$  is reached the resulting hydrodynamic impacts of each turbine is re-checked to ensure any re-positioning of turbines has not affected the velocity changes due to previously deployed turbines.

Finally, when all turbines are deployed (including re-positioning if necessary), the final resulting impacts are checked after steady state is reached, and  $P_{ext N_T}$  for the final tidal cycle is calculated and output at 0.25 hour time intervals.

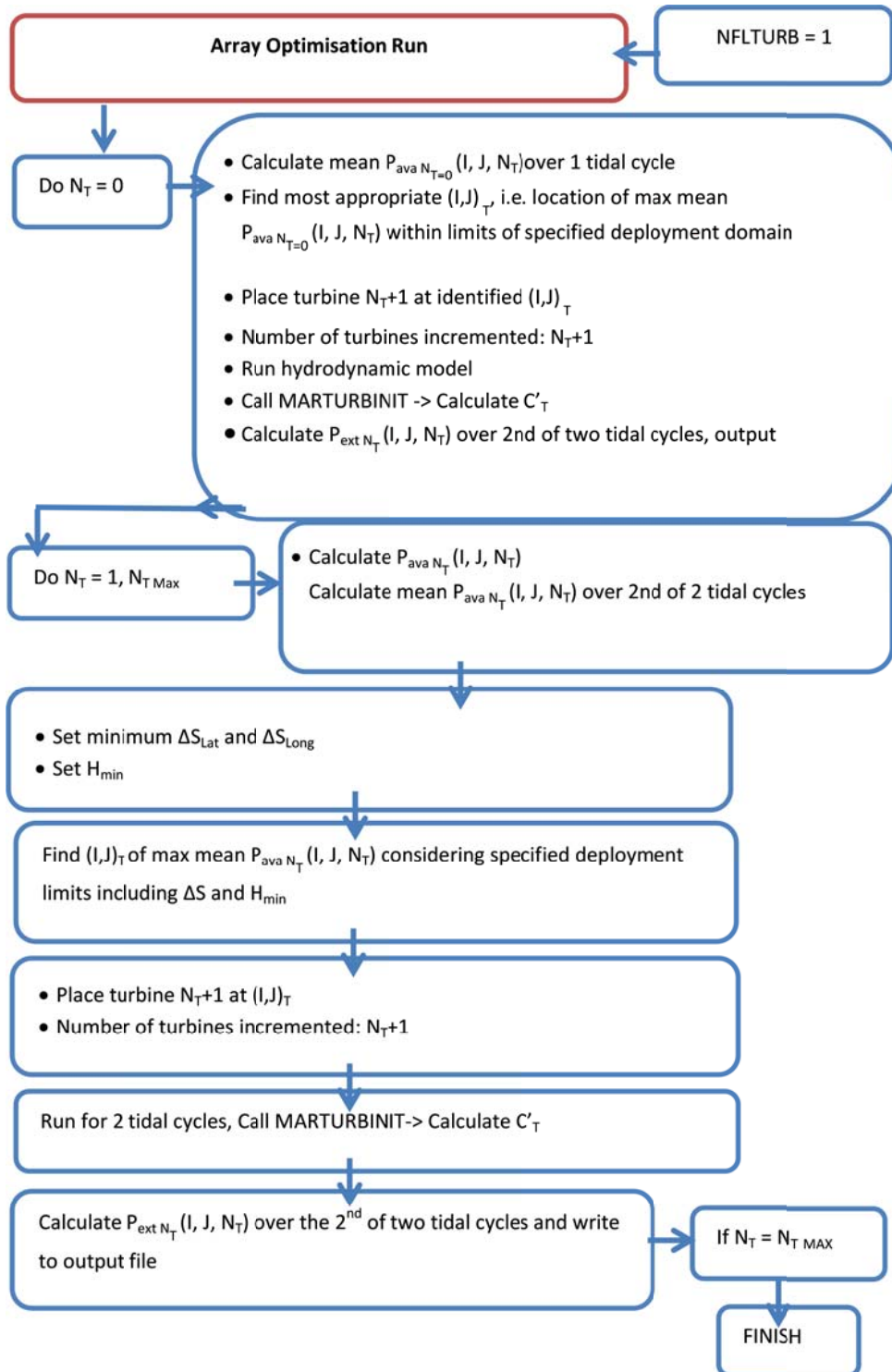


Figure 6.9: Optimisation algorithm based on power.

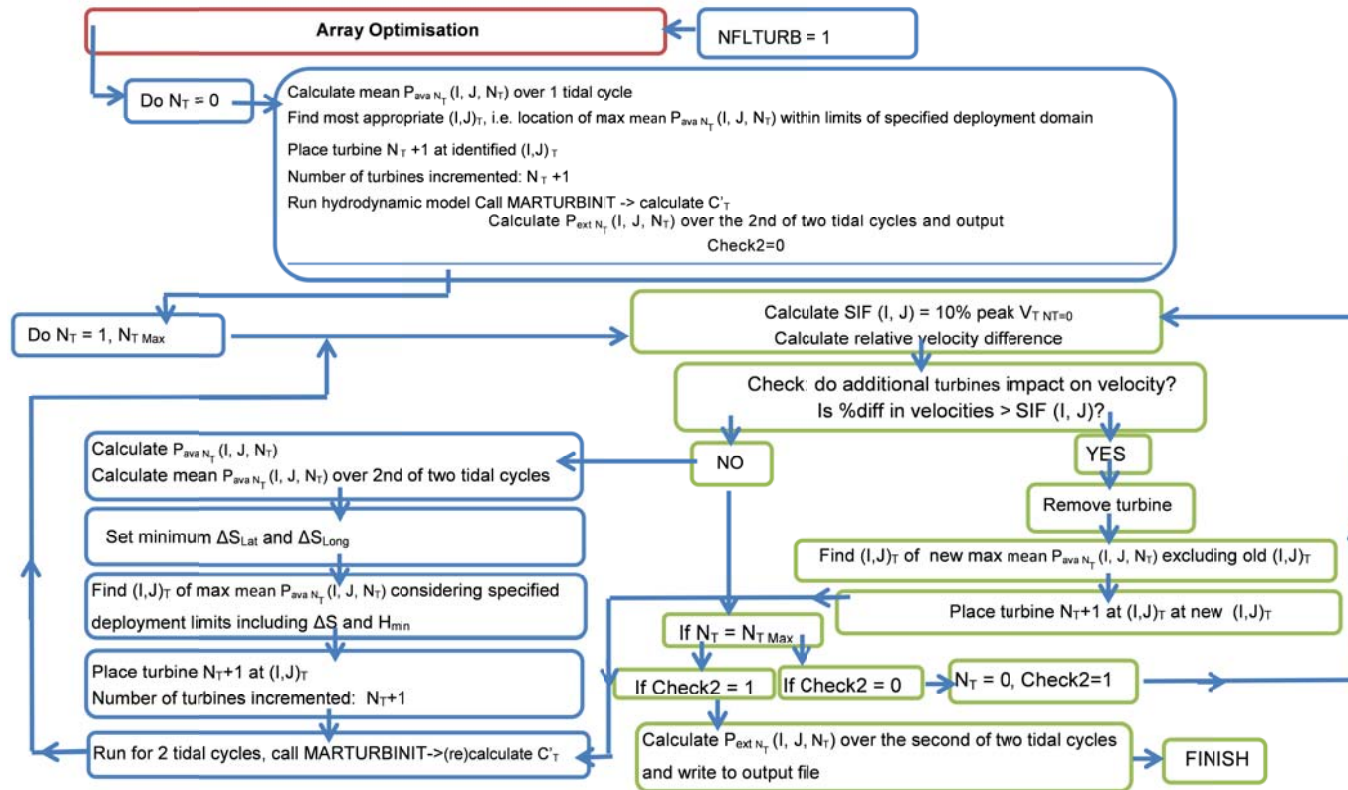


Figure 6.10: Optimisation algorithm based on power and velocity impacts.

## 6.4 Development of Model Architecture

Development of the optimisation model involved extending the existing energy extraction model architecture by amending existing subroutines and adding new subroutines to the DIVAST and MSN models. Each model was developed to include both of the optimisation algorithms described in the previous section. Figure 6.11 presents a flow chart of the modified DIVAST architecture, showing all subroutines called in the main program and highlighting the sections developed for inclusion of power optimisation. Similar alterations were made in the MSN model (shown in Figure 6.12).

The subroutine TURB\_DATA has been modified to read input data required for the optimisation. This consists of the extents of the deployment domain, lateral and longitudinal spacings between adjacent turbines ( $\Delta S_{lat}$  and  $\Delta S_{long}$  respectively), and the maximum number of turbines to be deployed. The subroutine OPT was added to implement the optimisation code. The purpose of this subroutine is to carry out calculations to determine optimal turbine deployment sites based on (a) locations of maximum mean  $P_{ava N_T}$  and (b) locations where deployment will result in a velocity change of less than SIF. Extracted power is also calculated and output within this subroutine. Subroutine MARTURBINIT has been modified to include the  $C'_T$  calculation, which is executed for each added turbine.

**Table 6.4: Sections of code modified or added to incorporate array optimisation.**

| <b>Program Section</b>              | <b>Function and Modification</b>   |
|-------------------------------------|--|
| <b>TURB_DATA</b>                    | Read input deployment domain, $\Delta S_{lat}$ and $\Delta S_{long}$ , and $N_{T\ Max}$ data   |
| <b>OPT (Power)</b>                  | Determines optimal turbine sites based on locations of maximum available power in coarse domain.   |
| <b>OPT (Power &amp; Velocity)</b>   | Determines optimal turbine sites in coarse domain based on (a) locations of maximum available power and (b) locations in which energy extraction does not significantly impact current velocities. |
| <b>MARTUBRINIT</b>                  | Calculates $C'_T$ for each turbine added / moved in coarse grid.   |
| <b>OPT_F (Power)</b>                | Determines optimal turbine sites based on locations of maximum available power in fine domain.   |
| <b>OPT_F (Power &amp; Velocity)</b> | Determines optimal turbine sites in fine domain based on (a) locations of maximum available power and (b) locations in which energy extraction does not significantly impact current velocities.   |
| <b>MARTUBRINIT_F</b>                | Calculates $C'_T$ for each turbine added / moved in fine grid  |

| MAIN PROGRAM    |   |
|-----------------|---|
| 1. FILINP       | •Opens file for input data  |
| 2. FILOUT       | • Opens file for data output  |
| 3. BOUND        | • Reads open boundary (OB) data   |
| 4. FIELD        | • Reads computational domain  |
| 5. FIND         | • Establishes the integration sections  |
| 6. DEPTH        | • Reads water depths  |
| 7. INITL        | • Initialises depths, elevations, concentrations and chezy values   |
| 8. TURB_DATA    | • Reads input deployment domain, $\Delta s$ and $N_T$<br>Max data   |
| 9. OPT          | <ul style="list-style-type: none"> <li>• Calculates difference in peak velocities and SIF</li> <li>• Determines optimal <math>(I, J)_T</math> based on mean <math>P_{avg NT}</math></li> <li>• Places Turbines only if impact on velocities is not significant</li> <li>• Calculates and outputs <math>P_{est NT}</math></li> </ul> |
| 10. MARTURBINIT | <ul style="list-style-type: none"> <li>• Calculates turbine area and cells that in which turbines are deployed</li> <li>• Recalculates <math>C_T</math></li> </ul>  |
| 11. HYDBND      | • Assigns hydrodynamic data at OB   |
| 12. HYDMODX     | • Solves hydrodynamics in x-direction   |
| 13. SIDEH       | • Recalculates water depths   |
| 14. FLDRY       | • Checks for flooding and drying of cells   |
| 15. HYDBND      | • Assigns hydrodynamic data at OB   |
| 16. HYDMODY     | • Solves hydrodynamics in y-direction   |
| 17. SIDEH       | • Recalculates water depths   |
| 18. FLDRY       | • Checks for flooding and drying of cells   |
| 19. CHEZY       | • Recalculates chezy values   |
| 20. EDDY        | • Recalculates eddy viscosities   |
| 21. PRINT       | • Outputs time series and snapshots   |

Figure 6.11: Flowchart of DIVAST model subroutines. Including optimisation code based on both power and impact on velocities (subroutines which have been modified/ added to include optimisation are shaded).

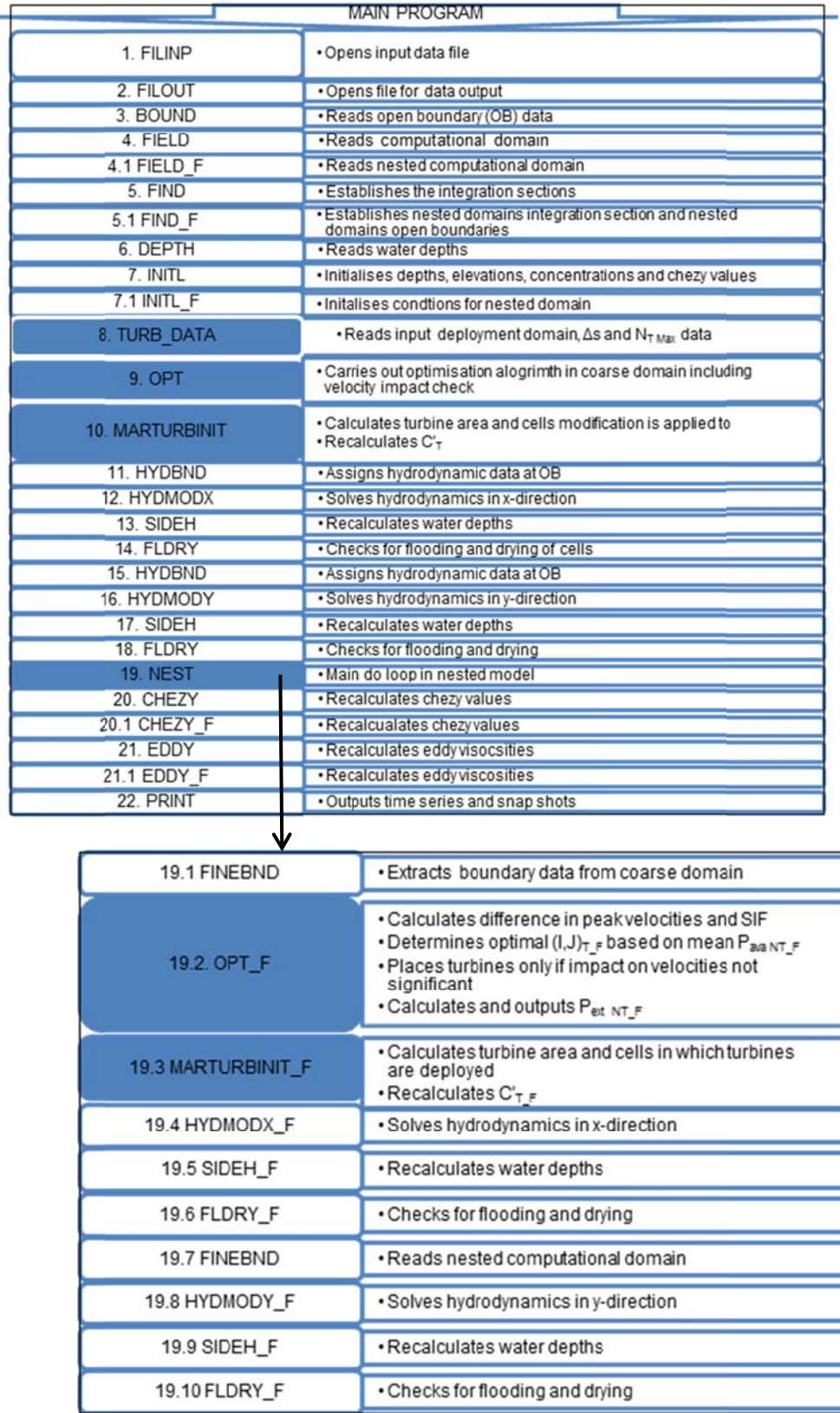


Figure 6.12: Flowchart of nested MSN model subroutines. Including optimisation code based on both power and impact on velocities (subroutines which have been modified/ added to include optimisation are shaded).

## 6.5 Testing Power Calculations for Multiple Turbines

Development of the power equation in Chapter 5 was based on analysis of a single turbine, since the optimisation model concerns deployment of multiple turbines, it was necessary to check the validity of the developed power equation for scenarios where more than one turbine is deployed.

### 6.5.1 Model Set-up

An idealised channel, 3.2km long x 0.67km wide, subject to tidal flows was used to assess the validity of the power calculation. The model was set-up with a spatial resolution of 16m x 16m resulting in a computational domain of 200 x 42 grid cells. 16m turbine diameter was again employed. Based on the model grid cell blockage ratio, a  $C'_T$  value of 1.3 was selected from the thrust sensitivity chart (Figure 5.8). All other model details were unchanged from the idealised model set-up discussed in Section 5.4.1.

### 6.5.2 Power Quantification

The assessment was based on four devices (T1-T4) deployed in an inline formation, turbines are positioned at  $\Delta S_{Lat} = 3RD$  and  $\Delta S_{Long} = 3RD$ . The array configuration is shown in Figure 6.13.

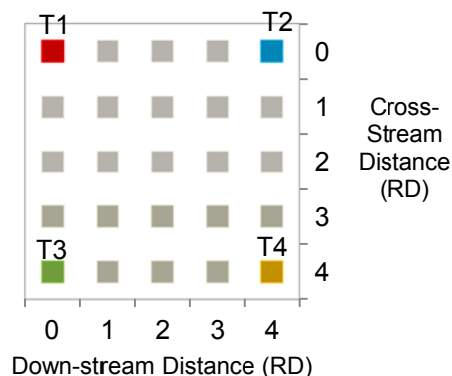


Figure 6.13: Position of four deployed turbines.

Five simulations were run in total. To calculate the undisturbed resource available to each turbine, four simulations were run, each excluding one turbine (T1-T4) and including the other three. A final run was then carried out in which all four turbines were deployed.

Assessment of the validity of the power calculation is based on two parameters: (1) modelled extracted power ( $P_{E(mod)}$ ) and (2) the undisturbed and available turbine efficiencies, denoted  $\epsilon_{Undis}$ ,  $\epsilon_{ava}$  respectively. These efficiencies are used to determine the proportion of available and undisturbed resource each turbine extracts.

The theoretical extracted power ( $P_{E(th)}$ ) is determined based on the undisturbed flow,  $u$ , as:

$$P_{E(th)} = 0.5 \rho A_T u^3 C_P \quad (6.4)$$

where  $u$  was calculated separately at each turbine location with that turbine omitted but the remaining three included.

Throughout this research modelled turbines are intended to have a  $C_P$  of 0.4. If our power calculation is valid for the case of multiple deployed turbines then the following condition must be satisfied for each turbine:

$$P_{E(mod)} = P_{E(th)} \quad (6.5)$$

Figure 6.14 compares  $P_{E(th)}$  and  $P_{E(mod)}$  for each of the 4 turbines (shown in Figure 6.13) over the final tidal cycle of the simulation. The results show minimal difference between theoretical and modelled power outputs, with RMSE values less than 0.001MW for all cases, demonstrating that the power equation is appropriate for  $N_T > 1$ .

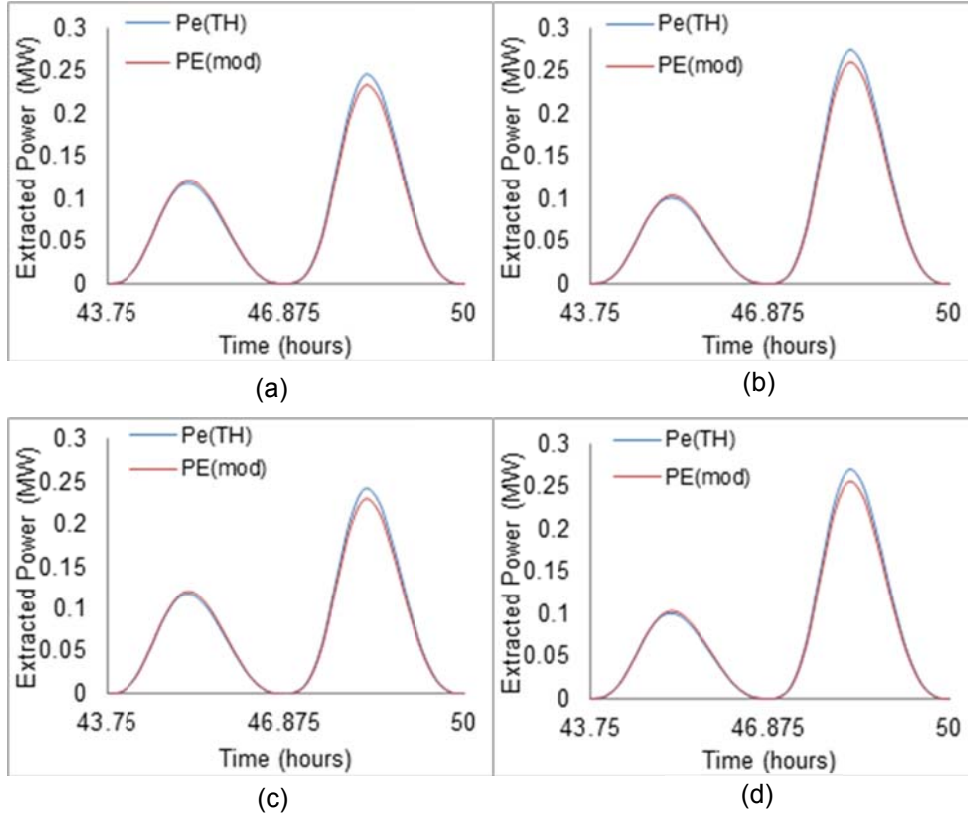


**Figure 6.14: Comparison of  $P_{E(th)}$  and  $P_{E(mod)}$  for (a) T1, (b) T2, (c) T3, (d) T4.**

In order to further demonstrate the validity of the power calculation we calculate the efficiency of each turbine relative to the available resource,  $\epsilon_{ava}$ , once all neighbouring turbines are deployed. For instance, consider turbine 1: to determine the power that is available to T1 when T2-4 are deployed the turbine model is run with only T2-4 deployed and the available power at the intended T1 location is determined as  $P_{ava\ T1}$ .  $\epsilon_{ava}$  for T1 is then calculated as follows:

$$\epsilon_{Ava\ T1} = \frac{\text{mean } P_{E(th)\ T1}}{\text{mean } P_{ava\ T1}} \quad (6.6)$$

In both equation (6.6) and (6.7) the mean values are calculated per tidal cycle for each turbine.

The  $\epsilon_{ava}$  calculated for each of the four turbines in the test array is shown in Figure 6.15(a). Each turbine has a  $\epsilon_{ava}$  of 0.4 which matches the desired  $C_p$  of 0.4 and demonstrates that the model is

correctly calculating  $P_{E(mod)}$ . Regardless of the position of a turbine within an array, it's  $\epsilon_{ava}$  should always equal the turbine  $C_P$ .

To demonstrate the effect of neighbouring turbines on a turbines level of power capture, a second efficiency is defined.  $\epsilon_{Undis}$  is the ratio of the turbine extracted power relative to the undisturbed available resource ,i.e. without any turbines deployed, and is expressed mathematically for T1 as follows:

$$\epsilon_{Undis\ T1} = \frac{\text{mean } P_{E(th), T1}}{\text{mean } P_{ava\ T=0}} \quad (6.7)$$

Figure 6.15(b) shows  $\epsilon_{Undis}$  for each of the four turbines in the test array. Results show  $\epsilon_{Undis}$  values are less than the desired  $C_P$  of 0.4, with  $\epsilon_{Undis}$  for T1 and T3 = 0.38 and  $\epsilon_{Undis}$  for T2 and T4 = 0.37. These lower than expected efficiencies are a result of turbine interactions in the inline configuration. As discussed in Section 6.2, placing downstream turbines in the wake of upstream turbines reduces the available power. A more efficient configuration may therefore be to stagger the turbines.

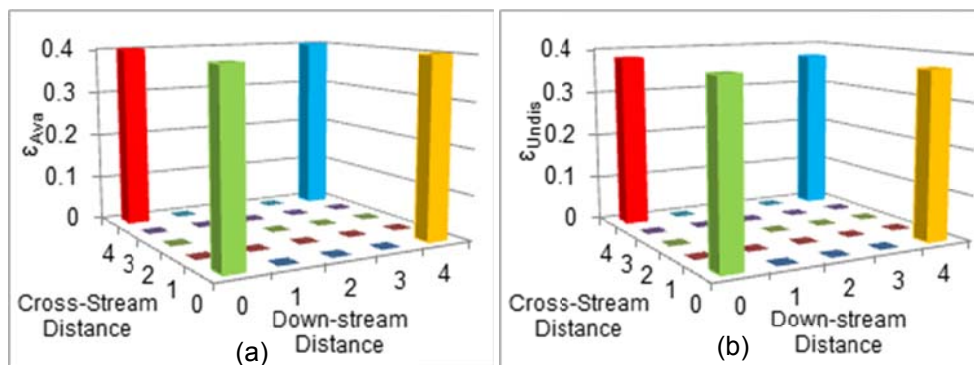


Figure 6.15 (a):  $\epsilon_{ava}$  (b)  $\epsilon_{Undis}$  calculated for T1 – T4.

## 6.6 Testing the Optimisation Model

Once the optimisation model was fully developed and the power calculation was proved valid for multiple turbine deployments, the next step was to ensure that the power optimisation algorithms had

been correctly implemented. This involved checking that the model was correctly deploying turbines in locations of maximum mean available power and re-positioning any turbines whose deployment generated an impact on velocities greater than the SIF. These checks were carried out using the same idealised channel model from the previous power calculation tests for a deployment of three turbines.

### **6.6.1 Testing of Turbine Placement based on Available Power**

Optimisation based only on maximising power was examined first. As per the algorithm, the mean  $P_{ava N_T}$  over a tidal cycle is initially determined without any turbines (i.e.  $N_T=0$ ) and is then recalculated after each turbine is deployed (i.e.  $N_T=1, 2, 3$ ), the results are presented in Figure 6.16. In the figure, the location of the next deployed turbine (turbine number  $N_T+1$ ) are illustrated by the hollow circle while turbines already deployed (up to and including turbine number  $N_T$ ) are shown by filled circles. The contoured power maps show the power available after  $N_T$  turbines have been added, i.e. they show the power available to next turbine taking account of the impacts of all of the previously added turbines. It can be seen that in each of the four cases shown, the next turbine location does indeed correspond to the location of maximum power. It was therefore concluded that the power optimisation algorithm was working correctly.

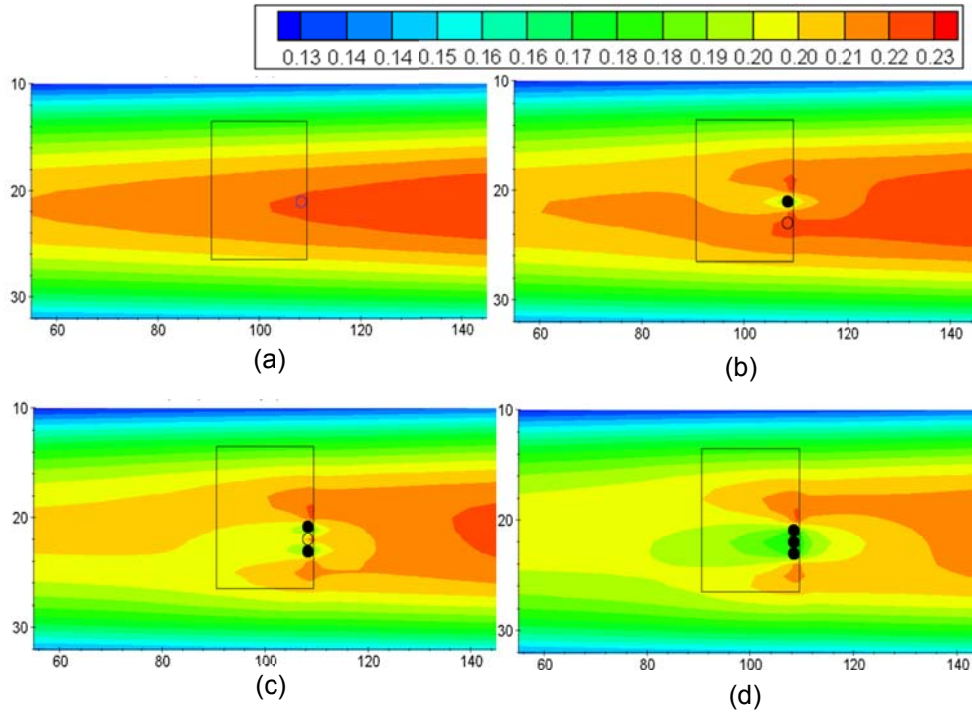


**Figure 6.16: Mean  $P_{ava NT}$  for (a)  $N_T=0$ , (b)  $N_T=1$ , (c)  $N_T=2$ , (d)  $N_T=3$  (legend shows power in MW). Filled circles indicate turbines already added. Hollow circles indicate location of next turbine to be added.**

### 6.6.2 Testing of Turbine Placement based on Velocity Constraint

To test the velocity impact constraint, two turbines were initially placed laterally with  $\Delta S_{Lat}=1RD$ , then the optimisation was run. The positions of T1 and T2 were purposefully placed so that the optimisation model would place T3 in the location of maximum power between T1 and T2. Figure 6.17 shows the turbine configuration along with the peak flood current velocities after deployment of the three turbines. A notable wake is generated downstream of the turbines, with greatest reductions occurring downstream of T3. After deployment of all three turbines, the change in peak velocities exceeds the SIF downstream of T3. T3 is therefore removed and placed in the next location of maximum power. Figure 6.18 shows the mean  $P_{ava NT}$  when T1 and T2 are deployed (represented by the filled white circles) and after T3 is removed (represented by the filled green circles). The location T3 is moved to is shown by the blue

circle, it can be seen that this is indeed the next location of maximum  $P_{ava N_T}$ . Peak current velocities due to the new configuration are shown in Figure 6.19, it can be seen the wake shape and extent has been altered, with smaller velocity reductions at downstream locations close to the turbines which now fall within the SIF. These results have demonstrated that the algorithm is correctly removing turbines if their resulting hydrodynamic impact is too great, and also correctly repositioning them in the next location of maximum available power.

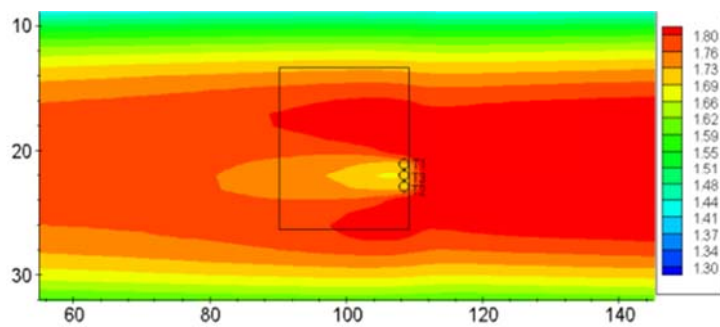


**Figure 6.17: Peak current velocity after 3 turbines deployed (legend shows peak current velocity in m/s).**

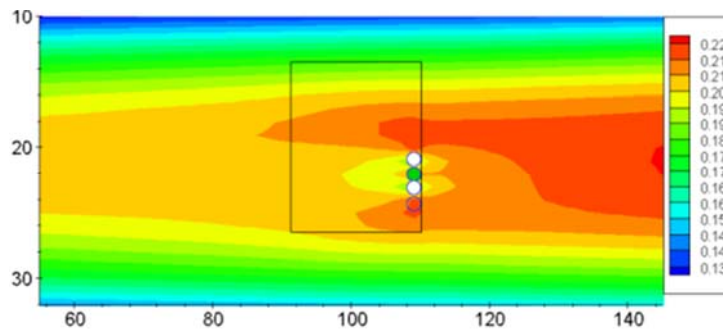


**Figure 6.18: Mean  $P_{ava TN}$  for  $N_T=2$  (legend shows power in MW).**

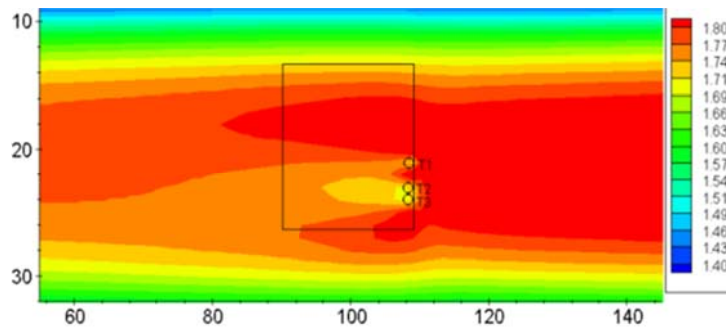


**Figure 6.19: Peak current velocity after T3 is re-positioned (legend shows peak current velocity in m/s).**

## 6.7 Comparison with a Published Study

After establishing that the optimisation model was working correctly, a test was conducted to compare an optimised array output from the model with results from a published study. The study selected for comparison was a novel optimisation model developed by Funke et al. (2014). Their gradient-based algorithm was implemented into a shallow water numerical model. In their optimisation approach, turbines are initially placed in an inline formation and then re-positioned by the model to their optimal locations. Funke's approach was applied to four idealised scenarios and a case study site.

The scenario selected as the most suitable comparison with the model used in this research is an idealised rectangular domain (Figure 6.20 (a)), in which hydrodynamics are driven by an idealised sinusoidal tidal wave and solved using non-stationary shallow water equations. The north, south and east boundaries were specified as no-slip walls and a Dirichlet tidal boundary condition enforcing sinusoidal flow was specified on the western boundary. A tidal period of 10min was defined, resulting in a tidal range of  $\pm 12\text{m}$ . This short tidal period was selected to avoid an excessively large tidal range due to the small basin size. The model simulation time is one full tidal period with a time-step of  $\Delta t = 12\text{s}$ . The model is initialised with 32 turbines placed in an inline 8 x 4 grid. A deployment area constraint is applied to ensure the re-positioned turbines remain inside a

specified extent (320m x 160m). The optimisation did not employ a spacing constraint between adjacent turbines. The model parameters are given in Table 6.5 and the initial and optimised turbine layouts are shown in Figure 6.20. The turbine effects were modelled using an enhanced bed friction approach.

**Table 6.5: Model parameters (Source: Funke et al. (2014)).**

| Parameter                    | Value                      |
|------------------------------|----------------------------|
| Water depth                  | $H=50\text{m}$             |
| Viscosity coefficient        | $\nu=3\text{m}^2/\text{s}$ |
| Turbine friction coefficient | $K=21$                     |
| Acceleration due to gravity  | $G=9.81\text{ m/s}^2$      |
| Water density                | $\rho=1000\text{ kg/m}^3$  |
| Bottom friction coefficient  | $C_b=0.0025$               |
| Turbine radii                | $r=10\text{m}$             |

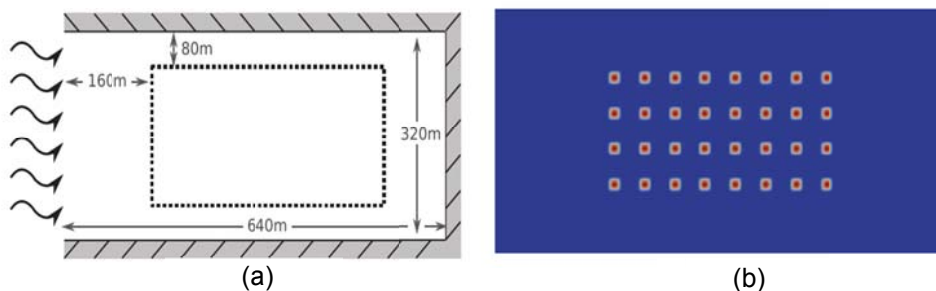


**Figure 6.20: (a) Model scenario selected for comparison (dashed lines show the specified turbine area) (b) initial turbine positions (Source: Funke et al. (2014)).**

For comparison, the optimisation model developed in this research was applied to the model domain described in Section 6.5.1. Minor changes have been made to the model set-up to facilitate a better comparison with the optimisation study of Funke et al. (2014) - the model resolution and turbine diameter were set to 20m. The water depth was maintained at a constant 50m across the channel. The resulting grid cell blockage ratio resulted in a  $C'_T$  value of 1.2. Water density was set to  $\rho = 1000\text{kg/m}^3$ . In keeping with the set-up of

Funke et al. (2014), the deployment area was constrained by a 320m x 160m rectangular area and no minimum spacing between adjacent turbines was employed. The model set-up is illustrated in Figure 6.21.

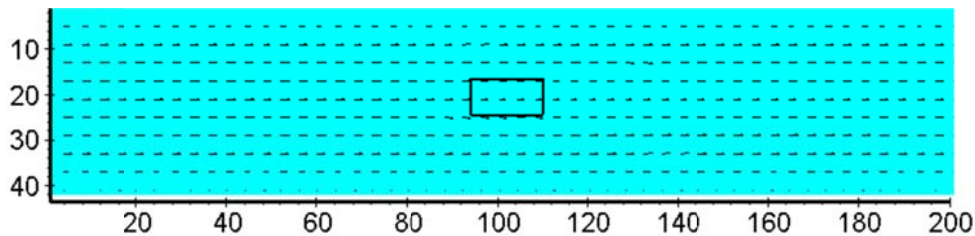
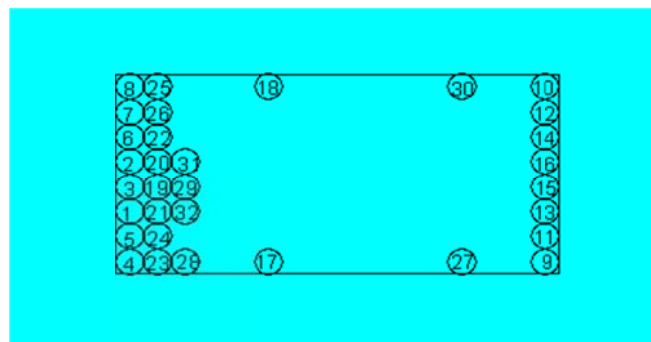
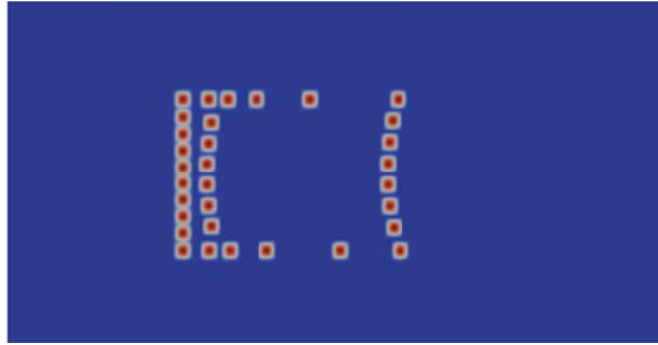


**Figure 6.21: Model domain showing peak velocity vectors and turbine deployment site (deployment site represented by black rectangle and total velocity vectors shown at every 4<sup>th</sup> grid cell).**

The resulting optimised array formations are shown in Figure 6.22. Very close agreement is found between the two array layouts, with both configurations having similar structures comprising a wall of turbines on either edge of the deployment site, with turbines building up from this wall on the inflow side of the site and a few turbines at the top and bottom of the site. The order of turbine deployment in the author's model is depicted by numbers 1 – 32 in Figure 6.22 (a). As the channel is flood-dominant the 1<sup>st</sup> turbine row is deployed at the flood inflow edge, with the 2<sup>nd</sup> row then positioned at the opposite edge of the deployment domain.



(a)

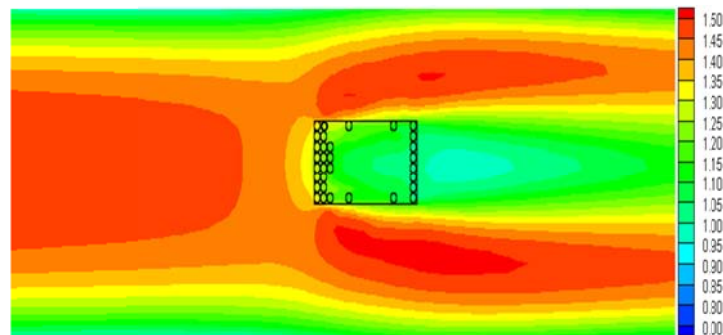


(b)

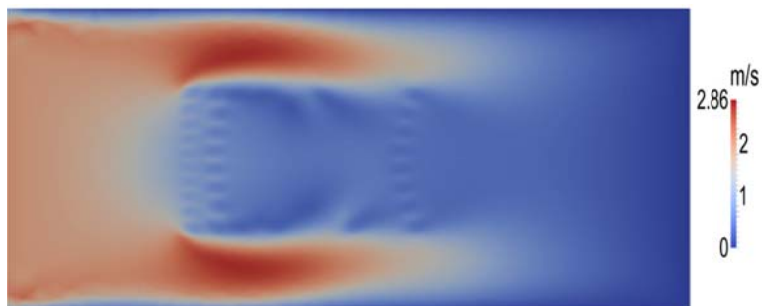
**Figure 6.22: Optimised turbine positions; (a) author's model (b) Funke's model.**

The resulting impact of array deployment on peak flood current velocities was also compared, results for both models are presented in

Figure 6.23. Again similar results are observed, with flow accelerating around the array and a clear wake generated downstream of the array.



(a)



(b)

**Figure 6.23: Peak flood current velocities after array deployment; (a) author's model (b) Funke's model.**

The similarity between the optimised layouts from the two optimisation approaches was encouraging and gave further confidence that the author's optimisation algorithms had been developed and implemented correctly. The model was next applied to other idealised domains and the Shannon estuary case study site.

## 6.8 Model Application: Idealised Domain

Using the developed optimisation model, an idealised channel was used to assess various array configurations. A number of optimised array layouts were determined for different turbine spacing constraints and the array power outputs compared with that from a standard inline arrangement. Energy capture is computed for each array and the resulting impacts on current velocities used as an indicator of the hydro-environmental impacts.

### 6.8.1 Model Set-up

The idealised model domain described in Section 6.5.1 was again used for this study. An array size of twelve turbines was selected. Since the optimisation model is iterative, the simulations were run until all twelve turbines were deployed; this resulted in a simulation time of 156.5 hours. All other model parameters were kept the same as in Section 6.5.1. Principal model details are given in Table 6.6. In all instances, cold start effects had dissipated by the end of the first tidal cycle and the first turbine was added at the end of the third tidal cycle. All model results are presented from the final tidal cycle and for the dominant flood tide.

**Table 6.6: Principal model details**

| Grid Resolution | Turbine Diameter | Simulation Time (hours) | Half time-step (s) | Bed Roughness (mm) | Density (kg/m <sup>3</sup> ) | Depth(m) | C <sub>T</sub> |
|-----------------|------------------|-------------------------|--------------------|--------------------|------------------------------|----------|----------------|
| 16m             | 16m              | 156.5                   | 2.5                | 200                | 1026                         | 50       | 1.3            |

The optimised arrays are determined based on (a) the power optimisation model (Opt\_P) and (b) the power and velocity impact optimisation model (Opt\_P&V). Results from both models are now presented and discussed.

### 6.8.2 Array Configurations

The twelve turbines were deployed in the channel based on the following scenarios:

1. INL: A 4 x 3 inline array with  $\Delta S_{Long} = 5RD$  and  $\Delta S_{Lat} = 5RD$
2. O1: An optimised array with no minimum spacing constraints between turbines
3. O2: An optimised array with  $\Delta S_{Long} = 1RD$  and  $\Delta S_{Lat} = 1RD$
4. O3: An optimised array with  $\Delta S_{Long} = 3RD$  and  $\Delta S_{Lat} = 3RD$
5. O4: An optimised array with  $\Delta S_{Long} = 5RD$  and  $\Delta S_{Lat} = 3RD$

The different turbine spacings were informed by the results of Section 6.2. Different longitudinal spacings were examined, all of which would place any downstream turbines within the wakes of upstream turbines. Lateral spacings were selected which would induce acceleration between turbines. The largest of the selected spacings was chosen for the inline array so all arrays had similar spatial extents, allowing comparisons to be drawn between them.

In all cases, a deployment domain has been specified outside of which turbines cannot be placed (illustrated by the black rectangle in Figure 6.24 - Figure 6.26). Since a constant mean water depth of 50m is specified throughout the channel a minimum deployment depth is not necessary. The resulting array configurations from Opt\_P and Opt\_P&V, based on scenarios (1–5) described above, are presented in Figure 6.25 and Figure 6.26, respectively. It is to be noted that for the O4 array determined using the velocity constraint only ten turbines are placed. This is due to the limitations of deployment domain and turbine spacing specified.

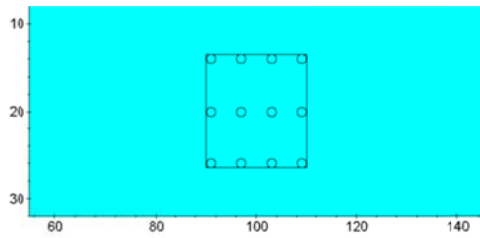


Figure 6.24: Inline array layout.

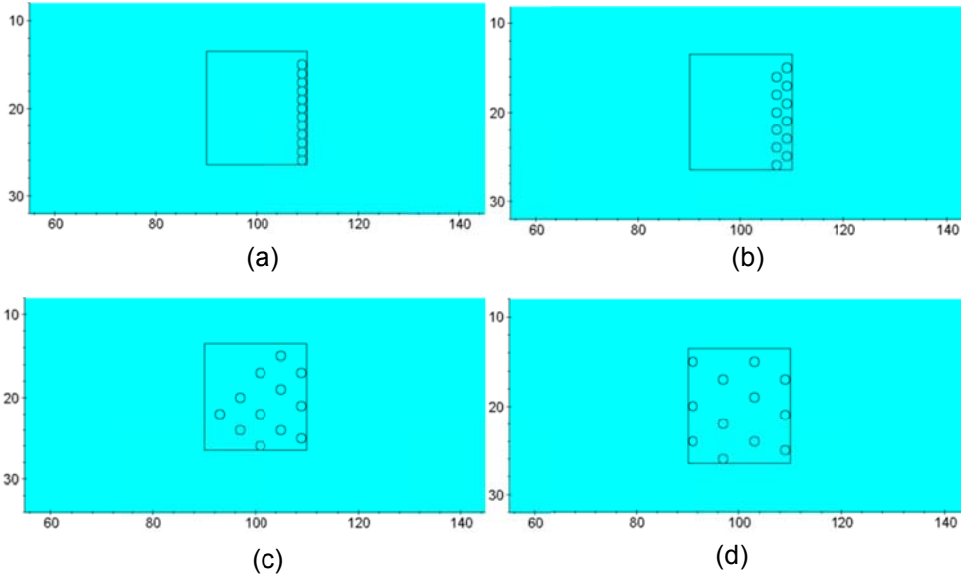


Figure 6.25: Opt\_P array configurations resulting from scenario (a) O1, (b) O2, (c) O3, (d) O4.

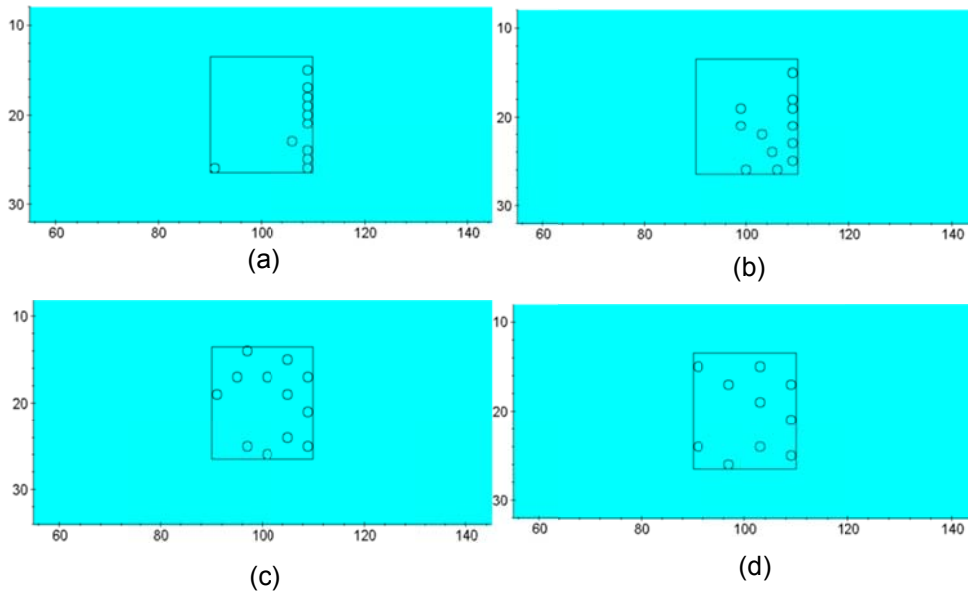


Figure 6.26: Opt\_P&V array configurations resulting from scenario (a) O1, (b) O2, (c) O3, (d) O4.

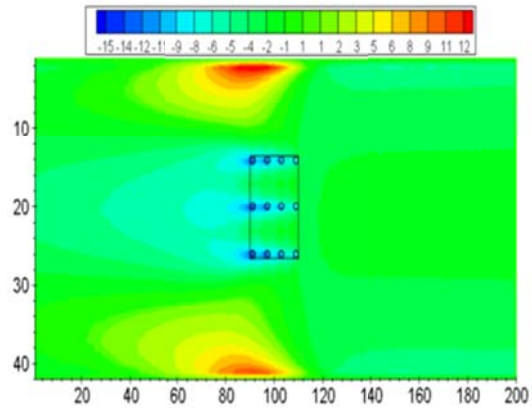
### 6.8.3 Opt\_P Results

The four optimised arrays determined by the Opt\_P model (presented in Figure 6.25) are now assessed in terms of energy capture, array efficiency and resulting impacts on velocities. Results for each optimised array are compared with each other and with those of the regular-spaced inline array (shown in Figure 6.24). Impacts on velocities are demonstrated through peak flood velocity percentage difference plots, in which the difference is calculated using equation (6.1). Extracted power is calculated for each turbine and energy capture per turbine is found by integrating extracted power over a tidal cycle. The total energy capture of the array is then calculated as the sum of energy captured by each individual turbine. Array efficiency is determined based on the undisturbed available power using equation (6.7).

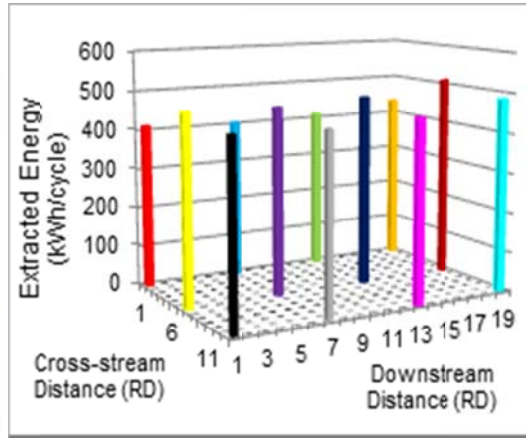
The percentage difference in peak flood current velocities due to inclusion of the tidal arrays, and the energy capture and efficiency ( $\epsilon_{Undis}$ ) of individual turbines over the course of a tidal cycle, are presented in Figure 6.27. Each turbine is represented by a different colour shown in Table 6.7.

**Table 6.7: Legend for turbine colours.**

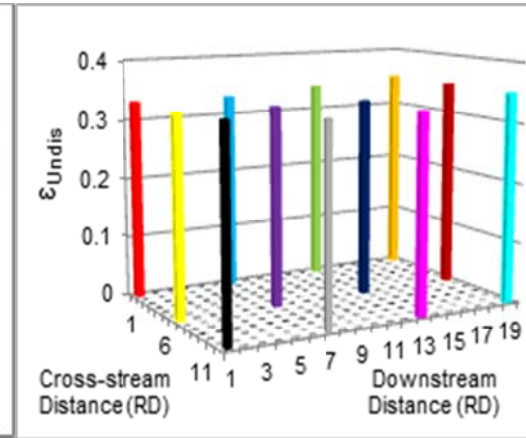
| Turbine # | Bar Colour | Turbine # | Bar Colour | Turbine # | Bar Colour |
|-----------|------------|-----------|------------|-----------|------------|
| 1         | Red        | 5         | Yellow     | 9         | Black      |
| 2         | Cyan       | 6         | Purple     | 10        | Grey       |
| 3         | Green      | 7         | Dark Blue  | 11        | Magenta    |
| 4         | Orange     | 8         | Brown      | 12        | Light Blue |



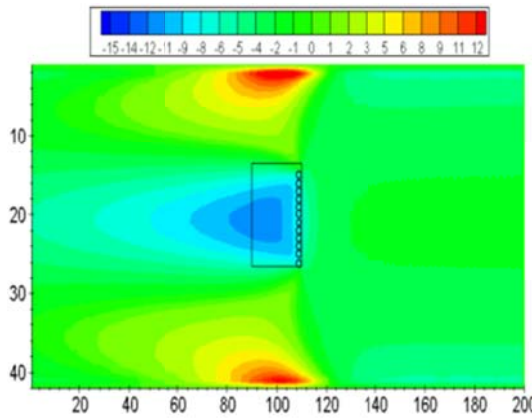
(a1)



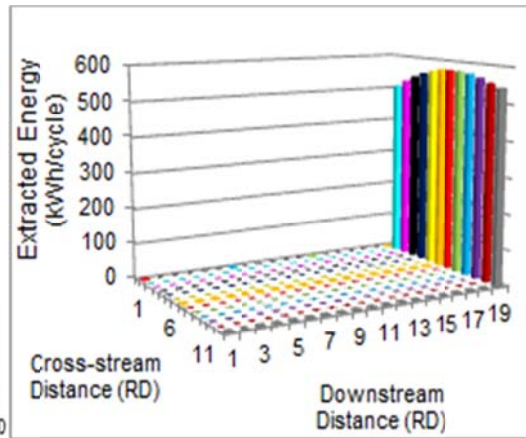
(b1)



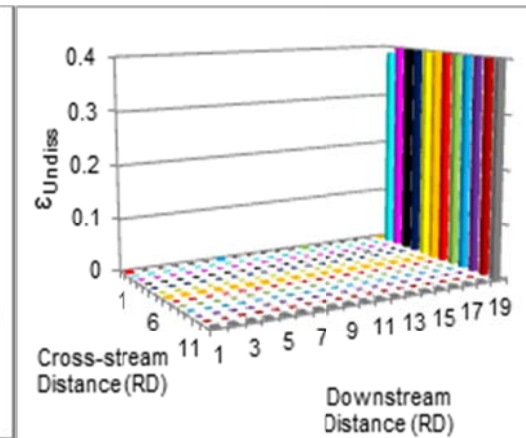
(c1)



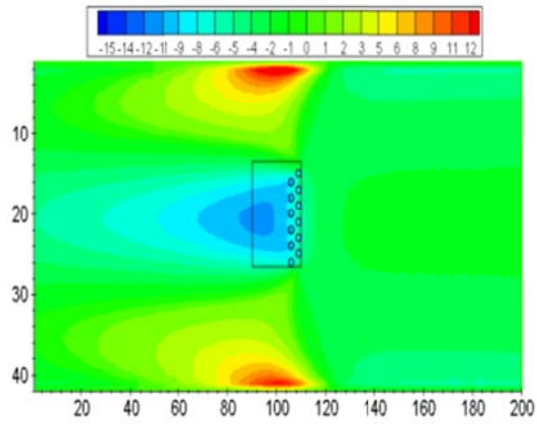
(a2)



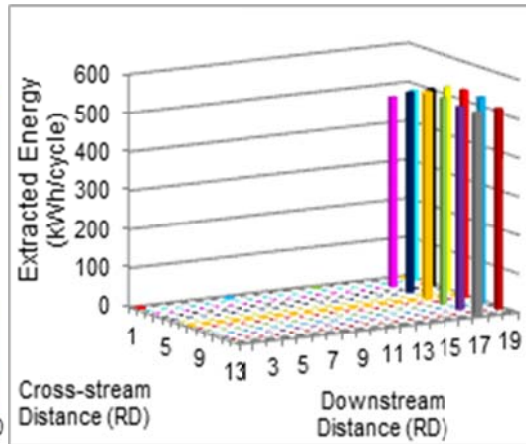
(b2)



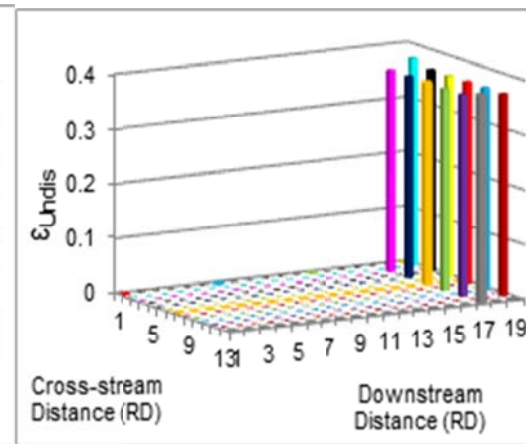
(c2)



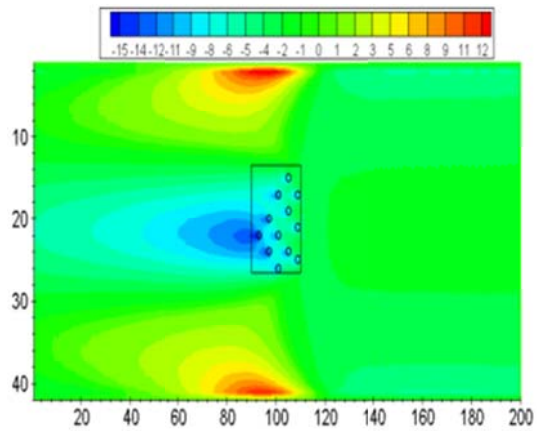
(a3)



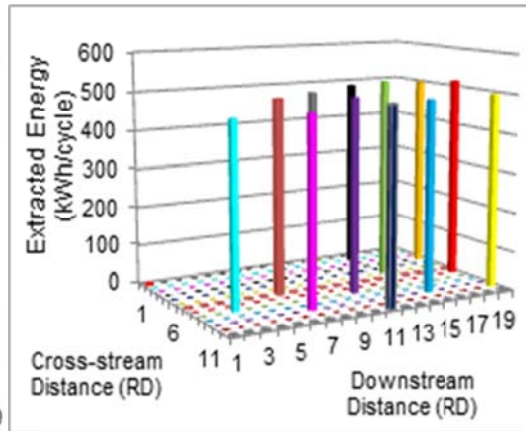
(b3)



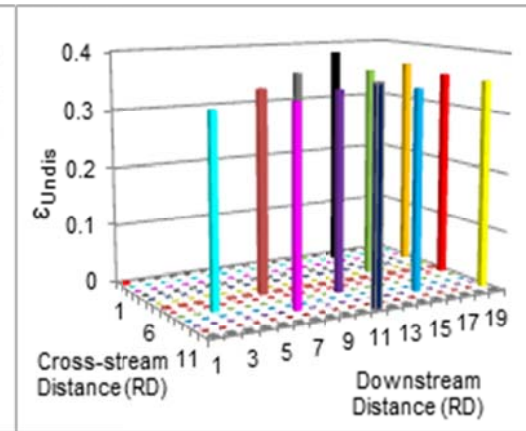
(c3)



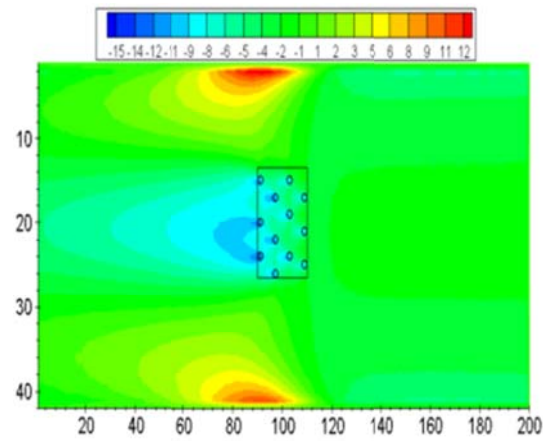
(a4)



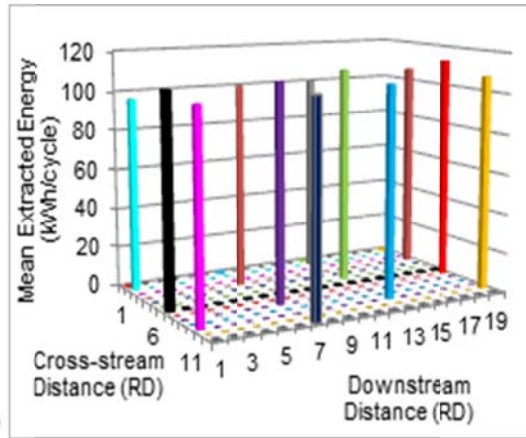
(b4)



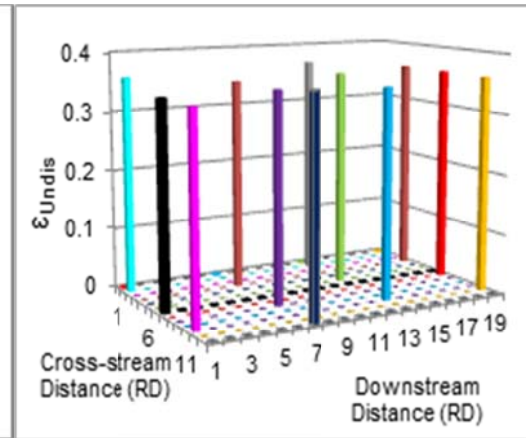
(c4)



(a5)



(b5)



(c5)

**Figure 6.27: (a) % difference in peak flood current velocities (b) energy capture (kWh/cycle) (c) turbine efficiency ( $\epsilon_{Undis}$ ), for scenarios 1-5 (INL-O4)**

The total energy captured and undisturbed efficiency of each array is presented in Table 6.8. The energy capture and  $\epsilon_{Undis}$  for the inline array is lower than that for any of the optimised arrays. The poorer performance of the inline array is due to the positioning of downstream turbines in the wakes of upstream turbines, whilst the performance of the optimised arrays is enhanced by making use of accelerated flows between turbines.

**Table 6.8: Total mean energy capture (kWh/cycle) and undisturbed efficiency of each array.**

| Scenario | Array Symbol | Total Energy Captured (kWh/cycle) | $\epsilon_{Undis}$ |
|----------|--------------|-----------------------------------|--------------------|
| 1        | INL          | 5445                              | 0.33               |
| 2        | O1           | 6671                              | 0.40               |
| 3        | O2           | 6239                              | 0.37               |
| 4        | O3           | 5932                              | 0.35               |
| 5        | O4           | 5920                              | 0.36               |

The array with the highest energy capture is O1, the scenario with no minimum spacing constraints specified between turbines. Comparing the  $\epsilon_{Undis}$  of each array, O1 is shown to be the most efficient, with each turbine reaching the desired efficiency of 0.4 (Figure 6.27(c2)). Without a spacing constraint, the optimum layout with regard to power capture is in a fence stretched across the channel. No turbines are placed downstream of other turbines, therefore reductions in power available for extraction due to turbine wakes is not a concern. The energy capture of each turbine decreases marginally as the devices are deployed (Figure 6.27 (b2)), having a maximum capture of 576kWh by turbine 1 and dropping to 511kWh by turbine 12. This is due to lower velocities nearer the channel walls compared to those in the centre and not a result of velocity changes due to energy removal. This is verified by the turbine efficiencies (see Figure 6.26 (c2)); although a drop in energy capture is found for turbines placed near the channel walls, all turbines have  $\epsilon_{Undis}=0.4$ .

The second highest energy capture is observed for O2, in which 1RD lateral and longitudinal spacings are used. The undisturbed array efficiency of 0.37, while lower than the 0.4, is still higher than the inline array efficiency of 0.33. The better performance of this configuration (relative to the inline) is a result of downstream turbines being placed outside the wakes of neighbouring turbines. The energy capture of the turbines in the centre of the channel is slightly higher than that of the turbines nearer the channel sides but this again is mostly due to the natural lowering of velocities from the centre of the channel outwards towards the walls. For instance turbine 3 captures 529kWh, whilst turbine 12, positioned at the edge, captures 490kWh, however, both turbines have the same  $\epsilon_{Undis} = 0.37$ . The variation in current velocities across the channel is shown in Figure 6.28

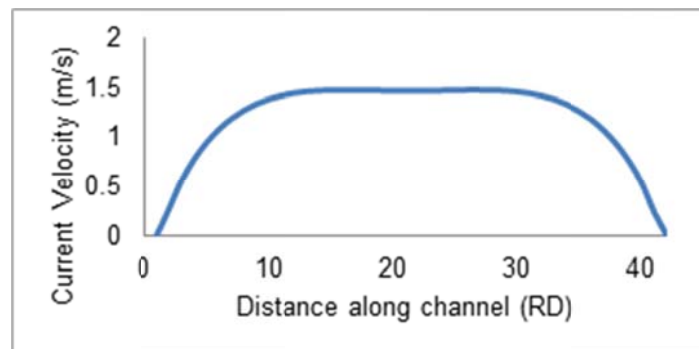


**Figure 6.28: Undisturbed current velocities across the channel.**

Arrays O3 and O4 capture similar amounts of energy and have similar efficiencies, this is a due to the similar spacing constraints applied. The reduced performance in these configurations compared to O1 and O2 is a result of some turbines being placed inline, or almost inline, and therefore partially within the wakes of upstream turbines. For instance, consider array O3, turbine 12 is positioned 7RD downstream of turbine 6, which is not sufficiently far apart for full velocity recovery of turbine 6's wake to take place before flow reaches turbine 12. As result turbine 12 suffers reduced efficiency and captures only 466kWh compared to the 497kWh captured by turbine 6. The reduced performance of O3 and O4 compared to O1

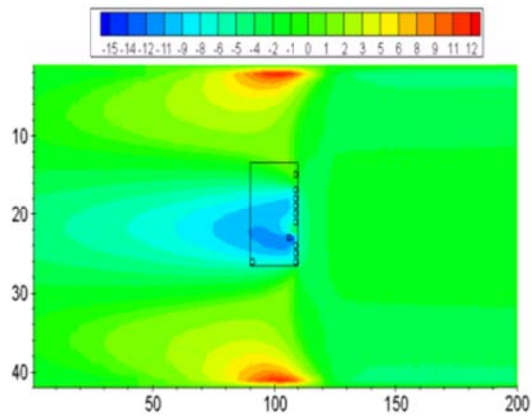
and O2 is further demonstrated in their lower efficiencies of 0.35 and 0.36, respectively.

The array efficiencies confirm the results of the energy capture assessment, with better performance achieved by the optimised arrays compared to the inline configuration which had the poorest performance with an array efficiency 0.33. This is a direct result of the inline turbines being positioned in the wakes of others, leading to reductions in available resource, and hence lower energy capture.

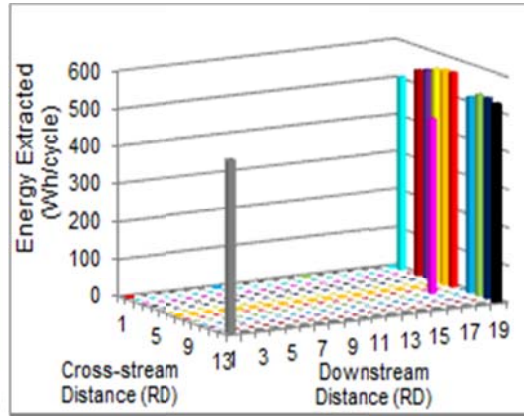
Figure 6.27(a) shows percentage changes in peak flood current velocities due to deployment of each array. For the inline configuration, the cumulative effect of energy extraction by each subsequent downstream turbine means the velocity deficit increases through the array, reaching a maximum at the fourth turbine in each row. On the ebb tide, the first turbine in each row will experience similar levels of reductions in velocities. Considering the optimised arrays, O1 and O2 generate similar wake shapes, both producing wakes with larger widths than O3 or O4. This is due to the array configurations, with all turbines in O1 placed in a fence and turbines in O2 placed in a two column fence formation. O1 produces greater changes in velocities, which exist further downstream, than O2, this is due to interactions between the turbines enhancing the wake. O3 generates strong deficits downstream of turbines placed at the bottom end of the turbine domain, this is a result of the cumulative effects of energy extraction of turbines placed inline, or close to inline, for instance turbine 6 and 12. Deployment of the O4 array results in the smallest changes in peak flood velocities, with the wake extent and magnitude being reduced from the other optimised arrays. This is due to the increased turbine spacings, leading to reduced cumulative wake impacts and adverse turbine interactions.

#### **6.8.4 Opt\_P&V Results**

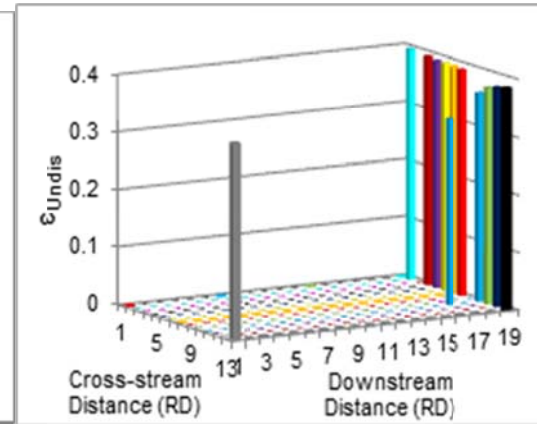
The array scenario results obtained using the Opt\_P&V model are now discussed. The impact on peak flood velocities, energy capture per cycle and undisturbed turbine efficiencies for the optimised arrays determined based on the velocity constraint are presented in Figure 6.29. Since the model was only able to deploy 10 of the 12 turbines in the O4 array, these results are excluded from the discussion as they are not comparative to the other arrays. The total energy captured by array O1, O2 and O3 is given in Table 6.9 along with their efficiencies.



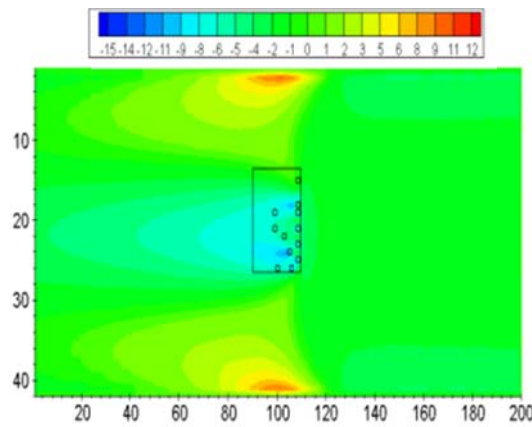
(a1)



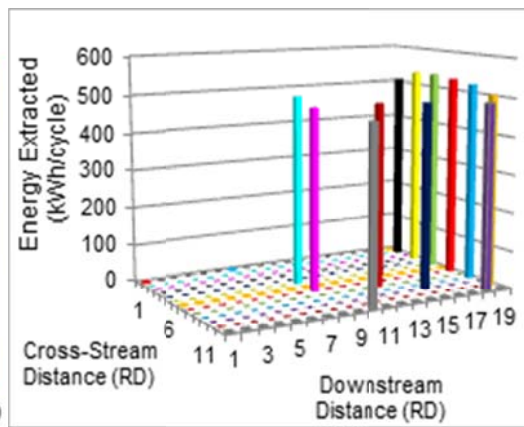
(b1)



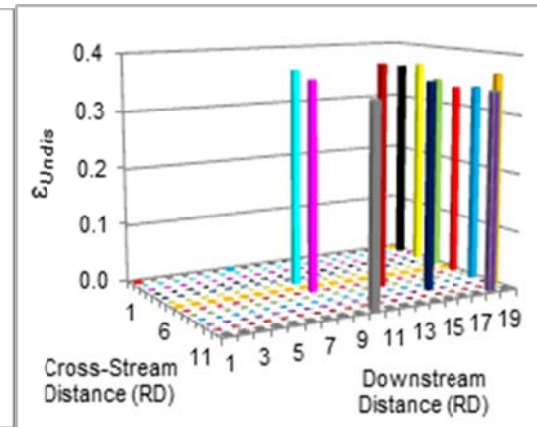
(c1)



(a2)



(b2)



(c2)

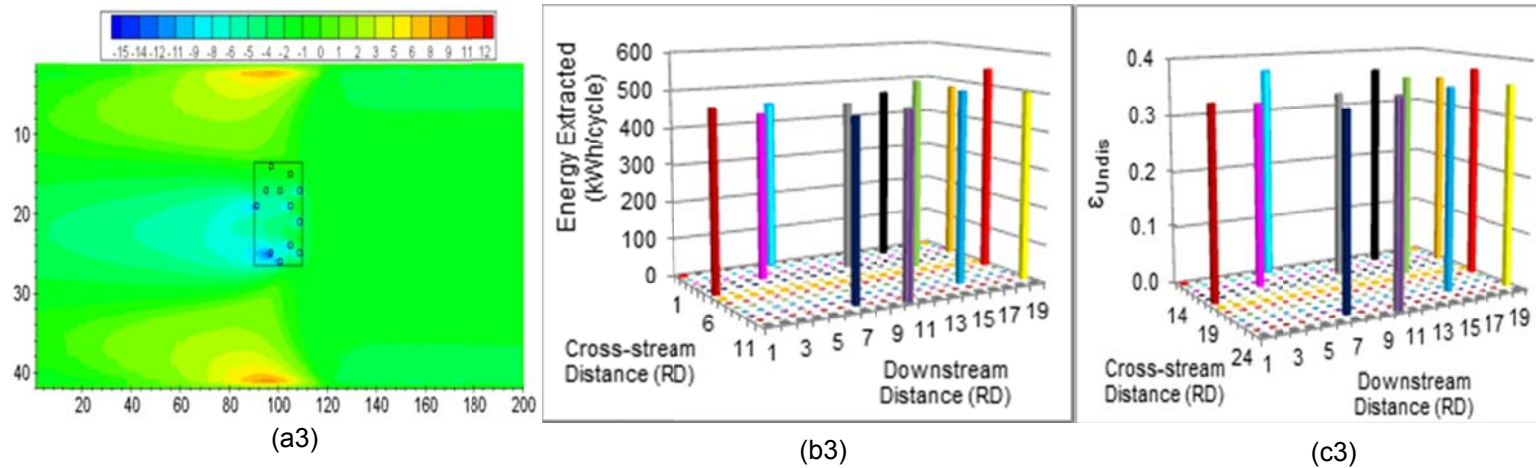


Figure 6.29: (a) % difference in peak flood current velocities (b) energy capture (kWh/cycle) (c) turbine efficiency ( $\epsilon_{Undis}$ ), for scenarios (1) O1, (2) O2, (3) O3.

**Table 6.9: Total energy captured (kWh/cycle) and power coefficient,  $C_{P\_Undis}$ , for array O1, O2, O3**

| Scenario | Array Symbol | Total Energy Captured (kWh/cycle) | $\epsilon_{Undis}$ |
|----------|--------------|-----------------------------------|--------------------|
| 2        | O1           | 6376                              | 0.38               |
| 3        | O2           | 6044                              | 0.36               |
| 4        | O3           | 5809                              | 0.35               |

Comparing results from Figure 6.27(a) and Figure 6.29 (a) it can be clearly seen that applying the velocity constraint leads to considerable reductions in changes to velocities. Looking at array O1, two turbines have been moved from the fence formation and placed downstream. As a result, the wake width narrows and the wake magnitude immediately downstream of the array is reduced. For O2, a substantial decrease in changes to velocity is observed. A number of turbines have been re-positioned from the two column formation to a more scattered layout with a clear improvement to the impact on velocities as a result of less merging of adjacent wakes. The downstream wake has been reduced to mostly single wakes behind individual turbines, the magnitude of which is relatively low compared to the wake generated by the O2 layout determined without the velocity constraint. A substantial improvement is also noted for O3. Turbines have been moved further apart and the wake downstream of the array is significantly reduced, with maximum changes in velocities dropping from around 15% to approximately 10%. High percentage differences in velocities are observed at the channel walls in all cases, this is a result of low velocities occurring near the walls (Figure 6.28).

Re-positioning of turbines has a marginal impact on the energy captured compared to the total capture of each array, with reductions in total energy captured reduced by 295kWh, 195kWh and 123kWh for O1, O2 and O3, respectively. After applying the velocity

constraint, O1 is still the most efficient array, however, the difference in all 3 arrays is relatively minimal. This is further demonstrated by the array efficiencies.  $\varepsilon_{Undis}$  of individual turbines is shown in Figure 6.29 (c1-3) and the average  $\varepsilon_{Undis}$  for each array given in Table 6.9. For O1,  $\varepsilon_{Undis}$  is reduced from 0.4 to 0.38, however, this is still a desirable efficiency and is the highest of the arrays.  $\varepsilon_{Undis}$  for O2 drops from 0.37 to 0.36, but this is a marginal difference. And  $\varepsilon_{Undis}$  for O3 remains at 0.35 as the decrease in energy output (123kWh) is minimal.

Application of the array optimisation model has demonstrated that the optimised arrays determined by the model are more efficient than a standard, regularly-spaced, inline array. Applying the velocity constraint is proven to reduce the impact of energy extraction on current velocities, as desired, whilst maintaining similar levels of energy capture by the arrays to those achieved by the arrays optimised with regard to maximising power only.

## **6.9 Case Study of the Shannon Estuary**

The optimisation model has been tested and applied to an idealised domain to demonstrate its ability to determine optimised turbine arrays which capture more energy and generate smaller hydro-environmental impacts than regularly-spaced, inline arrays. To demonstrate the model's applicability to a real tidal environment, it was applied to the Shannon estuary case study site.

### **6.9.1 Hydrodynamic Numerical Model**

The nested optimisation model was applied to the Shannon with a similar setup to the 2D multi-scale nested model (MSN) described in Chapter 5. Two levels of one-way nesting are applied to the Shannon estuary model at a 3:1 spatial nesting ratio to determine optimised arrays and simulate the effects of the resulting energy extraction at spatial resolutions of 189x189m for the coarse grid (CG189), and

63x63m and 21x21m for the nested fine grids (NG63 and NG21). The model extents for each domain are shown in Figure 6.30. The Shannon MSN model set-up and validation were previously presented in Sections 5.5.2 and 5.5.3, respectively, and the principal model parameters are listed again in Table 6.10.

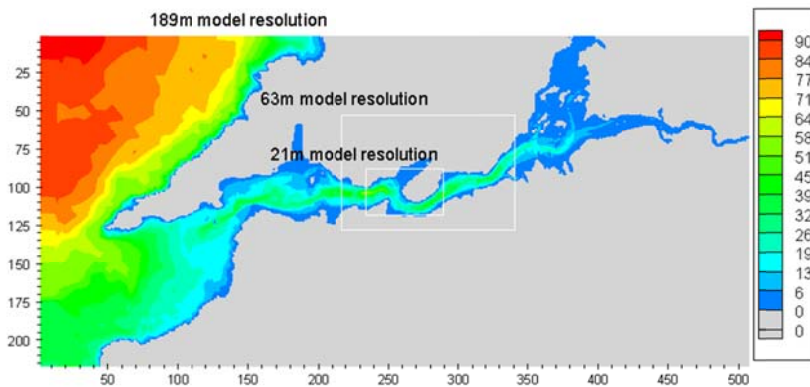


**Figure 6.30: Extent of domains and mean water depths for Shannon model (legend shows mean water depth in m).**

**Table 6.10 Principal Model Parameters of the MSN Shannon Estuary Model.**

| Model | Grid   | Grid Spacing (m) | No Cells (x-direction) | No Cells (y-direction) | Time -step (s) | Bed Roughness (mm) | Eddy Viscosity Coeff. |
|-------|--------|------------------|------------------------|------------------------|----------------|--------------------|-----------------------|
| CG189 | Parent | 189              | 507                    | 217                    | 36             | 50                 | 0.1                   |
| NG63  | Child  | 63               | 1521                   | 651                    | 12             | 50                 | 0.1                   |
| NG21  | Child  | 21               | 4563                   | 1953                   | 4              | 50                 | 0.1                   |

### 6.9.2 Model Scenarios

The resource assessment of the Shannon estuary presented in Chapter 4 highlighted three main areas of high tidal resource and identified suitable deployment locations based on power availability and flow direction, which are illustrated in Figure 6.31. Based on these findings a deployment area was selected for this assessment, highlighted by the red box in Figure 6.31.

Eighteen turbines were deployed in the nested Shannon model based on the following scenarios:

1. INL: A 6 x 3 inline array with no minimum spacing constraints
2. O1: An optimised array with no minimum spacing constraints
3. O2: An optimised array with  $\Delta S_{Long} = 2RD$  and  $\Delta S_{Lat} = 2RD$



**Figure 6.31: Suitable deployment locations based on power availability and flow direction.**

The simulated turbine diameter was set to 21m to match the grid resolution of the finest nested domain, thereby facilitating simulation of flow between individual turbines. Due to the different grid resolutions and varied mean water depth across the estuary a constant  $C'_T$  value was considered not suitable, therefore, the model calculated a  $C'_T$  value for each turbine added to a domain using equation (6.2).

As with the application to the idealised model, a deployment domain was specified outside of which turbines cannot be placed (illustrated by the black rectangle in (a) Figure 6.32 (CG189), Figure 6.34 (a) (NG63) and (b) (NG21). Since mean water depth varies throughout the estuary a minimum deployment depth,  $H_{min}$ , is required.  $H_{min}$  is specified at 25m relative to mean water depth to ensure the turbines are fully submerged at all times. To demonstrate the minimum depth constraint was working, optimised turbine positions were plotted across the 21m nested domain. This is illustrated in Figure 6.32 which shows the O1 array and the power available across the

deployment domain after energy extraction. The areas where mean water depth ( $H$ ) was less than  $H_{min}$  are shaded grey.

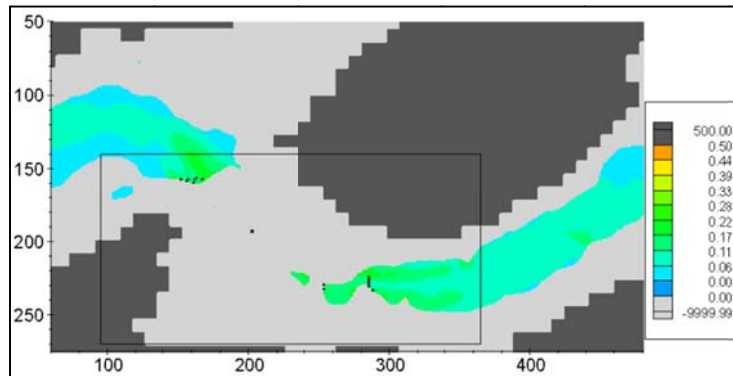


**Figure 6.32: NG21 optimised array configuration (locations where  $H < H_{min}$  are shaded grey, legend shows  $P_{ava N_T=18}$  in MW).**

### 6.9.3 Array Configurations

The O1 and O2 array optimisation scenarios were both initially run based on the power maximisation algorithm (Opt\_P). The optimisation process was simulated on each of the nested grids to study the effect of spatial resolution on the final array layouts. For the CG189 grid, only the inline array was simulated (Figure 6.32) and at ORD spacing all turbines could be placed in a single grid cell. Running the optimisation was pointless as the large grid cell size (189x189m) meant that it merely resulted in the turbines being divided over two grid cells. Finally, as a demonstration of its applicability, the power and velocity impact optimisation (Opt\_P&V) was applied to determine optimised arrays using the O1 scenario. The resulting array configurations from the Opt\_P and Opt\_P&V optimisations are presented in Figure 6.34 and Figure 6.35, respectively.

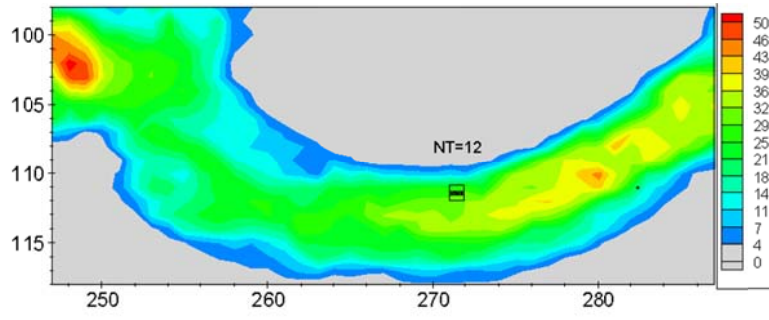


**Figure 6.33: Opt\_P array configurations for CG189 Inline array.**

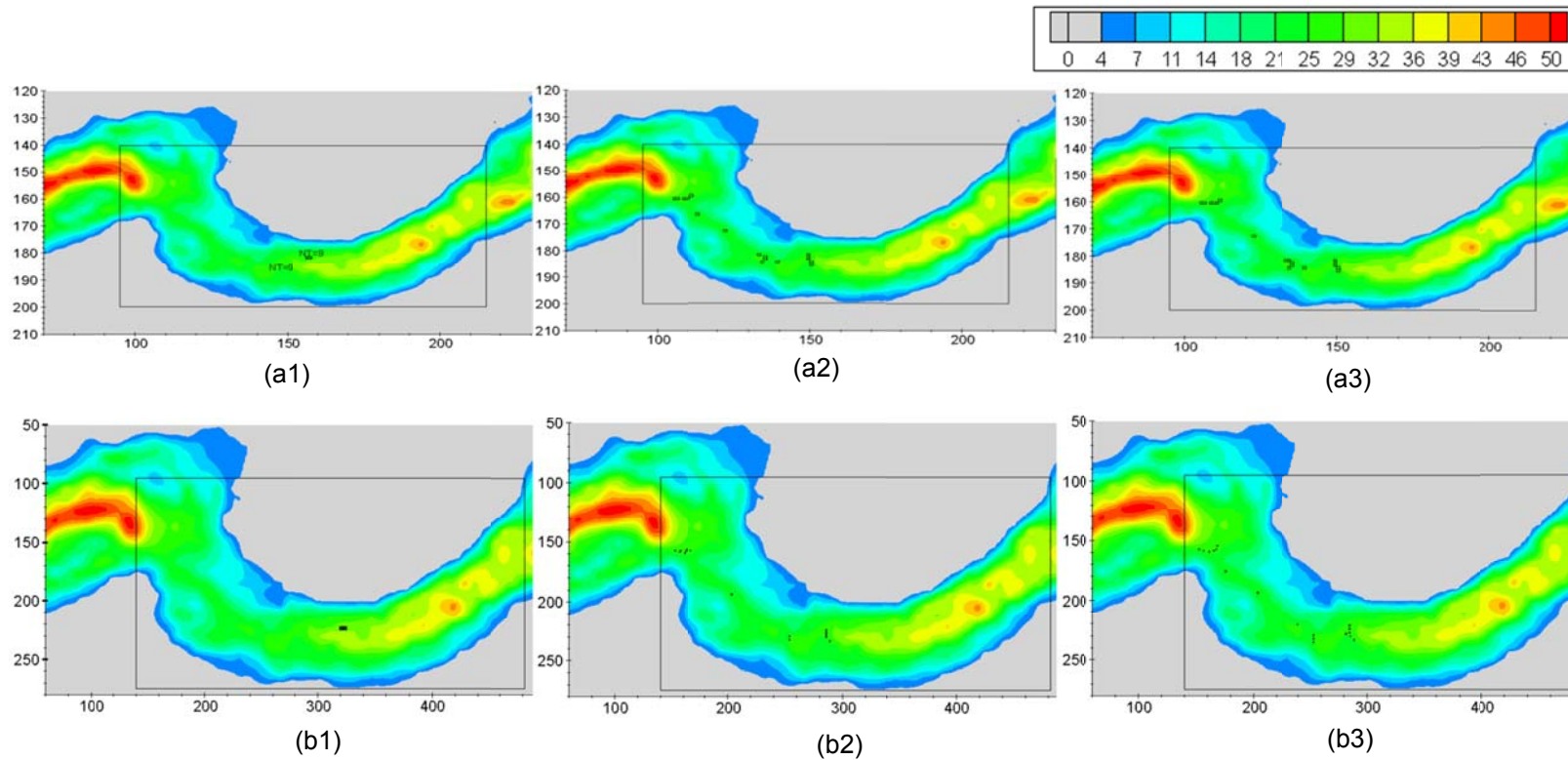


**Figure 6.34: Opt\_P array configurations for (a) NG63, (b) NG21, resulting from scenario (1) INL, (2) O1, (3) O2 (contour shows mean water depth in m).**

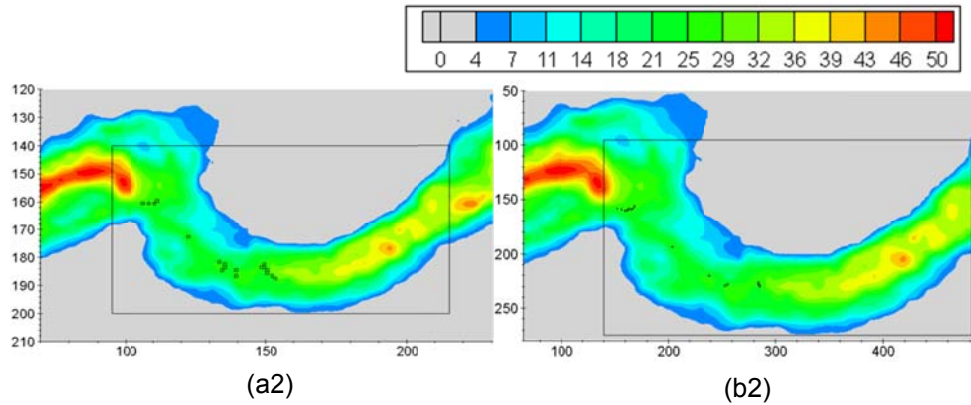


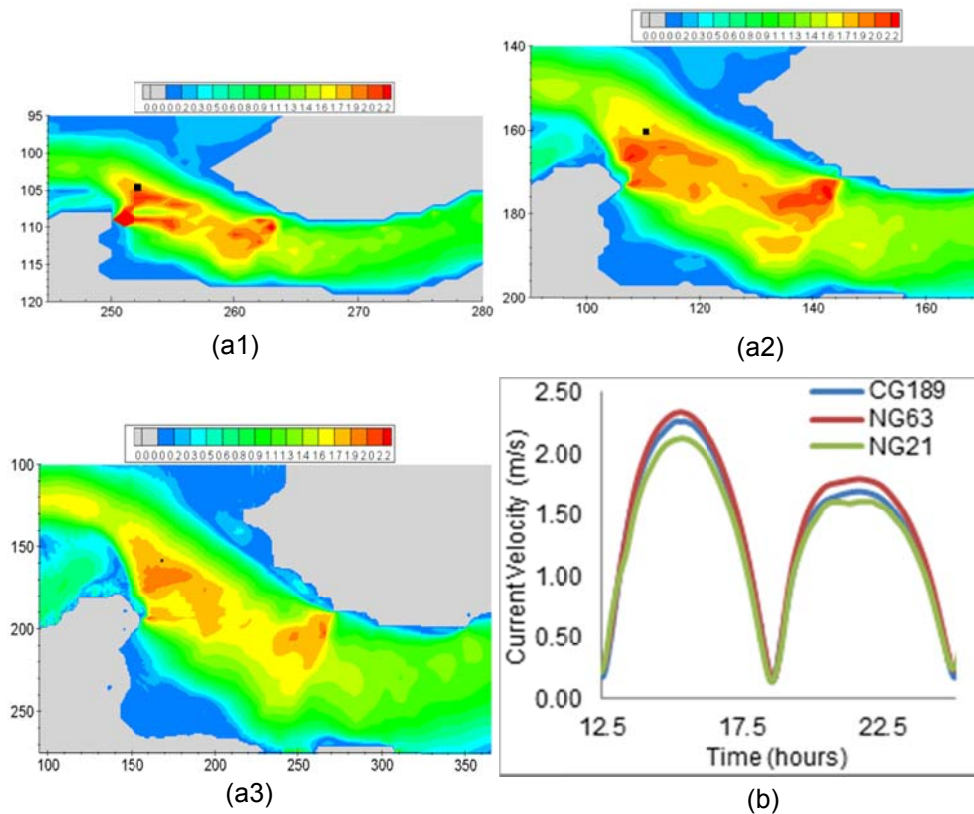
**Figure 6.35: Opt\_P&V array configurations for (a) NG63, (b) NG21, resulting from scenario (2) O1 (contour shows mean water depth in m).**

The grid resolution of the NG63 model is three times the turbine diameter, hence multiple turbines could be deployed in a single grid cell, depending on the specified spacing constraint. However, this only occurred for the inline configuration, with the eighteen turbines being placed evenly over two adjacent grid cells. For the optimised configurations only one turbine was placed per cell (see Figure 6.34 (a2) and (a3)). It was found that when a turbine was deployed it lowered the available power in that cell to such an extent that it was no longer the location of maximum available resource; hence no other turbines were deployed in that cell. For the finest resolution model, NG21, the grid spacing was equal to the turbine diameter so only one turbine could be deployed in a single grid cell.

A similar pattern is observed for the optimised arrays determined in the NG63 and NG21 domains. This was mainly due to the fact that only one turbine is placed in any one cell in both models. Combined with the finer resolutions this means these models better capture energy extraction and turbine impacts/interactions.

Whilst the optimised arrays for NG63 and NG61 showed similar patterns, there are differences in the layouts. This is mainly due to the fact that there were differences in the velocity fields computed across the deployment domain at the different grid resolutions. This is as would be expected. The velocities computed across each

domain, whilst similar, were not exactly the same; hence, the locations of maximum power computed by the optimisation models will not be located in exactly the same places for the different model resolutions. This is illustrated in Figure 6.36 which shows contour maps of peak flood velocities computed by the three different grids and time-series of current velocities at a comparison point (shown as the black square in Figure 6.36(a)). Since power has a cubic dependence on velocities, these velocity differences might result in differences in the resulting energy capture by the modelled arrays at the different grid resolutions depending on where the turbines are located.

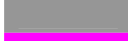
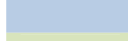


**Figure 6.36: (a) Undisturbed peak flood current velocities across (1) CG189, (2) NG63, (3) NG21 model domains, (b) time trace velocities for each domain.**

### 6.9.4 Energy Capture

Energy capture per tidal cycle was determined for each simulated array by integrating the extracted power output of each turbine over the last tidal cycle of the simulation and summing across turbines. The results are presented in Figure 6.37. Each individual turbine is again assigned a colour (listed in Table 6.11). Where more than one turbine is deployed in a grid cell, the selected reference colour is that of the first turbine deployed in that cell.

**Table 6.11 Legend for turbine colours.**

| Turbine # | Bar Colour  | Turbine # | Bar Colour  | Turbine # | Bar Colour  |
|-----------|---|-----------|---|-----------|---|
| 1         |    | 7         |    | 13        |    |
| 2         |    | 8         |    | 14        |    |
| 3         |    | 9         |    | 15        |    |
| 4         |    | 10        |    | 16        |    |
| 5         |   | 11        |   | 17        |   |
| 6         |  | 12        |  | 18        |  |

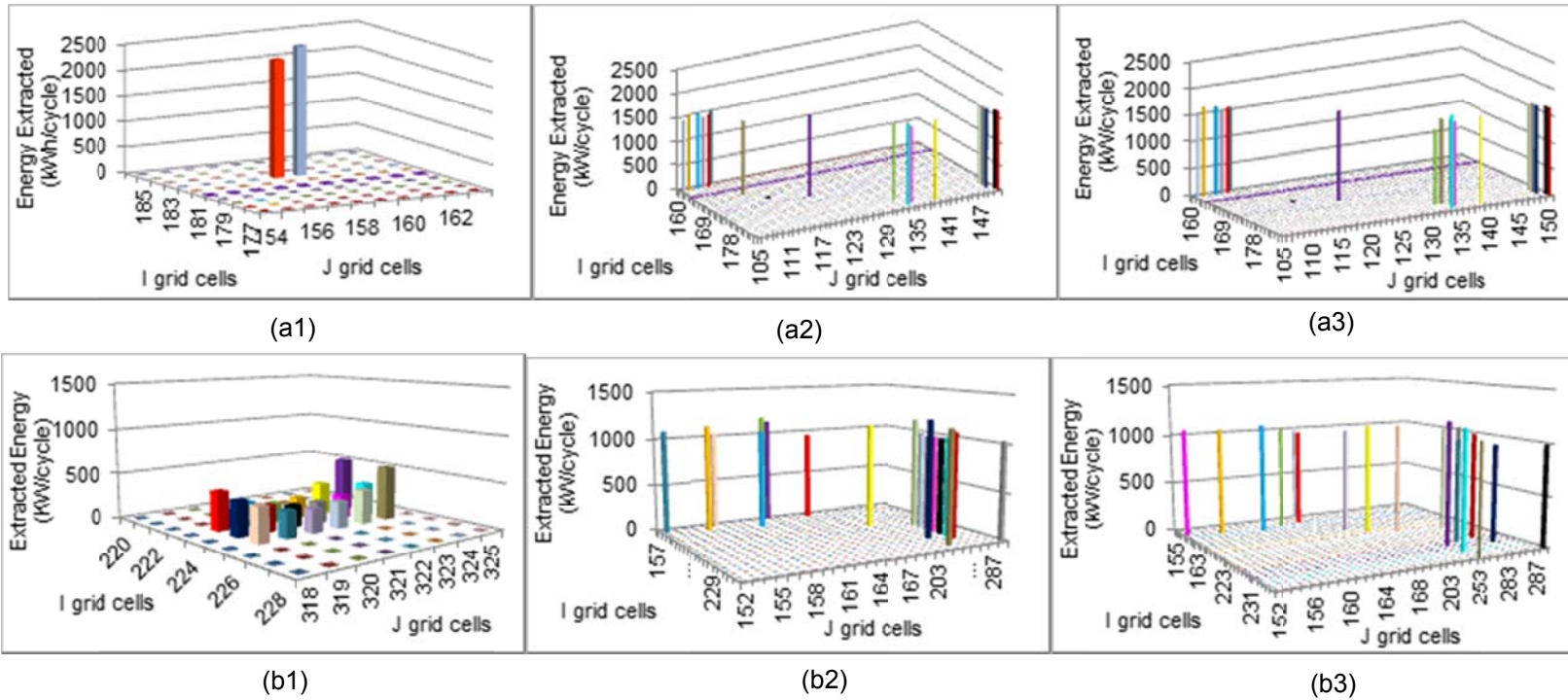


Figure 6.37: Energy capture (kWh/cycle) for (a) NG63 and (b) NG21 resulting from scenario (1) INL, (2) O1, (3) O2.

Comparison of the energy captured by each array is made using the undisturbed turbine efficiencies ( $\epsilon_{Undis}$ ) which are calculated relative to the undisturbed available resource for each model grid resolution. The resulting  $\epsilon_{Undis}$  for the inline array in CG189 and for each array at the NG63 and NG21 grid resolutions are given in Table 6.12.

**Table 6.12:  $\epsilon_{Undis}$  for each array modelled within each domain.**

| Model | $\epsilon_{Undis}$ |      |      |
|-------|--------------------|------|------|
|       | INL                | O1   | O2   |
| CG189 | 0.22               | ---  | ---  |
| NG63  | 0.19               | 0.35 | 0.35 |
| NG21  | 0.10               | 0.33 | 0.33 |

The low resolution of CG189 meant that the inline array fitted within a single grid cell. The resulting  $\epsilon_{Undis}$  of the array was 0.22 which is quite low considering the turbines are modelled to have a  $C_p$  of 0.4. The reason for this lower than expected performance was the reduction in power availability due to energy extraction by the turbines, and the resulting lowering in the grid cell velocity.  $\epsilon_{Undis}$  of the inline array in NG63 (0.19) is lower than in CG189 and it is lower again for NG21 (0.10). This was assumed to be due to the more accurate simulation of turbine velocity impacts and turbine interactions at the higher resolutions. NG21 is assumed to be the most accurate model of the three as only a single turbine is placed in each grid cell.

The effects of energy removal by one turbine on the power availability and subsequent energy removal by another can be clearly seen in Figure 6.37(b1) which shows the energy capture by turbines in the inline array for NG21. Power to the outside turbines is reduced for those periods when flow is travelling through the array and their upstream/downstream neighbours are removing energy. They therefore experience reduced power availability for half of the tidal cycle (on either the ebb or flood tide). As a result it can be seen that

the energy extracted by the outer turbines of the inline array is roughly half that extracted by any of the turbines in the optimised arrays (Figure 6.37(b2/b3)). Looking at the inner turbines of the inline array, their rates of energy extraction were lower than the outer turbines as they suffered reduced power availability over the full tidal cycle (on both flood and ebb tides).

As was hoped, the optimised arrays were found to give improved performance from the inline arrays for both the NG63 and NG21 domains. For NG63,  $\epsilon_{Undis} = 0.35$  for both of the optimised arrays and this is substantially higher compared to the 0.19 performance of the inline array and is much closer to the turbine  $C_p$  of 0.4. For NG21,  $\epsilon_{Undis}$  was 0.33 and was therefore again much improved relative to the 0.1 for the corresponding inline array. The improvements in performance of the optimised arrays was primarily due to the fact the optimisation program will not place a turbine such that it was overly adversely affected by its neighbours and will not therefore suffer from any significant reductions in power availability. However, given the spatial constraints, it was impossible for the optimisation routines to place turbines such that they completely avoid any adverse interaction, hence the small reduction in the expected array efficiencies compared to the turbine  $C_p$ . Overall, the optimisation algorithm was demonstrated to be successful in increasing the energy capture by a turbine array and achieving array efficiencies close to the value of the turbine  $C_p$ .

### **6.9.5 Impact on Current Velocities**

The impact of array deployment on current velocities is shown in Figure 6.38, which shows the relative change in peak flood velocities for INL in CG189 and each array in the NG63 and NG21 domains.

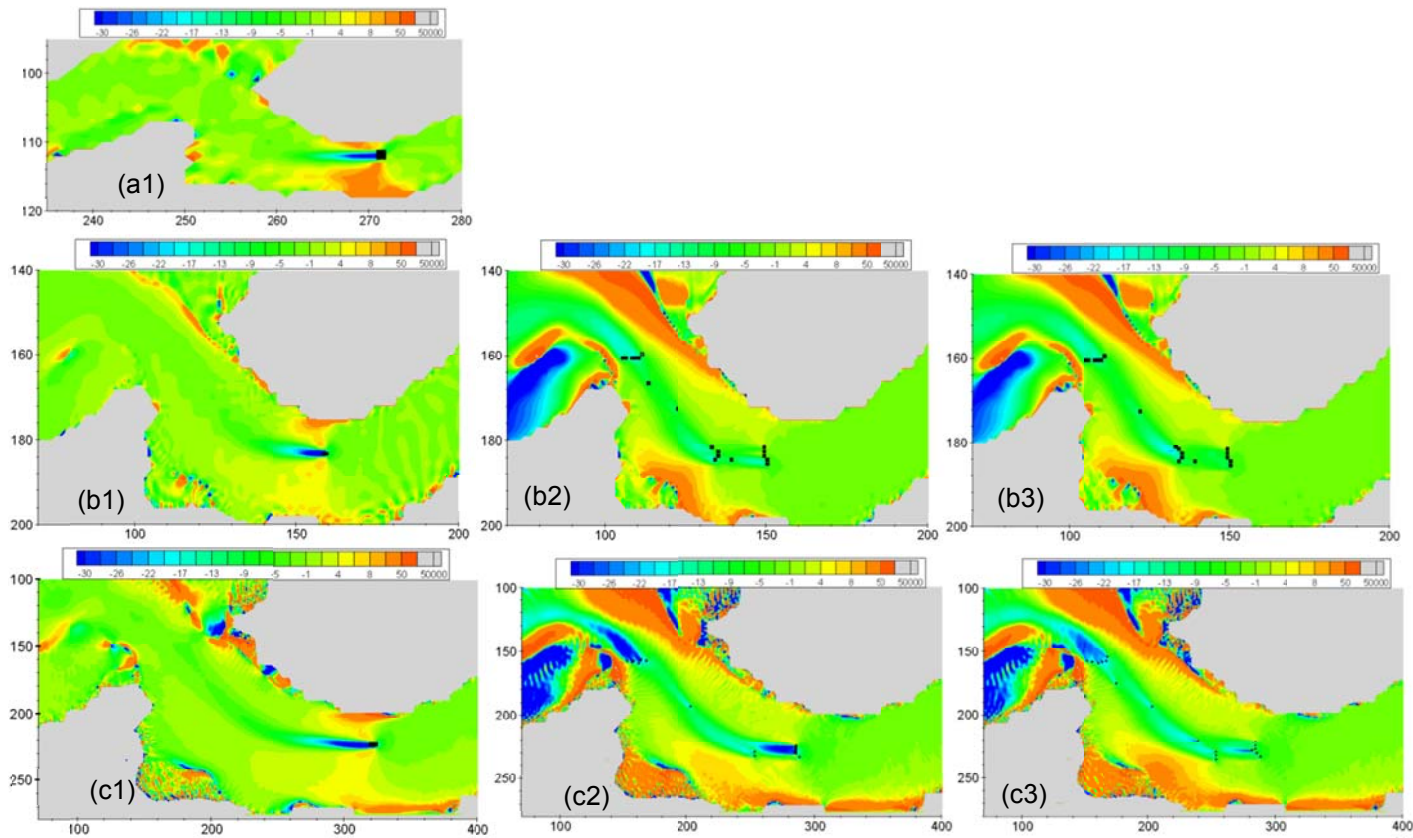


Figure 6.38: % change in peak flood velocities after array deployment for (a) CG189, (b) NG63, (c) NG21, resulting from scenario (1) IN, (2) O1, (3) O2.

For the CG189 model, a significant wake is formed with reduced velocities and accelerations observed around the array. As this is the coarsest resolution grid and allows multiple turbines to be deployed within a grid cell, it is expected that this model will not accurately capture the turbine impacts.

For the NG63 and NG21 models, the inline arrays clearly have a greater impact on current velocities than the optimised scenarios. The inline array in both the NG63 and NG21 models is seen generate a single wake with maximum changes in velocities of over 100%. This is due to the very close spacing of the turbines in NG21 and the placement of multiple turbines in the same grid cells in NG63. In comparison, for the optimised O1 and O2 scenarios, changes in velocities are considerably less with maximum differences of approximately 15% and 30% observed for the NG63 and NG21 models respectively.

The impact on velocities is larger for the optimised arrays deployed in the NG21 model compared to the NG63 model; this is thought to be a result of the difference in spatial resolutions. For the NG63 domain, only one turbine is deployed in each turbine grid cell and as the cell area is much larger than the turbine rotor diameter the blockage ratio is less, therefore the change in velocity will be lower compared to the NG21 model in which blockage ratios are greater (where the spatial resolution is equal to the turbine diameter). This also means turbines placed in adjacent grid cells are closer together in NG21 than NG63, resulting in more wake merging and greater deficits in the NG21 domain for similar levels of power extraction in the NG63 domain.

Overall it can be concluded that the impacts of an optimised turbine array layout will extract more power and still result in less significant hydrodynamic impacts than an inline array.

### **6.9.6 Application of the Impact Constraint**

The final model simulation involved re-running the O1 scenario for optimisation with respect to both power and velocity impacts. A SIF of 10% was used for the velocity impact constraint. The percentage change in peak flood current velocities due to energy extraction is shown for each domain in Figure 6.39 and the resulting undisturbed efficiencies are given in Table 6.13.

Figure 6.39 shows changes in velocities close to 50% at the top and bottom sections of the channel. Although these changes are significant (i.e. greater than the SIF) they actually constitute only small changes in low velocities and are not significant in terms of the overall estuary hydrodynamics. These areas of low current velocity proved problematic upon first application of the optimisation model. The model was unable to place any turbines without exceeding the SIF. It was therefore impossible to apply the SIF constraint across the entire deployment domain.

A simple solution was adopted in order to demonstrate how the optimisation model could be implemented. This was to limit the SIF check to the changes in current velocities at 1RD downstream of each turbine. This did mean however, that the SIF may have been exceeded in other locations. The author suggests improvements could be made to the model in regards to determining an approach to apply the SIF check at all points in the deployment domain. This might involve some filter to exclude areas of low velocity from the SIF check; due to time constraints this could not be investigated within this research.

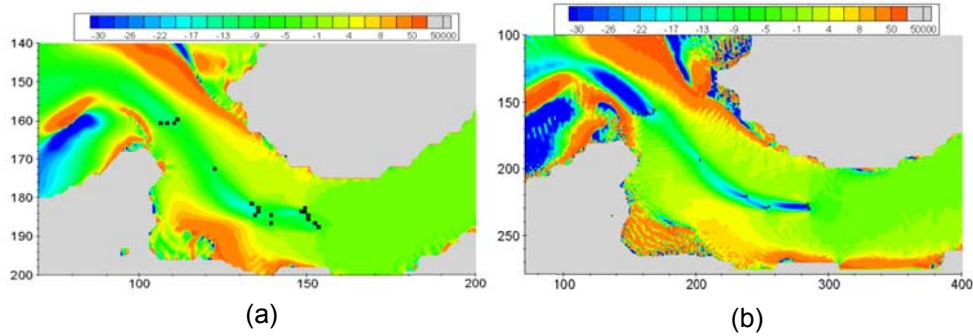


**Figure 6.39: % change in peak flood velocities after array deployment for (a) NG63, (b) NG21, resulting from scenario O1.**

**Table 6.13:  $\epsilon_{Undis}$  for each O1 array modelled within NG63 and NG21.**

| Model | Array | $\epsilon_{Undis}$ |
|-------|-------|--------------------|
| NG63  | O1    | 0.35               |
| NG21  | O1    | 0.31               |

Comparison of the impacts of the optimised O1 array on peak velocities when the impact constraint is included (Figure 6.39) to when it is excluded (Figure 6.38 (b2)-NG63, (c2)-NG21)) demonstrated that the constraint did reduce the impacts on current velocities. Turbines have been repositioned resulting in reductions in the cumulative downstream effects, leading to smaller wake effects. As the velocity impacts were only checked at 1RD downstream of turbines, there are still % differences greater than 10% due to the cumulative wake effects of all 18 turbines. This is particularly the case for the 21m domain in which wake effects are more accurately captured.

The undisturbed efficiencies of each array were compared to their counterparts when arrays were optimised for power only (Table 6.13). Considering the NG63 domain, it's  $\epsilon_{Undis}$  of 0.35 is unchanged from the Opt\_P model result. Looking next at the finest NG21 resolution,  $\epsilon_{Undis}$  has marginally decreased from 0.33 to 0.31 when the impact constraint is included. However, for both resolutions,

efficiencies still show considerable improvement from the inline cases.

Although the application of the OPT\_P&V model to the Shannon domain is relatively crude considering the enforced limitation of the SIF check, the findings still show that when turbine positions are optimised with regard to both energy capture and impact on velocities, the resulting configurations generate more energy than inline arrays and can also generate similar levels of energy to arrays optimised with regard to power only but with less significant impacts.

## **6.10 Summary and Conclusions**

The primary aim of this research was the development of a two-dimensional hydrodynamic flow model for optimising tidal turbine arrays relative to both power output and potential hydro-environmental impacts. This chapter presented the development of the optimisation model. The importance of turbine placement regarding energy capture was first explored. The development of the algorithm to determine optimal array configurations, and the implementation of this algorithm into the developed energy extraction model were presented and described in detail. The final optimisation model was applied to an idealised domain and a case study site, the Shannon estuary. Results from different array configurations including inline formations and the model's optimised outputs, resulting from different turbine spacing constraints, were presented.

The following conclusions can be drawn from this study:

- Investigation into the influence of turbine placement on energy capture showed staggered array configurations to be more efficient than turbines placed inline. And demonstrated the importance of array formation regarding energy capture.
- The optimisation model was developed in two stages; the first considers maximising energy capture and the second stage incorporates a velocity impact constraint. Each aspect of the

developed algorithm has been tested and demonstrated to be working correctly.

- Comparison of optimisation results to a similar published optimisation study, developed by Funke et al. (2014) showed good qualitative agreement. Similar optimised array configurations and velocity impacts were obtained.
- For an idealised channel, optimal arrays showed improved performance compared to a regular inline configuration. Comparison of the two optimisation algorithms (i.e. with and without a SIF constraint) demonstrated that applying the impact constraint indeed reduces the impact of energy extraction on current velocities without significantly reducing the energy capture of the array.
- It can be concluded that the developed optimisation model has the ability to determine optimised array configurations which result in high levels of energy capture and low impacts on current velocities. It has been shown how a velocity impact constraint can be used to re-position turbines in order to ensure that hydrodynamic impacts fall below a specified significant level.

## 7 Summary and Conclusions

### 7.1 Summary

This research is concerned with the development of a two-dimensional hydrodynamic flow model to facilitate simulation of tidal energy extraction and determine optimised tidal turbine array layouts relative to power output and potential hydro-environmental impacts. Commercial tidal energy extraction will likely require hundreds of turbines deployed in arrays. To date, limited research has been carried out to assess the viability of large-scale deployments, which will depend on both the expected energy yield and potential adverse hydro-environmental impacts. A major focus of this research is the accurate simulation of energy removal by tidal turbines within the numerical model, to allow simulation of the hydrodynamic impacts of tidal energy extraction and interactions between individual turbines in an array. This facilitates more accurate quantification of the energy capture of a turbine or array and also the power available to adjacent turbines in an array which will be affected by the turbine interactions. The models used in this research are the 2D finite difference Depth Integrated Velocity and Solute Transport model (DIVAST) and the Multi-Scale Nested model (MSN).

This research involved a number of objectives. The first was the development of a methodology for quantifying the resource available for extraction by a tidal turbine and the implementation of this methodology into the tidal flow model. The DIVAST model was developed to include tidal harmonic analysis software (HTAS) which was used to analyse the hydrodynamics simulated by the flow model. This enabled deconstruction of tidal currents into elliptical parameters which were used to indicate the direction of current flow. Available resource was then quantified based on the prevailing flow direction. A resource assessment analysis of the Shannon estuary was carried out based on two traditional approaches and the author's developed

methodology. All three assessments indicated three main areas of high tidal resource, with maximum power availability estimated at approximately  $2500\text{W/m}^2$ . Whilst the same areas of greatest available power were identified by each approach, substantial differences were observed between the three resource estimates. For example, maximum resource determined by the Fraenkel formula (FFA) was  $2544\text{W/m}^2$ ; at the same location power estimates by TVA and PDA were considerably lower at  $85\text{W/m}^2$  and  $46\text{W/m}^2$  respectively. Tidal current ellipses were used to indicate the nature and prevailing direction of current flow. An ellipse ratio map was used to distinguish between areas of rectilinear flows (which are optimum for HAT deployment) and rotary flows. This was then used in conjunction with available resource estimates to identify suitable turbine deployment sites. The angle of ellipse inclination was used to determine the prevailing direction of current flow, which can be used to determine optimum HAT orientations for maximum energy capture. Results from this case study assessment were then used to select potential tidal energy berths within the estuary, at which more detailed resource assessments were undertaken. As available resource estimates from each approach were considerably different and findings indicated the author's approach to be the most sophisticated for deployment of HAT. This comprehensive resource assessment of the Shannon estuary is a novel contribution of this research.

The second objective was the development of the tidal flow model to enable simulation and quantification of tidal energy extraction. The process of energy extraction via tidal turbines was incorporated into the hydrodynamic model based on a momentum sink approach, which involved modifying the governing momentum equations to include the turbine thrust as a sink term. This approach requires specification of the turbine thrust coefficient which is theoretically defined based on the undisturbed flow but is generally incorporated in far-field momentum sink-based models in conjunction with the

local current velocity at the turbine site. A problem here is that energy extraction will alter the flow regime, reducing the localised velocity at the turbine below free-stream levels. This is particularly problematic for high resolution models in which the discrepancies in free-stream and local velocities may be substantial and thus the use of typical thrust coefficient values (0.8-1.0) will result in lower than desired levels of energy removal. This research instead introduces a localised thrust coefficient,  $C'_T$ , which is more appropriate to use in combination with the local turbine velocity. A high resolution model of an idealised channel was used to determine suitable  $C'_T$  values, which were identified based on a desired level of energy removal / power capture. Based on this methodology, appropriate  $C'_T$  values were determined for various model grid cell blockage ratios. The results were used to create a localised thrust sensitivity chart describing the relationship between  $C'_T$  and the blockage ratio, from which suitable  $C'_T$  values can be identified for any combination of model water depth and spatial resolution. Findings showed that simulation of energy extraction was highly sensitive to  $C'_T$  specification, particularly for high spatial resolution, and adoption of the commonly used values, 0.8-1.0, resulted in underestimations of power capture and resulting impacts on current velocities.

The energy extraction model was further developed to allow quantification of the power capture of a turbine / array. The optimum  $C'_T$  values were determined to result in a turbine  $C_p$  of 0.4, i.e. extraction of 40% of the available power. Accuracy of the power quantification method was assessed by comparing of modelled power output with the expected theoretical output based on  $C_p = 0.4$ . Results from 40 different idealised model scenarios, demonstrated the developed model's ability to accurately simulate and quantify tidal power extraction.

The localised thrust approach was tested using a nested model of the Shannon estuary with two levels of nesting. Application to four turbines deployed in various water depths showed the model was able to successfully simulate the desired turbine efficiencies ( $C_p = 0.4$ ), thus validating both the selection of suitable  $C'_T$  values and the method of extracted power quantification. This test also demonstrated the applicability of the developed model to real tidal domains.

The concept of using flushing as a proxy for environmental impact was explored with a view to incorporating a flushing analysis into the final optimisation model. The solute transport module of the DIVAST model was used to carry out a flushing study, focusing on determination of residence times. Two idealised tidal domains were developed at turbine scale and the power capture, resulting impact on current flow and residence times of turbine arrays were assessed. Turbines were positioned in a regularly-spaced inline configuration and a number of scenarios using different turbine numbers and spacing were run. Results indicated that energy extraction had minimal impact on residence times and it was concluded that, unless modelling a very large number of turbines, flushing is not a suitable indicator of the environmental impacts of array deployment. Based on this finding, it was decided to use changes to current velocities as the environmental constraint within the array optimisation algorithm.

The final objective was the development and implementation within the model code of an optimisation algorithm to determine optimal array configurations. The algorithm was developed in two stages: first, with the sole aim of maximising power output, and, second, with an included environmental constraint based on changes to current velocities. Both the DIVAST and MSN model source codes were modified to include the optimisation code. Through an iterative

process, turbines are sequentially positioned in the locations of maximum available power. For each new turbine location, the grid cell blockage ratio is calculated and the appropriate  $C'_T$  value determined from the  $C'_T$  chart relationships. The velocity impact constraint rejects deployment of turbines in locations at which energy extraction will result in a change in velocities greater than a pre-defined significant impact factor (SIF). Based on literature, the SIF was set to a 10% change in the undisturbed velocity. In such cases, a new location is then sought. User-specified deployment constraints may also be incorporated into the optimisation. These include (1) a deployment area extents constrained by (I, J) grid cell values, (2) a minimum water depth constraint for turbine deployment, and (3) a turbine spacing constraint involving specification of minimum lateral and/or longitudinal turbine spacings. Each stage of the optimisation algorithm was tested and found to work correctly. Development of this optimisation model is the major novel contribution of this research.

The final array optimisation model was tested for an idealised domain by modelling a number of optimised arrays with different turbine spacing constraints and comparing the power outputs of the optimised arrays with each other and with that of a regularly-spaced, inline array. To demonstrate the model's suitability to a real world application, the nested optimisation model was again applied to the Shannon estuary. Two levels of nesting were employed with the highest resolution being equal to the modelled turbine rotor diameter. The optimised arrays were found to give superior power performance compared to a regularly-spaced inline configuration and also resulted in less significant impacts on current velocities.

## 7.2 Conclusions

The work carried out during this research has led to the following conclusions:

- Harmonic analysis software was successfully incorporated into the existing hydrodynamic flow model. Comparison of resulting tidal ellipses with measured current data showed the developed model was able to correctly determine ellipse data across the Shannon estuary.
- The ellipse ratio defined in the research was shown to be an extremely useful indicator of the nature of current flow. It distinguishes between rectilinear flows suitable for turbine deployment and less suitable rotary flows. The ellipse ratio map of a model domain can be combined with the resource assessment map and suitable criteria applied to determine areas of high resource and rectilinear flows. The ellipse inclination can be used to identify the primary flow direction and so determine the optimum orientation of a HAT for maximum energy extraction.
- Incorporating the primary flow direction into the resource assessment methodology is important for horizontal axis turbines with fixed orientation and leads to a more sophisticated approach in comparison to the traditional methods which employ the total velocity. Application of each approach to the Shannon estuary resulted in significant differences between the available power estimates. It is therefore recommended that resource assessments for horizontal axis turbines should incorporate flow direction.
- When using a momentum sink approach for turbine modelling, it has been shown that levels of energy removal and resulting hydrodynamic impacts are highly sensitive to the thrust

coefficient. Using typical values of the thrust coefficient (0.8-1) resulted in too little energy removal. Instead a localised thrust coefficient was used to calculate the turbine thrust and was shown to work extremely well. The approach developed here can be used in other far-field models using the momentum-sink approach and the  $C'_T$  - blockage ratio relationship can likely also be used to determine likely values of  $C'_T$  in such models.

- The influence of array layout on the resulting hydro-environmental impacts of tidal energy extraction was assessed through two high resolution idealised tidal domains, namely flow around a headland and flow constrained by an island and nearby headland. Results showed that the developed energy extraction model can provide accurate simulation of tidal energy extraction, including capturing the wake and blockage effects of individual turbines as well as interactions between turbines within an array.
- Assessment of the environmental impacts of energy extraction involved a flushing study. Results showed energy extraction does not substantially impact on the flushing capability of a water body, with residence times relatively unchanged from the undisturbed scenario. It can be concluded that flushing is not a suitable environmental impact indicator.
- Application of the energy extraction model to a number of array scenarios (in which turbine number and spacing are varied) deployed in two idealised domains concluded that array configurations can be used to enhance power capture. Optimal turbine spacings can induce flow acceleration, which can be exploited by strategically placed downstream turbines. Results suggested optimal array configurations are likely to be staggered to intercept accelerated flows from upstream turbines and avoid negative wake effects from adjacent turbines.

- Successful application of the array optimisation model to the Shannon estuary has shown that the developed model is valid for realistic tidal environments.
- To the author's knowledge this is the first automated turbine array optimisation model developed at estuary scale level and the first to employ an environmental constraint with the aim of reducing adverse impacts whilst maximising energy capture. The optimisation model has the potential to be applied to any coastal environment at any spatial resolution, providing a very valuable tool for turbine developers and tidal energy researchers alike. Optimum turbine arrays will generate the highest energy yield whilst maintaining acceptable environmental impacts. While this research utilised a 10% change in current velocities as a measure of environmental impact, further research is required into a more accurate determination of 'acceptable' impacts. This will enable environmentally 'safe' levels of energy extraction to be determined.
- The array optimisation model has the ability to facilitate sophisticated resource assessment studies, which allow determination of suitable sites for turbine deployment. It has the capacity to accurately simulate tidal energy extraction in any tidal environment and quantify energy capture from potential turbine arrays. It also has the ability to determine optimised tidal turbine arrays with respect to power capture and hydro-environmental impacts. The model could therefore be extremely useful when determining the economic viability of proposed arrays, allowing more realistic and accurate cost-benefit analyses for tidal energy projects to be conducted at an early stage in the project, thus saving money in the long term.

### 7.3 Recommendations for Further Research

The energy extraction model developed in this research is a very effective modelling system in its own right, it provides accurate simulation and quantification of tidal energy extraction and has the capacity to automate optimised turbine arrays for maximum energy capture whilst minimising adverse hydro-environmental impacts and hence has many uses within the realms of scientific research, tidal energy extraction and turbine development. The following are recommendations for future research which would, in the author's opinion, enhance the functionality and usage of the optimisation modelling system:

- Implementation of the optimisation model within a three-dimensional tidal flow model. This will allow simulation of current velocities over the depth of the water column, enhancing the accuracy of velocities modelled at turbine depth and facilitating improved accuracy in estimation of velocity deficits and thus turbine interactions.
- Use of a high resolution Computational Fluid Dynamic (CFD) tidal turbine model to determine thrust coefficients for various flow conditions (similar to the works of Koh & Ng (2017)). The results could then be incorporated into the optimisation model, enhancing the model accuracy.
- The model could be improved by incorporating a full water quality model to enable further investigation into effective ways to incorporate environmental constraints into the array optimisation. This could allow a more detailed relationship to be developed between environmental and hydrodynamic impacts and determine a better quantification of the environmental significance of varying levels of tidal energy extraction.

- A PhD research project ongoing within the Marine Modelling Group, NUI Galway involves calculation of a localised turbine thrust coefficient based on downstream reductions in current flow and accelerated by-pass flow following linear momentum actuator disc theory. The thrust coefficient is therefore updated at every model time-step and incorporated into the governing momentum equations to include the presence of a turbine(s). A further development of this research could involve combining the developed array optimisation algorithm with the alternative method of calculating thrust coefficients, allowing comparison of the resulting energy capture and associated impacts and perhaps improving the accuracy of the model.

## References

Adcock, T. A. A., Draper, S., Houlby, T., Borthwick, A. G. L. and Serhadlioglu, S. (2013) The available power from tidal stream turbines in the Pentland Firth. In: Proceedings of the Royal Society A: Mathematical, Physical and Engineering Science, 469(2157), pp. 1471–2946.

Adcock, T. A. A. and Draper, S. (2014) Power extraction from tidal channels - Multiple tidal constituents, compound tides and overtides, Renewable Energy, 63, pp. 797–806.

Ahmadian, R. and Falconer, R. A. (2012) Assessment of array shape of tidal stream turbines on hydro-environmental impacts and power output. Renewable Energy. Elsevier Ltd, 44, pp. 318–327.

Ahmadian, R., Falconer, R. and Bockelmann-Evans, B. (2012) Far-field modelling of the hydro-environmental impact of tidal stream turbines. Renewable Energy. Elsevier Ltd, 38(1), pp. 107–116.

Anthes, R. A. (1974) Data Assimilation and Initialization of Hurricane Prediction Models. Journal of the Atmospheric Sciences, pp. 702–719.

Atlantis Project (2017) Project development and operation: MeyGen. Atlantis Project. Available online:  
<https://www.atlantisresourcesltd.com/projects/meygen/>  
(accessed on 22.08.2017)

Bahaj, A., Myers, L. and Thompson, G. (2007) Characterising the wake of horizontal axis marine current turbines. In: Proceedings of the 7th European Wave and Tidal Energy Conference. Porto, Portugal, 11-14 September 2007.

Bahaj, A.S., Molland, A.F., Chaplin, J.R., and Batten, W.M.J. (2007) Power and thrust measurements of marine current turbines under various hydrodynamic flow conditions in a cavitation tunnel and a towing tank. *Renewable Energy*, 32(3), pp. 407–426.

Batten, W.M.J., Bahaj, A.S., Molland, A.F. and Chaplin, J.R. (2007) Experimentally validated numerical method for the hydrodynamic design of horizontal axis tidal turbines. *Ocean Engineering*, 34(7), pp. 1013–1020.

Batten, W.M.J., Harrison, M.E. and Bahaj, A.S. (2013) Accuracy of the actuator disc-RANS approach for predicting the performance and wake of tidal turbines. *Philosophical Transactions of the Royal Society A: Mathematical, Physical and Engineering Sciences*, 371(1985), pp. 1 - 15.

Black & Veatch (2005) Phase II UK Tidal Stream Energy Resource Assessment. Technical report 107799/D/2200/03, Carbon Trust, London.

Black & Veatch (2011) UK Tidal Current Resource & Economics. A report prepared for the UK Carbon Trust, London.

Black and Veatch (2004) UK, Europe and global tidal stream energy resource assessment. Peer review issue 107799/D/2200/04. Carbon Trust, London.

Blunden, L.S. and Bahaj, A.S. (2006) Initial evaluation of tidal stream energy resources at Portland Bill, UK. *Renewable Energy*, 31(2), pp. 121–132.

Blunden, L.S. and Bahaj, A.S.(2007) Tidal energy resource assessment for tidal stream generators. In: *Proceedings of the Institute of Mechanical Engineers, Part A: Journal of Power and Energy*, 221, pp. 137–146.

- Boon, J. (2017) Tide and Tidal Current Analysis. Virginia Institute of Marine Science. Available online:  
[http://www.vims.edu/research/units/labgroups/tc\\_tutorial/tide\\_analysis.php](http://www.vims.edu/research/units/labgroups/tc_tutorial/tide_analysis.php) (accessed on 15.04.2015)
- Boyle, G. (2004) Renewable Energy: Power for a sustainable future (3rd edition). Oxford: Oxford University Press.
- Bryden, I.G., Couch, S.J., Owen, A and Melville, G. (2007) Tidal current resource assessment. In: Proceedings of the Institution of Mechanical Engineers, Part A: Journal of Power and Energy, 221(2), pp. 125–135.
- Builtjes, P.J. (1978) The interaction of windmill wakes. In: Proceedings of the 2<sup>nd</sup> International Symposium on Wind Energy Systems, BHRA Fluid Engineering, Amsterdam, Netherlands, pp B5-49,58.
- Burton, T., Sharpe, D., Jenkin, N. and Bossanyi, E. (2001) Wind Energy Handbook, John Wiley & Sons, Ltd.
- Carballo, R., Iglesias, G. and Castro, A. (2009) Numerical model evaluation of tidal stream energy resources in the Ria de Muros (NW Spain). *Renewable Energy*, 34(6), pp. 1517–1524.
- Cartwright, D., Spencer, R., Vassie, J. and Woodworth, P. (1988) The Tides of the Atlantic Ocean, 60 degrees N TO 30 degrees S. *Philosophical Transactions of the Royal Society of London. Series A, Mathematical and Physical Sciences*, 324(1581), pp. 513–563.
- Chamorro, L.P., Hill, C., Morton, S., Ellis, C., Arndt, R.E.A. and Sotiropoulos, F. (2013) On the interaction between a turbulent open channel flow and an axial-flow turbine. *Journal of Fluid Mechanics*, 716, pp. 658–670.

Churchfield, M.J., Li, Y. and Moriarty, P.J. (2011) A Large-Eddy Simulation Study of Wake Propagation and Power Production in an Array of Tidal- Current Turbines. In: 9th European Wave and Tidal Energy Conference, Southampton, UK 5th - 9th September.

Connel, J.R. and George, R.L. (1982) The wake of the MOD-0A1 wind turbine at two rotor diameters downwind on 3 December 1981. Report no. PNL-4210, Pacific Northwest Laboratory, Battelle, USA.

Corren, D., Colby, J. and Adonizio, M.A. (2013) Improved Structure and Fabrication of Large, High-Power KHPS Rotors - Final Scientific/Technical Report (No. DOE/GO18168). Verdant Power Inc. United States.

Couch, S. J. and Bryden, I. G. (2007) Large-scale physical response of the tidal system to energy extraction and its significance for informing environmental and ecological impact assessment. In: Proceedings of Oceans 2007 - Europe. Aberdeen, Scotland.

Dabrowski, T. (2005) A flushing analysis of selected Irish water bodies. PhD Thesis, National University of Ireland, Galway.

Bahaj, A., Blunden, L, Anwar, A. (2008) Tidal-current Energy Device Development and Evaluation Protocol. Prepared by University of Southampton. Department of Energy and Climate Change.

Divett, T., Vennell, R. and Stevens, C. (2009) Maximising energy capture by fixed orientation tidal stream turbines in time-varying off axis current. In: Proceedings of the Australasian Coasts and Ports Conference, 16<sup>th</sup> - 18<sup>th</sup> September,. Wellington, New Zealand.

Divett, T., Vennell, R. and Stevens, C. (2011) Optimisation of multiple turbine arrays in a channel with tidally reversing flow by numerical modelling with adaptive mesh. Philosophical transactions. Series A, Mathematical, physical, and engineering sciences, 371(1985), p. 2012.0251.

Doodson, A.T. and Warburg, H.D. (1941) Admiralty Manual of Tides. HMSO, London.

Draper, S., Adcock, T. A.A., Borthwick, A.G.L. and Houlby, G.T. (2014) Estimate of the tidal stream power resource of the Pentland Firth. *Renewable Energy*, 63, pp. 650–657.

Draper, S., Houlby, G.T., Oldfield, M.L.G. and Borthwick, A.G.L. (2010) Modelling tidal energy extraction in a depth-averaged coastal domain. *IET Renewable Power Generation*, 4(6), p. 545.

European Commission (2017a) 2030 Energy Strategy. Available online: <https://ec.europa.eu/energy/en/topics/energy-strategy-and-energy-union/2030-energy-strategy> (accessed on 26.08.2017)

European Commission (2017b) Report from the commission to the European parliament, the council, the European economic and social committee and the committee of the regions. *Renewable Energy Progress Report*. Brussels.

European Marine Energy Centre (2015) Tidal Devices. Available online:<http://www.emec.org.uk/marine-energy/tidal-devices/> (accessed on 29.05.2017)

Evans, E.M. (1987) Tidal stream energy. PhD Thesis. Plymouth Polytechnic.

[https://scholar.google.com/scholar\\_lookup?hl=en&publication\\_year=1987&issue=A8&author=E.+M.+Evans&title=Tidal+stream+energy](https://scholar.google.com/scholar_lookup?hl=en&publication_year=1987&issue=A8&author=E.+M.+Evans&title=Tidal+stream+energy)

Fairley, I., Masters, I. and Karunaratna, H. (2015) The cumulative impact of tidal stream turbine arrays on sediment transport in the Pentland Firth. *Renewable Energy*. Elsevier Ltd, 80, pp. 755–769.

Falconer, R.A. (1986) A two-dimensional mathematical model study of the nitrate levels in an inland natural basin. In: Proceedings of the International Conference on Water Quality Modelling in the Inland Natural Environment, BHRA Fluid Engineering, Bournemouth, pp. 325–344.

Falconer, R.A.(1988) A short course on flow and water quality modelling of coastal waters, estuaries, rivers, lakes and reservoirs: Lecture 7 - Solution Procedures. 20-22<sup>nd</sup> September.

Falconer, R.A., Lin,B., Wu,Y. and Harris,E.(2001) DIVAST Model Reference Manual (User Manual). Cardiff University, Hydro-Environmental Research Centre, Cardiff University.

Fallon, D. (2012) Numerical Modelling of the Far-field Impacts of Tidal Turbines. PhD Thesis, National University of Ireland, Galway. National University of Ireland, Galway.

Fallon, D., Hartnett, M., Olbert, A. and Nash, S. (2014) The effects of array configuration on the hydro-environmental impacts of tidal turbines. Renewable Energy. Elsevier Ltd, 64, pp. 10–25.

Foreman, M.G.G. and Bay, P. (1996) Manual for Tidal Heights Analysis and Prediction. Pacific Marine Science Report 77-10, Institute of Ocean Sciences, Patricia Bay, Sidney, B.C., Canada.

Foreman, M.G.G., Cherniawsky, J.Y. and Ballantyne, V.A. (2009) Versatile harmonic tidal analysis: Improvements and applications. Journal of Atmospheric and Oceanic Technology, 26(4), pp. 806–817.

Foreman, M.G.G and Henry, R.F. (1989) The harmonic analysis of tidal model time series, Advances in water resources. 12(3), pp. 109–120.

Fraenkel, P.L. (2007) Marine current turbines: pioneering the development of marine kinetic energy converters. In: Proceedings of the Institution of Mechanical Engineers Part A-Journal of Power and Energy, 221, pp. 159–169.

Fraenkel, P.L. (2002) Power from marine currents. In: Proceedings of the Institution of Mechanical Engineers, Part A Journal of Power and Energy, 216(1), pp. 1–14.

Fraenkel, P.L. and Musgrove, P.J. (1979) Tidal and River Current Energy Systems. In: International Conference on Future Energy Concepts, London, England, 30<sup>th</sup> January - 1<sup>st</sup> February, pp. 114–117.

Funke, S.W., Farrell, P.E. and Piggott, M.D. (2014) Tidal turbine array optimisation using the adjoint approach. Renewable Energy, 63, pp. 658–673.

Gebreslassie, M.G., 2012. Simplified CFD modelling of tidal turbines for exploring arrays of devices. PhD Thesis. University of Exeter.

Gillibrand, P., Walters, R. and McIlvenny, J. (2016) Numerical simulations of the effects of a tidal turbine array on near-bed velocity and local bed shear stress. Energies, 9(10), p. 852.

Gunawan, B., Neary, V., Hill, C. and Chamorro, L.P. (2012) Measurement of velocity deficit at the downstream of a 1:10 axial hydrokinetic turbine model. In: proceedings of the ASCE Hydraulic Measurements and Experimental Methods. Snowbird, Utah, USA.

Harrison, M.E., Batten, W.M.J., Myers, L.E. and Bahaj, A.S. (2010) Comparison between CFD simulations and experiments for predicting the far wake of horizontal axis tidal turbines. IET Renewable Power Generation, 4(6), p. 613-627.

Hartnett, M. and Nash, S. (2004) Modelling nutrient and chlorophyll - a dynamics in and Irish brackish waterbody. *Environmental Modelling and Software*, 19, pp. 47–56.

Hasegawa, D., Sheng, J., Greenberg, D.A. and Thompson, K.R. (2011) Far-field effects of tidal energy extraction in the Minas Passage on tidal circulation in the Bay of Fundy and Gulf of Maine using a nested-grid coastal circulation model. *Ocean Dynamics*, (61), pp. 1845–1868.

Hicks, S.D. (2006) Understanding tides. NOAA: Center for Operational Oceanographic Products and Services.

Houlsby, G.T., Draper, S. and Oldfield, M.L.G. (2008) Application of Linear Momentum Actuator Disc Theory to Open Channel Flow. University of Oxford. pp. 1–23.

Javaherchi, T., Stelzenmuller, N., and Aliseda, A. (2013) Experimental and numerical analysis of the DOE Reference Model 1 horizontal-axis hydrokinetic turbine. In: *The 1st Marine Energy Technology Symposium*. Washington, Seattle, WA, USA.

Kadiri, M., Ahmadian, R., Bockelmann-Evans, B., Rauen, W. and Falconer, R.A. (2012) A review of the potential water quality impacts of tidal renewable energy systems. *Renewable and Sustainable Energy Reviews*. Elsevier Ltd, 16(1), pp. 329–341.

Karsten, R.H., McMillan, J.M., Lickley, M.J. and Haynes, R.D. (2008) Assessment of tidal current energy in the Minas Passage, Bay of Fundy. *Proceedings of the Institution of Mechanical Engineers, Part A: Journal of Power and Energy*, 222(5), pp. 493–507.

Keenan, G., Sparling, C., Williams, H., Fortune, F. and Davison, A. (2011) SeaGen environmental monitoring programme: Final report. Royal Haskoning UK Ltd. (on behalf of Marine Current Turbines Ltd).

Korres, G. and Lascaratos, A. (2003) A one-way nested eddy resolving model of the Aegean and Levantine basins: implementation and climatological runs. *Annales Geophysicae*, 21(1), pp. 205–220.

Kowalik, Z. and Luick, J. (2013) *The Oceanography of Tides*. University of Alaska, Fairbanks, Alaska.

Kramer, S.C. and Piggott, M.D. (2016) A correction to the enhanced bottom drag parameterisation of tidal turbines. *Renewable Energy*. Elsevier Ltd, 92, pp. 385–396.

Lewis, M.J, Neill, S.P., Robins, P.E. and Hashemi, M.R. (2015) Resource assessment for future generations of tidal-stream energy arrays. *Energy*, 83, pp. 403–415.

MacEnri, J., Reed, M. and Thiringer, T. (2011) Power quality performance of the tidal energy converter, SeaGen. In: *Proceedings of the ASME 30th International Conference on Ocean, Offshore and Arctic Engineering*, p. 8.

Maganga, F., Germain, G., King, J., Pinon, G. and Rivoalen, E. (2010) Experimental characterisation of flow effects on marine current turbine behaviour and on its wake properties. *IET Renewable Power Generation*, 4(6) p. 498-509.

Mann, K.H. and Lazier, J.R.N. (2013) *Dynamics of Marine Ecosystems: Biological-Physical Interactions in the Oceans: Third Edition* pp 1-496

Marine Institute (2017) Irish National Tide Gauge Network Real Time Data, Oceanographic Services, Marine Institute, Co. Galway. Available Online: <http://data.marine.ie/Dataset/Details/20932> (accessed on: 28.04.2017).

Marone, E., Raicich, F. and Mosetti, R. (2003) Harmonic tidal analysis methods on time and frequency domains: similarities and differences for the Gulf of Trieste, Italy and Paranagua Bay, Brazil. *Bollettino di Geofisica Teorica ed Applicata*, 54(2), pp. 183–204.

Martin-Short, R., Hill, J., Kramer, S.C., Avdis, A., Allison, P.A. and Piggott, M.D. (2015) Tidal resource extraction in the Pentland Firth, UK: Potential impacts on flow regime and sediment transport in the Inner Sound of Stroma. *Renewable Energy*. Elsevier Ltd, 76, pp. 596–607.

Masters, I., Malki, R., Williams, .A and Nick-Croft, T. (2013) The influence of flow acceleration on tidal stream turbine wake dynamics: A numerical study using a coupled BEM CFD model. *Applied Mathematical Modelling*, 37(16–17), pp. 7905–7918.

Masters, I., Williams, A., Nick-Croft, T., Togneri, M., Edmunds, M., Zangiabadi, E., Fairley, I. and Karunarathna, H. (2015) A Comparison of Numerical Modelling Techniques for Tidal Stream Turbine Analysis. *Energies*, 8, pp. 7833–7853.

McNaughton, J., Afgan, I., Apsley, D.D., Rolfo, S., Stallard, T. and Stansby, P.K. (2014) A simple sliding-mesh interface procedure and its application to the CFD simulation of a tidal-stream turbine. *International Journal for Numerical Methods in Fluids*, 74, pp. 250–269.

Meygen (2013) The Meygen Project. Available online: <http://www.meygen.com/> (accessed on: 01.06.2013)

Molen, J. Van Der, Ruardij, P. and Greenwood, N. (2016) Potential environmental impact of tidal energy extraction in the Pentland Firth at large spatial scales: results of a biogeochemical model. *Biogeosciences*, pp. 2593–2609.

Mozafari, A. T. J. (2010) Numerical Modeling of Tidal Turbines : Methodology Development and Potential Physical Environmental Effects. MSc Thesis, University of Washington, Seattle, WA, USA.

Mozafari, A.T.J. (2014) Numerical investigation of Marine Hydrokinetic Turbines : methodology development for single turbine and small array simulation, and application to flume and full-scale reference. PhD Thesis, University of Washington, Seattle, WA, USA.

Myers, L., Bahaj, A.S, Rawlinson-Smith, R.I, Thomson, M.D (2008) The effect of boundary proximity upon the wake structure of horizontal axis marine current turbines. In: Proceedings of the 27<sup>th</sup> International Conference on Offshore Mechanics and Arctic Engineering, 15<sup>th</sup> -20<sup>th</sup> June, Estoril, Portugal.

Myers, L., Bahaj, A., Germain, G. and Giles, J.(2008). Flow boundary interaction effects for marine current energy conversion devices. In: Proceedings of the 10th World Renewable Energy Congress. Glasgow, Scotland.

Myers, L. and Bahaj, A.S. (2005) Simulated electrical power potential harnessed by marine current turbine arrays in the Alderney Race. *Renewable Energy*, 30(11), pp. 1713–1731.

Myers, L. and Bahaj, A.S. (2007) Wake studies of a 1/30th scale horizontal axis marine current turbine. *Ocean Engineering*, 34(5–6), pp. 758–762.

Myers, L. and Bahaj, A.S. (2009) Near wake properties of horizontal axis marine current turbines. In: Proceedings of the 8<sup>th</sup> European Wave and Tidal Energy Conference. Upssala, Sweden, pp. 558–565.

Myers, L.E. and Bahaj, A.S. (2010) Experimental analysis of the flow field around horizontal axis tidal turbines by use of scale mesh disk rotor simulators. *Ocean Engineering*. Elsevier, 37(2–3), pp. 218–227.

Myers, L.E. and Bahaj, A.S. (2012) An experimental investigation simulating flow effects in first generation marine current energy converter arrays. *Renewable Energy*. Elsevier Ltd, 37(1), pp. 28–36.

Nash, S. (2010) Development of an efficient dynamically-nested model for tidal hydraulics and solute transport. PhD Thesis. National University of Ireland, Galway.

Nash, S., Berry, A. and Hartnett, M. (2005) Nutrient dynamics in Cork Harbour. In: Brebbia CA and Antunes do Carmo JS (eds), *River Basin Management III*, WIT Press, UK, 83, pp. 369–380.

Nash, S. O'Brien, N, Olbert, A and Hartnett, M (2014) Modelling the far field hydro-environmental impacts of tidal farms – A focus on tidal regime, inter-tidal zones and flushing. *Computers & Geosciences*. Elsevier, pp. 1–8.

Nash, S. and Hartnett, M. (2009) A nested hydrodynamic model incorporating flooding and drying. In: *Proceedings of the Twelfth International Conference on Civil, Structural and Environmental Engineering Computing*. Civil-Comp Press, Stirlingshire, UK.

Nash, S. and Hartnett, M. (2010) Nested circulation modelling of inter-tidal zones: details of a nesting approach incorporating moving boundaries. *Ocean Dynamics*, 60; pp1478-1495.

Nash, S. and Hartnett, M. (2014) Development of a nested coastal circulation model: Boundary error reduction. *Environmental Modelling and Software*, 53, pp. 65–80.

Nash, S., Hartnett, M. and Dabrowski, T. (2011) Modelling phytoplankton dynamics in a complex estuarine system. In: *Proceedings Of The Institution Of Civil Engineers-Water Management*, 164(1), pp. 35–54.

Nash, S., Olbert, A.I. and Hartnett, M. (2015) Towards a low-cost modelling system for optimising the layout of tidal turbine arrays. *Energies*, 8, pp. 13521–13539.

Nash, S. and Phoenix, A. (2017) A review of the current understanding of the hydro-environmental impacts of energy removal by tidal turbines. *Renewable and Sustainable Energy Reviews*, 80, pp. 648–662.

National Oceanic and Atmospheric Administration (NOAA) (2017) Tides & Currents. Available online: <https://tidesandcurrents.noaa.gov/harcon.html?id=9410170> (accessed: 28.04.2017)

Naval Postgraduate School (Department of Oceanography) (2015) Basic Concepts in Physical Oceanography: Tides. Available online: <http://www.oc.nps.edu/nom/day1/partc.html> (accessed on: 12.05.2017)

Neill, S.P. and Couch, S.J. (2011) Impact of tidal energy converter (TEC) array operation on sediment dynamics. In: *Proceedings of the 9th European Wave and Tidal Conference*. Southampton, UK.

Neill, S.P., Jordan, J.R. and Couch, S.J. (2012) Impact of tidal energy converter (TEC) arrays on the dynamics of headland sand banks. *Renewable Energy*. Elsevier Ltd, 37(1), pp. 387–397.

Neill, S.P., Litt, E.J., Couch, S.J. and Davies, A.G. (2009) The impact of tidal stream turbines on large-scale sediment dynamics. *Renewable Energy*, 34(12), pp. 2803–2812.

Olbert, A.I., Comer, J., Nash, S. and Hartnett, M. (2017) High-resolution multi-scale modelling of coastal flooding due to tides, storm surges and rivers inflows. A Cork City example. *Coastal Engineering*, 121, pp. 278–296.

Pingree, R.D. and Griffiths, D.K. (1979) Sand transport paths around the British Isles resulting from  $M_2$  and  $M_4$  tidal interactions. *Journal of the Marine Biological Association of the UK*, 59(2), pp. 497–513.

Plew, D.R. and Stevens, C.L. (2013) Numerical modelling of the effect of turbines on currents in a tidal channel - Tory Channel, New Zealand. *Renewable Energy*. Elsevier Ltd, 57, pp. 269–282.

Polagye, B., Van Cleve, B., Copping, A. and Kirkendall, K. (2011) Environmental effects of tidal energy development. U.S. Dept. Commerce, NOAA Tech. Memo. F/SPO-116.

Polagye, B.L. (2009) Hydrodynamic effects of kinetic power extraction by in-stream tidal turbines. PhD Thesis, University of Washington

PSMSL (Permanent Service for Mean Sea Level) (2017) Tidal Analysis and Prediction. Available online:  
[http://www.psmsl.org/train\\_and\\_info/software/analysis.php](http://www.psmsl.org/train_and_info/software/analysis.php) (accessed 20.06.2017)

Pugh, D.T. (1996) Tides, surges and mean sea-level. *Marine and Petroleum Geology*, 5(3), p. 301.

Rachmayani, R., Nagara, G.A., Suprijo, T. and Ningshi, N.S. (2006) Marine Current Potential Energy for Environmental Friendly Electricity Generation in Bali , Lombok and Makassar Straits. In *Environmental Technology and Management Conference*. 7<sup>th</sup> -8<sup>th</sup> September, Bandung, West Java, Indonesia.

Ramos, V., Carballo, R., Álvarez, M., Sánchez, M. and Iglesias, G. (2013) Assessment of the impacts of tidal stream energy through high-resolution numerical modeling. *Energy*. Elsevier Ltd, 61, pp. 541–554.

Ramos, V., Carballo, R., Sanchez, M., Veigas, M. and Iglesias, G. (2014) Tidal stream energy impacts on estuarine circulation. *Energy Conversion and Management*. Elsevier Ltd, 80, pp. 137–149.

Renewable Energy Focus, (2017). Available online:  
<http://www.renewableenergyfocus.com/view/12197/dnv-confirms>  
(accessed on: 25.09.2017)

Robins, P.E., Neill, S.P. and Lewis, M.J. (2014) Impact of tidal-stream arrays in relation to the natural variability of sedimentary processes. *Renewable Energy*. Elsevier Ltd, 72, pp. 311–321.

Rourke, F.O., Boyle, F., and Reynolds, A. (2010) Tidal Current Energy Resource Assessment in Ireland: Current Status and Future Update Future Update. *Renewable and Sustainable Energy Reviews*, 14(9), pp. 3206–3212.

Sanderse, B. (2009) Aerodynamics of wind turbine wakes: Literature review. Energy research centre of the Netherlands, ECN-E-09-016.

Schmitt, P., Elsaesser, B., Bischof, S. and Starzmann, R. (2015) Field testing a full-scale tidal turbine Part 2: Inline Wake Effects. In: *Proceedings of the 11th European Wave and Tidal Energy Conference*. Nantes, France.

SEAI (2017) Tidal energy and tidal energy devices. Available online:  
<http://www.seai.ie/Renewables/Ocean-Energy/Ocean-Energy-Explained/Tidal-Energy-and-Tidal-En> (accessed on 29.05.2017)

SEI (2004) Tidal & Current Energy Resources in Ireland. Dublin, Sustainable Energy Ireland.

SEI (2004) Tidal & Current Energy Resources, Appendix A: ADCP deployments at Achill Island and Shannon Estuary., Water. Sustainable Energy in Ireland.

Sheng, J., Thompson, K., Greenberg, D. and Hill, P. (2012) Assessing the Far Field Effects of Tidal Power Extraction on the Bay of Fundy , Gulf of Maine and Scotian Shelf. Department of Oceanography , Dalhousie University , Halifax. USA. OEER Newsletter (2)

Siemens UK (2010) SeaGen tidal current turbine. Accessed online: [http://www.siemens.co.uk/en/news\\_press/pictures/seagen-tidal-current-turbine.htm](http://www.siemens.co.uk/en/news_press/pictures/seagen-tidal-current-turbine.htm) (accessed on 07.09.2017)

SIFP (2013) Strategic Integrated Framework Plan for the Shannon Estuary management of the Shannon Estuary Volume 1: Written Statement.

Smith, P., Bugden, G. and Wu, Y. (2013) Final Report: Impacts of tidal energy extraction on sediment dynamics in Minas Basin, Bay of Fundy, NS, Research Project #: 300-170-09-13.

SRM Projects LTD (Sustainable Resource Mechanical Engineering and Project Management - Nanaimo, BC, C. (2012) Axial tidal turbine array. SRM Projects LTD (Sustainable Resource Mechanical Engineering and Project Management - Nanaimo, BC, C.

Stallard, T., Collings, R., Feng, T. and Whelan, J. (2013) Interactions between tidal turbine wakes: Experimental study of a group of 3-bladed rotors. *Philosophical Transactions of the Royal Society of London: A*, 371(1985), pp. 1471–2962.

Stallard, T., Feng, T. and Stansby, P. (2015) Experimental study of the mean wake of a tidal stream rotor in a shallow turbulent flow. *Journal of Fluids and Structures*, 54, pp. 235–46.

Staneva, J., Stanev, E., Wolff, J.O., Badewien, T.H., Reuter, R., Flemming, B., et al. (2009) Hydrodynamics and sediment dynamics in the German Bight. A focus on observations and numerical modeling in the East Frisian Wadden Sea. *Continental Shelf Research*, 29(1), pp. 302–319.

Sun, X., Chick, J.P. and Bryden, I.G. (2008) Laboratory-scale simulation of energy extraction from tidal currents. *Renewable Energy*, 33(6), pp. 1267–1274.

Sutherland, G., Foreman, M. and Garrett, C. (2007) Tidal current energy assessment for Johnstone Strait, Vancouver Island. In: *Proceedings of the Institution of Mechanical Engineers, Part A: Journal of Power and Energy*, 221(2), pp. 147–157.

Takeoka, H. (1984) Fundamental concepts of exchange and transport time scales in a coastal sea. *Continental Shelf Research*, 3(3), pp. 311–326.

The Florida Department of Environmental Protection (DEP) & Florida's five water management districts (WMDs), 2013. *Environmental Resource Permit Applicant's Handbook, Volume I (General and Environmental)*

OPW. Hydro-metric website of the Office of Public Works. Hydro-Data. Available online: <http://waterlevel.ie/hydro-data/search.html> (accessed on: 11.09.2015)

Thiebot, J., Bois, P. and Guillou, S. (2015) Numerical modeling of the effect of tidal stream turbines on the hydrodynamics and the sediment transport - Application to the Alderney Race (Raz Blanchard), France. *Renewable Energy*, 75, pp. 356–365.

Thompson, L. (2007) Tides Intro, Lecture Notes, University of Washington. Available online:  
<http://faculty.washington.edu/luanne/pages/ocean420/notes>  
(accessed on: 27.04.2016)

Thyng, K.M. and Riley, J.J. (2010) Idealized headland simulation for tidal hydrokinetic turbine siting metrics. In: proceedings of Oceans, 2010. Seattle, USA. pp 1-6

Tidal Energy Today (2016) Estimate of global potential tidal resources. Available online:  
<http://tidalenergytoday.com/2015/02/17/estimate-of-global-potential-tidal-resources/> (accessed on: 25.11.2016)

Turnock, S.R., Phillips, A.B., Banks, J. and Nicholls-Lee, R. (2011) Modelling tidal current turbine wakes using a coupled RANS-BEMT approach as a tool for analysing power capture of arrays of turbines. Ocean Engineering. Elsevier, 38(11–12), pp. 1300–1307.

University of Massachusetts (2012) The effect of tidal power generation on sediment transport in Muskeget Channel. report by University of Massachusetts, pp27

Vermeulen, P.E.J. (1979) Mixing of simulated wind turbine wakes in turbulent shear flow. MT-TNO Report 79-09974

Vermeulen, P.E.J. and Builtjes, P. (1982) Turbulence measurements in simulated wind turbine clusters. MT-TNO Report 82-03003

Whittaker, T., Fraenkel, P.L., Bell, A. and McClure, K., (2003) The potential for the use of marine current energy in Northern Ireland. Published by the Department of Enterprise, Trade and Investment, Belfast, NI.

Willis, M., Masters, I., Thomas, S., Gallie, R., Loman, J., Cook, A., et al. (2010) Tidal turbine deployment in the Bristol Channel: a case study. In: proceedings of the Institution of Civil Engineers, Energy 163, pp. 93–105.

Wyman, P.R. and Peachey, C.J. (1979) Tidal Current Energy Conversion. In: International Conference on Future Energy Concepts, London, England, 30<sup>th</sup> January 30-1<sup>st</sup> February 1, Proceedings. pp. 164–166.

Yang, Z., Wang, T. and Copping, A. (2013) Modeling tidal stream energy extraction and its effects on transport processes in a tidal channel and bay system using a three-dimensional coastal ocean model. *Renewable Energy*, 50, pp. 605-613

Zhang, C. & Tang, H., 2009. Advances in Water Resources and Hydraulic Engineering. In: Proceedings of the 16<sup>th</sup> IAHR-APD Congress and 3<sup>rd</sup> Symposium of IAHR-ISHS, Vol 6

Zhang, D.L., Chang, H.R., Seaman, N. L., Warner, T.T. and Fritsch, J.M. (1986) A two-way interactive nesting procedure with variable terrain resolution. *Monthly Weather Review*, 114(7), pp. 1330–1339.

## **Appendix A: Review of Hydro-environmental Impacts of Tidal Energy Extraction**

## A.1 Hydrodynamic Impacts of Tidal Turbines

### A.1.1 Hydrodynamic Effects: Single Turbine

Extraction of energy from a fluid via a tidal stream turbine will cause a reduction in momentum (and by extension velocity) in the downstream flow known as the turbine wake. The hydrodynamic effects of a single tidal turbine as deduced from theoretical models are illustrated in Figure A.1 which identifies 5 points: (1) far upstream of the turbine where the velocity is unaffected by the turbine, (2) immediately upstream of the turbine, (3) immediately downstream of the turbine, (4) the region where slow moving fluid from the turbine's wake merges with free stream fluid from the by-pass flow, (5) further downstream where flow has fully recovered. The following hydrodynamic effects can be observed:

1. reduced wake velocities,  $U_w$ , downstream of the turbine due to energy removal
2. accelerated bypass velocities,  $U_b$ , around the turbine due to blockage
3. elevated turbulence levels and turbulent mixing of the wake with bypass flows
4. a drop in water level across the turbine

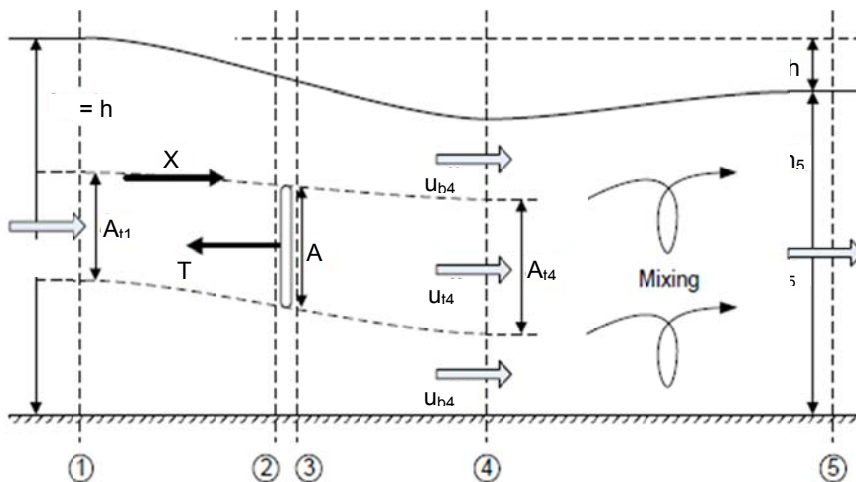


Figure A.1: Theoretical hydrodynamic impacts of tidal energy extraction  
(Source: Houlsby et al. 2008).

### A.1.1.1 Reduced Wake Velocities

Reduced wake velocities are the most obvious and significant impact of tidal turbines and are thus the most widely-studied to date. Wake velocities will be influenced by a number of factors including the amount of power extracted by a turbine,  $P$ . The change in momentum across a turbine caused by power extraction can be quantified by the non-dimensional turbine thrust coefficient,  $C_T$ . Using actuator disc theory,  $C_T$  can be related to the wake velocity as follows:

$$C_T = \frac{T}{\frac{1}{2}\rho AU_0^2} = 4a(1-a) = 1 - \left(\frac{U_w}{U_0}\right)^2 \quad (\text{A.1})$$

where  $T$  is the turbine thrust,  $U_0$  is the free-stream velocity and  $a$  is the axial induction factor (i.e. the ratio of the reduction in the wake velocity to the free-stream velocity).  $U_w$  thus decreases for increasing  $C_T$ .  $C_p$  and  $C_T$  are interdependent and are a function of the turbine design, e.g. blade numbers, size, shape and aerodynamic properties.

Wakes are complicated features; however, their structures are typically characterised by:

- Wake length: downstream distance where wake velocities return to free-stream levels.
- Wake width: lateral extents of the wake.
- Depth profile: variation in wake velocities through the water column.

#### ***Wake length***

Velocity changes from experiments are generally reported as velocity deficits ( $U_d$ ) where:

$$U_d = 1 - (U_w/U_0) \quad (\text{A.2})$$

Wake length is governed by the rate of wake recovery and is typically assessed by measuring and plotting  $U_d$  along the downstream longitudinal turbine centreline, i.e. the longitudinal  $U_d$ . Figure A.2 (a) compares longitudinal  $U_d$  from six different laboratory studies of singular scaled turbines. Despite the differences in experimental setups (see Table 2.1), the shapes of the deficit curves are quite similar. As would be expected, deficits are highest adjacent to the turbine and decrease with distance downstream as velocities recover to free-stream levels. Near the turbine, wake velocities are reduced to 60-90% of free-stream levels while at 10RDs downstream they recover to between 10-25% of free-stream levels and at 20RD they further recover to within 5-10%.

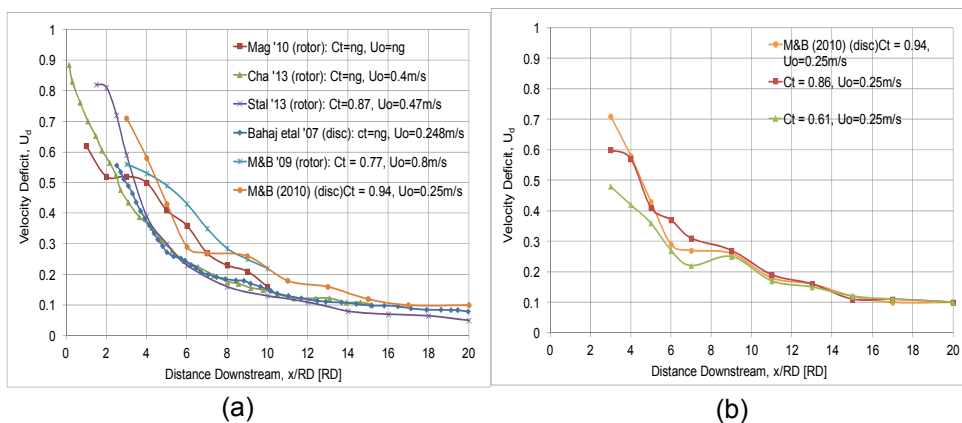


**Figure A.2: Longitudinal variation in  $U_d$  for (a) single scaled rotors (reproduced from: Bahaj et al. (2007); Myers & Bahaj (2009); Myers & Bahaj (2010); Stallard et al. (2013)) and (b) 3 porous discs of different  $C_T$  values (reproduced from: Bahaj et al. (2007); Myers & Bahaj (2009); Myers & Bahaj (2010); Stallard et al. (2013)).**

Turbine wakes can be divided into two regions. The near-wake lies immediately downstream of the turbine and comprises slow moving fluid characterised by high pressure/shear gradients, intense turbulence levels and large amounts of swirl (Myers & Bahaj, 2009). The far-wake is the region where the wake is primarily dissipated by turbulent mixing between the slower-moving wake and the adjacent faster-moving free-stream flow.

From Figure A.2 (a), near-wake deficits are seen to be strongly influenced by experimental setup, i.e. flow conditions and turbine characteristics, with a large range in near-wake deficits across experiments (e.g.  $U_d$  ranges from 0.44 - 0.71 at 3RD). By comparison, the laboratory results show that far-wake deficits, particularly those >16RD appear to be relatively independent of experimental setup (e.g. values at 16RD only range from 0.07 - 0.11). This agrees with the commonly accepted understanding that the far-wake structure is primarily controlled by turbulent mixing and proximity to bounding surfaces and is relatively independent of the near-wake structure (Myers & Bahaj, 2010).

The influence of  $C_T$  on wake velocity deficits has been investigated by (Myers & Bahaj (2007); Myers & Bahaj (2010)) who used porous discs of differing porosities to simulate three different  $C_T$  values (0.61, 0.86 and 0.94). They found that near-wake velocities were reduced with increasing  $C_T$ , but that far-wake velocities converged (Figure A.2 (b)) suggesting that far-wake recovery and, by extension wake length, is independent of  $C_T$ . Chamorro et al. (2013) also found that wake velocities were reduced for increasing tip-speed ratios; this dependence is understandable given that  $C_T$  is a function of tip-speed ratio.

Myers & Bahaj (2008) and Myers & Bahaj (2010) found that varying the proximity of the porous discs to the water surface/bed introduced differential mass flow rates above and below the discs that can cause the wake to persist much further downstream. While there was little difference in wake deficits for disc centres at 0.75d, 0.66d or 0.5d (above tank bottom), far-wake deficits were persistently higher when the disc centre was at 0.33d, resulting in a much longer wake. In the same studies, the introduction of additional turbulence through increased sea bed roughness was found to have a negligible effect on the wake extents of the disks centred at 0.75d, 0.66d or 0.5d as

the wake and the turbulent layer of fluid created by the elevated bed roughness did not mix but, for the disk at  $0.33d$ , mixing of the wake and the bed-induced turbulent layer resulted in reduced mixing of the wake with free-stream flow which in turn yielded higher far-field velocity deficits and thus a longer wake. Maganga et al. (2010) and Myers & Bahaj (2010) showed that increasing upstream turbulence increased wake recovery. The turbine support structure will also affect wake velocities as it will exert a drag force on the flow. Myers & Bahaj (2009) found that the support structure of their scaled turbine induced higher near-wake velocity deficits, contributing approximately 15% of the centreline deficit at 3RD, but had no noticeable effects beyond 6RD.

Laboratory measurements of velocity deficits beyond 20RD are not available, most likely due to test tank sizes and the time needed to collect data. Numerical models have no such limitation and have been shown to be capable of accurately capturing turbine wake dynamics when compared with experimental data (e.g. Batten et al. (2013); Harrison et al. (2010); Masters et al. (2013); Nash et al. (2015)). When simulating the wake of a single turbine, Nash et al. (2015) found that velocity deficits of approximately 2% still persisted at 40RD and full recovery to free-stream levels did not occur until approximately 70RD.

Longitudinal wake deficit data from field studies is extremely limited but for typical operating conditions of the SCHOTTEL 50kW turbine Schmitt et al. (2015) measured near-field centreline deficits in the region of 0.6 immediately downstream of the turbine, and in the region of 0.4 at 2RD downstream. From the upstream and downstream velocity time-series data presented in Corren et al. (2013) for the field tests of Verdant Power's 5m diameter turbine, peak velocity deficits are estimated in the range of 0.2-0.25 at approximately 2RD downstream. Meanwhile, for the SeaGen device, Keenan et al. (2011) reported that there was no noticeable evidence

of the wake beyond 300m (approximately 7RD taking  $D$  = full device width of approximately 42m). These data suggest that full-scale turbine wakes at sea may be shorter than those recorded in labs. This may be due to the more constrained nature of the flows in test tanks and possibly higher levels of turbulence in the field affecting more wake mixing.

### ***Wake width and vertical profile***

The wake immediately downstream of a turbine will have approximately the same width as the turbine but will undergo lateral and vertical expansion with distance downstream due to turbulent mixing of the lower-velocity wake flow with the higher-velocity flow outside it. Expansion of the far-field wake will depend on ambient turbulence levels, surface constraint effects and shear effects (Bahaj et al. 2007).

The scale model studies of Stallard et al. (2013) and Stallard et al. (2015) measured velocity deficits laterally through the wake at various distances downstream of the turbine and recorded wake widths of approximately 1.5RD at 1.5RD downstream, 2RD at 4RD downstream and 3RD at 8RD downstream. In addition, they observed that the lateral wake profile was approximately symmetric and followed a nearly Gaussian profile, particularly from 4RD downstream (see Figure A.3 (a)). Nash et al. (2015) modelled the wake of a single turbine and observed the velocity deficits along various lateral transects (0RD, 2RD, 5RD, 40RD) through the wake. Their findings were generally in agreement with Stallard et al. (2013) and Stallard et al. (2015); the lateral wake profile was approximately Gaussian and the wake width increased from 2RD in the immediate near-field to 4RD at 5RD downstream. Beyond 5RD, the wake width did not undergo any further expansion before it had almost fully dissipated by about 40RD.

The vertical velocity profile of a single turbine (Figure A.3 (b)) has been shown to be asymmetrical about the wake centreline for the near-wake, with greater velocities occurring slightly above the centreline than below it (Maganga et al. (2010); Myers & Bahaj (2009); Stallard et al. (2013)). This causes the maximum deficit to occur slightly below the centreline - approximately  $0.1RD$  below according to Myers & Bahaj (2009) and Stallard et al. (2013). Myers & Bahaj (2009) concluded that this may be due to the combination of the turbulent shear layer and the bounding free surface forcing a greater proportion of flow over the disk. As the wake transitions between the near- and far-wake regions, the vertical profile becomes more symmetric and the profile becomes much flatter so that by  $12RD$  (Stallard et al. 2013) to  $15RD$  (Myers & Bahaj, 2009) downstream, the deficit is nearly constant over the wake depth.

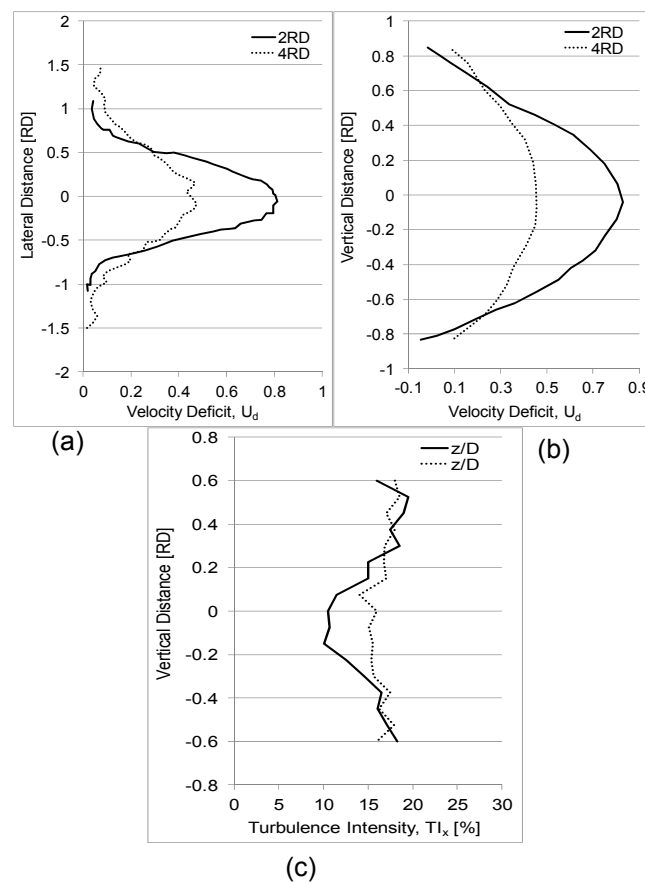


**Figure A.3: (a) Lateral profiles of  $U_d$ , (b) vertical profiles of  $U_d$  and (c) vertical profiles of  $TI_x$  at 2RD and 4RD downstream of a single scaled rotor (reproduced from Stallard et al. 2013).**

### **A.1.1.2 Accelerated Bypass Velocities**

The blockage to flow presented by the physical structure of a turbine and its support structure, and the slowing of water as it passes across the device, means that some flow will be diverted around the device, to the sides and/or possibly above/below. The 2RD velocity deficits in Figure A.3 (b) recorded by Stallard et al. (2013) show acceleration of flows above and below the scaled rotor in the range of 6-8%. Myers & Bahaj (2010) showed that acceleration of bypass flow in the vertical plane depends on the position of the rotor in the water column; they observed that flow acceleration occurred beneath rotors placed in the upper half of the water column but did not occur when the rotor was positioned in the lower half of the water column. During tests of a 1/30th scale turbine, Myers & Bahaj (2007) observed strong lateral bypass flows, with faster bypass flows observed for higher free-stream flow speeds, and concluded that increasing the area of a channel occupied by rotors will cause more extreme blockage-type effects such as flow acceleration around the sides of the rotors.

### **A.1.1.3 Turbulence**

Tidal turbine wakes are typically characterised by elevated turbulence levels. Sources of turbulence include the shear layer generated as a result of the velocity differences inside and outside the wake, the blade tips and the support structure. Turbulence levels are typically expressed as turbulence intensity,  $TI$ , defined as:

$$TI = \frac{\sigma}{\overline{U}_0} \quad (A.3)$$

where  $\sigma$  is the root-mean square of the turbulent velocity fluctuations and  $\overline{U}_0$  is the mean free-stream velocity.

Experiment results show that turbulence profiles are quite different in the near- and far-wakes. In the near-wake, turbulence levels are highest at the outsides of the wake due to the strong shear layer. Lateral and vertical profiles of  $TI$  will therefore have two peaks at the

edges of the wake (see Figure A.3 (c)). Further downstream, turbulent mixing of the wake and bypass flows mean that  $Tl$  levels within the wake become more uniform (Figure A.3 (c)). Stallard et al. (2015) showed that uniformity of turbulence levels throughout the wake had occurred by 10-12RD downstream and that  $Tl$  levels had returned to background levels (approximately 12%) by 12RD from initial highs in the near-wake of 22-23%. Stallard et al. (2015) also observed turbulence generated by the support structure in the immediate near-field (0.5RD) but this had dissipated by 1RD downstream.

#### **A.1.1.4 Water Levels**

In their laboratory test of a 1/30th scale rotor and support tower, Myers & Bahaj (2007) showed that water levels were affected by an increase in level upstream of the rotor and a decrease in level downstream of the rotor; these findings are in accordance with the theoretical model of Figure A.1. The upstream increase was approximately 10% of the free-stream level and was attributed to the blockage from the physical structure and the slowing of water across the turbine. The downstream drop persisted for 2RD in a free-stream flow speed of 1.8m/s and 5RD in a speed of 2.35m/s. The drop was approximately 12% at 1.8m/s and 25% at 2.35m/s but the 2.35m/s drop was enhanced as a result of the test set-up. The authors concluded that full-scale devices are unlikely to experience such extreme changes since Froude numbers at deployment sites would be expected to be much lower ( $<0.2$ ) than those occurring in their test tank given the much greater water depths at sea.

Divett et al. (2011) modelled a maximum 1m drop in water level (2% of water depth) across a 20m diameter turbine in 50m of water using the adaptive mesh flow solver, Gerris, whilst representing the turbines as rectangular areas of increased bed friction. On the upstream side, water level increased as one moved closer to the turbine. This was followed by the 1m drop in level across the turbine,

after which water levels began to increase again with distance downstream. Comparing water levels at 5RD upstream and downstream, the difference in levels was only of the order of 0.2-0.3m (approximately 0.5%) of the water depth which would be considered negligible.

### **A.1.2 Hydrodynamic Effects: Arrays**

The recorded hydrodynamic effects of a single turbine described above are unlikely to have any significant large-scale environmental effects beyond those in their immediate vicinity. However, the cumulative hydrodynamic effects of large numbers of turbines packed relatively closely together have the potential to be much greater than those of a single device and could therefore have greater environmental consequences. The most significant cumulative impacts are the greater levels of energy extraction and merging of individual turbine wakes resulting in greater potential for velocity and water level changes. The following sections summarise the findings of laboratory studies which have examined merging of turbines using small numbers (<10) of scaled turbines and, subsequently, numerical modelling studies that have examined the potential effects of much larger arrays.

#### **A.1.2.1 Wake Merging**

Stallard et al. (2013) studied the interactions between wakes of a single row of 2, 3 and 5 scaled, three-bladed rotors and found that for lateral spacings of 3RDs (between the centres of adjacent turbines) the wake of each rotor was very similar to that of an isolated rotor but for lateral spacings of 2RDs or less the wakes of adjacent turbines merged to form a single expanded wake. Myers & Bahaj (2012) noted similar results in their porous disc experiments as did Nash et al. (2015) in their numerical modelling study. Where merging occurred, Stallard et al. (2013) noted that the immediate near-field wakes were the same as those of isolated rotors, that merging began at about 2RDs downstream and that the wakes were fully merged by

6RDs downstream with lateral  $U_d$  profiles beyond that having a constant  $U_d$  throughout.

Myers & Bahaj (2012) investigated wake interactions for a two row array of porous discs comprising two upstream discs at 3RD lateral separation (centre-to-centre) and a 3rd disc placed 2.5RDs downstream and offset to intercept the bypass flow between the upstream discs. Inclusion of the third disc resulted in merging of the three wakes creating a much stronger far-field wake than for a single disc. The merged wake had an increased width which the authors concluded reduced the ability of the outer free-stream flow to penetrate to the wake-centreline resulting in a longer wake recovery.

Myers & Bahaj (2012) also observed that the lateral spacing between adjacent rotor discs could be optimised to achieve acceleration of the bypass flow between them. For a centre-to-centre spacing of 2.5RDs they achieved increased bypass velocities that resulted in a 22% increase in available kinetic energy. At spacings less than 2.5RD, the between-disc bypass flows were slowed to below free-stream levels due to wake merging.

#### **A.1.2.2 Array Effects on Velocities**

Nash et al. (2015) used a 2D, depth-averaged, nested far-field model to simulate an array of 24 turbines in an idealised channel. The nested grid spacing around the array was set to match the rotor diameter (10m) so that hydrodynamic interactions between turbines could be captured. Placing downstream turbines in the wakes of upstream turbines was shown to result in successively higher velocity deficits in each turbine wake due to the additional extraction of energy from the flow (Figure A.4). This 'inline' array resulted in less than optimum array performance as the positioning of downstream turbines in the wakes of their upstream neighbours resulted in reduced power availability to the downstream turbines. It was found

that accelerated bypass flows could be induced between turbines by using a lateral spacing of 4RD. By placing downstream turbines in a staggered manner to intercept the accelerated flows the staggered array captured significantly more energy than its inline counterpart but resulted in peak velocity deficits no greater than those of an isolated turbine. Maximum depth-averaged velocity deficits were in the region of 16% for the staggered array compared to 25-30% for the inline array. Thus, increased power extraction does not necessarily mean increased adverse impact. The results also show that the merging of the turbine wakes creates a combined array wake which creates sufficient blockage to induce accelerated bypass flows around the array.

Ramos et al. (2013) also used a 2D, depth-averaged, nested modelling approach to simulate the impacts of a tidal array in the Ria de Ribadeo estuary, Spain. The farm comprised eight 5m rotor diameter turbines deployed in three rows at 3RD spacing in both the lateral and longitudinal directions with the model grid spacing at the farm set to 5m to match the rotor diameter. High and low energy extraction scenarios were modelled using  $C_T$  values of 0.8 and 0.4, respectively. In both scenarios, array wakes were seen to extend significant distances upstream and downstream of the array; several kilometres in the case of the flood tide due to flood tide dominance. Not surprisingly, the velocity changes were greater for the high extraction case with velocity reductions as high as 10% (or 0.25m/s) from undisturbed speeds. Significant accelerations in bypass flows to either side of the array were observed for both extraction cases.

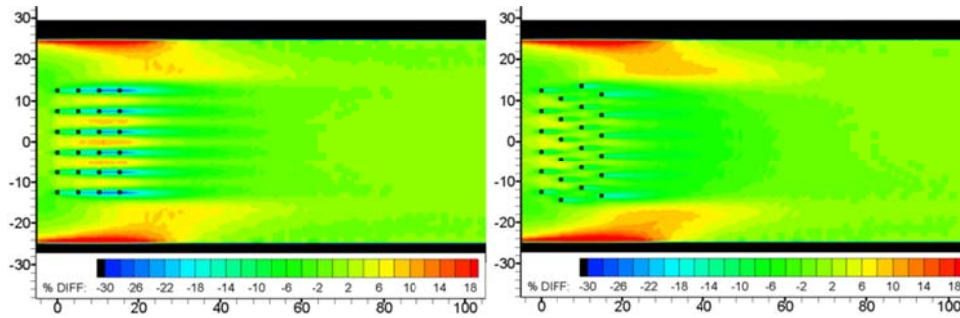


**Figure A.4: Changes in current speed for in-line and staggered arrays (Nash et al. 2015).**

Ahmadian et al. (2012) used a 2D depth-averaged model to simulate the impacts of an array of 2000 10m diameter turbines in the Severn Estuary, UK. The array was rectangular in shape covering an area roughly 7km x 1km meaning the turbine spacing was approximately 5RDs. The model grid spacing in the vicinity of the farm was 200m. The array resulted in significantly reduced current velocities inside the array and within the upstream and downstream array wakes with peak spring velocities being reduced from 2.0m/s to 1.5m/s. The model was run for a number of different values of  $C_p$ , from 0.25 to 0.45, (although it is unclear how  $C_p$  was related to  $C_T$ ) and, as would be expected, velocity reductions increased with increasing  $C_p$ . Accelerated flow speeds were again observed in the model either side of the array.

Plew & Stevens (2013) utilised a 2D, depth-averaged far-field model to assess the impacts of turbine arrays in Tory Channel, New Zealand. Turbines were simulated using a drag force distributed evenly over the extents of the array which was approximately 4km in length along the longitudinal channel axis. Different array capacities, from 5-1000MW, were simulated by varying the applied drag. Low capacity arrays had little effect on the flow velocities and only became significant at 50MW. For the 1,000MW array, the peak flow was reduced by 27%. Increasing the array capacity led to progressive slowing of flow speeds within the array and acceleration of flow speeds to either side of the array. It also resulted in more

persistent wake arrays. Fallon et al. (2014) also investigated the effect of array capacity / turbine density on hydrodynamic impacts. They modelled an array of 16m diameter turbines with the same array extents but different turbine spacings (0.5RD, 2RD and 5RD from blade tip-to-tip). The higher array densities resulted in greater velocity reductions within the array and in the upstream and downstream array wakes, and greater velocity accelerations around the array. 2,900MW-, 720MW- and 180MW-rated arrays affected reductions in peak velocities in the region of approximately 60%, 35% and 15% on the dominant ebb tide. Neill & Couch (2011) modelled 40MW and 120MW arrays in an idealised channel using a 2D depth-averaged model at 250m grid spacing. They found reductions of flow velocities within the array at peak tide conditions were of the order of 5% and 20% for small and large arrays, respectively, and that reductions were even higher in the array wakes, being of the order of 10% and 30%, respectively.

The general findings from the far-field models of tidal turbine arrays described above and others identified (e.g. Neill et al. (2012); Smith et al. (2013); Thiebot et al. (2015)) are that current velocities will be substantially reduced within the array and in the array wakes that will form upstream and downstream of the array, and that bypass flows will be accelerated around the array due to the blockage effects of the turbines and the slow moving water within the array and its wakes.

### **A.1.2.3 Array Effects on Water Levels**

A number of modelling studies have reported negligible changes in water levels due to turbine arrays. University of Massachusetts (2012) recorded just 3mm of surface elevation change in water depths of 15m from a model study of a proposed 5MW cross-flow turbine installation in the Muskeget Channel, New England, USA. Although negligible, the elevation changes were found to extend several kilometres in all directions from the installation. In their model

study, Ramos et al. (2013) noted increased water levels on the upstream side of their eight turbine array and reduced water levels on the downstream side, depending on the flood and ebb tides. The water level changes extended a significant distance upstream and downstream of the array. The maximum differences were in the region of 25mm for increases and 15mm for decreases and occurred in the immediate device-wakes; changes further afield were less than 10mm. Given that the local water depths were approximately 8m, the variations were considered negligible. In their idealised channel model study of 40MW and 120MW arrays, Couch & Bryden (2007) observed negligible changes in surface elevations (0.09% and 0.37%, respectively). For their model study of 2,000 turbines in the Severn estuary, Ahmadian & Falconer (2012) found that the maximum changes in water level in the vicinity of the array were less than 10cm and were thus negligible since local water depths were in the region of 20m. Plew & Stevens (2013) also recorded negligible changes in modelled water levels for their Tory Channel array, even for the largest array capacity of 1,000MW, and Smith et al. (2013) found that the changes in tidal elevations were only 0.5 to 1% of the tidal amplitudes in the natural case when modelling a linear array of turbines in the Minas Passage.

The common theme in the above studies is the relatively large spacing employed between turbines. The typical minimum spacing was 5RDs. In contrast, some studies have shown that when overly small spacings are used, then water level changes can be more significant and that the magnitudes of water level changes are also sensitive to the level of power extraction. Fallon et al. (2014) found that increasing the number and density of turbines in the Shannon estuary resulted in significant differences in the magnitudes of the resulting water level changes (Figure A.5). The highest density array (0.5RD spacing tip-to-tip) resulted in a 27% reduction in spring tidal range within the array but when a more realistic 5RD spacing was used the impact on water elevations was negligible. In all cases, the

arrays increased the low tide level and reduced the high tide level and the changes extended far upstream and downstream of the array. Hasegawa et al. (2011) showed that increasing the level of power extraction from the Minas Passage in the Bay of Fundy resulted in greater changes in water levels. The turbines were modelled using increased friction in a 3D model and a suite of models was run for different friction coefficient values (corresponding to 1.6GW, 3.6GW and 7.6GW of power extraction). The effects included a drop in water levels upstream of the array in the Bay of Fundy and an increase in water levels downstream of the array in the Gulf of Maine. The effects were negligible for 1.6GW extraction (approximately 3% of the  $M_2$  surface elevation amplitude in the Bay of Fundy) but 7.6GW extraction resulted in maximum decreases in the elevation amplitudes of the three major tidal constituents in the Bay of Fundy of about 2.4m for  $M_2$ , 0.49m for  $N_2$ , and 0.43m for  $S_2$ , and increases in the Gulf of Maine of up to 0.2m for  $M_2$  and 0.02m for  $N_2$  and  $S_2$ . Higher levels of extraction also resulted in a change in the phase of the tide upstream of the array due to the turbine drag; 7 GW extraction produced increases in phases of about  $25^\circ$  (or about 50 min) in the upper Bay of Fundy. Fallon et al. (2014) also noted a change in tidal phase for higher levels of power extraction.

In their Minas Passage study, Hasegawa et al. (2011) also investigated the effect of two different array configurations, one where turbines were considered to extend through the full water column and the other where the turbines were only placed in the lowest 20m of the water column. For the same level of power extraction (1.6GW), they noted that the latter configuration produced greater changes in water levels - a 5.8% reduction in  $M_2$  elevation amplitude in the Bay of Fundy compared to 3.4% for the former. This suggests that turbine placement within the water column could have a strong influence on the magnitudes of likely hydrodynamic impacts.

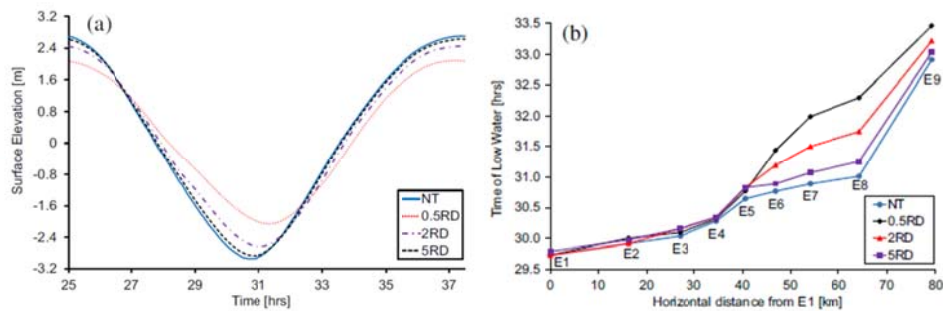


**Figure A.5: Comparison of water surface elevations inside array (NT = no tubrine, E1 = location at mouth of estuary) (Fallon et al., 2014).**

## A.2 Environmental Impacts of Tidal Turbines

The previous section showed that energy removal by tidal stream turbine arrays has the potential to considerably alter the existing velocities and water levels of tidal flows. Any changes to the prevailing hydrodynamics may in turn have consequential environmental impacts such as changes to mixing and transport processes which may affect water quality, or impacts on flora and fauna. Numerical models have been used to study the water quality impacts of tidal turbine arrays, primarily sediment transport impacts (Ahmadian et al. (2012); Ahmadian & Falconer (2012); Fairley et al. (2015); Gillibrand et al. (2016); Martin-Short et al. (2015); Mozafari (2014); Neill et al. (2009); Neill & Couch (2011); Neill et al. (2012); Robins et al. (2014); Sheng et al. (2012); Smith et al. (2013); Thiebot et al. (2015); University of Massachusetts (2012)) but also impacts on bacteria levels (Ahmadian et al. (2012); Ahmadian & Falconer (2012)), salinity and temperature levels (Sheng et al. 2012), flushing times (Nash et al. (2014); Yang et al. (2013)) and primary production (Sanderse 2009).

### A.2.1 Suspended Sediments

Sediment transport (bed load + suspended load) is a high order function of velocity ( $\sim U^{3.4}$ ) (Robins et al. 2014), and bed shear stress which plays an important role in sediment transport is a function of  $U^2$ ; therefore, even relatively small changes to current velocities

could have a measureable impact on sediment transport processes. In turn, changes to erosion/deposition patterns and bed levels may have consequential impacts on bed ecosystems.

In what was the first published study on the impacts of large-scale arrays of tidal turbines on sediment transport, Neill et al. (2009) used a 1D model of the Severn estuary/Bristol Channel to demonstrate that tidal stream energy extraction can affect the morphodynamics of a large-scale tidal system, particularly where energy is removed from a region of strong tidal asymmetry. They showed that energy removal from regions of tidal asymmetry by a relatively small 250MW array resulted in a 20% increase in the magnitude of bed level change (averaged over the length of the estuary) compared to the case where extraction took place in a region of tidal symmetry. Erosion and deposition patterns were affected over a region much larger than the extent of the array; changes in bed levels occurred up to 50km from the array. However, regardless of the location of a tidal stream farm within a tidal system, energy extraction was shown to reduce the overall magnitude of bed level change in comparison with non-extraction cases; this was thought to be due to the reduction in velocities (and thus net sediment transport) within the array and its upstream and downstream wakes.

Strong tidal flows past headlands and islands result in large eddy systems which can lead to the generation of sandbanks. Portland Bill in the English Channel, Admiralty Head in the Puget Sound, and flow past the island of Alderney in the Channel Islands are examples of such coastal flow systems that have also been identified as potential sites for tidal farms (by Batten et al. (2007); Myers & Bahaj (2005); Thyng & Riley (2010), respectively). Neill & Couch (2011) showed that while a 300MW array located in the vicinity of an idealised headland did not affect spatial deposition patterns, it did cause a 30% reduction in the magnitude of deposition at the centres of the sand banks relative to the no-turbine scenario. Neill et al. (2012)

modelled the impact of a 300MW array (200 x 1.5MW turbines) on sediment transport rates and changes in bed levels due to erosion/deposition near Alderney Island for two different deployment locations. Qualitatively, changes in transport rates were similar to the changes in velocity, i.e. transport rates were reduced where velocities were reduced within the array itself and within its flood and ebb wakes, and transport rates were increased in areas of accelerated bypass flows, particularly between the array and the island. The bed level changes were non-localised, with changes of around 0.01m occurring over a relatively large area (approximately 100km<sup>2</sup>), but particularly focussed at the sites of energy extraction. In addition, regardless of position, the array caused about 0.002m of erosion of the South Banks (located southwest of the array) over a spring-neap cycle, with a corresponding region of deposition located approximately 1km to the northeast of the array. The authors concluded that this demonstrates that over their lifetimes of 20-30 years, tidal arrays have the potential to significantly affect the long-term maintenance of sand banks.

Smith et al. (2013) found that when a linear array of turbines (capacity not specified) was placed in Minas Passage, sediment was found to move less actively at the turbine sites and in their wake flow areas due to the reduced velocities. The relative magnitudes of the reductions in transport rates were as high as 50%. Increases in transport rates occurred in the accelerated bypass flows between the array and the northern and southern coastlines with relative magnitudes of increases as great as 100%.

Ahmadian et al. (2012) and Ahmadian & Falconer (2012) modelled the impact of a number of tidal arrays (comprising 1000 and 2000 turbines) on suspended sediment concentrations in the Severn Estuary and Bristol Channel. Results showed a strong correlation between changes in suspended sediment levels and changes in velocities caused by the array with reduced sediment levels occurring

in areas of reduced velocities inside, upstream and downstream of the array, and elevated sediment levels in the areas of higher bypass velocities to the sides of the array. Changes to suspended sediments inside the array of 2000 turbines at times of peak flow were of the order of 25% reduction. The changes affected by the 1000 turbine array were also shown to be sensitive to the layout of the array. Changes in sediment levels were recorded up to 15km away from the array. According to Ahmadian et al. (2012) and Ahmadian & Falconer (2012), their results suggest that sediment deposition is likely to occur within, upstream and downstream of arrays, while erosion streams might be expected alongside arrays. This is confirmed by University of Massachusetts (2012) who recorded increases in bed level in the wake of a 5MW array placed in the Muskeget Channel, New England, USA, and decreases in bed level in the waters to either side of the array where bypass flows occurred.

Sheng et al. (2012) modelled the effect of power extraction (up to 7.1GW) on sediment transport processes in the Minas Passage between the Bay of Fundy and the Gulf of Maine by simulating the changes in bed shear stress. They showed that bed shear stresses could be significantly affected and that, as might be expected, the changes correlated with changes in velocities. Bed shear stresses were reduced in areas where velocities were reduced and were increased in areas where velocities were increased. Maximum changes were of the order of 1Pa for reductions in stresses, and 0.1Pa for increases.

Robins et al. (2014) and Martin-Short et al. (2015) both investigated the influence of array capacity on sediment transport. Robins et al. (2014) simulated the effects of an array deployed at a headland location off the northwest coast of Anglesey, Wales, where strong velocities and tidal asymmetries exist (Pingree & Griffiths, 1979). Using a 2D model of the Irish Sea, they studied effects on bed shear stress and bed load transport for arrays ranging from 10-300MW and

found that the sedimentary impacts of arrays less than 50MW were within the bounds of natural variability. At a location inside the array, changes to suspended load transport, bed stresses and bed load transport were approximately 1%, 2% and 4%, respectively, while at a similar location inside the 300MW array these changes were approximately 2%, 5% and 17%, respectively. The changes to velocities and sedimentary processes were found to be non-linear with respect to array capacity. In all cases, the changes to sediment load were less than those to velocities and the authors hypothesised that this was due to the increased turbulence from array operation in some ways counteracting the effect of reduced velocities. Ten km from the array, the changes to sedimentary processes were negligible (<1%), even for the 300MW array. Martin-Short et al. (2015) studied the effects of increasing numbers of turbine deployments (0-400 devices) on sediment transport on the Inner Sound of Stroma, in the Pentland Firth, Scotland, a region renowned for its large tidal currents. It was found that arrays in excess of 85 turbines have the potential to affect bed shear stress distributions in such a way that the most favourable sites for sediment accumulation migrate from the edges of the Inner Sound towards its centre. Deposits of fine gravel and coarse sand were indicated to occur within arrays of greater than 240 turbines with removal of existing deposits in the shallower channel margins also possible.

Also in the Pentland Firth, Fairley et al. (2015) studied the cumulative impact of a number of separate tidal turbine arrays on sediment transport in order to determine if the cumulative impact was greater than the sum of the individual array impacts. Using a 3D model, four arrays were simulated individually and collectively. The arrays comprised 200, 86, 95 and 66 turbines and were simulated using a drag-related momentum sink. Turbine spacing of 2.5RD and 10RD were used in the lateral and longitudinal directions. The results showed there was little difference (<2cm) between the bed level changes when the four arrays were included together and the sum of

the bed level changes resulting from the individual modelling of each array. This suggested that the combined impacts of arrays at the study site accumulated linearly. In addition, the differences in bed level changes with and without the arrays were less than 0.2m, which were negligible when compared to the natural changes of up to 5m that were simulated.

### **A.2.2 Tidal Flushing**

Tidal flushing is defined as the repeated exchange of inter-tidal water between a bay or an estuary and its receiving water body due to tidal flow. Coastal domains experience flushing due to the repeated circulation of water induced by tides, wind and density gradients (Dabrowski, 2005). Water is carried into an embayment during the flood tide and mixes with the existing water volume, the inter-tidal volume of water will then be carried out of the embayment on the ebb tide. Flushing is an important water parameter as it gives an indication of a water body's self-purification rate or ability to 'recover' (Nash, 2014).

A flushing study is a time-scale analysis which enables assessment of the exchange of water and sediment transport within a particular body of water. It can therefore be used to combine assessment of the impacts of energy extraction on hydrodynamics and water quality parameters.

There are a number of different factors that can be used to describe a water body's flushing ability. Dabrowski (2005) has distinguished nine important characteristics and defined them as follows:

- Flushing time,  $\tau_f$ : the time required to replenish existing freshwater in an estuary at a rate equal to the freshwater discharge.
- Flushing rate,  $F$ : the rate at which freshwater is exchanged with the sea.

- Average residence time,  $\tau_r$ : the expected amount of time a material exists in a specific region.
- Turn-over time,  $\tau_o$ : ratio of the total mass of the material within a reservoir to the total flux of the material.
- Age,  $\tau_a$ : the amount of time that has elapsed since the particle entered the reservoir.
- Transit time,  $\tau_t$ : the time interval for the material to pass from the inlet to the outlet.
- Estuarine residence time (*ERT*): the time required to flush a given fraction of water from the estuary, if it is initially uniformly distributed throughout the estuary.
- Pulse residence time (*PRT*): the time required to flush a conservative constituent from the estuary if it is introduced at a specific location as an instantaneous injection.
- Exchange per tidal cycle coefficient,  $E$ : fraction of water in a basin which is removed and replaced with ambient water during each tidal cycle.
- Flushing Efficiency,  $\chi$ : measure of the effectiveness of tidal flushing, expressed as the ratio of the exchange per tidal cycle coefficient to the tidal prism ratio.

Yang et al. (2013) and Nash et al. (2014) have investigated the potential effects of tidal arrays on flushing within estuaries dominated by strong tidal currents. Yang et al. (2013) used a 3D coastal model to simulate the effect of an array on the flushing time of an idealised tidal channel linked to an open bay. They showed that the average flushing time was significantly affected by energy extraction and increased non-linearly with respect to the number of turbines included in the array. The flushing time without any turbines was approximately 50 days; this was doubled to 100 days for an array of about 16 turbines and further doubled to 200 days for an array of 35 turbines. The flushing time was also shown to increase exponentially with the reduction in volume flux that arose as more energy was

removed. Nash et al. (2014) looked at the effect of arrays of different densities on local flushing times in the Shannon estuary, Ireland. They showed that the flushing time of the waters immediate to the array was increased as a result of the array and that the increase in flushing time was greater for higher numbers of turbines. However, they showed that using a relatively large spacing between turbines (5RD) significantly reduced the increase in flushing time even for very large numbers (1000s) of turbines.

### **A.2.3 Other Water Quality Measures**

The majority of bacteria living in tidal stream waters will become attached to sediments in the water body; thus, a direct interaction between the levels of suspended sediment and bacterial concentrations might be expected. In their modelling studies of array impacts in the Severn Estuary / Bristol Channel, Ahmadian et al. (2012) and Ahmadian & Falconer (2012) confirmed this expectation with increased faecal bacteria levels found in areas of increased suspended sediment levels (for example in the bypass flows to either side of the array) and decreased bacteria levels found in areas of decreased suspended sediments within the array and its wake. There were very strong similarities between the gradients and extents of the changes in bacteria levels to those of suspended sediments. Similar to suspended sediment impacts, Ahmadian et al. (2012) found that significant changes in bacteria concentrations existed up to 15km downstream from the array. Corren et al. (2013) examined the impacts of different array layouts and showed that higher density arrays (with smaller spacings between turbines) affected the greatest change in bacteria levels due to them also affecting the greatest change in velocities and suspended sediment levels.

In their study of the impacts of a tidal array in the Minas Passage, Sheng et al. (2012) investigated the possibility of changes to salinity and temperature. Results are only presented for two months (May

and August) and they show that the surface temperature of the waters in the Minas Passage and Basin, and upstream in the Bay of Fundy, are increased by 1-2°C whilst salinity levels are reduced slightly by about 0.3psu. The authors do not postulate as to the reason for the changes but they could have arisen due to a reduction in mixing due to reduced wake velocities.

According to Kadiri et al. (2012), since water quality parameters such as salinity, nutrient levels and bacterial concentrations are all interconnected, then an alteration to one will have a consequential effect on another. As an example, they state that changes in suspended sediment levels may lead to a change in the turbidity of a water body, thus affecting light penetration and primary production, and could also have implications for the sediment-attachment of metals, nutrients and pathogens in the water. Thus, the modelling of the impacts of tidal turbines on water quality parameters in isolation of each other, as many studies have done to date, cannot provide a complete picture and should be accompanied by full hydrodynamic-biogeochemical modelling. A good example of this is the work of Molen et al. (2016) who used a 3D combined hydrodynamic-biogeochemical model to assess the potential environmental impacts of a realistic 800MW array, and a massively expanded 8GW array, in the Pentland Firth. While the impacts of the 800MW array were negligible, the 8GW array resulted in up to 10% changes in ecosystem variables including reductions in bed shear stress and suspended particulate matter, and increased primary production, secondary production and benthic biomass due to increased light availability.

## **Appendix B: Recursion Formulae**

## B.1 Derivation of Continuity Equation Recursion Coefficients

### Continuity Equation

*Partial differential form:*

$$\frac{\partial \zeta}{\partial t} + \frac{\partial q_x}{\partial x} + \frac{\partial q_y}{\partial y} = 0 \quad (\text{B.4})$$

*Finite difference form:*

$$\zeta_{i,j}^{n+1/2} = \zeta_{i,j}^n - \frac{\Delta t}{2\Delta x} \left[ q_x \Big|_{i+1/2, j}^{n+1/2} - q_x \Big|_{i-1/2, j}^{n+1/2} + q_y \Big|_{i, j+1/2}^n - q_y \Big|_{i, j-1/2}^n \right] \quad (\text{B.5})$$

Rearrange (B.2) moving all unknowns to the left hand side, giving:

$$\zeta_{i,j}^{n+1/2} + \frac{\Delta t}{2\Delta x} \left[ q_x \Big|_{i+1/2, j}^{n+1/2} - q_x \Big|_{i-1/2, j}^{n+1/2} \right] = \zeta_{i,j}^n - \frac{\Delta t}{2\Delta x} \left[ q_y \Big|_{i, j+1/2}^n - q_y \Big|_{i, j-1/2}^n \right] \quad (\text{B.6})$$

Multiplying out left hand side:

$$-\frac{\Delta t}{2\Delta x} q_x \Big|_{i-1/2, j}^{n+1/2} + \zeta_{i,j}^{n+1/2} + \frac{\Delta t}{2\Delta x} q_x \Big|_{i+1/2, j}^{n+1/2} = \zeta_{i,j}^n - \frac{\Delta t}{2\Delta x} \left[ q_y \Big|_{i, j+1/2}^n - q_y \Big|_{i, j-1/2}^n \right] \quad (\text{B.7})$$

Replacing known terms in (B.4) gives:

$$-d_i q_x \Big|_{i-1/2, j}^{n+1/2} + e_i \zeta_{i,j}^{n+1/2} + f_i q_x \Big|_{i+1/2, j}^{n+1/2} = A_i^n \quad (\text{B.8})$$

where  $d_i$ ,  $e_i$  and  $f_i$  are recursion coefficients such that:

$$d_i = f_i = \frac{\Delta t}{2\Delta x} \quad (\text{B.9})$$

$$e_i = 1 \quad (\text{B.10})$$

and  $A_i^n$  is the combination of known variables

$$A_i^n = \zeta_{i,j}^n - \frac{\Delta t}{2\Delta x} \left[ q_y \Big|_{i, j+1/2}^n - q_y \Big|_{i, j-1/2}^n \right] \quad (\text{B.11})$$

## B.2 Derivation of X direction Momentum Equation Recursion Coefficients

### X direction Momentum Equation:

*Partial differential form:*

$$\frac{\partial q_x}{\partial t} + \beta \left[ \frac{\partial U q_x}{\partial x} + \frac{\partial U q_y}{\partial y} \right] = f q_y - g H \frac{\partial \zeta}{\partial x} + \frac{\rho_a C^* W_x (W_x^2 + W_y^2)^{\frac{1}{2}}}{\rho} - \frac{g U (U^2 + V^2)^{\frac{1}{2}}}{C^2} + 2 \frac{\partial}{\partial x} \left[ \epsilon H \frac{\partial U}{\partial x} \right] + \frac{\partial}{\partial y} \left[ \epsilon H \left[ \frac{\partial U}{\partial y} + \frac{\partial V}{\partial x} \right] \right] \quad (B.12)$$

*Partial differential form:*

$$\begin{aligned} q_x \Big|_{i+\frac{1}{2}, j}^{n+\frac{1}{2}} &= q_x \Big|_{i+\frac{1}{2}, j}^{n-\frac{1}{2}} \\ -\frac{\beta \Delta t}{2 \Delta x} &\left[ U' q_x \Big|_{i+1, j}^n - U' q_x \Big|_{i, j}^n + U' q_y \Big|_{i+\frac{1}{2}, j+\frac{1}{2}}^n - U' q_y \Big|_{i+\frac{1}{2}, j-\frac{1}{2}}^n \right] \\ + \Delta t f q_y \Big|_{i+\frac{1}{2}, j}^n &- \frac{g \Delta t}{2 \Delta x} H_{i+\frac{1}{2}, j}^n \left[ \zeta_{i+1, j}^{n+\frac{1}{2}} + \zeta_{i+1, j}^{n-\frac{1}{2}} - \zeta_{i, j}^{n+\frac{1}{2}} - \zeta_{i, j}^{n-\frac{1}{2}} \right] \\ + \frac{\rho_a \Delta t C^* W_x (W_x^2 + W_y^2)^{\frac{1}{2}}}{\rho} &- \frac{g \Delta t n^2 (U^{n+\frac{1}{2}} + U^{n-\frac{1}{2}}) (U'^2 + V^2)^{\frac{1}{2}}}{2 C^2} \Big|_{i+\frac{1}{2}, j}^n \\ + \frac{\Delta t}{\Delta x^2} \epsilon H_{i+\frac{1}{2}, j}^n &\left[ 2 \left( U'_{i+\frac{3}{2}, j} + U'_{i-\frac{1}{2}, j} \right) + U'_{i+\frac{1}{2}, j+1} + U'_{i+\frac{1}{2}, j-1} \right. \\ &\left. - 6 U'_{i+\frac{1}{2}, j} - V_{i, j+\frac{1}{2}} + V_{i, j-\frac{1}{2}} - V_{i+\frac{1}{2}, j-\frac{1}{2}} + V_{i+\frac{1}{2}, j+\frac{1}{2}} \right] \end{aligned} \quad (B.13)$$

Moving from the left hand side of the equation to the right hand side the terms represent the following:

- Local acceleration
- Advective accelerations
- Coriolis force

- Pressure gradient
- Wind shear force
- Bed shear resistance
- Turbulence induced shear force

Rearrange (B.10) moving all unknowns to the left hand side, giving:

$$\begin{aligned}
& q_x \Big|_{i+\frac{1}{2},j}^{n+\frac{1}{2}} + \frac{g\Delta t}{2\Delta x} H_{i+\frac{1}{2},j}^n \left[ \zeta_{i+1,j}^{n+\frac{1}{2}} - \zeta_{i,j}^{n+\frac{1}{2}} \right] \\
& + \frac{g\Delta t (q_x'^2 + q_y'^2)^{\frac{1}{2}}}{2(HC)^2} \Big|_{i+\frac{1}{2},j}^n q_x \Big|_{i+\frac{1}{2},j}^{n+\frac{1}{2}} = q_x \Big|_{i+\frac{1}{2},j}^{n-\frac{1}{2}} \\
& - \frac{\beta\Delta t}{2\Delta x} \left[ U' q_x \Big|_{i+1,j}^n - U' q_x \Big|_{i,j}^n + U' q_y \Big|_{i+\frac{1}{2},j+\frac{1}{2}}^n - U' q_y \Big|_{i+\frac{1}{2},j-\frac{1}{2}}^n \right] \\
& + \Delta t f q_y \Big|_{i+\frac{1}{2},j}^n - \frac{g\Delta t}{2\Delta x} H_{i+\frac{1}{2},j}^n \left[ \zeta_{i+1,j}^{n-\frac{1}{2}} - \zeta_{i,j}^{n-\frac{1}{2}} \right] \\
& + \frac{\rho_a \Delta t C^* W_x (W_x^2 + W_y^2)^{\frac{1}{2}}}{\rho} - \frac{g\Delta t (q_x'^2 + q_y'^2)^{\frac{1}{2}}}{2(HC)^2} \Big|_{i+\frac{1}{2},j}^n q_x^{n-\frac{1}{2}} \\
& + \frac{\Delta t}{\Delta x^2} \varepsilon H_{i+\frac{1}{2},j}^n \left[ 2 \left( U'_{i+\frac{3}{2},j} + U'_{i-\frac{1}{2},j} \right) + U'_{i+\frac{1}{2},j+1} + U'_{i+\frac{1}{2},j-1} \right. \\
& \left. - 6U'_{i+\frac{1}{2},j} - V_{i,j+\frac{1}{2}} + V_{i,j-\frac{1}{2}} - V_{i+1,j-\frac{1}{2}} + V_{i,j+\frac{1}{2}} \right]^n
\end{aligned} \tag{B.14}$$

Rearrange left hand side of (B.11) to give:

$$\begin{aligned}
& - \left[ \frac{g\Delta t}{2\Delta x} H_{i+\frac{1}{2},j}^n \right] \zeta_{i,j}^{n+\frac{1}{2}} + \left[ 1 + \frac{g\Delta t (q_x'^2 + q_y'^2)^{\frac{1}{2}}}{2(HC)^2} \Big|_{i+\frac{1}{2},j}^n \right] q_x \Big|_{i+\frac{1}{2},j}^{n+\frac{1}{2}} + \\
& \left[ \frac{g\Delta t}{2\Delta x} H_{i+\frac{1}{2},j}^n \right] \zeta_{i+1,j}^{n+\frac{1}{2}} = q_x \Big|_{i+\frac{1}{2},j}^{n-\frac{1}{2}}
\end{aligned}$$

$$\begin{aligned}
& -\frac{\beta\Delta t}{\Delta x} \left[ U' q'_x |_{i+1,j}^n - U' q'_x |_{i,j}^n + U' q'_y |_{i+\frac{1}{2},j+\frac{1}{2}}^n - U' q'_y |_{i+\frac{1}{2},j-\frac{1}{2}}^n \right] \\
& + \Delta t f q_y |_{i+\frac{1}{2},j}^n - \frac{g\Delta t}{2\Delta x} H_{i+\frac{1}{2},j}^n \left[ \zeta_{i+1,j}^{n-\frac{1}{2}} - \zeta_{i,j}^{n-\frac{1}{2}} \right] \\
& + \frac{\rho_a \Delta t C^* W_x (W_x^2 + W_y^2)^{\frac{1}{2}}}{\rho} - \frac{g\Delta t (q'_x{}^2 + q'_y{}^2)^{\frac{1}{2}}}{2(HC)^2} |_{i+\frac{1}{2},j}^n q_x^{n-\frac{1}{2}} \\
& + \frac{\Delta t}{\Delta x^2} \varepsilon H_{i+\frac{1}{2},j}^n \left[ 2 \left( U'_{i+\frac{3}{2},j} + U'_{i-\frac{1}{2},j} \right) + U'_{i+\frac{1}{2},j+1} + U'_{i+\frac{1}{2},j-1} - 6U'_{i+\frac{1}{2},j} \right. \\
& \left. - V_{i,j+\frac{1}{2}} + V_{i,j-\frac{1}{2}} - V_{i+1,j-\frac{1}{2}} + V_{i+1,j+\frac{1}{2}} \right]^n
\end{aligned} \tag{B.15}$$

Replacing the known terms in (B.12) gives:

$$-a_i \zeta_{i,j}^{n+\frac{1}{2}} + b_i q_x |_{i+\frac{1}{2},j}^{n+\frac{1}{2}} + c_i \zeta_{i+1,j}^{n+\frac{1}{2}} = b_i^n \tag{B.16}$$

where  $a_i$ ,  $b_i$  and  $c_i$  are recursion coefficients such that:

$$a_i = c_i = \frac{g\Delta t}{2\Delta x} H_{i+\frac{1}{2},j}^n \tag{B.17}$$

$$b_i = 1 + \frac{g\Delta t (q'_x{}^2 + q'_y{}^2)^{\frac{1}{2}}}{2(HC)^2} |_{i+\frac{1}{2},j}^n \tag{B.18}$$

And  $b_i^n$  is the combination of known variables:

$$\begin{aligned}
B_i^n &= q_x |_{i+\frac{1}{2},j}^{n-\frac{1}{2}} - \frac{\beta\Delta t}{\Delta x} \\
& \left[ U' q'_x |_{i+1,j}^n - U' q'_x |_{i,j}^n + U' q'_y |_{i+\frac{1}{2},j+\frac{1}{2}}^n - U' q'_y |_{i+\frac{1}{2},j-\frac{1}{2}}^n \right]
\end{aligned}$$

$$\begin{aligned}
& +\Delta t f q_y \Big|_{i+\frac{1}{2},j}^n - \frac{g\Delta t}{2\Delta x} H_{i+\frac{1}{2},j}^n \left[ \zeta_{i+1,j}^{n-\frac{1}{2}} - \zeta_{i,j}^{n-\frac{1}{2}} \right] \\
& + \frac{\rho_a \Delta t C^* W_x (W_x^2 + W_y^2)^{\frac{1}{2}}}{\rho} - \frac{g\Delta t (q_x'^2 + q_y'^2)^{\frac{1}{2}}}{2(HC)^2} \Big|_{i+\frac{1}{2},j}^n q_x^{n-\frac{1}{2}} \\
& + \frac{\Delta t}{\Delta x^2} \varepsilon H_{i+\frac{1}{2},j}^n \left[ 2 \left( U'_{i+\frac{3}{2},j} + U'_{i-\frac{1}{2},j} \right) + U'_{i+\frac{1}{2},j+1} + U'_{i+\frac{1}{2},j-1} \right. \\
& \left. - 6U'_{i+\frac{1}{2},j} - V_{i,j+\frac{1}{2}} + V_{i,j-\frac{1}{2}} - V_{i+1,j-\frac{1}{2}} + V_{i,j+\frac{1}{2}} \right]^n
\end{aligned} \tag{B.19}$$

### B.3 Recursion Equations:

Now take equations (B.13) and (B.5). The unknown values  $q_x$  and  $\zeta$  can now be determined by process of elimination of the unknowns. Starting with  $i = 1$  of an  $x$ -direction integration section and assuming that  $\zeta_{1,j}^{n+1/2}$  is an upper closed boundary and is therefore known, the unknown  $q_x \Big|_{1+\frac{1}{2},j}^{n+\frac{1}{2}}$  in (B.13) can be written as:

$$q_x \Big|_{1+\frac{1}{2},j}^{n+\frac{1}{2}} = -R_1 \zeta_{2,j}^{n+\frac{1}{2}} + S_1 \tag{B.20}$$

At  $i = 2$  the flux  $q_x \Big|_{1+\frac{1}{2},j}^{n+\frac{1}{2}}$  can be eliminated by substituting equation (B.17) into (B.5).  $\zeta_{2,j}^{n+1/2}$  can then be written in the form:

$$\zeta_{2,j}^{n+\frac{1}{2}} = -P_2 q_x \Big|_{2+\frac{1}{2},j}^{n+\frac{1}{2}} + Q_2 \tag{B.21}$$

At  $i = 3$   $\zeta_{2,j}^{n+1/2}$  can be eliminated by substituting (B.18) back into (A.13). The process continues for  $i = 1, \dots, i_{max}$  for the integration section. This process of elimination is called Gaussian elimination.

Using Gaussian elimination, the general recursive forms of the continuity and x-direction momentum equations can be written respectively as:

$$\zeta_{i,j}^{n+\frac{1}{2}} = -P_i q_x \Big|_{i+\frac{1}{2},j}^{n+\frac{1}{2}} + Q_i \quad (\text{B.22})$$

$$q_x \Big|_{i+\frac{1}{2},j}^{n+\frac{1}{2}} = -R_i \zeta_{i+1,j}^{n+\frac{1}{2}} + S_i \quad (\text{B.23})$$

where  $P_i$ ,  $Q_i$ ,  $R_i$ ,  $S_i$  are recursion terms computed at  $i = 2, \dots, i_{max}$  as follows:

$$P_i = \frac{f_i}{e_i + d_i R_{i-1}}; \quad Q_i = \frac{A_i^n + d_i S_{i-1}}{e_i + d_i R_{i-1}} \quad (\text{B.24})$$

$$R_i = \frac{C_i}{b_i + a_i P_i}; \quad S_i = \frac{B_i^n + a_i Q_i}{b_i + a_i P_i} \quad (\text{B.25})$$

If  $i = 1$  is an open water elevation boundary the recursion terms are computed as:

$$R_1 = \frac{C_1}{b_1} \quad S_1 = \frac{B_1^n + a_1 \zeta_{1,j}^{n+\frac{1}{2}}}{b_1} \quad (\text{B.26})$$

However, if  $i=1$  is an open flow boundary or a closed boundary then:

$$R_1 = 0 \quad S_1 = q_x \Big|_{\frac{1}{2},j_1}^{n+\frac{1}{2}} \quad (\text{B.27})$$

The value of  $q_x \Big|_{\frac{1}{2},j_1}^{n+\frac{1}{2}}$  is specified at a flow boundary or zero at a closed boundary.

$P_i$  and  $Q_i$  are not needed at  $i = 1$ .

At  $i = i_{max}$   $\zeta_{i_{max},j}^{n+\frac{1}{2}}$  in equation (B.17) can be expressed in terms of a single unknown value of  $q_x \Big|_{i_{max}+\frac{1}{2},j}^{n+\frac{1}{2}}$ , which is deduced from the

upper open boundary condition, hence  $\zeta_{imax,j}^{n+\frac{1}{2}}$  can be determined.

Backward substitution can then be used to determine  $q_x|_{i+\frac{1}{2},j}^{n+\frac{1}{2}}$  and  $\zeta_{i,j}^{n+\frac{1}{2}}$  for each  $i$  value.

#### B.4 DIVAST Representation:

In the DIVAST model water elevation  $\zeta_{i,j}^{n+\frac{1}{2}}$  is calculated first from (B.19), back substitution is then used to determine flux at the previous grid cell  $q_x|_{i-\frac{1}{2},j}^{n+\frac{1}{2}}$ . using equation (B.20)

The general form of the recursion equations are represented in DIVAST as follows:

$$\zeta_{i,j}^{n+\frac{1}{2}} = -P_i q_x|_{i+\frac{1}{2},j}^{n+\frac{1}{2}} + Q_i \quad \rightarrow EU(I,J) = -P(I) * QXU(I,J) + Q(I) \quad (B.28)$$

$$q_x|_{i-\frac{1}{2},j}^{n+\frac{1}{2}} = -R_{i-1} \zeta_{i,j}^{n+\frac{1}{2}} + S_{i-1} \quad \rightarrow QXU(IM1,J) = -R(IM1) * EU(I,J) + S(IM1) \quad (B.29)$$

The recursion terms  $P_i$ ,  $Q_i$ ,  $R_i$ ,  $S_i$ , are represented in DIVAST as follows:

$$P_i = \frac{f_i}{e_i + d_i R_{i-1}} \quad \rightarrow P_i = \frac{C1}{1 + C1.R_{i-1}} \quad (B.30)$$

$$Q_i = \frac{A_i^n + d_i S_{i-1}}{e_i + d_i R_{i-1}} \quad \rightarrow Q_i = \frac{A1 + C1.S_{i-1}}{1 + C1.R_{i-1}} \quad (B.31)$$

$$R_i = \frac{c_i}{b_i + a_i P_i} \quad \rightarrow R_i = \frac{D1DPC}{TEMP1} = \frac{D1DPC}{(1 + D4BDFR) + D1DPC.P_i} \quad (B.32)$$

$$S_i = \frac{B_i^n + a_i Q_i}{b_i + a_i P_i}$$

$$\rightarrow S_i = \frac{BI + D1DPC.P_i}{TEMP1} = \frac{BI + D1DPC.q_i}{(1 + D4BDFR) + D1DPC.P_i} \quad (B.33)$$

From equations (B.31) – (B.34) it can be seen that the model representations of the recursive coefficients  $a_i$ ,  $b_i$ ,  $c_i$ ,  $d_i$ ,  $e_i$ ,  $f_i$ ,  $A_i$ ,  $B_i$  are as follows:

$$a_i = c_i = D1DPC \quad (B.34)$$

$$b_i = 1 + D4BDFR \quad (B.35)$$

$$d_i = f_i = C1 \quad (B.36)$$

$$e_i = 1 \quad (B.34)$$

$$A_i^n = AI \quad (B.37)$$

$$B_i^n = BI \quad (B.38)$$

For the special case  $i = 1$ ,  $R_i$  and  $S_i$  are expressed as follows:

$$R_1 = \frac{c_1}{b_1} \rightarrow R_i = \frac{D1DPC}{TEMP1} = \frac{D1DPC}{1 + D4BDFR} \quad (B.39)$$

$$S_i = \frac{B_1^n + a_1 \zeta_{1,j}^{n+\frac{1}{2}}}{b_1} \rightarrow S_i = \frac{BI + D1DPC.EU(I,J)}{TEMP1} = \frac{BI + D1DPC.EU(I,J)}{(1 + D4BDFR)} \quad (B.40)$$

## **Appendix C: Method of Least Squares Fit for Tidal Harmonic Analysis**

### C.1 Derivation of Least Squares Matrix

The tidal signal  $y_i = \sum_{j=1}^N A_j \cos[2\pi(\delta_j t_i - \theta_j)]$  cannot be solved as it is over-determined, hence the least squares technique is applied as an optimisation criterion and the signal equation is re-expressed as

$$\sum_{j=1}^N C_j \cos(2\pi\delta_j t_i) + S_j \sin(2\pi\delta_j t_i) \quad (C.1)$$

where  $A_j = (C_j^2 + S_j^2)^{\frac{1}{2}}$  and  $2\pi\theta_j = \arctan S_j/C_j$  allowing the parameters  $S_j$  and  $C_j$  to be solved as the fitting function is linear.

The objective of the least squares technique is to minimise

$$T = \sum_{i=1}^N \left[ y_i - \sum_{j=1}^N (C_j \cos(2\pi\delta_j t_i) + S_j \sin(2\pi\delta_j t_i)) \right]^2 \quad (C.2)$$

Letting:

$$C_k = \sum_{i=1}^N \cos 2\pi\delta_k t_i \quad (C.3)$$

$$S_k = \sum_{i=1}^N \sin 2\pi\delta_k t_i \quad (C.4)$$

$$CC_{kj} = \sum_{i=1}^N (\cos 2\pi\delta_k t_i)(\cos 2\pi\delta_j t_i) = CC_{jk} \quad (C.5)$$

$$SS_{kj} = \sum_{i=1}^N (\sin 2\pi\delta_k t_i)(\sin 2\pi\delta_j t_i) = SS_{jk} \quad (C.6)$$

$$CS_{kj} = \sum_{i=1}^N (\cos 2\pi\delta_k t_i)(\sin 2\pi\delta_j t_i) = SC_{jk} \quad (C.7)$$

The matrix equation  $Bx = y$  resulting from the least squares fit for constituent amplitudes and phases can be expressed as:

$$\begin{pmatrix} N & C_1 & C_2 & \dots & C_M & S_1 & S_2 & \dots & S_M \\ C_1 & CC_{11} & CC_{12} & \dots & CC_{1M} & CS_{11} & CS_{12} & \dots & CS_{1M} \\ C_2 & CC_{21} & CC_{22} & \dots & CC_{2M} & CS_{21} & CS_{22} & \dots & CS_{2M} \\ \vdots & \vdots & \vdots & \ddots & \vdots & \vdots & \vdots & \ddots & \vdots \\ C_M & CC_{M1} & CC_{M2} & \dots & CC_{MM} & CS_{M1} & CS_{M2} & \dots & CS_{MM} \\ S_1 & SC_{11} & SC_{12} & \dots & SC_{1M} & SS_{11} & SS_{12} & \dots & SS_{1M} \\ S_M & SC_{M1} & SC_{M2} & \dots & SC_{MM} & SS_{M1} & SS_{M2} & \dots & SS_{MM} \end{pmatrix} \begin{pmatrix} C_0 \\ C_1 \\ C_2 \\ \vdots \\ C_M \\ S_1 \\ S_2 \\ \vdots \\ S_M \end{pmatrix} = \begin{pmatrix} \sum_{i=1}^N y_i \\ \sum_{i=1}^N y_i \cos 2\pi\delta_1 t_i \\ \sum_{i=1}^N y_i \cos 2\pi\delta_2 t_i \\ \vdots \\ \sum_{i=1}^N y_i \cos 2\pi\delta_M t_i \\ \sum_{i=1}^N y_i \sin 2\pi\delta_1 t_i \\ \sum_{i=1}^N y_i \sin 2\pi\delta_2 t_i \\ \vdots \\ \sum_{i=1}^N y_i \sin 2\pi\delta_M t_i \end{pmatrix} \quad (C.8)$$

For  $C_0$  and all  $C_j, S_j, j=1, M$ . This is done by solving the simultaneous equations for  $j=1, M$ .

$$0 = \frac{\partial T}{\partial C_0}$$

$$= 2 \sum_{j=1}^N (y_i - C_0 - \sum_{j=1}^M C_j \cos 2\pi \delta_j t_i - \sum_{j=1}^M S_j \sin 2\pi \delta_j t_i) (-1) \quad (\text{C.9})$$

$$0 = \frac{\partial T}{\partial C_0}$$

$$= 2 \sum_{j=1}^N (y_i - C_0 - \sum_{j=1}^M C_j \cos 2\pi \delta_j t_i - \sum_{j=1}^M S_j \sin 2\pi \delta_j t_i) (-\cos 2\pi \delta_j t_i) \quad (\text{C.10})$$

$$0 = \frac{\partial T}{\partial C_0}$$

$$= 2 \sum_{j=1}^N (y_i - C_0 - \sum_{j=1}^M C_j \cos 2\pi \delta_j t_i - \sum_{j=1}^M S_j \sin 2\pi \delta_j t_i) (-\sin 2\pi \delta_j t_i) \quad (\text{C.11})$$